SIMULATION BASED STRATEGIES FOR CLINICAL TRANSLATION OF MAGNETIC NANOPARTICLE HYPERTHERMIA

by

Sri Kamal Kandala

A dissertation submitted to The Johns Hopkins University in conformity with the requirements for the degree of Doctor of Philosophy

Baltimore, Maryland

September, 2017

Abstract

Magnetic nanoparticles have gained significant importance in the recent past for their use in biomedical applications such as drug delivery, imaging, diagnosis, and therapy. Magnetic nanoparticle hyperthermia is the selective heating of tumor tissue using magnetic nanoparticles which generate heat when exposed to an alternating magnetic field. It is a minimally invasive method which can cause effective and localized tumor thermal damage. The challenge to achieve consistent heating with this modality is the variable distribution upon delivery, which results in variable heat distribution in the tumor and surrounding normal tissue.

In this thesis, using computational methods we explore optimization strategies to modulate magnetic field amplitude using limited temperature feedback to achieve clinically effective thermal dose in tumor and minimize healthy tissue damage. The magnetic field amplitude is modulated by using a Proportional-Integral-Derivative (PID) controller based on temperature feedback from tumor-healthy tissue boundary. We

consider nanoparticle distributions obtained from animal studies and idealized mathematical constructs. Two and three dimensional (2D & 3D) models of tumor and healthy tissue were considered. Temperature effects on perfusion were considered. Results of thermal damage, temperature distributions and thermal dose obtained from modulated power heating were then compared to constant power heating. It is shown that controlling the tumor-healthy tissue boundary temperature by modulating the heating power of the nanoparticles can compensate for variable nanoparticle distributions to deliver effective treatment. The strategy was then implemented in mouse models of liver cancer. Two nanoparticle distributions were generated by using two injection methods. It was shown that the temperature at the tumor-healthy tissue boundary can be consistently controlled for the two nanoparticle distributions. The challenges associated with implementation of our proposed strategy have been identified and future steps for further accurate testing have been presented.

Another challenge for magnetic nanoparticle hyperthermia is the onset of eddy current heating when the treatment modality is applied to tumors in large organs. Monitoring of eddy current heating in *in vivo* studies is challenging. Hence, we developed a computational tool which couples thermal and electromagnetic modeling to predict the temperatures achieved due to eddy current heating. The model was verified with the analytical solution and validated with gel phantom experiments. We then implemented it to generate 3D liver model from computed tomography (CT) images of rabbit liver. The temperatures attained due to eddy current heating from exposure to alternating magnetic fields were calculated to demonstrate the utility of the model in estimating temperature during magnetic nanoparticle hyperthermia of large organs.

In the last chapter, we characterized the thermal and magnetic properties of dual contrast nanoparticle formulations used in image guided thermal therapy of liver cancer. Dual contrast nanoparticle formulations are magnetic iron oxide nanoparticles combined with lipiodol. The heating potential of these lipiodol nanoparticle formulations was extensively characterized by measuring their thermal properties at fixed frequency with different magnetic field amplitudes. These were then compared to original aqueous formulations for assessing the differences between both the formulations. Bulk magnetic properties of both the formulations was measured and compared. It is observed that when nanoparticles are mixed with lipiodol, the specific loss power of these particles is reduced. These results highlight the importance of evaluating the heating performance of new nanoparticle formulations.

Advisor and Primary Reader: Robert Ivkov

Co-Advisor and Secondary Reader: Louis Whitcomb

Tertiary Readers: Gretar Tryggvason, Anilchandra Attaluri, Cindi Dennis, Eleni Liapi

.

Acknowledgements

I wish to express my sincere gratitude to all the people who have helped me in different ways, throughout my time as a graduate student at Johns Hopkins. First and foremost, I would like to express my sincere thanks and gratitude to my advisor, Dr. Robert Ivkov, for his support and for giving me the unique opportunity to work on projects which spanned multiple fields – from engineering, physics to biology. It has been a great privilege to work under him and one that I will remember throughout my life.

I would like to thank Professor Louis Whitcomb for his immense support and guidance and for serving on my dissertation committee. I am grateful to Dr. Anilchandra Attaluri for introducing me to Rob, without which none of this work would have been possible. I also thank him for all the insightful discussions, guidance and for serving on my dissertation committee. I thank Dr. Cindi Dennis for providing the magnetic characterization data for the lipiodol formulations and also for her helpful comments and

thorough review of my thesis. Finally, I would like to thank Prof. Gretar Tryggvason and Dr. Eleni Liapi for being on my dissertation committee and providing me their insights and comments. I would also like to thank Steven Marra for the opportunity to work under him as a teaching assistant for almost four years. I thank him very much for his support and it is only because of him that I discovered my love for teaching.

I would like to thank all the past and present members of Ivkov's lab for their support. I would especially like to thank Haoming Zhou (for teaching me cell culture and animal work), Preethi Korangath (for her support and guidance especially in animal experiments), Anirudh Sharma (for his assistance and support), Jackie Stewart (for making sure that I have everything), Frederik Soetaert, Rajeev Hatwar, James Barnett, Elizabeth Henderson, Arlene Oei, Chun-ting Yang, and Mikko Helenius.

My life at Hopkins would not have been enjoyable without the company and support of my friends. To my friends, Kaushik, Prakruthi, Vignesh, Kiran, Kavita, Venkat, Sayee, Aditya, Ismail, Akanksha, Leen, and many more. Thank you for your constant support and for all the fun memories, which I will cherish forever. Finally, I would like to thank my family for their love, affection, and support through all these years. I cannot express my gratitude in words for all the sacrifices my mother made, for making me what I am today. And most of all my heartfelt thanks to my wonderful wife Sugathri, for being my greatest support in every aspect of my life. Thank you!

Dedication

I would like to dedicate my dissertation,

To my parents, especially my mother for her endless love, support, and sacrifices;

To my wife for always being there for me.

Contents

List of Tables

List of Figures

Chapter 1

Introduction

1.1 Cancer

Cancer is one of the major health problems worldwide and is the second leading cause of death in the United States [1]. In 2017, a projected 1.7 million new cancer cases and 0.6 million cancer deaths are expected to occur in the United States [1]. The World Health Organization estimated in 2011 that cancer causes more deaths than coronary heart disease or all stroke [2]. With the continuing global demographic and epidemiologic transitions, cancer burden is expected to increase across the world with over 20 million new cancer cases projected annually from 2025 [2]. In the coming decades, cancer is set to become the major source of morbidity and mortality across the whole world [3]. In the United States alone, nearly $125 billion was spent for cancer in 2010 which is expected to

go up to $156 billion in 2020 [4]. In the past century, significant research efforts have been focused on understanding cancer and developing treatments. The recently launched Cancer Moonshot^{SM} [5] initiative launched by the National Cancer Institute to accelerate cancer research highlights this importance.

Current standard therapies for cancer include surgery, radiation therapy, chemotherapy, or a combination. Surgery involves complete or partial removal of cancerous tumor from the body. Radiation therapy is the use of ionizing radiation such as x-rays, gamma rays, electron beams, or protons, to destroy cells by inflicting DNA damage [6]. Chemotherapy is the use of chemotherapeutic agents such as cisplatin, doxorubicin, for destroying cells by altering or damaging their DNA. They achieve this by binding to DNA resulting in crosslinking of DNA inhibiting replication, repair, and/or synthesis [7,8]. These standard therapies have multiple drawbacks and have not been entirely successful in treatment of all types of cancers. For surgery, the location of tumor can pose difficulty in complete removal of cancerous tissue. Additionally, during or post-surgery, infections, blood clots and other complications are possible. Radiation therapy can cause damage to surrounding healthy tissue, resulting in fibrosis, fatigue, and has even the potential to cause secondary cancer [6]. Common side effects for chemotherapy include fatigue, pain, mucositis, diarrhea, hair loss, loss of appetite, and nerve damage, depending on the drug used. Also, cancer cells are known to develop resistance to chemotherapeutic drugs and sometimes a patient's condition can preclude them from standard treatments. Thus, many research efforts are currently focused on developing alternative treatment strategies which can complement these standard therapies or can be stand-alone therapies. With advances

in science and technology, hyperthermia, one such alternative treatment strategy, has gained prominence.

1.2 Hyperthermia

Hyperthermia cancer therapy involves raising and sustaining the temperature of malignant tumors and adjacent tissues to about 41 - 45 ºC for 30-60 min, to achieve a therapeutic thermal effect (dose) [9,10]. While hyperthermia is generally defined as heat treatment in the temperature range of 41 – 45 °C, there are other definitions based on temperature that is applied. For temperatures in the range of 39 – 41 °C, it is defined as mild/low temperature hyperthermia and for temperatures > 45 °C, it is defined as thermal ablation [11,12].

1.2.1 History of hyperthermia

The benefits of heat as a therapeutic agent have been recognized since the early ages by Romans, Greeks, Indians, and Egyptians, and is probably one of the oldest cancer therapies known [13]. The earliest recorded application dates back to 5000 years ago, when Egyptians treated breast cancer with heat [13,14]. In 3000 BC, Indian physicians used hyperthermia as part of a five stage clinical process known as Panchakarma prescribed for purificatory, curative or nutritional purposes [15]. In ancient Rome, Cornelius Celsus Aulus, a Roman encyclopedic doctor (25 BC – 50 AD), was the first one to note that first stages of cancer are extremely thermosensible [16]. In the middle ages, fever was considered to be an agent of purification and detoxification of the body. However, this enthusiasm in hyperthermia diminished after Ambriose Paré reported the negative consequences due to cauterization of wounds in 1537. Later in the 17th century, many

instances of spontaneous tumor regression in patients with malaria, smallpox, influenza, tuberculosis, accompanied by fever, were reported [13,16].

Interest in hyperthermia was again revived in the 19th century when Carl Busch published the first paper on hyperthermia claiming that fever caused by erysipelas cured the sarcoma on the face of a 43-year old woman [16]. Westermark was the first person to deliberately use hyperthermia for treatment of cancer, when he used circulating water cisterns at 42 - 44 °C to treat inoperable carcinomas of the uterus [13,16]. With reports from the 17th century and work by Busch, further studies were based on observations that febrile diseases can cause tumors to shrink. Based on this, Friedrich Fehleisen infected patients with bacteria causing erysipelas to treat cancer. William Coley then treated almost 900 inoperable cancer patients with bacterial extracts called Coley's toxins, inducing fever and achieving more than 60% regression rate and 20% cure rate [17]. Despite initial promise, the lack of better technologies and temperature measurement techniques reduced the use of hyperthermia for cancer treatment.

However, the development of radiation therapy for cancer and the role of hyperthermia in increasing the sensitivity to radiation therapy, reinvigorated the interest in hyperthermia [12,14]. This led to multiple clinical and fundamental studies which resulted in new heating technologies being developed. Multiple *in vitro* and *in vivo* studies were carried out to show the potential of hyperthermia as a sensitizer for both radiation therapy and chemotherapy. The fundamental concepts of thermal dose and mechanisms of hyperthermia were developed. In the period 1981-1984, the three hyperthermic oncology societies in the United States, Europe, and Japan were formed [16]. This further catalyzed the interest in hyperthermia and led to multiple research studies. However, the lack of

proper heating equipment and temperature monitoring methods, led to ambiguous clinical reports dampening the interest in hyperthermia [14]. Since the start of the 21st century, advancements and availability of better technology led to a resurgence in hyperthermic research [14].

As mentioned hyperthermia is distinguished based on temperature as, mild/low temperature hyperthermia (39 – 41 °C), hyperthermia (41 – 45 °C), and ablation (> 45 °C). Other than temperatures, hyperthermia is also distinguished based which body part is treated. When the complete body is increased to an elevated temperature, usually in the mild hyperthermic temperature range, it is called as whole body hyperthermia. Regional hyperthermia is the increase of temperature regionally in an isolated part of body, such as body cavity, limb, or organ. Local hyperthermia is when only the tumor is heated [12]. Based on these distinctions multiple technologies have been developed. We review these technologies in the next subsection. Before reviewing the mechanisms to deposit heat at various tissue/organ levels, we need to understand the significance of hyperthermia as a potent sensitizer for radiation therapy and chemotherapy.

1.2.2 Synergy with radiation therapy and chemotherapy

Hyperthermia is one of the most effective radiation sensitizers known [13]. In *in vitro* studies, it has been shown that hyperthermia and radiation act in a synergistic way [18] and this happens in all cells, both normal and neoplastic [13]. This synergy is influenced by multiple factors such as temperature, heating time, sequence, and time interval between the two treatments. It has been shown that higher temperature results in larger sensitization to radiation while a similar increase effect with saturation was observed

for treatment time. Simultaneous hyperthermia and irradiation has proven to be most effective for cells and as the gap between radiation therapy and hyperthermia increases, the effect decreases [13]. The mechanism by which heat sensitizes cells to radiation damage is by interfering with the cells ability to repair DNA damage induced by radiation.

In vivo hyperthermia sensitizes tumors to radiation therapy by inhibition of DNA repair processes and/or by tumor reoxygenation [13,19]. Tumor vascular structure is structurally and functionally abnormal when compared to the normal tissue [13]. It is characterized by oxygen depletion, high lactate levels, glucose deprivation, significant interstitial fluid flow, and pressure [20]. The imbalance between blood perfusion and consumption leads to hypoxic and anoxic conditions. Cells that survive in these conditions are referred to as hypoxic cells and have been known to have a significant negative effect on the tumor response to radiation therapy [13]. Hyperthermia increases the blood flow resulting in tumor reoxygenation, thereby sensitizing the tumor for radiation therapy [21]. Datta et al. [14] analyzed clinical outcomes from 38 clinical trials conducted between 1987 and 2014, comparing radiotherapy with thermoradiotherapy (hyperthermia + radiation therapy) in various tumors sites namely: breast, cervix, head and neck, rectum, urinary bladder, esophagus, lung, skin, melanoma, choroidal melanoma, and other sites. They showed that an overall complete response of 54.9% was observed with thermoradiotherapy compared to 39.8% with radiation therapy alone [14]. No significant increase in acute or late toxicity was evident from these studies [14].

Thermal enhancement ratio (TER) is often used to express the synergy between hyperthermia and radiation, and hyperthermia and chemotherapy. It is defined as the ratio of radiation or chemotherapy dose required to produce a given level of biological damage

with versus without heat [22]. Most clinical studies have reported a TER of 1.5 indicating the synergy of hyperthermia with radiotherapy and chemotherapy.

Hyperthermia has also been known to significantly enhance the effectiveness of several chemotherapeutic drugs [21]. The proposed mechanisms for interaction between hyperthermia and chemotherapeutic drug action are increased drug uptake, increased DNA and protein damage, and other pharmacological changes [21]. The damage to cell membranes by hyperthermia results in increased permeability of the membranes leading to increased drug uptake. Additionally, as mentioned previously hypoxic tumor regions have less blood supply leading to lower uptake of cytotoxic drugs. These regions are more sensitive to hyperthermia, plus hyperthermia increases blood flow to these regions, resulting in increased drug uptake [19,23]. Hyperthermia is also known to have the ability to reverse the resistance to certain chemotherapeutic drugs such as methotrexate, cisplatin, and mitomycin-C [19]. In clinical studies, the efficacy of chemotherapy and loco regional hyperthermia was evaluated. The recurrence rate for 83 intermediate/high risk non-muscle invasive bladder cancers reduced from 80% treated with mytomycin-C alone to 40% treated with hyperthermia and mytomycin-C and disease free survival increased from 15% to 53% with thermochemotherapy [14]. These results show that combining hyperthermia with radiation therapy and/or chemotherapy enhances the effectiveness of both the treatments.

1.2.3 Thermal dose

For comparison of hyperthermic treatments, a thermal dose parameter needs to be defined. Hyperthermia treatments are performed at different temperatures and with different treatment times. An appropriate dose parameter is needed to compare the

effectiveness of these treatments [24]. The main requirements of a thermal dose parameter are that it should provide a means for predicting a treatment outcome as a function of applied hyperthermia treatment, allow for comparison of treatment responses at different temperatures and times, should be related to the biological mechanisms involved and should be a physical quantity which is measurable and well-defined [24]. The complexity of the biological effects of hyperthermia makes it difficult to define a single dose parameter that satisfies all the above requirements. However, two thermal dose models are extensively used in the hyperthermia community. Both of these models are based on the assumption that hyperthermia causes death of cells by an irreversible process, described by a first-order chemical reaction [25–27].

The thermal isoeffective dose (TID) model was proposed by Sapareto et al. [25] based on their *in vitro* clonogenic survival experiments carried out on Chinese Hamster Ovary (CHO) cells exposed to heat. Clonogencity is the ability of cells to divide and form colonies and the clonogenic survival assay tests for the cell's ability to divide [28]. The thermal isoeffective dose is a normalizing method for comparing the cytotoxic effects of different temperatures and times. It normalizes these thermal histories by converting heat exposures at different temperatures and exposure times, to an equivalent exposure time at 43 °C. The reference temperature was chosen to be 43 °C, as their original measurements show a break point in the survival curves at that temperature [25]. This equivalent exposure time at 43 °C, referred to as cumulative equivalent minutes at 43 °C, CEM43 is given by

$$CEM43 = \int_0^t R_{CEM}^{[43-T(\tau)]} d\tau \tag{1.1}$$

where $T(\tau)$ is the temperature at any time τ and R_{CEM} is the ratio of exposure times required to result in the same survival for a 1°C rise in temperature [29]. The values of R_{CEM} are

0.25 for $T \leq 43$ °C and 0.5 for $T > 43$ °C, which were based on the CHO experiments [25]. The TID model only converts different thermal histories into equivalent minutes of exposure at 43 °C. It cannot predict the outcome or survival fraction after the treatment. For clinical application, minimum thresholds are often used for comparison. Since the temperatures throughout the tumor can vary significantly ($\Delta T \sim 4 - 5$ °C) during a heat treatment, it is important to establish criteria to compare these treatments [30,31]. T_{90} is the criteria often used, where T_{90} is the temperature attained by 90% of tumor volume. A similar criteria *CEM43T90* often used in clinical experiments for thermal dose comparison.

The Arrhenius thermal damage model is based on the assumption that thermally induced cell injury is a first order irreversible kinetic process and the resultant cell survival fraction is given by,

$$S = e^{-\int_0^t k d\tau} \tag{1.2}$$

$$k = Ae^{-\left(\frac{\Delta E_a}{RT}\right)} \tag{1.3}$$

where S is the cell survival fraction after heating at temperature T (K), A is the frequency factor (s^{-1}), ΔE_a the activation energy (J/mol) and R is the universal gas constant (8.314 J/ (mol-K)). Survival fraction is the ratio of the living cells at a given time point and the initial concentration. The parameters A and ΔE_a will need to be determined experimentally [27]. They are often determined by conducting multiple isothermal experiments and plotting the survival fraction with time to determine k and then plotting the natural logarithm of k versus the inverse of temperature. Then the two model parameters A and ΔE_acan be determined by doing a linear fit with A being the intercept and ΔE_abeing the slope [27].

Both thermal damage models have been extensively used for hyperthermia studies. The thermal isoeffective dose (TID) is the standard thermal dose measure for clinical studies [30,32]. The Arrhenius thermal damage is mostly used for predicting the survival fraction / thermal damage for thermal ablation [27]. Despite the different approaches, both models are based on the same assumptions that cell killing is a first-order irreversible chemical reaction [26,29,30]. The TID model is derived from the Arrhenius thermal damage model but leads to different results because of some assumptions and simplifications [25,27,30].

There are several limitations for both the models. The models predict cell killing to be an irreversible first order chemical process. However, cell killing is a complex reaction with multiple pathways [24,29]. Moreover, the models neglect the initial shoulder region in the clonogenic survival and only model the exponential region. This can result in overestimation of thermal damage at lower temperatures. They also predict that cell killing can happen even at lower temperatures for long treatment times, whereas this has not been observed experimentally [24,29]. Various statistical and higher order models have been proposed to model thermal damage [29,33] which account for reversible thermal damage and thermotolerance. However, the difficulty in designing experiments to determine the parameters (often more than three) makes the implementation of these models challenging. Additionally, all the above models are based on *in vitro* experiments which are conducted in controlled conditions. In *in vivo* experiments, tumors are always in heterogeneous conditions with abnormal vasculature and hypoxic conditions. Thus, the application of these models *in vivo* is still questionable. However, clinical results do show a relationship

between the existing models for thermal dose measurement and the treatment outcome [34].

1.2.4 Mechanisms of heating

There are hundreds of medical devices used for thermal treatment, but they are all based on three mechanisms of heat delivery to tissue: thermal conduction, mechanical losses, and electromagnetic losses [11,22].

Thermal conduction is the most fundamental mechanism of heat transfer, where heat flows from higher temperature to lower temperature. The rate of heat transfer is dependent on the temperature difference and the thermal properties of tissue. Examples of thermal conduction heat sources are heated fluids, heated air, or hot blankets. Thermal conduction is often used for whole body hyperthermia [11].

Mechanical losses from molecular collisions induced by ultrasound pressure waves result in heating. The intensity of ultrasound waves attenuate exponentially with depth in soft tissue. For tissue heating, frequencies of 0.5 – 10 MHz which correspond to a wavelength of 0.1 – 3 mm are often used. These shorter wavelengths allow for more focused heating and the frequency range is low enough allowing for deeper penetration. One of the disadvantages of ultrasound therapy is that bone absorbs 50 times more energy compared to soft tissue. This restricts the usage of ultrasound if there is a bone in between the applicator and tissue [22].

Multiple technologies have been developed based on the interaction of electric and magnetic fields with tissue to generate heat. These technologies include radiofrequency ablation (RF ablation), microwave thermal therapy, laser or photothermal therapy, and

magnetic nanoparticle hyperthermia. RF ablation involves use of radiofrequency electromagnetic waves in the frequency range of 3 kHz to 300 GHz to generate heat by resistive or Joule heating. For RF ablation, frequencies in the range of 500 kHz are generally used [35]. It involves heating of tissue using inserted electrodes and application of radiofrequency currents. It is one of the leading hyperthermia techniques and is proven to be an effective treatment for primary liver cancer.

Microwave therapy is the use of ultrahigh frequency electromagnetic waves (300 MHz to 300 GHz) for heating the tissue. The heating is produced by oscillation of water molecules. Laser or photothermal therapy uses high intensity light waves to treat tumors directly. This method has been traditionally used for superficial tumors because of their ability to cause damage to normal healthy tissue for deep tumors. However, new interstitial therapy methods have been developed which use waves in the near infrared range (NIR) that have maximum transmissivity in normal tissue. These waves can be used to reach deep tumors injected with photosensitizers such as gold and silver nanoparticles to generate focused heat [36].

1.3 Magnetic nanoparticle hyperthermia

Magnetic nanoparticle hyperthermia is the use of magnetic nanoparticles to generate heat. Magnetic nanoparticles generate localized heating when exposed to an alternating magnetic field. It has emerged as one of the promising hyperthermia modalities because of its ability to produce effective localized heating [37,38]. This modality offers benefits over the other modalities described above because the heat sources, i.e. nanoparticles, can be embedded within the target tissue. Once magnetic nanoparticles are

embedded into the tumour tissue, the region is exposed to an alternating magnetic field generating heat by the particles via hysteresis losses in the magnetic nanoparticles while minimal energy is deposited in the surrounding tissues because the AC magnetic fields (low radiofrequency) couple poorly with tissue [37–53]. Heat generated by the nanoparticles is then transferred to tissues/fluids of the tumor by convective and conductive processes within the tumour to realize efficient distribution, while offering potential to minimize energy deposition outside the treatment margins. Magnetic fields are long range in nature and can therefore act from a distance allowing for remotely controlled heating. Additionally, low frequency alternating magnetic fields show little attenuation in biological tissues. This allows for precisely controlled targeted heating of tumor tissue.

Magnetic nanoparticle hyperthermia was first proposed by Gilchrist et al. [40] in their seminal paper published in 1957. With the emergence of new technology in the past two decades, especially in the manufacturing of high loss power nanoparticles, this method has gained more prominence [38]. Magnetic nanoparticle formulations typically consist of magnetic nanoparticles suspended in a carrier fluid (typically water). Iron based nanoparticles such as magnetite (Fe_3O_4) and maghemite (γ-Fe_2O_3) are the most commonly used nanoparticles because of their biocompatibility [54]. The typical sizes of these nanoparticles are in the range of 10 – 100 nm in diameter. They are usually coated with surfactants to prevent agglomeration. The two iron based nanoparticles used in this dissertation are: Bionised nano ferrite (BNF) nanoparticles [55,56] and Johns Hopkins University (JHU) nanoparticles [53]. BNF nanoparticles are synthesized by a high temperature and high pressure homogenization process [55]. JHU nanoparticles are synthesized by high gravity controlled precipitation process [53,57]. Different synthesis

methods are used to maximize the heating potential of the nanoparticles. The properties of magnetic nanoparticles that influence the high heating potential of nanoparticles and the physical mechanisms that result in magnetic nanoparticle heating are briefly reviewed here.

1.3.1 Physics of magnetic nanoparticle heating

Magnetism in a material is a result of the orbital and spin motions of electrons in atoms which produce an atomic magnetic moment [51]. In some materials, there exists a strong interaction among the individual atomic magnetic moments (exchange interaction) while in others no such interaction is present. Different types of magnetic materials are classified based on their net magnetic moment in zero field and their response to an externally applied magnetic field [51].

Magnetic materials are colloquially referred to as “non-magnetic” and “magnetic” based on their net magnetic moment in zero field. “Non-magnetic” materials have no net magnetic moment in zero field [51]. These are scientifically classified into three classes of materials – diamagnets, paramagnets, and antiferromagnets. All materials have diamagnetic contributions since they have paired electrons. When a non-zero magnetic field is applied, the individual electrons oppose this field by changing their angular momentum. In diamagnets, a net negative response is obtained for an applied positive field. Paramagnetic materials have unpaired electrons which are oriented in all directions resulting in a zero net magnetic moment in zero field conditions [51]. When a positive magnetic field is applied, these unpaired electrons align with the applied field resulting in a net positive magnetic moment. This paramagnetic response dominates the diamagnetic response. Antiferromagnetic materials exhibit a temperature dependent positive exchange interaction. Below a critical temperature, called the Nèel temperature, the atomic moments

align themselves antiparallel to their neighbors due to this strong positive exchange interaction. Below this temperature, no net magnetization exists as the atomic moments cancel out each other [51]. Above this temperature, the thermal energy overcomes this interaction and the antiferromagnets act as a paramagnet.

"Magnetic" materials have a non-zero magnetic moment in zero field. These materials are further scientifically classified into two classes – ferromagnetic and ferrimagnetic [51]. Ferromagnetic materials have a strong negative exchange interaction present resulting in the atomic moments aligning parallel to their neighbors. This dominates the diamagnetic response. Hence, they have non-zero magnetic moment at zero magnetic field, below the Curie temperature. Above the Curie temperature, the thermal energy is sufficient to overcome this exchange interaction and the material becomes a paramagnet [51]. When a saturating magnetic field is applied, all the moments align parallel to the applied field. Ferrimagnets are a special case of antiferromagnets, where the antiparallel atomic moments have different magnitudes. Because of unequal neighboring atomic magnetic moment magnitudes, ferrimagnets can have a net magnetic moment below the Nèel temperature. Under the application of a saturating applied magnetic field, the atomic moments spontaneously align with the applied field resulting in a net positive magnetic moment. The iron oxide nanoparticles used in magnetic nanoparticle hyperthermia, magnetite (Fe_3O_4) and maghemite (γ-Fe_2O_3) are both ferrimagnets [51].

Under an applied magnetic field, in addition to aligning their magnetic moments, magnetic nanoparticles exhibit certain additional characteristic features, shown in Figure 1.1. When an alternating magnetic field is applied, the change in polarity results in change in the direction of magnetic moment of the material (related to the coercivity, H_c). In ferro-

/ferri- magnets, $H_c \neq 0$, resulting in energy being added to the material to reverse the magnetization. In addition, H_c is dependent upon the frequency of the alternating magnetic field, with H_c typically increasing with increase in magnetic field. This is called hysteresis and is always accompanied by losses, which manifest as heat [51]. Schematic of a hysteresis loop is shown in Figure 1.1.

When the magnitude of the applied field is increased, the magnetization of the magnetic material increases until reaches a maximum value where all the magnetic moments in the material are aligned parallel to the direction of the applied magnetic field [51]. This maximum value is known as the saturation magnetization, denoted by M_S in Figure 1.1. When the applied magnetic field is reduced to zero, the magnetization of the material does not necessarily return to zero. This remaining magnetization is called as remanent magnetization, denoted by M_R in Figure 1.1. The magnetic field required to coerce the magnetization to zero is called the coercive field, H_C. The anisotropy field H_K, related to the energy needed to align the magnetic moments. Specifically, most magnetic materials have a preferred direction of orientation of the magnetic moments, which is referred to as magnetic anisotropy. This magnetic anisotropy is dependent on multiple material properties such as crystal structure, shape, etc. [51].

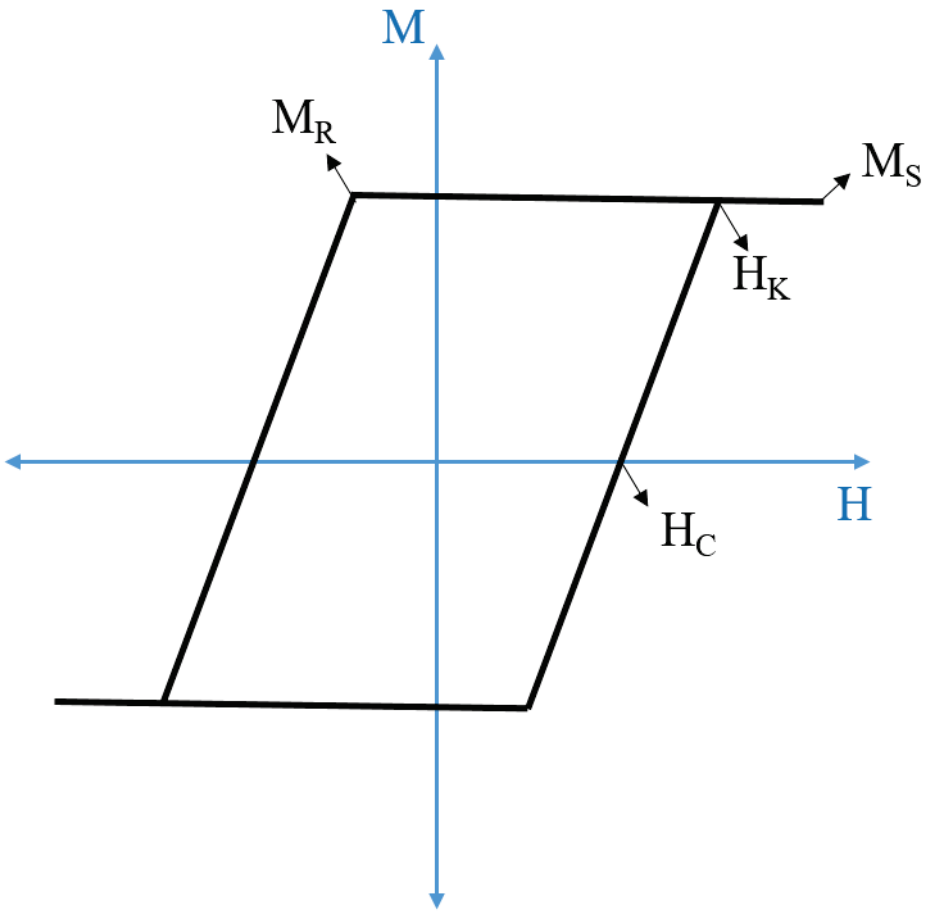

Figure 1.1 Schematic of hysteresis loop

The heat generated due to hysteresis losses can be explained by the application of first law of thermodynamics [51]. Work needs to be done by the applied external magnetic field to magnetize the magnetic material. This is given by,

$$dW = \vec{H}.d\vec{M} \tag{1.4}$$

where H is the applied magnetic field, and M is the magnetization. Assuming there is no mass transfer happening in the magnetic system, the change in internal energy is given by,

$$\Delta U = Q + W \tag{1.5}$$

where Q is heat. Assuming the material returns to the original state, and assuming there is no change in the internal energy of the material, implying that all work done by the external magnetic field on the magnetic material is manifested as heat [51]. Thus, during one traversal of hysteresis loop, the heat generated is equal to area of the hysteresis loop given by,

$$Q = \oint \vec{H}.d\vec{M} \tag{1.6}$$

The power dissipated per unit volume of magnetic material $P_{hysteresis}$ is then given by (in S. I. units),

$$P_{hysteresis} = \mu_o f \oint \vec{H}.d\vec{M} \tag{1.7}$$

Here, f is the applied frequency and μ_o is the vacuum permeability ($\mu_o = 4\pi \times 10^{-7}$ H/m). Calculation of area under the hysteresis loop given by equation (1.7) is not trivial [51]. No analytical model exists except for few simple cases so it is often determined by numerical simulations. Several theoretical models have been developed and are well known in the magnetic nanoparticle hyperthermia research community. However, most of them are simplified and are often freely applied without considering the inherent limiting assumptions [51,58]. The description of these models and their limitations are beyond the scope of this thesis and the readers are referred to excellent reviews given by Carrey et al. [58] and Dennis et al. [51].

1.3.2 Eddy currents

When an electrically conducting material is exposed to an alternating magnetic field, eddy currents are induced due to Faraday's law of induction. In the case of human body, this can lead to unwanted heating of healthy tissue, eliciting a thermoregulatory

response resulting in complex thermal gradients [38,61]. The power dissipated due to eddy currents is given by [62],

$$P_{eddy} = \sigma_t . G\ (H.f.r)^2 \tag{1.8}$$

where σ_t is the electrical conductivity of the tissue, G is a geometric coefficient and r is the radius of the exposed tissue. Results from Atkinson et al. [61] show that the permissible limits for frequency and applied field for a 30 cm diameter torso is given by,

$$H.f \leq 4.85 \times 10^8 \frac{A}{m.s} \tag{1.9}$$

For smaller exposure areas (~ 10 cm diameter), this limit can be exceeded by a factor of 10, Dutz et al. [62] suggested an upper limit given by,

$$H.f \leq 5 \times 10^9 \frac{A}{m.s} \tag{1.10}$$

These limits indeed pose a challenge on the heating performance of the magnetic nanoparticles as they are required to generate significant heating at low amplitudes and frequencies. It is therefore critical to consider eddy current heating effect when optimizing both magnetic nanoparticle properties and operating conditions for magnetic nanoparticle hyperthermia. In this thesis, we develop a computational tool that couples both electromagnetic and thermal effects in tissues to account for eddy current heating. This model can help predict the temperature distributions to gain a better insight and to develop new treatment strategies that can translate magnetic nanoparticle hyperthermia into the clinic.

1.3.3 Delivery of nanoparticles

Nanoparticles are primarily delivered by two methods – systemic delivery and direct delivery. In systemic delivery, magnetic nanoparticles are administered via a

systemic injection. The size of the nanoparticles allows for selective uptake by the tumors because of their leaky vasculature known as the enhanced permeability and retention effect (EPR). Compared to endothelial cells of normal tissue vasculature, tumor endothelial cells are often larger allowing particles of up to 1-2 μm to pass through [63]. However, not enough nanoparticles can be deposited in the tumor by this method. Another method of systemic delivery, is the use of targeted nanoparticles. Targeted nanoparticles are nanoparticles to which tumor selective ligands are attached to the surface of the nanoparticles which can then bind to specific biomarkers expressed by tumor cells. One example is the binding of Chimeric L6 (ChL6) to iron oxide nanoparticles by DeNardo et al. [49,50]. ChL6 is human mouse antibody chimera that reacts with an integral membrane glycoprotein expressed on human breast, ovary, colon, and lung carcinomas. Despite multiple efforts being undertaken for targeted nanoparticle delivery, it has still been challenging to achieve significant deposition of nanoparticles in the tumor [64].

Direct delivery of nanoparticles involves injection of nanoparticles directly into the tumors. It has been the most widely used method of nanoparticle delivery [65] for both *in vivo* studies [52,66] and in clinical trials [39,43,67]. The nanoparticle distribution and retention are dictated by both tumor physiological properties and injection parameters [52]. While multiple efforts have been made to optimize injection parameters for reproducible and repeatable nanoparticle distributions, [68,69], the applicability of these methods for different tumors is limited. Considering the heterogeneity of nanoparticle distributions and the resulting temperature distribution, clinical translation of magnetic nanoparticle hyperthermia has been challenged. In this thesis, we seek to develop methods to overcome this challenge using power modulation and temperature feedback.

1.3.4 Challenges

In 2010, magnetic nanoparticle hyperthermia achieved clinical approval for treatment of glioblastoma multiforme in Europe [39]. Despite this, challenges remain and further work is needed to harness the full potential of magnetic nanoparticle hyperthermia in cancer therapy [65]. Delivery of substantial quantity of nanoparticles to the target region, distribution of nanoparticles in the tumor, identifying the safe combinations of alternating magnetic field magnitude and frequency to generate substantial heat in tumor and minimize off target heating, are some of the challenges for magnetic nanoparticle hyperthermia to become a clinical modality. For developing methods to address the above challenges, further work is necessary to understand the mechanisms of thermal damage, the physical principles of nanoparticle heating, and the bio-distribution and toxicity of nanoparticles. In this thesis, we present methods and develop tools to address some of the challenges identified above.

1.4 Thermodynamics and heat transfer

Heat is defined as the form of energy that is transferred across the boundary of a system at a given temperature to another system (or surroundings) at a lower temperature by virtue of temperature difference between two systems [70]. Heat transfer is the transport of energy due to a temperature difference between different amounts of matter. Before we review the different modes of heat transfer, the first law of thermodynamics is presented as it applies to all heat transfer processes.

The first law of thermodynamics [71] states that the rate of change in internal energy stored in a system is equal to summation of the net change in energy transferred into the system and the energy generated by the system. This is the law of conservation of energy expressed as,

$$\frac{dU}{dt} = \sum \dot{Q} - \dot{W} + \sum \dot{m}(h_{in} - h_{out}) + \dot{Q_{gen}} \tag{1.11}$$

Here U is the energy of the system, $\sum \dot{Q}$ is the sum of all heat flows, $\dot{W}$ is the work done by the system on the environment, $\sum \dot{m}(h_{in} - h_{out})$ is the sum of all mass flows crossing the system boundary, each having an enthalpy h, as it enters and leaves the system, and $\dot{Q_{gen}}$ is the rate of energy generated by the system.

There are three basic modes of heat transfer – conduction, convection, and radiation [72]. Conduction may be viewed as the transfer of energy from the more energetic particles to the less energetic particles of a material due to interaction of particles. Conduction occurs in all phases of material: solids, liquids, and gases. Higher energy particles are associated with higher temperature and when these particles interact with lower energy particles via collision, energy transfer takes place. Thus, the diffusion of heat due to random of molecular motion is known as conduction. The fundamental expression that describes the conduction of heat is called the Fourier's law given by:

$$q''_x = -k\frac{dT}{dx} \tag{1.12}$$

here q''_x is the heat transferred per unit area (W/m^2), x is the direction normal to the direction of heat transfer, k is the thermal conductivity and $\frac{dT}{dx}$ is the temperature gradient along the x direction.

Heat transfer by convection comprises of two mechanisms – diffusion and advection [72]. Diffusion as described previously is the energy transfer due to random molecular motion, while advection is the transfer of heat due to macroscopic or bulk motion of the fluid. Convection heat transfer takes place when a surface and a fluid at two temperatures come in contact with each other. The rate equation that describes convection is known as Newton's law of cooling, given by:

$$q" = h(T_s - T_\infty) \tag{1.13}$$

where $q"$ is the convective heat flux (W/m^2), h is the convective heat transfer coefficient, T_s is the surface temperature and T_∞ is the fluid temperature. Convection heat transfer may be further classified into three types based on nature of flow. Forced convection occurs when the fluid is driven by an external force such as a fan, or a pump. Free convection occurs when the flow is driven by buoyancy forces, which are due to internal density differences caused by temperature variations in the fluid. Mixed convection occurs when heat transfers by both free and forced convection.

The third mode of heat transfer is radiation. Thermal radiation is the energy emitted by matter at a non-zero temperature [72]. These emissions can occur for all forms of matter and may be attributed to the changes in electron configurations of the constituent atoms or molecules. The energy is transmitted via electromagnetic waves and this mode of heat transfer does not require a medium unlike conduction and convection. The rate of thermal energy emitted is given by the Stefan Boltzmann law,

$$E_b = \epsilon \sigma_R T_s^4 \tag{1.14}$$

where ϵ is the emissivity of the material, σ_R is the Stefan-Boltzmann constant (5.67×10^{-8} W/m^2.K^4) and T_s is the absolute temperature (K) of the surface.

1.5 Heat transfer in biological tissue

The human body is a complex thermal system with heat generation and heat transfer occurring at multiple scales [73]. The vast heterogeneity in the vascular structure, variable blood flow in a complex arterial and venous network, varying tissue thermophysical properties and metabolic heat generation makes heat transfer analysis challenging. Heat generation occurs at cellular level due to various biochemical reactions while heat transfer occurs at multiple levels, cellular and molecular level, tissue and organ level, and interaction between the body and environment. The human body efficiently controls these processes to maintain its temperature in a narrow range. Any irregular thermal deviations from this state are often associated with abnormal physiological conditions. To identify these deviations, it is important to have a proper understanding of heat generation and heat transfer processes in the human body [73]. This is essential for multiple applications such as cancer diagnosis [74], hyperthermia [52,75], burn injury estimation [76] etc.

Over the past 70 years, multiple efforts have been made to model the heat transfer processes occurring in tissue [73,77–79]. These models can broadly be classified as continuum and vascular heat transfer models [73,80]. Continuum models are models in which the effect of blood flow in individual vessels is ignored and instead is averaged across the control volume. Vascular models, on the other hand, account for effects of blood flow through individual blood vessels. This allows for the consideration of the effects of blood flow direction on the temperature distribution. Numerous applications have used these models to understand various heat transfer phenomena in the human body.

Pennes was the first one to develop a bioheat transfer model based on his experimental analysis of resting human forearm [81]. He modified the transient heat

conduction equation by including two heat source terms – one due to perfusion and other due to metabolism. This model is one of the simplest and oldest forms of perfusion based heat transfer models. The primary assumption made by Pennes was that energy exchange between blood vessels and the surrounding tissue occurs across the capillary walls. This was based on the fact that exchange of nutrients and waste takes place between tissues and blood distributed by capillaries. Pennes also introduced a thermal equilibrium factor κ to correlate the arterial, venous and tissue temperatures. If thermal equilibrium is achieved between the blood and tissue ($\kappa = 0$), then the venous flow temperatures should be equal to the tissue temperature. Pennes also assumed that heat exchange due to blood flow can be modeled as a non-directional heat source. The original Pennes bioheat equation is given by,

$$\rho c_p \frac{\partial T}{\partial t} = k\nabla^2 T + \rho_b c_b \omega_b (1-\kappa)\,(T_b - T\,) + Q_m \qquad (1.15)$$

here ρ is the tissue density, c_p is the specific heat capacity of tissue, k is the tissue thermal conductivity, Q_m is the metabolic heat generation rate, T is the tissue temperature and κ is the thermal equilibrium factor ($0 \leq \kappa \leq 1$). Density, specific heat, temperature and perfusion rate of blood are denoted by ρ_b, c_b, T_b, and ω_b respectively. Most studies that use the Pennes' bioheat equation, including Pennes himself in his study, assume that complete thermal equilibrium is achieved ($\kappa = 0$). Equation 1.2 represents the energy balance in the tissue due to conduction, blood perfusion, and metabolic heat generation. The left hand side of the equation represents the change in internal energy of the tissue. On the right hand side, the first term represents the conductive diffusion of heat in the tissue, the second term

represents the heat source term due to blood perfusion, and the last term denotes a heat source due to tissue metabolism.

Wulff [82] identified four fundamental shortcomings in the Pennes' bioheat equation. He pointed out that combining local (tissue) and global (blood) control systems is not permissible. Pennes' assumption of choosing three media with three temperatures at the same point in space, viz. tissue with temperature T, and two blood stream temperatures at the same point T_{in} and T_{out}, omits two additional equations. Pennes' equation also neglects the convective contribution of other bio-fluids which are in motion and the heat transfer between tissue and blood flow is driven by the difference in tissue and blood temperatures rather than the temperature difference between blood flow temperatures. Wulff proposed a new model where in the blood flow contribution is modeled by a directional term and is given by,

$$\rho c_p \frac{\partial T}{\partial t} = k\nabla^2 T - \rho_b c_b \boldsymbol{U_h}.\nabla \mathrm{T} + \rho_b \boldsymbol{U_h} \Delta H_f \nabla \epsilon \tag{1.16}$$

$$\rho_b h_b \boldsymbol{U_h} = \frac{1}{4\pi} \int_{\Omega} (\rho_b h_b \boldsymbol{u}) d\Omega, \tag{1.17}$$

here $\boldsymbol{U_h}$ local mean apparent blood velocity, h_b is the specific enthalpy of blood, ΔH_f is the specific enthalpy of metabolic reaction, ϵ is the extent of reaction, $\boldsymbol{u}$ is the actual blood velocity in the capillary and Ω is the spherical solid angle. Wulff suggested that thermal equilibrium between blood and tissue is achieved because of efficient heat transfer in porous media. Thus he considered the blood temperature to be equal to that of tissue. He also assumed that the metabolic reaction term as equivalent to metabolic heat generation. The most important feature of Wulff's model is that he considered the directional nature of

heat transfer due to blood perfusion. The main limitation of this model is the assumption of thermal equilibrium between blood and tissue, which may not be necessarily true.

In vascular models, the effect of blood perfusion on an individual vessel-by-vessel basis is taken into account to determine the temperature in and near individual blood vessels. Mitchell and Myers [83] were the first to develop a bioheat model which included the effects of countercurrent heat exchange between adjacent arteries and veins in addition to the heat exchange between each vessel and surrounding tissue. However, their model does not consider heat conduction in the tissue and their assumption of constant blood flow rate restricts the applicability to the main supply blood vessels [77,83]. Keller and Seiler [84] in their model, included both the countercurrent heat exchange between artery and vein, and also added an energy conservation equation for the surrounding tissue coupled to the artery and vein equations.

Chen and Holmes [85] addressed the issue of thermal equilibrium between blood and tissue by proposing a blood-tissue continuum model based length scale analysis. They defined a thermal equilibrium length, the length at which the temperature difference between blood and tissue drops by *1/e* its initial value. Based on this, they classified blood vessels into two categories, thermally significant and thermally insignificant blood vessels. They observed that thermal equilibrium was achieved mostly in medium size blood vessels (diameter of 50-300 μm) compared to capillaries (diameter < 50 μm). The model is given by,

$$\rho c_p \frac{\partial T}{\partial t} = \nabla.((k + k_p)\nabla T) + \rho_b c_b \omega_b^* (T_a^* - T) - \rho_b c_b \boldsymbol{U_h}.\nabla \mathrm{T} + Q_m \tag{1.18}$$

where k_p is the thermal conductivity due to blood perfusion, T_a^* is the blood temperature in the largest artery included in the continuum model, ω_b^* is the blood perfusion rate for blood vessels which are smaller in diameter than the largest artery in the model. The Chen and Holmes model is an extension of Pennes' model with contributions of microvasculature both to the effective thermal conductivity and a contribution proportional to local blood perfusion velocity. It also includes the directionality effect of blood flow.

Weinbaum et al. [86,87] conducted an in-depth evaluation of thermal equilibrium lengths for various geometrical configurations of vasculature in the peripheral tissue layer and developed three-layer models for tissue-vessel thermal interaction due to countercurrent flow. A deep tissue layer was modeled as an isolated countercurrent large vessel in a tapered cylinder. The intermediate layer was modeled as a pair of countercurrent terminal vessels. The outer cutaneous layer was modeled as a single or pair of vessels in the skin plexus. Their main observation from experiments and the results from their models was that temperature differences are due to incomplete countercurrent energy exchange in the thermally significant vessels. Weinbaum and Jiji recognized that their model required detailed information about the vascular structure and also that there is an uncertainty regarding the temperature of the blood entering the thermally significant blood vessels. Realizing this, they proposed a new simplified model [88] by approximating the mean tissue temperature with an average temperature of adjacent countercurrent pair of closely spaced and nearly equilibrated vessels. While this model included the effect of blood flow and vascular architecture on heat transfer, they removed the isotropic blood perfusion term as its contribution was negligible compared to heat transfer due to countercurrent blood flow. They also assumed that most of the heat conducted out through the wall of the

arteriole arrives through the wall of its paired vein. For a one dimensional case, where blood vessels and temperature gradient are in the same direction, the differential equation for tissue temperature is given by [77,89],

$$\frac{\partial}{\partial x}\left(k_{eff}\frac{\partial T}{\partial x}\right) + q_m = \rho c \frac{\partial T}{\partial x} \tag{1.19}$$

$$k_{eff} = k\left[1 + \frac{n\{\pi r_b^2 \rho_b c_b V cos\ \gamma\}^2}{\sigma_\Delta . k^2}\right] \tag{1.20}$$

here k_{eff} is the effective thermal conductivity, n is the vessel number density, r_b is the vessel radius, V is the blood velocity within the vessel, γ is the relative angle between the direction of blood vessel and local tissue temperature gradient, σ_Δ is the shape factor of the vessels. Simulations conducted by Baish et al. [80,90], Wissler [91], and by Charny et al. [92], showed that the Weinbaum-Jiji model can only be applied to either tissues where $\varepsilon < 0.3$ (ε – ratio of equilibrium length and actual vessel length) or muscle tissue (with low perfusion) that contains blood vessels with diameter < 0.2 mm. Wissler [91] also criticized the model for simplifying assumptions such as the tissue temperature is average of arterial and venous blood temperatures and tissue temperature has no influence on the heat transfer between the countercurrent vessels.

Several other bioheat transfer models have been developed to address the limitations of the above and to give a more accurate prediction of temperatures in the tissue. Of these, the statistical steady state bioheat transfer model by Baish [93], dual-phase-lag bioheat model by Xu et al. [94], porous media based bioheat transfer models [78,95–97], discrete vasculature models [98–102], and recent models by Shrivastava et al. [103,104] improve and address the limitations of the models mentioned above.

Despite the drawbacks and criticism of Pennes' equation, and being widely documented as incorrect with several shortcomings, it is still the most widely used equation for numerical studies in biological tissue [105]. This can be attributed to the linear microscopic thermal energy balance for perfused tissue in the Pennes' model. Also, predicted temperatures using the Pennes' model demonstrate good agreement with experimental measurements [106–108]. For tissues situated away from large blood vessels, the new terms added by the different models contribute minimally to the overall heat transfer [77]. We use the Pennes bioheat transfer model in all the numerical studies carried out in this dissertation. We assume complete thermal equilibrium has been achieved ($\kappa = 0$, in equation 1.1). However, we modify the blood perfusion term to include the effects of thermal damage on the change in perfusion (explained in section 3.2.3).

1.6 Computational modeling

In the past two decades, a quantitative understanding of biological processes has developed to make computational modeling and simulation an important tool for biomedical applications [109]. Computational modeling has been widely used in multiple applications ranging from aerospace, automotive, biomedical, public policy, climate modeling etc. In biomedical applications, models allow for better and improved understanding of complex biological processes and to test and optimize new treatment procedures before translation to animal studies or patient trials. This can result in significant savings of both time and money, reduced ethical concerns associated with animal studies, in addition to improving the overall safety and performance of the new treatment procedure.

Building a computational model for a biomedical problem consists of the following four steps: 1. defining the biomedical problem/process, 2. Preparing/developing a mathematical formulation, 3. implementing the model in an algorithm and code, 4. interpreting the solution and optimization [109]. The first step in building a computational model involves defining the biomedical problem to be solved. In this thesis, we focus on building a computational model for magnetic nanoparticle hyperthermia to understand and devise strategies for its improvement.

In the second step, an equivalent mathematical formulation of the problem defined in step 1 is created. This involves developing equations which accurately describe the physical process. The equations are based on fundamental laws of physics which govern the given process. In this thesis, the fundamental laws of physics that are used are – conservation of total mass (continuity equation) and conservation of energy (more specifically thermal energy, described in section 1.4). Setting up the mathematical formulation is the most critical step as the validity and relevance of the results obtained depend entirely on the formulation. The process of developing the mathematical formulation involves the following steps. The first step involves defining the goal of the simulation. In the current thesis, the main goal of the models used is to determine the temperature distribution in a given domain. The next step involves determining the geometry or the region on which we run the simulations. These geometries can be simple mathematical shapes (ellipse, ellipsoid, sphere, and cylinder – chapters 2 - 6) or can be complex shapes imported from images (rabbit liver model, chapter 5). Then, the governing equations and boundary conditions that describe the biomedical problem in step 1 are chosen. The governing equations used in this thesis are: heat conduction equation (chapter

5 & 6) and Pennes' bioheat transfer equation (chapters 2 – 6). The implementation and limitations of Pennes' bioheat equation have been explained in section 1.5. For the boundary conditions, Dirchlet and Neumann boundary conditions [72] were used depending on the problem. The equations were then solved by using the material properties and parameters relevant to the problem.

The third step involves implementing or solving the mathematical formulation using an algorithm and a code. These can be developed in the lab or can be commercially available. In the studies reported in this thesis, COMSOL Multiphysics® 5.2a [110] was used to solve the computational models. COMSOL is a finite element method (FEM) based commercial software that solves partial differential equations across multiple physics such as heat transfer, fluid flow, mass transfer, electromagnetism, etc. Implementation of a mathematical formulation in COMSOL requires three main steps: preprocessing, processing, and post-processing [109]. Preprocessing involves setting up the problem in COMSOL by building a geometry, choosing the appropriate governing equations, boundary conditions, initial conditions, properties, and parameters, meshing the computational domain, choosing an appropriate solver, and setting the tolerances/convergence criteria. Processing involves solving the partial differential equations by transforming them into a set of algebraic equations and determining the unknown variables. Post-processing involves visualizing the obtained results, analyzing and interpreting them.

As described previously, the geometry chosen in the mathematical formulation step is now implemented in COMSOL. This geometry can be simple mathematical shapes or complex realistic geometries imported from images using image processing software. The

necessary COMSOL physics modules are then chosen depending on the physics involved (bioheat transfer – chapters 2-4, 6; coupled electromagnetic and bioheat transfer physics, chapter 5). The initial and boundary conditions are then chosen based on the problem formulations. Properties and parameters are chosen to depict the real scenario as closely as possible. After this, the computational domain is then meshed. Meshing involves discretizing the computational domain into finite number of small, simple shapes. These small discretized shapes are known as elements and the points describing them are called nodes. Depending on the dimensionality of the problem (1-D, 2-D, or 3-D), the elements can be lines, triangles, quadrilateral, tetrahedrons, hexahedrons etc. The size and number of elements defines the fineness of the mesh. The more number of elements, the more finer the mesh is. Large number of elements however can lead to higher computational load and more solution time. Generally unstructured mesh is chosen, so as to have finer elements at boundaries and interfaces where the solution variables are expected to change rapidly, while coarse elements are chosen at nodes where there is little expected change in the solution variable.

Solution method in COMSOL involves finite element method (FEM), which is a numerical method for solving partial differential equations (PDE) by discretizing the domain into elements and approximating them with numerical model equations. For example, a dependent variable f in a PDE can be approximated by a linear combination of basis functions, given as

$$f \approx f_h = \sum_i f_i \varphi_i \tag{1.21}$$

here φ_i denotes the basis functions and f_i denotes the coefficients of the functions which approximate the f with f_h. The set of linear algebraic functions are then solved by two classes of methods – direct and iterative. Direct methods are based on Gaussian elimination either by matrix operations or by LU decomposition. Iterative methods, generally used for large system of equations, involve starting with an initial approximation and iteratively changing this approximation to approach an exact solution [109]. Rate of convergence is improved by use of appropriate preconditioners. Examples of direct solvers used by COMSOL are PARDISO (parallel direct sparse solver), MUMPS (multifrontal massively parallel sparse direct solver) [110]. GMRES (generalized minimum residual), FGMRES (flexible generalized minimum residual), Conjugate Gradient, BiCGStab (Biconjugate gradient stabilized) are some of the iterative solvers used by COMSOL. FEM offers many advantages compared to other methods such as greater flexibility for modeling complex geometries, for modeling changing geometries (moving boundaries), and for choosing different basis functions across the domain.

COMSOL generally uses FEM for spatial discretization while for time discretization in transient studies it uses finite difference method (FDM) to save computational memory and to improve computational speed. FDM methods are numerical methods for solving PDEs by approximating the differential operator using differential quotients to replace the derivatives. For example, a first order time derivative at a node can be approximated by,

$$\frac{\partial f}{\partial t}|_t = \lim_{\Delta t \to 0} \frac{f(t+\Delta t) - f(t)}{\Delta t} \tag{1.22}$$

COMSOL uses implicit methods such as IDA, variable-order variable-step-size backward differentiation formulas (BDF) and Generalized-α, a second-order accurate method with a parameter α to control damping of high frequencies [110].

The fourth step in the building of computational model involves analyzing the numerical solution obtained and verifying and validating it with analytical solutions and experimental measurements. Once the model is verified and validated, it can then be optimized to understand the physics and also to develop new treatment strategies.

1.7 Thesis overview

In this thesis, we report the development of methods and tools to address the specific challenges that limit the clinical application of magnetic nanoparticle hyperthermia. The challenge of delivering a therapeutic thermal dose in the tumor with minimal healthy tissue damage despite variable nanoparticle distributions is addressed in Chapters 2 – 4. Different biological tissues have different electrical conductivities, making the monitoring of eddy current heating difficult in *in vivo* studies. To study this, we developed and validated a computational tool that can be used to predict temperature elevations due to eddy current heating in large tissue (Chapter 5). In the final chapter, we characterized and determined the heating potential of nanoparticle formulations that can be used for combination therapies.

The content of the thesis is summarized below.

Chapter 2 focuses on understanding the effect of nanoparticle distribution and heat output on temperature evolution in tumor using computational models. Two extreme cases of nanoparticle distributions, uniform and concentrated, were considered. We conducted

constant power simulations to highlight the differences in temperature distributions achieved for different nanoparticle distributions. We then showed that modulating the heat output of nanoparticles based on temperature measured at tumor-healthy tissue boundary can compensate for variable nanoparticle distributions in delivering a minimum effective thermal dose.

In Chapter 3, an improved modulated power heating method is described and results from implementation in 2D and 3D computational models for a range of nanoparticle distributions including those derived from animal studies are reported. Temperature effects on perfusion were implemented by modeling perfusion as a function of thermal damage. A new method for modulating power using a PID controller with temperature feedback from tumor-healthy tissue boundary was presented. Comparisons between constant power and modulated power heating were carried out to highlight the advantages of modulated power heating over constant power heating. We show that modulated power heating can compensate for variable nanoparticle distributions and deliver effective tumor treatment with minimal healthy tissue damage.

Chapter 4 presents the results of *in vivo* implementation of modulated power heating in mice models of liver cancer. We test the strategy on sub cutaneous xenograft tumors with two nanoparticle distributions generated by two intratumor nanoparticle injection methods using a syringe pump. The results from this study are then compared to results from computational models.

In Chapter 5, we report the development of a new computational model to simultaneously solve the electromagnetic and heat transfer physics for magnetic nanoparticle hyperthermia. This model was built in COMSOL 5.2a using the AC/DC

module and Heat Transfer module. The model was verified using the existing analytical model and validated by comparing with results from gel phantom experiments. Results from the implementation of this model to rabbit liver models generated from computed tomography (CT) images and computed temperatures in the liver due to non-specific eddy current heating are presented.

Chapter 6 presents the thermal and magnetic characterization of magnetic formulations used for image-guided magnetic nanoparticle hyperthermia. For the thermal characterization, the specific heat capacity and heating rates of the aqueous and lipiodol formulations was measured. Specific loss powers (SLPs) were then determined and compared for both the formulations. Bulk magnetization measurements were conducted to effect of lipiodol of the saturation magnetization of these nanoparticles. Additionally, simulations were carried out to further understand the change in thermal properties on the heat generated by these nanoparticle formulations. Also, simulations were conducted to predict the temperatures and thermal damage due to these nanoparticle formulations inside tumor tissue.

The conclusions from this thesis are discussed in chapter 7. Challenges and future directions for magnetic nanoparticle hyperthermia in becoming a clinical treatment are also presented.

Chapter 2

Understanding the effect of nanoparticle distributions and heat output on temperature evolution in tumor

This chapter focuses on developing computational models to understand the physics of heat distributions within the context of magnetic nanoparticle hyperthermia (mNPH) and to develop strategies that can be translated to the clinic to achieve reasonable therapeutic outcomes. In this chapter, two simple computational models are studied to understand the relationships between nanoparticle distributions, heat output, and the resulting temperature evolution in a two dimensional tumor-healthy tissue model. Two

extreme cases of nanoparticle distributions, uniform and concentrated, were considered. It is shown that varying the nanoparticle heat output can compensate for variable nanoparticle distributions to achieve a minimum effective thermal dose at the tumor-healthy tissue boundary. Modulating the nanoparticle heat output by controlling the temperature at the tumor-healthy tissue boundary can achieve therapeutic thermal dose at the tumor-healthy tissue boundary while simultaneously minimizing the healthy tissue damage.

2.1 Introduction

Principal challenges encountered with all thermal therapies; arise from an inability to effectively deliver energy and control the delivered dose [10,111]. The main challenges for clinical implementation of mNPH are (1) the difficulty in effective targeting of tumors with magnetic nanoparticles, (2) the lack of precise control of nanoparticle distribution within tumors with percutaneous delivery, to enable precise energy deposition throughout the tumor volume [39,43–46]. The former results in too little material being deposited into the tumor while the latter leads to variable temperature distributions resulting in ineffective treatment. Nanoparticle distributions in the tumor after direct injection are dependent upon both injection parameters (e.g. injection rate, needle size, volume, viscosity, number of injection points) and also on tumor mechanical and physiological properties (e.g. interstitial pressure, density, vascularity). While studies [112] have been conducted to control the injection parameters, controlling the tumor mechanical and physiological properties is impossible. Thus, it is important to accept that variable nanoparticle distributions are a part of ‘clinical reality’ and robust treatment strategies should be developed to address these variable distributions to deliver sufficient tumor thermal damage.

Thermal dose [25], defined as 'time at temperature', deposited to the tumor determines the effectiveness of hyperthermia. While achieving a uniform thermal dose in the tumor is ideal, effectiveness of thermal therapy is defined by/limited to the region of tumor receiving the lowest thermal dose [9]. The goal of hyperthermia is to achieve a minimum effective thermal dose in 90% of tumor volume while simultaneously minimizing the surrounding healthy tissue damage [9,113]. Thus, for mNPH the thermal dose deposited in the tumor depends on the concentration of the nanoparticles and the distribution of these nanoparticles. Given the small size of these nanoparticles, controlling the distribution inside the tumor is difficult. However, the variable heat output of these nanoparticles mainly depend on the applied AMF amplitude and frequency. This allows for non-invasive dynamic control of the heat output which results in controlled thermal dose deposition to the tumor. It is thus of interest to test whether these dynamic adjustments of the nanoparticle heat output can compensate for variable nanoparticle distributions in delivering an effective tumor thermal dose while simultaneously minimizing healthy tissue damage.

Computational models enable easy and relatively inexpensive variation of model parameters (tumor and healthy tissue geometries and properties, nanoparticle distributions, temperature dependence of properties, etc.) as well as heating conditions, to improve understanding of the effects of intratumor nanoparticle distribution on tissue temperature distribution, thermal dose, and overall therapeutic effect and to devise new strategies to achieve effective treatment. They can be used to gain knowledge about temperature distributions which otherwise would be impossible considering the limitations in technology to accurately measure the temperature distributions throughout the tumor.

Considerable effort was devoted to developing mathematical models describing tissue heating with mNPH [114–121]. Andra et al. [114] were the first to analytically determine the temperature distributions achieved during mNPH. They modeled the tumor as a finite spherical region of homogeneous tissue containing magnetic nanoparticles, surrounded by an infinite spherical region of healthy tissue. The effects of blood perfusion were ignored. Bagaria and Johnson [115] considered two concentric spherical regions, with the inner spherical region having nanoparticles with distribution determined by a polynomial function. Variation of capillary blood perfusion was considered for both the healthy tissue and tumor. Durkee et al. [116] obtained exact analytical solutions in cylindrical coordinates with homogeneous, time-dependent heat sources and constant perfusion. Giordano et al. [117] derived fundamental solutions to the Pennes bioheat equation with constant perfusion in rectangular, cylindrical, and spherical coordinates, and applied them to magnetic fluid hyperthermia to determine the temperature distribution inside the tumor and surrounding healthy tissue. Fasla et al. [118] analytically solved the Pennes bioheat equation in spherical coordinates by considering point-like particle heat sources and the effects of metabolic heat generation and blood perfusion on temperature distribution. Xu et al. [119] developed a three-dimensional model based on experimental observations. Their model consisted of cuboidal tumor periphery loaded with nanoparticles and a necrotic spherical core with no nanoparticles. They considered an inhomogeneous distribution of nanoparticles, and blood perfusion was assumed to be constant. Attar et al. [120] assumed a partial dispersion of nanoparticles in the cancerous tissue and investigated the effect of this assumption on the temperature distribution. All the above studies focused on determining the temperature distributions achieved in the tumor and healthy tissue with constant power heating.

The aim of this study is to compare the temperature distributions obtained in the tumor and healthy tissue with constant power and modulated power heating. The relationships among nanoparticle distribution, heat output and the evolution of temperature distributions with time are explored in the context of whether dynamic non-invasive control of nanoparticle heat output can compensate for variable nanoparticle distributions to deliver an effective thermal dose at the tumor-healthy tissue boundary. It is shown that power modulation with probe placement at the tumor-healthy tissue boundary is sufficient to achieve a minimum effective thermal dose at the tumor margins, while simultaneously minimizing the healthy tissue damage.

2.2 Model description

Two computational thermal models were created to represent a tumor and surrounding healthy tissue (Figure 2.1). As nanoparticle distributions in tumors vary, we used the computational phantom to analyze two extreme cases of nanoparticle distributions, to better understand the effect of physical parameters of the system. The tumors contained either (a) uniform or (b) concentrated distribution of nanoparticles (Figure 2.1). Both models contained an identical total number of nanoparticles and differed by nanoparticle distribution. In the uniform distribution model, the nanoparticles are evenly distributed throughout the tumor area. In the concentrated model nanoparticles are concentrated in only 40% of the tumor area extending from its center (Figure 2.1). The healthy tissue and tumor were modeled as circles with radii, r_{tissue} = 9.5 mm and r_{tumor} = 4.5 mm respectively. The model dimensions were chosen to ensure that the temperature at the outer edge of (healthy) tissue can be assumed to be at constant body temperature T = 37°C [121]. Heat

transfer throughout either tumor or tissue, produced by the nanoparticles was modeled by the Pennes' bioheat equation [81]:

$$\rho_n c_n \frac{\partial T_n}{\partial t} = k_n \nabla^2 T_n + \rho_b c_b \omega_{b,n} (T_b - T_n) + Q_{m,n} + Q_p \qquad (2.1)$$

where n and b represent tissue (tumor, n=1; healthy n=2) and blood parameters, respectively. For either tumor or healthy tissue, ρ_n, c_n, k_n, T_n, $Q_{m,n}$ denote the density, specific heat, thermal conductivity, local temperature, and metabolic heat generation rate. Correspondingly, for the blood ρ_b, c_b, ω_b, T_b denote density, specific heat, perfusion rate, and temperature, respectively. Thermophysical properties for healthy tissue, tumor, and blood are summarized in Table 2.1 [74,122–126]. Q_p denotes the total power generated by nanoparticles in each tumor. The nanoparticles are modeled as line heat sources with uniform heating strength. As a consequence, the total power generated within each of the model tumors is identical, in order to highlight differences in temperature distribution resulting from the two nanoparticle distributions.

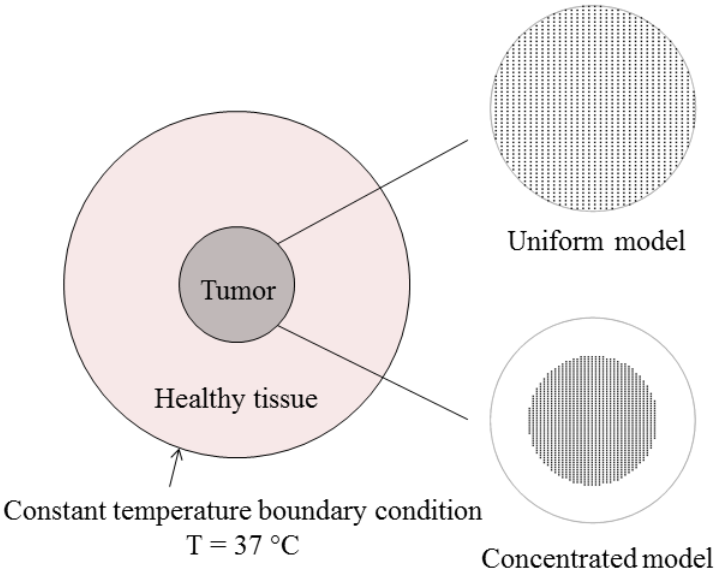

Figure 2.1 Schematic of the computational model of healthy tissue and tumor with uniform nanoparticle distribution, and concentrated nanoparticle distribution.

At the interface between healthy tissue and tumor, conservation of heat flux and continuity of temperature conditions are applied. Summarized, the boundary conditions are:

$$k_{tissue}\left.\frac{\partial T_{tissue}}{\partial r}\right|_{r=r_{tumor}} = k_{tumor}\left.\frac{\partial T_{tumor}}{\partial r}\right|_{r=r_{tumor}} \tag{2.2}$$

$$T_{tissue}(r = r_{tumor}, t) = T_{tumor}(r = r_{tumor}, t) \tag{2.3}$$

$$T(r = r_{tissue}) = 37\ ^{\circ}\mathrm{C} \tag{2.4}$$

The governing equations (Equation 1) with the boundary conditions (Equations 2.2 – 2.4) were solved numerically using COMSOL Multiphysics 4.4, a commercially available finite element solver. A grid size dependence study was carried out to ensure that calculated temperatures were sufficiently independent of a chosen model grid size. When the grid size was changed from coarse (14747 triangular elements) to fine (29804 triangular elements), the number of elements nearly doubled yet the calculated temperature along the radius of

the tumor changed by less than 0.01 %, indicating our chosen model parameters have negligible influence due to grid size. A similar comparative analysis was performed to determine whether calculated temperatures were affected by the chosen time step for the transient heating process. When the time step was increased from 0.2 s to 1 s, the change in calculated temperatures was negligible (<0.001%). The model results were validated by comparing the transient temperature profiles along the radius of tumor with the analytical solution given by Andra, et al. [114]. Satisfactory agreement between analytical and numerical solutions was observed, confirming the general validity of our model.

Table 2-1 Thermophysical properties of tumor and healthy tissue

	Density, ρ (kg/m^3)	Specific heat, c (J/kg K)	Thermal conductivity, k (W/m K)	Blood Perfusion rate, ω (1/s)	Metabolic heat generation rate, Q_m (W/m^3)
Tumor	1045 [122]	3760 [122]	0.51 [122]	0.0095 [123]	31872.5 [74]
Healthy tissue	1045 [122]	3760 [122]	0.51 [122]	0.003 [123]	6374.5 [74]
Blood*	1060 [125]	3770 [125]	N/A	N/A	N/A

*Temperature of blood (T_b) was fixed at 37ºC [125]. (N/A – not applicable)

Simulations in this study were conducted to approximate constant power and power modulated nanoparticle hyperthermia experiments for qualitative comparison. Thermophysical properties of tissues and blood were held constant for all simulations (Table 2.1). To approximate constant power heating, Q_p (= 4.6 × 10^5 W/m^2) was fixed for a simulated duration of 60 min. The total heating power was chosen to limit the maximum temperature in the tumor to <47 °C.

To simulate power modulated nanoparticle hyperthermia, the heating power of the nanoparticles ($Q_p(T)$) was varied with computed temperature at a specific intratumor location (T_{probe}) as the feedback control parameter. This was given by:

$$Q_p(T) = \begin{cases} 9.2 \times 10^5\ \mathrm{W/m^3}, & if\ T_{probe} \leq 43.5\ ^\circ\mathrm{C} \\ 0.92 \times 10^5\ \mathrm{W/m^3}, & if\ T_{probe} > 43.5\ ^\circ\mathrm{C}. \end{cases} \quad (2.5)$$

43.5 °C was the chosen temperature reference to control power input because it is the minimum (break-point) temperature considered clinically relevant for hyperthermia treatment of human cells from *in vitro* measurements [9,25,127]. To investigate the influence of temperature probe placement on the total thermal dose, three virtual temperature probe locations – (a) center of tumor, (b) halfway between tumor center and tumor-tissue boundary, (c) at the tumor-tissue boundary – were considered in the computational simulation as control points. Heating with modulated power was carried out for 60 min and the temperature distributions in both tumor and healthy tissues were obtained at the end of 60 min of heating.

2.3 Results

Temperature profiles obtained from simulations comparing idealized uniform (with nanoparticles uniformly distributed throughout 'tumor' area, Figure 2.1, top) with concentrated (nanoparticles at 'tumor' center extending to 40% of tumor volume, Figure 2.1, bottom) magnetic iron oxide nanoparticles (MIONP) distributions for 60 min heating with constant power (Q_p = 4.6 × 10^5 W/m^3) are shown in Figure 2.2. In both cases, a temperature gradient within the tumor is predicted, which results from heat generated by

MIONPs that conducts throughout the tumor and dissipates into the surrounding tissue. Temperatures calculated at the tumor boundary with respect to time for the two models are shown in Figure 2.3. Steady-state is achieved rapidly, within about 300 seconds for both models, although the tumor-tissue interface temperature achieved by a uniform MIONP distribution is predicted to be slightly higher (T = 40.9 ºC) than that achieved by a concentrated MIONP distribution (T = 40.6 ºC). Heat flux (loss) at the tumor-tissue interface (heating of healthy surrounding tissue) is also predicted to be greater for the uniform distribution (656 W/m^2) than for concentrated MIONP distribution (592 W/m^2).

Modulating power with computed temperature as the feedback control parameter ($Q_p(T)$) produces different temperature profiles within the tumor depending upon both MIONP distribution *and* control temperature probe placement (Figures 2.3 (a) and (b)). Temperature gradients produced within a tumor bearing a uniform MIONP distribution are similar to those produced by constant power heating, although the steady-state temperature achieved at the tumor-tissue boundary is determined by placement of temperature sensor used in the control algorithm described by Equation 2.5. Similarly, power-modulated heating with a concentrated MIONP distribution produces similar temperature gradients within the tumor as with constant-power heating. Power-modulated heating with temperature monitoring at the tumor-tissue interface, however achieves identical steady-state temperature at the tumor boundary for both concentrated and uniform MIONP distributions. By contrast, placement of temperature probes in either the tumor center or halfway between center and boundary for concentrated MIONP distribution limits heating significantly more than for uniform MIONP distribution (Figures 2.5 (a) and (b)).

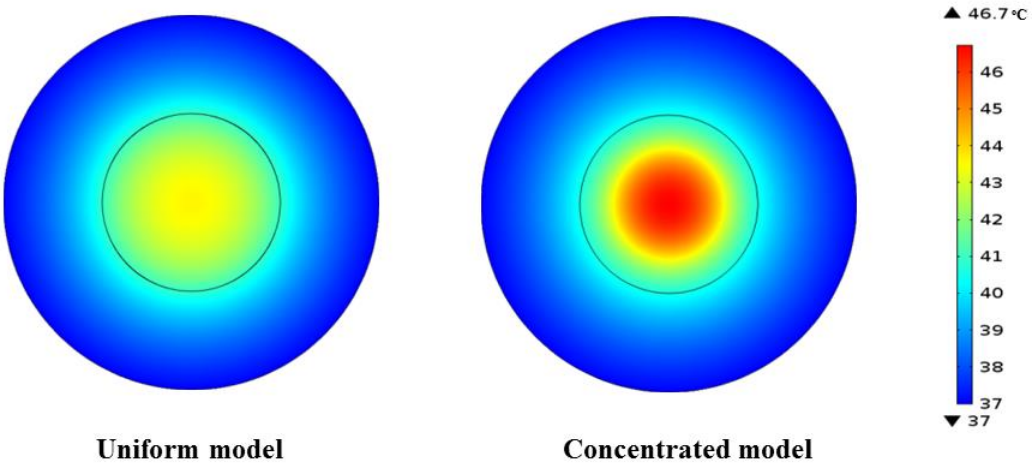

Figure 2.2 Temperature distribution of uniform distribution model and concentrated distribution model after 60 min of heating at constant power $Q_p = 4.6 \times 10^5$ W/m^3.

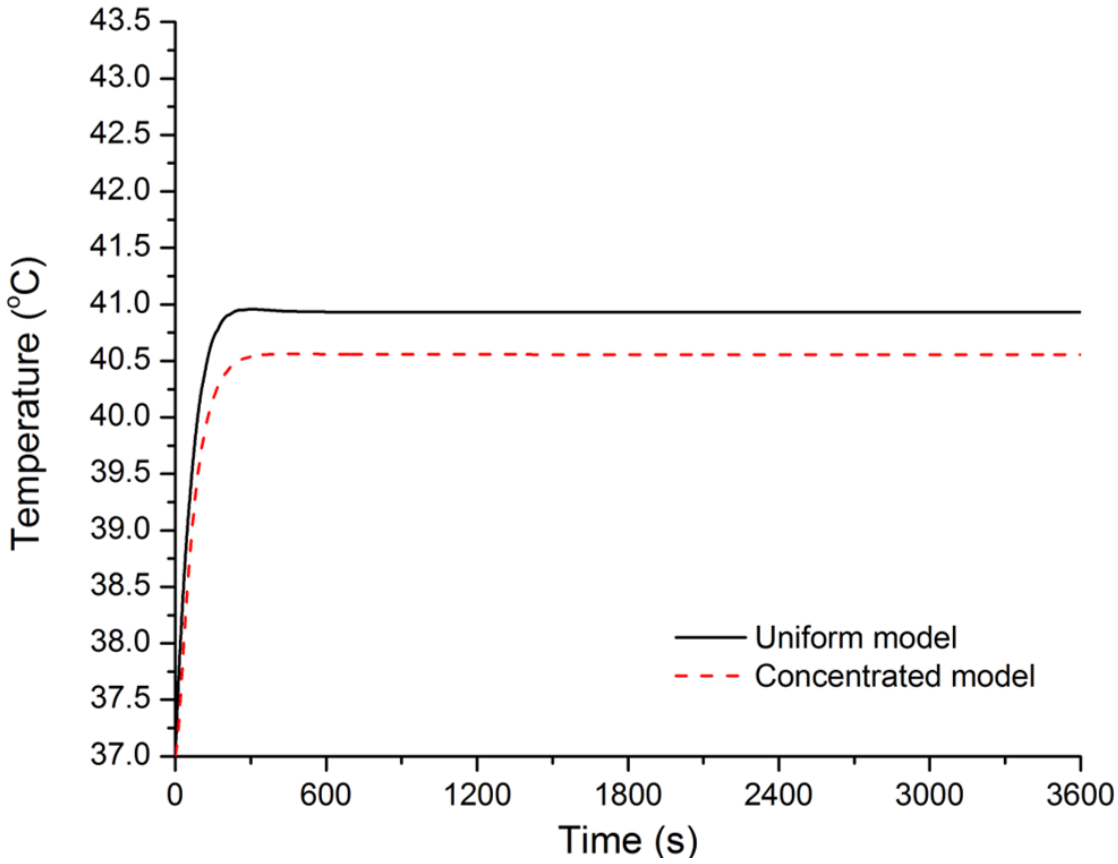

Figure 2.3 Variation of tumor-healthy tissue boundary temperature with time for uniform and concentrated distribution models under heating at constant power of $Q_P = 4.6 \times 10^5$ W/m^3.

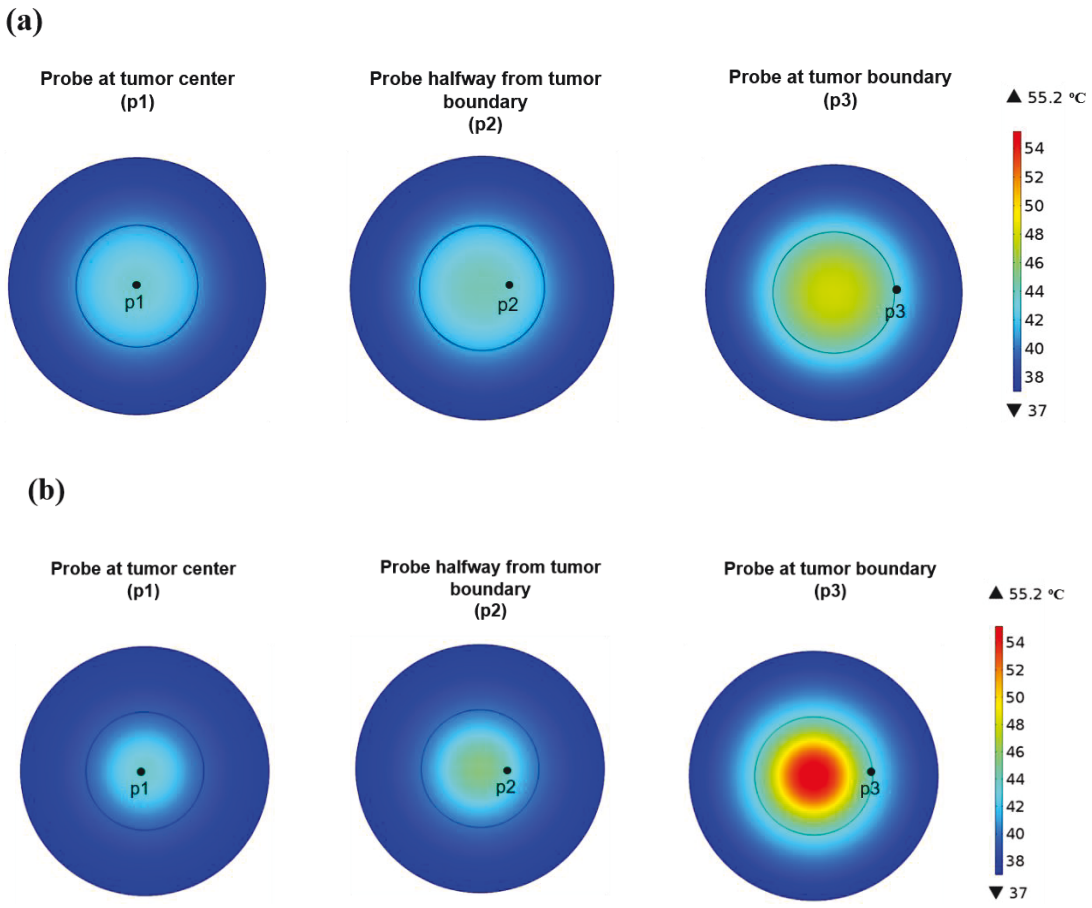

Figure 2.4 (a) Temperature distribution of uniform distribution model after 60 min of heating with modulated power based on temperature feedback from p1 – probe at tumor center, p2 – probe at halfway between tumor center and tumor-tissue boundary, p3 – probe at tumor-tissue boundary. (b) Same as (a) for concentrated model.

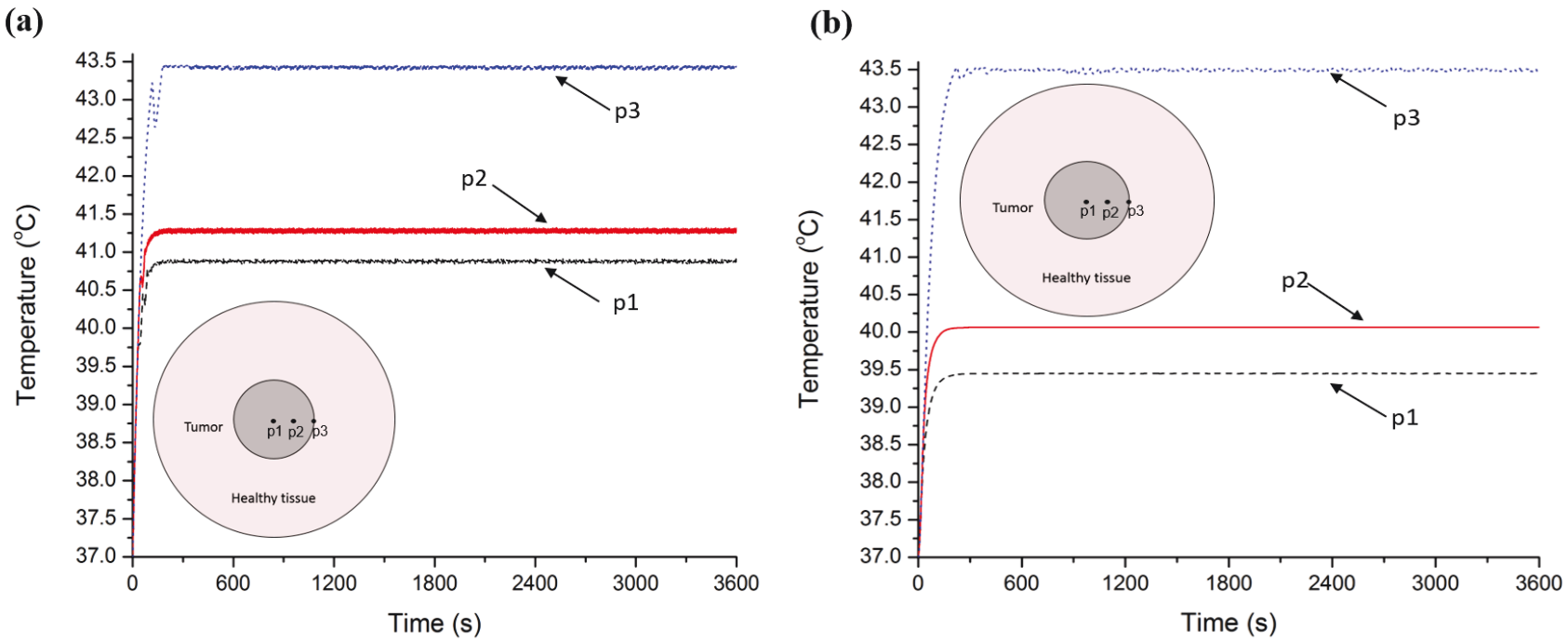

Figure 2.5 (a) Variation of tumor-tissue boundary temperature with time for uniform distribution model under heating at modulated power based on temperature feedback from , p1 – probe at tumor center, p2 – probe halfway between tumor center and tumor-tissue boundary, and, p3 – probe at tumor-tissue boundary. (b) Same as (a) for concentrated distribution model.

2.4 Discussion

Success of hyperthermia depends on the temperatures achieved inside the tumor and the treatment time (time at temperature). Temperature measurements in clinical trials for hyperthermia are often reported as index temperatures averaged over time. Index temperatures, denoted as *Tx*, are the temperatures which are exceeded by at least *x%* of the tumor volume [34]. Often *T90*, temperature achieved or exceeded in 90% of tumor volume, is used as a parameter to compare and correlate temperature measurements with treatment outcomes. Thermal dose, defined as time at temperature, is often measured as cumulative equivalent minutes normalized to 43 °C, denoted as CEM43. CEM43T90, defined as the thermal dose achieved or exceeded in at least 90% of tumor, is a superior indicator of treatment outcome over temperature alone [9,10,25,127]. Thus, rather than achieving a uniform temperature distribution (uniform thermal dose), the goal of hyperthermia therapy is to achieve a minimal effective thermal dose in >90% of tumor volume. In preclinical or clinical settings achieving this minimal thermal dose is often not realized due to technical challenges in energy deposition, inadequate temperature measurement, and lack of feedback control of energy deposition with temperature data.

Magnetic iron oxide nanoparticles, due to their biocompatibility, small size, and ability to generate substantial heat, offer great potential for cancer hyperthermia [39]. As the nanoparticles are the main source of heat in mNPH, their concentration, and distribution inside the tumor, determine the treatment outcome. Current methods of delivery such as image guided percutaneous delivery [128,129] or direct intratumor injection can ensure consistent and sufficient delivery of nanoparticles into the tumor but fail to address the issue of nanoparticle distribution inside the tumor. The varied tumor biology and

physiology significantly influences the achievable nanoparticle distribution inside a tumor. Additionally, redistribution of nanoparticles during and after mNPH has been observed [44,130–134]. Thus, it is reasonable to expect that consistently achieving a controlled uniform nanoparticle distribution inside the tumor is not possible. Tumor regions with higher concentration of nanoparticles, predictably, will result in rapidly increasing temperatures, when compared to other tumor regions, when constant power heating begins (Figure 2.2). Temperatures and temperature gradients decrease rapidly in regions far away from the nanoparticles. The heat generated by these concentrated nanoparticle regions propagate through the tumor at a higher rate ($\propto r^3$) rather than out of the tumor through the tumor-healthy tissue boundary (rate $\propto r^2$) to the surrounding healthy tissue (r is the distance from the heating zone). Thus, local concentration of nanoparticles is favorable, provided the volume of heating zones and power meet minimum threshold values [118]. For constant perfusion, the heat flux at the tumor-healthy tissue boundary is thus higher for uniform distribution of nanoparticles (656 W/m^2) compared to concentrated distribution (592 W/m^2), which potentially can lead to increased thermal damage to surrounding sensitive normal tissue and also result in under treatment regions within the tumor. Therefore, heat generation zones with volumes larger than a critical value, dependent on tumor volume, can lead to unfavorable heating of surrounding healthy tissue and tumor under treatment, as heat flux at the tumor-healthy tissue boundary will be higher than the rate of heat conduction within the tumor. Temperatures at the tumor-healthy tissue boundary reach a steady state (Figure 2.3), after an initial steep rise, depending on the nanoparticle distribution, the heating power applied and the heating duration.

Modulating power with single point thermometry can limit and control the thermal dose deposited in tumors with heterogeneous distribution of nanoparticles. In this case, placement of this single temperature sensor becomes crucial. If placed within a heating zone with nanoparticles, this temperature sensor will initiate an early reduction and control of applied power to limit the thermal dose within a prescribed value. This could lead to insufficient deposition of thermal dose to cover an adequate tumor volume (~ 90%) (Figures 2.4 & 2.5). When the temperature sensor is placed at or near the tumor-healthy tissue boundary, minimal thermal dose can be achieved in 90% of the tumor volume, for both the uniform and concentrated distributions. Power modulated mNPH with temperature feedback from the tumor-healthy tissue boundary can more likely achieve a minimal thermal dose of CEM43T90, compensating for variable nanoparticle distributions. However, for locally concentrated nanoparticle distributions, power modulated mNPH can likely produce higher intratumor temperatures to achieve the required tumor-healthy tissue boundary temperature. This could lead to ablation or necrosis in those local concentrated zones which can influence treatment outcomes for combination therapies. The simulations thus show that, with appropriate caveats, temperature monitoring at the tumor-tissue boundary is necessary to ensure a minimally effective thermal dose (CEM43T90).

2.5 Conclusions

This computational study focused on understanding the effect of nanoparticle distribution and heat output on the temperature evolution in a simple two dimensional model. Two nanoparticle distributions, uniform and concentrated, were considered. Pennes' bioheat equation was solved to compute the temperature distributions inside the

tumor and the surrounding healthy tissue. Constant power heating simulations were carried out to highlight the differences in temperature distributions achieved for the different distributions. It was shown that modulation of heat output of the nanoparticles based on temperature feedback from the tumor-healthy tissue boundary can compensate for variable nanoparticle distributions to deliver a minimum effective thermal dose (CEM43T90). However, to be clinically relevant, further simulations with more realistic parameters (eg. temperature effects on perfusion), different tumor shapes, and three dimensional models, with better strategies to modulate power will be necessary. The above results allow us to speculate that, with knowledge of nanoparticle distribution, obtained through imaging, combined with computational modeling, we can guide effective temperature sensor placement and modulated power heating to realize patient-specific hyperthermia treatment.

Chapter 3

Temperature-control via power modulation to compensate for varied particle distributions – a computational study

In this chapter, an improved modulated power heating method is described and results from implementation in 2D and 3D computational models for a range of nanoparticle distributions including those derived from animal studies are reported. For the 2D models, six nanoparticle distributions – three obtained from previous animal studies and three idealized mathematical constructs, were considered. For the 3D models, three

mathematically constructed nanoparticle distributions were considered. Temperature effects on perfusion was implemented by modeling perfusion as a function of thermal damage. A new method of modulating heating power of nanoparticles using a proportional-integral-derivative (PID) controller with temperature feedback from the tumor-healthy tissue boundary is presented. Comparisons between constant power heating and this new modulated power heating were carried out to highlight the advantages of modulated power heating. It is shown that modulated power heating with temperature feedback from the tumor-healthy tissue boundary can compensate for variable nanoparticle distributions and deliver effective tumor treatment with minimal healthy tissue damage.

3.1 Introduction

Among the challenges for clinical implementation of mNPH is the lack of precise control of nanoparticle distribution within tumors, to enable precise energy deposition throughout the tumour volume [43–46]. This could lead to under treatment of tumor and/or could result in significant thermal damage to the healthy tissue. Effectiveness of thermal therapy is defined by/limited to the region of tumor receiving the lowest thermal dose [9]. Given this, it has been generally accepted that achieving a minimum effective thermal dose ($\sim$ CEM43 $\geq$ 60 min) in a maximum volume ($\sim$ 90% or better) of tumor, to be the treatment objective or goal [9,25]. In addition, the treatment should also minimize the thermal dose deposition to the surrounding tissue to limit damage to the healthy tissue. Thermal dose, determined by time-at-temperature, is therefore dependent on the temperatures achieved. Thus, controlling the temperatures achieved inside the tumor would lead to control of the thermal dose deposited.

For mNPH, effective control of temperature requires controlled heat generation by nanoparticles and precise temperature measurement. Heat generated by nanoparticles, given by specific loss power (SLP, W/g of material), depends on the amount of magnetic material, its magnetic properties, magnitude of applied field and frequency. At fixed frequency, SLP increases non-linearly with increasing amplitude to a maximum value close to where magnetization saturation is achieved [51,56,57]. The heating output of the nanoparticles can therefore be controlled non-invasively and dynamically by modulating the amplitude of the applied alternating magnetic field (AMF). Real time temperature data can provide meaningful estimates of the heat that is being deposited into the tumor and healthy tissue, and can be used to modulate the AMF amplitude. However, measuring temperature continues to pose technical challenges in both clinical and preclinical settings [9,45]. Ideally, volumetric, *in situ*, real time and non-invasive temperature measurements are desired but lacking. In clinical settings, single point measurements are often used and are useful indicators of outcome [34]. While volumetric temperature information of the tumor and healthy tissue would be useful, single point temperature measurements, when the temperature probe is strategically placed, can offer valuable information for designing effective treatment strategies.

Computational studies have been conducted to develop optimal strategies for mNPH considering nanoparticle heat deposition, distributions and tissue thermal properties [112,114–120,135–141]. While considerable progress has been made, most of these studies incorporate simplifications such as homogeneous nanoparticle distributions, zero or constant blood perfusion etc., for computational ease and efficiency. Of the previous optimization studies [112,115,136–141] for mNPH, most of them focused on determining

optimal constant magnetic field amplitude and magnetic nanoparticle parameters, for effective tumor treatment and minimal healthy tissue damage. Bagaria and Johnson [115] proposed an optimal nanoparticle distribution for effective treatment of tumors. Candeo et al. [136] optimized energy density with respect to particle concentration, diameter, and magnetic field intensity. Salloum et al. [112] developed an optimization algorithm to inversely determine the optimal heat source parameters for a multi-injection strategy for irregular tumor geometries. They proposed a model to determine the ferrofluid injection rate, volume, and concentration for a multi-point injection of nanoparticle for MNPH. Mital and Tafreshi [137] applied genetic algorithms to optimize parameters to maximize thermal damage to tumors and minimize healthy tissue damage based on a fitness function. Bellizzi et al. [138,139] proposed optimal criteria for choice magnetic field amplitude, frequency, and diameter of nanoparticles for effective treatment of tumor and minimizing healthy tissue damage and tested it on a human head model. Koch et al. [140] and Soetaert et al. [141] looked at the effects of time-dependent power heating on tumor temperatures and thermal damage in comparison to constant power heating. Koch and Winfrey [140] built models to optimize energy density in tumors using time-dependent magnetic nanoparticle power dissipation. The nanoparticle distribution was governed by a Gaussian probability function and blood perfusion was assumed constant. They showed that time-varying power depositions increased tumor temperatures and simultaneously decreased healthy tissue temperatures. Soetaert et al. [141] evaluated different modulations of a constant frequency sinusoidal waveform and showed that power modulation resulted in more tumor thermal damage compared to constant power heating. All of the above studies either focused on optimizing different magnetic nanoparticle parameters with constant power heating or

evaluated different preset amplitude modulations to optimize tumor heating. These studies did not consider dynamically modulating power based on computed temperatures either from the tumor or healthy tissue.

Controlling the temperature at the tumor-healthy tissue boundary can ensure effective tumor treatment while simultaneously minimizing the healthy tissue damage. This temperature depends on the heat generated by the nanoparticles and controlling the nanoparticle heat output will enable control of the tumor-healthy tissue boundary temperature. Local temperature control using a proportional-integral-derivative (PID) controller is widely used in industry and in medicine [142–146]. Specifically in medicine, Salomir et al. [142] used a PID temperature control to regulate the temperature at a focal point during MR-guided focused ultrasound therapy. They obtained precise temperature control close to the precision of the temperature measurement both *in vitro* and *in vivo*. Mougenot et al. [143] further developed a three dimensional spatial and temporal control of temperature during MR thermometry guided focused ultrasound therapy. Haemmerich [144] implemented an automatic PI closed loop controller system and optimized the controller parameters for temperature controlled RF ablation.

In the current study, we present a strategy to modulate the AMF amplitude, based on single-point temperature feedback, to achieve effective tumor treatment and minimize healthy tissue damage. We hypothesized that controlling the tumor-healthy tissue boundary at a target temperature for sufficient time can compensate for variable nanoparticle distributions to deliver effective therapy. To test this hypothesis, we considered six nanoparticle distributions – three derived from animal studies and three idealized distributions. Heat transfer in the tumor and healthy tissue was modeled using the Pennes'

bioheat equation. Tumor and healthy tissue were modeled as ellipses and temperature effects on perfusion was considered. We implemented a proportional-integral-derivative (PID) controller to control the power output of nanoparticles in order to achieve a target temperature at the tumor-healthy tissue boundary and to minimize healthy tissue damage. The heating power of the nanoparticles was based on the experimental values for bionized nanoferrite (BNF) particles determined by Bordelon [56]. We compared the time-dependent change in temperatures and thermal dose (CEM43) obtained in the tumor and healthy tissue, for both constant power and PID controlled modulated power heating. Modulated power resulted in effective tumor treatment with overall lower and homogeneous temperatures, compared to constant power. We then implemented the above strategy in 3D computational models where the tumor was modeled as an ellipsoid and three mathematical nanoparticle distributions were considered. A clinically relevant thermal dose of CEM43 $\geq$ 60 min was achieved for all nanoparticle distributions. This shows that taking advantage of variable heating power potential of nanoparticles and controlling the tumor-healthy tissue boundary temperature can compensate for variable nanoparticle distributions to deliver effective treatment.

3.2 Model description

Two concentric elliptical regions, shown in Figure 3.1, representing the tumor and a region of interest of the surrounding healthy tissue were chosen as the representative geometry for our study. The inner elliptical region (major axis l_t = 9 mm, minor axis w_t = 6 mm) represents the tumor seeded with nanoparticles. The outer elliptical region (major axis l = 19 mm, minor axis w = 16 mm) corresponds to modelled healthy tissue. We assume that the outer boundary of the healthy tissue is in contact with the core body temperature

(infinite heat reservoir) maintained at 37°C. Heat transfer in the healthy tissue and tumor can be described by the Pennes bioheat equation [81] as

$$\begin{aligned}\rho_n c_n \frac{\partial T_n(x,y,t)}{\partial t} &= k_n \nabla^2 T_n(x,y,t) \\ &+ \rho_b c_b \omega_{b,n}(x,y,T_n)\,(\,T_b - T_n(x,y,t)\,) + Q_{m,n} \\ &+ Q_P(x,y,t)\end{aligned} \tag{3.1}$$

where the subscript n accounts for the tissue layer (n = 1 for the tumor and n = 2 for healthy tissue) and the subscript b the blood parameters, respectively. ρ_n is the density, c_n the specific heat, $T_n(x,y,t)$ the local temperature, k_n the thermal conductivity, $Q_{m,n}$ the metabolic heat generation rate in either the healthy tissue or tumor, and Q_P is the heat generated by the nanoparticles. The subscript m in Equation (3.1) refers to metabolic heat generation in tissue layer n. ρ_b, c_b, $\omega_{b,n}(x,y,T_n)$ and T_b denote density, specific heat, perfusion rate, and temperature of blood, respectively. Table 3-1 summarizes the thermophysical properties for healthy tissue, tumor, and blood [74,122–126] used in this study. We assumed that there is no heat generation due to eddy currents by AMF in the tissue. At the interface between the tumor and healthy tissue, continuity in temperature and heat flux were present, given by:

$$k_{tissue} \left.\frac{\partial T_{tissue}}{\partial j}\right|_{int} = k_{tumor} \left.\frac{\partial T_{tumor}}{\partial j}\right|_{int} \tag{3.2}$$

$$T_{tissue}|_{int} = T_{tumor}|_{int} \tag{3.3}$$

In Equation (3.2), the variable j denotes the surface normal to the elliptical boundary between tumor and healthy tissue. At the elliptical outer boundary of the healthy tissue, the temperature is constant, equal to the core body temperature

$$T_{tissue\ boundary} = 37\ °C \tag{3.4}$$

The initial temperature for both the tumor and healthy tissue was set at 37 °C in these simulations.

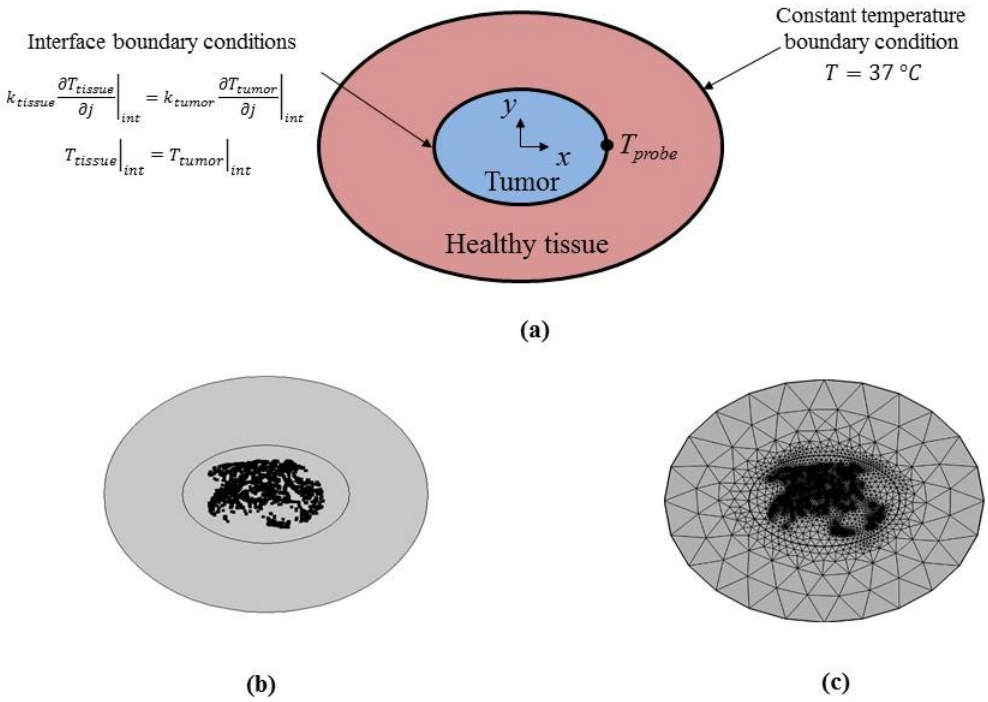

Figure 3.1 Schematic of the computational geometry, tumor region surrounded by healthy tissue, with the thermal boundary conditions. (b) Sample digitized E1 binary model showing the tumor with nanoparticles. (c) Sample mesh for the model under (b). Note: Figures not to scale.

3.2.1 Nanoparticle distributions

The model magnetic nanoparticle distributed in the tumor region (Figures 3.2(a), (b)) are line heat sources [118]. If the individual heating power of the nanoparticles is Q_N, and the number of nanoparticles N (1460 in our study) distributed in the tumor is known, the total power generated by the nanoparticles deposited in the tumor is

$$Q_p = N \times Q_N \tag{3.5}$$

In the present study, the heating power of nanoparticles was modeled based on experimentally determined SLP values for BNF nanoparticles at 150 kHz [56]. The corresponding alternating magnetic field amplitude at the chosen frequency can be estimated using the continuous polynomial approximation of SLP vs *H* given by Soetaert et al. [141]. The iron concentration in the tumor was assumed to be 5 mg Fe/cc of tumor [52]. The total heating power Q_p can be obtained from SLP (specific loss power) experimental data, using the expression

$$SLP = \frac{Q_p}{C_{Fe}} \tag{3.6}$$

For example, when the total heating power delivered to the tumor is $Q_p = 5.18 \times 10^5$ W/m^3 and the iron concentration C_{Fe} = 5 mg Fe/cc, the SLP is 103.6 W/g Fe. At 150 kHz frequency, the SLP of 103.6 W/g Fe corresponds to a peak magnetic field amplitude of ~ 13.5 kA/m.

Six nanoparticle distributions were considered in this study. Three distributions were derived from tissue sections (E1, E2, E3) obtained from tumors injected with nanoparticles as described previously in [52,53] (Figure 3.2), and three were mathematical functions representing 'idealized' distributions (M1, M2, M3, Figure 3.2).

Modeling nanoparticle distributions from tumor tissue sections

Images of nanoparticle distributions taken from archived sections of human prostate tumor xenografts grown in mice were used to generate models E1-E3 (Figure 3.2). Experimental details have been previously described [52,53]. These methods are briefly reviewed here for clarity. Nanoparticles were comprised of aqueous BNF-Starch (catalog no. 10-00-102), obtained from Micromod Partikeltechnologie, GmbH (Rostock,

Germany), and were injected into tumors. Particles were used as received [52,53]. Formalin-fixed tumors were sectioned and stained with Perls' reaction to visualize the distribution of BNF MIONs (i.e., ferric, Fe3+) in the three human prostate xenograft models.

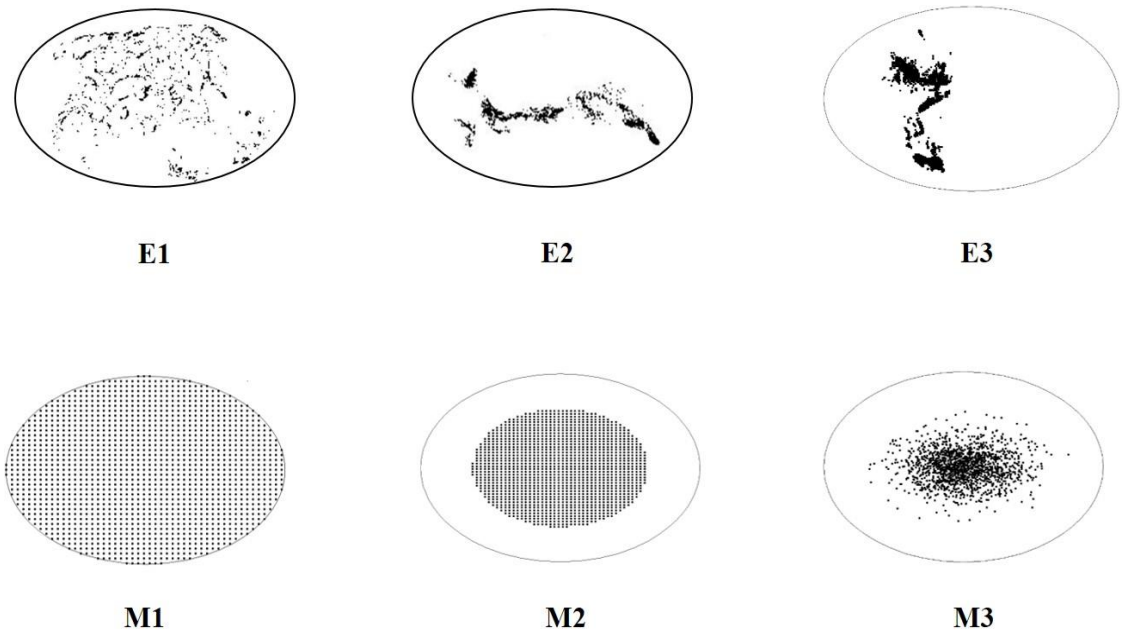

Figure 3.2 Nanoparticle distributions used in the computational study (a) obtained from stained tissue sections from human tumor xenografts obtained from nude mouse tumor models [52,53], (E1- nanoparticles relatively uniformly distributed, E2- concentrated distribution along the major axis, E3- concentrated and offset along the minor axis) and (b) ideal nanoparticle distributions, (M1 - uniform, M2 – uniformly concentrated in 40% of tumor area, and M3 - Gaussian) used in the computational model.

The stained tumor sections [52,53] were digitally imaged and these images were processed to display nanoparticle distributions in a format suitable for our computational model. The original high resolution (4752 × 3182 pixels) digital images of the stained sections were resized into smaller images (225 × 150 pixels), with no change in aspect ratio, to reduce the data volume and computational cost. The change in the ratio of stained

pixels to the total pixels in the resized image is minimal (~1.5 %). The images were then converted into binary form using MATLAB's image processing toolbox. In these binary images, the dark pixels represent stained nanoparticle clusters, each of them acting as a line heat source $Q_N(x, y, t)$, representative of the nanoparticle distribution in space in the tumor domain. Nanoparticle distributions obtained from the processed images of the three mouse models, E1, E2, and E3, are shown in Figure 3.2(a).

Idealized nanoparticle distributions

The three idealized distributions, were the uniform (M1) [114], concentrated (M2) [52], and Gaussian distributions (M3) [112,140,141] (Figure 3.2). In the M1 distribution, nanoparticles are evenly distributed throughout the tumor area. In the M2 distribution, the nanoparticles were arranged uniformly in an area occupying only the central 40% region of the tumor. For the M3 distribution, the nanoparticle distribution in the tumor was governed by a Gaussian probability function centered at the tumor center and extending to the tumor-tissue boundary. The Gaussian probability function in the Cartesian coordinate system is

$$P(x,y) = \frac{1}{2\pi\sigma_x\sigma_y}\, e^{\left(-\frac{1}{2}\left(\frac{x^2}{\sigma_x^2}+\frac{y^2}{\sigma_y^2}\right)\right)} \tag{3.7}$$

In Equation (3.7), σ_x, σ_y are the standard deviations of x and y, respectively. In the current simulation, σ_x and σ_y were arbitrarily chosen to be 2 and 0.5, and the generated Gaussian distribution of points was truncated to fit inside the tumor. To compare heating effects among the six tumor models, the total number of nanoparticles N (dark pixels) in a tumor was fixed at N ~1460 ± 5 for each model. This means that the total heating power

delivered to each of the six tumor models is identical, allowing a quantitative comparison of temperatures and thermal doses.

3.2.2 Perfusion models

Effects of temperature on perfusion were accounted with three models, the (i) constant perfusion model (e.g. 'classic' Pennes equation) as described by Equation 3.1, the (ii) Arrhenius perfusion model; and, the (iii) modified Arrhenius perfusion model; as described previously [147,148]. In the first model, blood perfusion in both tumor and healthy tissue is constant (independent of temperature),

$$\omega_b(T) = \omega_{bi} \tag{3.8}$$

In the Arrhenius model, blood perfusion is described as a function of temperature and time, correlated to the degree of microvascular stasis (DS) expressed as

$$\mathrm{DS} = 1 - \exp(-A \int_0^t e^{-E_a/RT(\tau)} d\tau \tag{3.9}$$

with

$$\omega_b(T) = \omega_{bi}(1 - DS) \tag{3.10}$$

In Equations (3.9) and (3.10), A is the frequency or pre-exponential factor, E_a the activation energy barrier, R the universal gas constant, $T(\tau)$ is the absolute tissue temperature as a function of time and ω_{bi} the initial blood perfusion rate. The degree of vascular stasis DS varies between 0 (no vascular damage) and 1 (complete vascular shutdown). The values for A and E_a are shown in Table 3-1.

The foundation for the modified Arrhenius perfusion model is the first-order kinetic Arrhenius model of vascular stasis (Equations 3.9 and 3.10), expanded by an additional term to increase the relative perfusion when vascular stasis is low. This latter model is

derived empirically from data determined experimentally by He et al. [147]. Schutt et al. [148] represented the resulting curve by four linear segments to improve computational efficiency, yielding

$$\omega_b(T)=\begin{cases} \omega_{bi}(30.DS+1), & (DS\leq 0.02) \\ \omega_{bi}(-13\ DS+1.86), & (0.02<DS\leq 0.08) \\ \omega_{bi}(-0.79\ DS+0.884), & (0.08<DS\leq 0.97) \\ \omega_{bi}(-3.87\ DS+3.87), & (0.97<DS\leq 1.0)\ . \end{cases} \quad (3.11)$$

When the degree of stasis is low ($DS \leq 0.02$), there is an increase in perfusion. As the degree of stasis increases ($0.02 < DS \leq 0.08$), perfusion first decreases moderately, and then more rapidly ($0.08 < DS \leq 0.97$), before eventually becoming zero ($0.97 < DS \leq 1.0$).

3.2.3 Constant power heating

For the constant power simulations, the total heating power of nanoparticles Q_p remained constant throughout the simulation. Temperature distribution $T(x, y, t)$ and thermal dose were evaluated as a function of time for each simulation. The total thermal dose achieved in the tumor was expressed as the cumulative equivalent minutes at 43 °C (CEM43) summed up during the course of heating [25]. Mathematically it is expressed as

$$CEM43 = \int_{t=0}^{t=final} R^{\frac{43\,℃ - T(x,y,t)}{1\,℃}}\, dt \quad (3.12)$$

In Equation (3.12), $R = 0.5$ for $T > 43$ °C, and $R = 0.25$ for $T \leq 43$ °C. CEM43 T90 is defined as the total thermal dose expressed as cumulative equivalent minutes at 43 °C achieved or exceeded in 90% of the tumor area [9,32], with treatment considered effective when achieved for 60min or longer, CEM43 T90 ≥ 60 [9,32]. The power required to achieve a clinically effective thermal dose (CEM43 T90) within 20 minutes was computed

for the situations considered in this study. The heating power necessary to achieve such a treatment effect for a given treatment time is defined as the isoeffective heating power, Q_{iso}. It was computed by iteratively carrying out a series of simulations with constant power settings until 90% of tumor area achieved thermal dose of CEM43 ≥ 60min.

3.2.4 Modulated power heating

For modulated-power heating, the heating power of nanoparticles was varied as a function of the temperature computed at the tumor-tissue boundary [19, 24]. As discussed in Attaluri et al [52], for a spherical tumor model with uniform distribution of nanoparticles, using the temperature at tumor-tissue boundary as feedback for power modulation results in effective thermal dose deposition in the tumor. In the current study, a 2D elliptical model was considered, which accounts for variability in two directions and different nanoparticle distributions, and thus required to precisely determine the location of temperature probe on the tumor-healthy tissue boundary. To determine this, eight probe locations (P1-P8, Figure 3.3) located on the tumor-tissue boundary, were considered. As in Chapter 2, for all the six nanoparticle distribution models, the heating power was alternated between two levels: the higher heating power was selected when the probe temperature was below 43.5 °C, and the lower heating power when T_{probe} exceeded 43.5 °C. The initial power and the heating algorithm are described mathematically as

$$Q_p(T) = \begin{cases} 1.5 \times Q_{iso}, & if\ T_{probe} < 43.5\ ^\circ C \\ 0.15 \times Q_{iso}, & if\ T_{probe} \geq 43.5\ ^\circ C \end{cases}. \quad (3.13)$$

The higher heating power was chosen to be greater than Q_{iso} to allow for the tumor to achieve the target temperature faster, which is clinically desired. The percentage area of tumor and healthy tissue with thermal dose CEM43 ≥ 60min, was used to determine the

best location for probe placement for each of the six nanoparticle distributions. The temperature feedback from a probe location (P1-P8), which results in achieving a thermal dose of CEM43 ≥ 60 in 90 ± 5% of tumor area and closer to 5% of surrounding healthy tissue was chosen as the best location for temperature feedback.

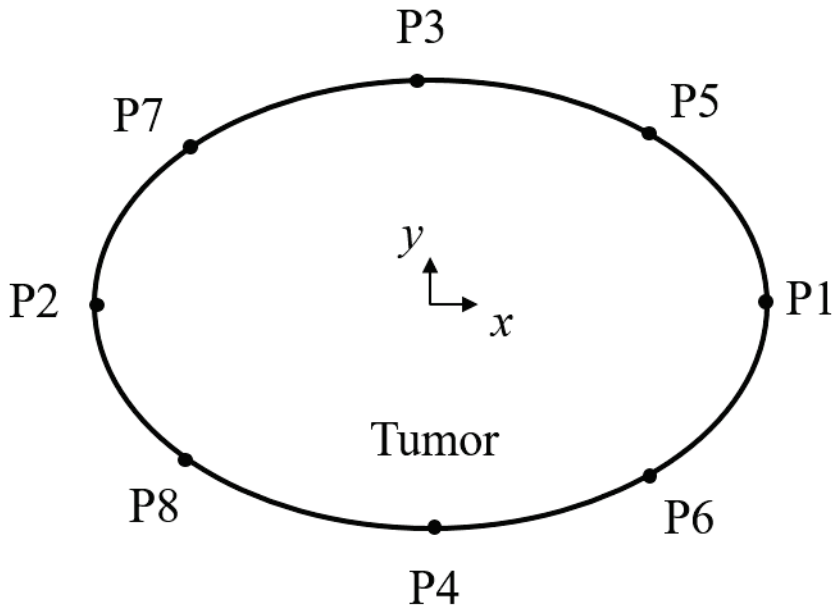

Figure 3.3 Eight locations on the tumor-tissue boundary tested as choices for temperature feedback during power modulated heating for delivering optimal thermal dose to the tumor and minimizing healthy tissue damage

Once the best location for probe placement for each of the six nanoparticle distributions was determined, a controller for modulating power based on temperature feedback was implemented. With this controller, we aimed to achieve the target temperature of 43.5 °C at the probe location rapidly, and maintain it at that temperature for the remainder of the treatment duration. The block diagram for the feedback loop of the developed temperature controller is shown in Figure 3.4. The temperature computed at the probe location T_{probe} is fed back into the controller with the reference temperature T_{ref}. The

difference between T_{probe} and T_{ref} is fed into the controller and the controller output is then fed into the model. The closed loop transfer function (*Tr)* for the closed-loop system (Figure 3.4) is given by

$$Tr = \frac{PC}{1 + PC} \tag{3.14}$$

Where *P* is the plant transfer function and C is the controller function. For the controller we used the general PID (proportional-integral-derivative) temperature control.

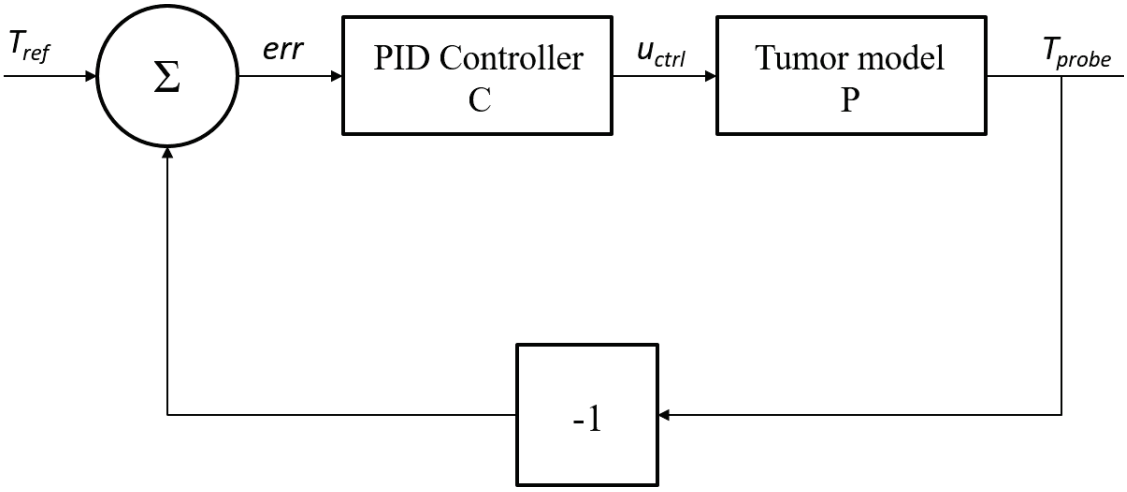

Figure 3.4 Block diagram of feedback loop with the PID (proportional-integral-derivative) controller for modulating nanoparticle heat output

A proportional controller would allow for increasing the heating power proportionally to the difference between the computed temperature at probe location and the target temperature. An integral controller ensures that the control output agrees with the target setpoint in steady state. A derivative controller ensures closed-loop stability and allows choice of a higher proportional controller gain and a faster integral controller, resulting in achieving the target temperature faster. While 90% of the controllers in the industry employ a PI controller, adding the derivative control would enable achieving the

target temperature faster at the target location and also minimizes temperature overshoot which would result in minimal healthy tissue damage. The PID controller is given by

$$u_{ctrl}(T) = K_p\theta(x,y,t) + K_i\int_0^t \theta(x,y,t)\,dt + K_d\frac{\partial\theta(x,y,t)}{\partial t} \tag{3.15}$$

$$Q_p(T) = u_{ctrl}(T)\,Q_{max} \tag{3.16}$$

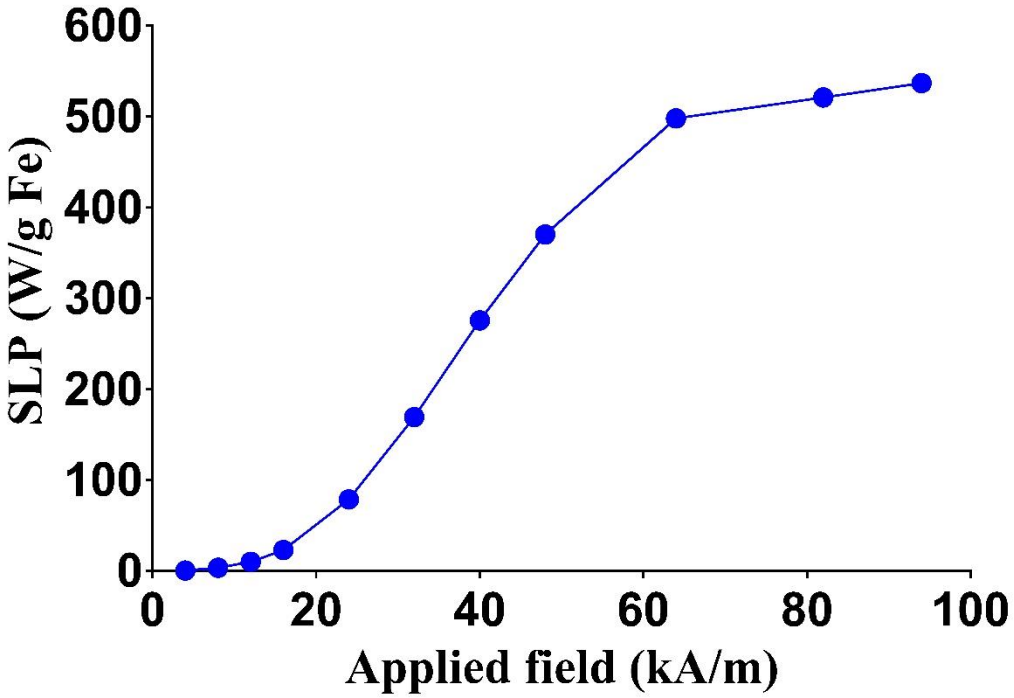

Figure 3.5 Specific loss power (W/g Fe) versus applied field (peak-to-peak, kA/m) for BNF-starch nanoparticles [56]

In Equation 15, $\theta(x,y,t)$ is the difference between computed temperature at the probe location $T_{probe}\ (x,y,t)$ and the target temperature T_{ref}. The gains K_p , K_i , K_d are the proportional, integral and derivative gains of the PID controller. u_{ctrl} adjusts the heat generation of nanoparticles by modulating the heating power applied based on the difference in measured temperature at the probe location and target temperature. Q_{max} is

the maximum power that can be generated by the nanoparticles at a given frequency. The maximum SLP of 537 W/g Fe (peak field strength of 47 kA/m at frequency 150 kHz) for BNF nanoparticles as reported by Bordelon [56] (Figure 3.5) was used for determining Q_{max}.

The PID controller gains K_p, K_i, K_d were determined by using model-based control design methods based on Youla parametrization (Q-parametrization) [145,146,149,150]. By Q-parametrization theory, for a single-input single-output stable plant transfer function $P(s)$, the family of all stabilizing controllers $C(s)$ can be expressed as,

$$C(s) = \frac{Q(s)}{1 - P(s)Q(S)} \tag{3.17}$$

where $Q(s)$ is any stable transfer function. We approximated our model system by a second order plant transfer function $P(s)$ with three parameters, given in Laplace domain by,

$$P(s) = \frac{g}{(1 + \tau_1 s)(1 + \tau_2 s)} \tag{3.18}$$

where g is the static gain for step input, τ_1 and τ_2 are time constants. The plant transfer function parameters were assessed by open loop step response. The power was stepped to 30% of maximum power and the temperature response was recorded at the probe location. The static gain g, is given by the ratio of temperature gain achieved with the step in control input.

$$g = \frac{\Delta T}{u_{ctrl}} \tag{3.19}$$

The time constant τ_1 was calculated as the delay between the maximum rate of change in temperature and the temperature response at the probe location. The time constant τ_2 is the difference between the time taken for the temperature response to reach 63% of total temperature gain and the time constant τ_1.

A second order transfer function *Tr* was chosen, given in the Laplace domain,

$$Tr(f,\zeta) = \frac{f^2}{s^2 + 2\zeta f s + f^2} \tag{3.20}$$

where *f* is the closed loop frequency and ζ is the damping ratio. Using equations 14, 17 and 20, the controller function *C(s)* was determined as,

$$C(s) = \frac{f^2(\tau_1 s + 1)(\tau_2 s + 1)}{gs(s + 2\zeta f)} \tag{3.21}$$

The individual gains can then be calculated as,

$$K_p = \frac{f}{2\zeta g}(\tau_1 + \tau_2 - \frac{1}{2\zeta f}) \tag{3.22}$$

$$K_i = \frac{f}{2\zeta g} \tag{3.23}$$

$$K_d = \frac{f}{2\zeta g}(\tau_1 + \tau_2 - \frac{1}{2\zeta f}) \tag{3.24}$$

After determining the PID controller gains, the power was modulated based on temperature feedback from the probe on the tumor-healthy tissue boundary determined previously. The computed temperature at the probe location $T_{probe,}$ was compared to a reference temperature signal T_{ref} and the difference was fed into the PID controller. In the current simulations, the reference temperature signal T_{ref} was chosen to be ramp signal, which begins at 37 °C, at t = 0 s, and reaches the target temperature at t = 30 s. This time point was chosen as it is clinically desirable to reach the target temperature as quickly as possible. The output from the PID controller u_{ctrl} modulates the nanoparticle heat output.

3.2.5 3D models

Three 3D nanoparticle distribution models (Figure 3.6) were considered to further test the PID controlled modulated power heating described above. Tumors were represented by 3D ellipsoids of total volume of 150 mm^3. The healthy tissue was a cube of length 5 cm. In the T1 (uniform) distribution model, the nanoparticles were evenly distributed inside the tumor. In the T2 (Gaussian-centered) distribution model, the nanoparticles were normally distributed at the tumor center. For the T3 (3pt-Gaussian), the nanoparticles were normally distributed at three centers (indicating points of injection). The same thermal model that was implemented for the 2D models was used for the 3D simulations.

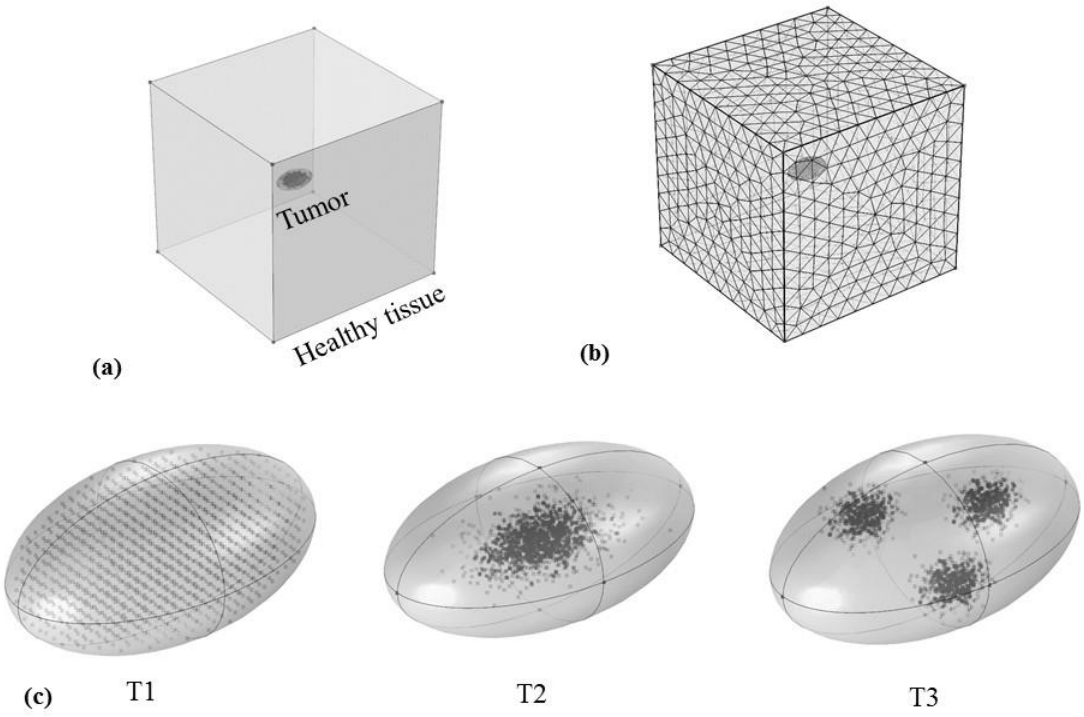

Figure 3.6 (a) Schematic of the 3D computational model with tumor and surrounding healthy tissue. (b) Sample mesh for the 3D model. (c) Three distributions, T1- Uniform,

T2 – Gaussian centered, T3 – 3pt-Gaussian distribution mimicking 3 point nanoparticle injection

3.2.6 Solution method

COMSOL Multiphysics 5.2a, a commercial finite element solver, was used to solve numerically the governing differential equations (Equation 3.1) subject to the boundary conditions described by Equations (3.2 – 3.4). A typical finite element grid for the E2 nanoparticle distribution is displayed in Figure 3.1 (c). In all models, the distance between adjacent nodes was very small in the vicinity of the nanoparticles and increased with distance from the nanoparticles. For example, the mesh used to compute heating for the E2 model consisted of 13932 triangular elements with a maximum element size of 2.47 mm and a minimum element size of 0.11 mm. To check the sensitivity of the solution to mesh size, the mesh size was refined by increasing the number of elements to 19060, which resulted in a change in maximum temperature of less than 0.01%. Similarly, for the transient solution, changing the time step from 1s to 0.5s had negligible (<0.01% change) effect on the maximum temperature. Thus, the chosen grid size and time step were deemed adequate.

Table 3-1 Thermophysical properties used in the simulation for tumor, healthy tissue and blood

Properties	Tumor	Tissue	Blood*
Thermal Conductivity (k, W/m-K)	0.51 [122]	0.51 [122]	N/A
Density (ρ,kg/m^3)	1045 [122]	1045 [122]	1060 [125]
Heat Capacity (C_p, J/kg·K)	3760 [122]	3760 [122]	3770 [125]
Initial Perfusion Rate (ω_{bi},1/s)	0.0095 [123]	0.003 [123]	N/A
Metabolic Heat Rate (Q_m, W/m^3)	31872.5 [74]	6374.5 [74]	N/A
Pre-factor (A, 1/s)	1.8e^{36} [151]	1.03e^{38} [151]	N/A
Activation Energy (E_a, J/mol)	2.38e^5 [151]	2.49e^5 [151]	N/A

*Temperature of blood (T_b) was fixed at 37ºC [125]. (N/A – not applicable)

3.3 Results

3.3.1 Temperature distributions

In mNPH, the primary heat sources are the magnetic nanoparticles. Hence, the distribution of nanoparticles significantly influences the achieved temperature distribution in the tumor and healthy tissue. Figure 3.7 shows the temperatures achieved inside the tumor and healthy tissue after 20 minutes of constant-power heating (Q_p = 10.6 × 10^5 W/m^3) and constant perfusion (Table 3-1). This power setting was chosen to yield a minimum thermal dose of CEM43 ≥ 60 min in 90% of tumor area in the uniform model.

Significant differences were observed in the temperature distributions among the six tumor models when nanoparticle heating was conducted using this constant power value for 20 min. The E3 model was characterized by concentrated nanoparticle clusters (parallel to the minor axis) with corresponding high temperatures, whereas the uniform model exhibited small temperature differences and gradients, consistent with the nanoparticle distribution. The E2 model with broadly scattered nanoparticles in the tumor region demonstrated a temperature distribution approximating the uniform distribution. The temperature distribution for the E1 model resembled the idealized concentrated model. These results are consistent with those previously described by Attaluri et al. [52].

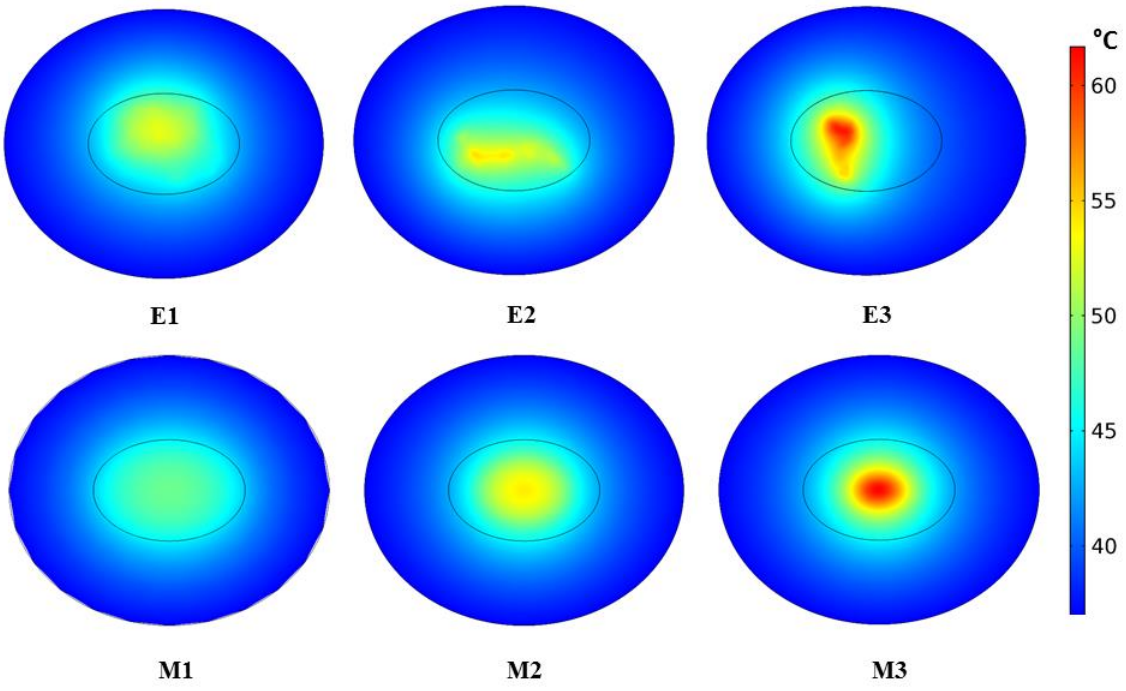

Figure 3.7 Localized nanoparticle distributions lead to higher temperatures Computed temperature distributions in the tumor and surrounding healthy tissue for six nanoparticle distributions after 20 min of heating at constant power $Q_p = 10.6 \times 10^5$ W/m^3 with constant perfusion

A quantitative comparison of the characteristic temperature profiles for the six nanoparticle distributions and three perfusion models is displayed in Figure 3.8. The results demonstrate that the three idealized models (M1, M2, and M3) produced a symmetrical distribution about the tumor center along both major and minor axes, mirroring the nanoparticle distributions. On the other hand, the results derived from mouse tumor images displayed asymmetric temperature distributions. The asymmetry was most pronounced for E3, a distribution characterized by significant clustering of nanoparticles along a narrow vertical region parallel to the minor axis. As expected, the maxima for the temperatures were observed at the locations of the highest nanoparticle density along the respective cross sections. The E3 model also exhibited the highest range of temperature variations in the tumor (for constant perfusion), with a minimum of 40.0 °C and a maximum of 59.4 °C. The idealized uniform nanoparticle (M1) distribution exhibited the lowest range of temperature variations (~43 – 49 °C) among all models studied. The idealized Gaussian nanoparticle (M3) distribution exhibited the maximum temperature (for example 61.7 °C, constant perfusion) among all the nanoparticle models across all the perfusion models. When temperature-dependent perfusion was considered (Figure 3.8 (b), (c), (e), (f)), the range of tumor temperatures increased for all nanoparticle distributions, except for the idealized uniform distribution. The temperatures were similar for the two temperature-dependent perfusion models.

3.3.2 Constant power heating

The isoeffective heating power Q_{iso} for 20-min treatment was calculated for the six nanoparticle distributions and three perfusion models. The results are summarized in Table 3-2. Conditions chosen for calculating the isoeffective power were based upon parameters

previously described by Attaluri et al. [52]. E3 required the highest heating power Q_{iso} to achieve the isoeffective thermal dose for the three perfusion models, when compared with the other nanoparticle distributions. Differences in the isoeffective heating power were most pronounced for constant perfusion: the maximum power (19.6×10^5 W/m^3) for E3 is contrasted to the minimum power (10.6×10^5 W/m^3) for the M1 (uniform) distribution. Conversely, when temperature-dependent perfusion was taken into account, the various nanoparticle distributions, except E3, required similar isoeffective heating power ($\sim 8.4 \pm 0.4 \times 10^5$ W/m^3). E3 nanoparticle distribution model required at least 20% more isoeffective heating power than the other nanoparticle distributions. This can be attributed to the asymmetry in the E3 nanoparticle distribution: regions of low nanoparticle concentration, away from the clusters, required more heating power than the high- or uniform-concentration regions to achieve the isoeffective dose and similar temperature levels.

The thermal dose (CEM43 $\geq$ 60 min) deposited into the healthy tissue after 20 minutes of heating for the respective isoeffective power (Q_{iso}) were compared for the six nanoparticle distributions (Table 3-2). E3, again, was found to be the least favorable distribution, depositing the highest thermal dose into the healthy tissue. The idealized uniform distribution (M1) deposited the lowest thermal dose into nearby normal tissue, independent of the perfusion model. The image-derived nanoparticle distributions (E1, E2, and E3) deposited more heat into adjacent normal tissues than any of the idealized models (M1, M2 and M3), regardless of perfusion model chosen for comparison. For temperature-dependent perfusion, the thermal dose deposited into the healthy tissue was less than for constant perfusion for all nanoparticle distributions, except for the idealized uniform

model. The uniform distribution exhibited a slight increase for temperature dependent perfusion, when compared with the constant perfusion model.

Table 3-2 Isoeffective heating powers for treatment time of 20 min for the six nanoparticle distributions with the three perfusion models.

Nanoparticle Distribution	Isoeffective heating power ($\times 10^5$ W/m^3)			Percent of healthy tissue with CEM43 ≥ 60 min (%)		
	Constant Perfusion	Arrhenius Perfusion	Modified Perfusion	Constant Perfusion	Arrhenius Perfusion	Modified Perfusion
M1	10.6	8.0	8.1	0.2	0.5	0.4
M2	11.8	8.0	8.1	2.0	2.0	1.9
M3	12.5	8.2	8.2	2.7	2.6	2.6
E1	13.6	8.8	8.9	6.6	5.1	5.2
E2	12.2	8.3	8.4	3.5	3.2	3.2
E3	19.6	10.5	11.0	18.4	13.8	14.5

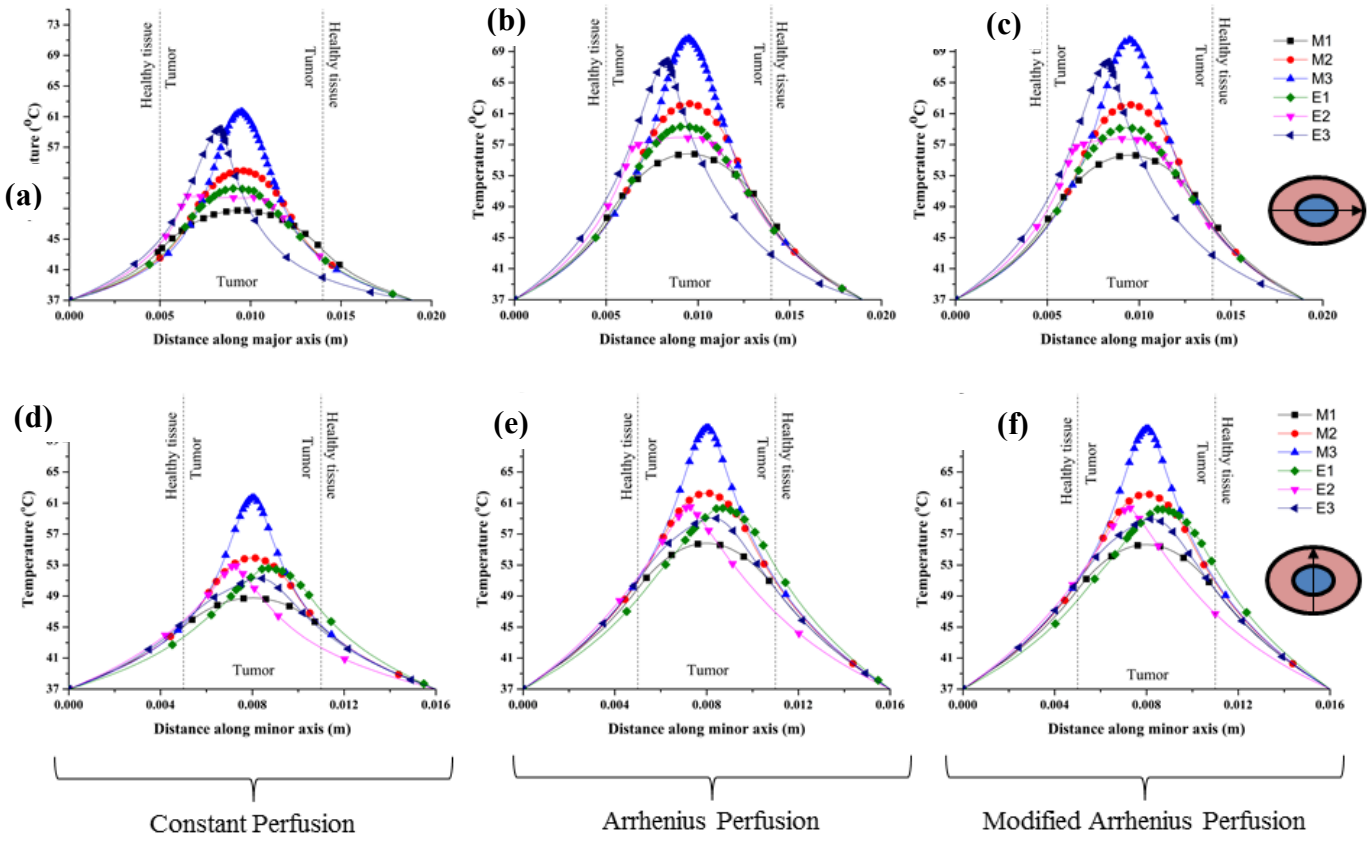

Figure 3.8 Choice of perfusion model influences model tumor and healthy tissue temperature distributions. Temperature distribution along the major and minor axes of computational model, for the six nanoparticle distributions after 20 min of heating at constant power $Q_p = 10.6 \times 10^5$ W/m^3, major axis: (a) constant perfusion, (b) Arrhenius perfusion and (c) modified Arrhenius perfusion; and minor axis: (d) constant perfusion, (e) Arrhenius perfusion and (f) modified Arrhenius perfusion model.

3.3.3 Modulated power heating

Eight probe locations (P1-P8, Figure 3.3), equidistant on the tumor-tissue boundary, were chosen to determine the best probe location for temperature feedback to modulate power for each of the nanoparticle distributions. The percent of tumor area and healthy tissue area with thermal dose of CEM43 $\geq$ 60 min was computed for the six nanoparticle distributions after 20 minutes of power modulated heating (Equation 3.13) with temperature feedback from each of the eight probe locations. The results were summarized in Table 3-3. For the ideal mathematical distributions M1 and M2, identical values were obtained due to symmetry. For each nanoparticle distribution, the probe location for which ~90% of tumor area having a thermal dose of CEM43 $\geq$ 60 min and ~5% area of healthy tissue having thermal dose of CEM43 $\geq$ 60 min was chosen. E3 distribution model had no probe location which satisfied both the criteria simultaneously, hence probe location P6 was chosen, which had a tumor thermal dose (CEM43 $\geq$ 60 min in 86.74% of tumor area) and healthy tissue thermal dose (CEM43 $\geq$ 60 min in 12.77% of healthy tissue area) closest to our criteria. It can be observed that for both the idealized symmetric and image-derived asymmetric nanoparticle distributions, the ideal probe locations are the farthest from the nanoparticle distribution centers.

The probe locations for each of the nanoparticle distributions determined above were used as temperature feedback locations for the PID controller. The gains for the PID controller were calculated by computing the open loop response for an input of 30% maximum power (u_{ctrl} = 0.3). The gain, g, and the time constants for each of the nanoparticle distributions were calculated from the open loop response. The gains K_p, K_i, K_d for the PID controller were then calculated (Table 3-4). Of the six nanoparticle

distributions, the uniform distribution (M1) has the highest open loop gain (23.8 K) while the off center concentrated nanoparticle distribution E3 had the least gain (17.63 K). This can be attributed the proximity of the probe (P1) to the nanoparticles in the uniform distribution, while for E3 distribution the feedback probe P6 is farther away from the nanoparticle distributions. For controlled open loop response, the probes located nearest to the nanoparticle distributions generated the highest open loop temperature gain. The proportional gain K_p was the highest (14.93 1/K) for off center nanoparticle distribution (E3) while the uniform distribution (M1) had the least (7.45 1/K). The integral gain K_i, which controls the temperature at the probe location to the reference temperature, was similar for all the distributions (0.042-0.047 1/s-K) except for E3 (0.057 1/s-K). The differential gain K_d , which allows for ramping up the proportional gain to achieve target temperature rapidly, was negligible for the uniform distribution (M1) while the E3 distribution had the highest gain (145.54 s/K).

Figure 3.9 shows the variation of power applied with time for each of the nanoparticle distributions when the temperature at the probe location (Table 3-3) was controlled using a PID controller with gains as in Table 3-4. Comparison of the variation in applied power for the six nanoparticle distributions show some significant differences. For distributions where nanoparticles were distributed uniformly in the tumor (M1 and E1), the applied power increased initially to the maximum and then gradually dampened and decreased to a lower value of ~30% maximum power. For distributions with concentrated regions of nanoparticles (E1, E3 and M2, M3), the applied power initially increased to maximum power available and after the probe temperature reached the target temperature of 43.5 °C, the input power oscillated between the maximum and a minimum power level.

The temperature profiles along the major and minor axis for each of the nanoparticle distributions after 20 minutes of modulated power heating with PID control are shown in Figure 3.10(a). All nanoparticle distributions except E3 attained a minimum temperature of 43.5 °C along both the major and minor axis inside the tumor. For E3 distribution, the area near the tumor-tissue boundary away from the nanoparticles does not reach the target temperature. This can be attributed to the effect of offset and concentrated nanoparticle distribution away from the control probe. E3 distribution model attained the maximum temperature along the major axis (59.2 °C) while M3 (Gaussian) distribution achieved the maximum temperature along the minor axis (56.5 °C). Figure 3.10(b) shows the degree of survival α, for each of the nanoparticle distributions along the major and minor axis after modulated power heating with PID control. Significant damage can be observed for areas with or adjacent to nanoparticles inside the tumor ($\alpha = 0$). Of all the models, E3 model has the highest damage in the surrounding healthy tissue (less α) along the major and minor axis.

The thermal dose deposited in the tumor and healthy tissue for the six nanoparticle distributions, after 20 minutes of heating with power modulated heating using PID control, with modified Arrhenius perfusion model is shown in Figure 3.10(c). With power modulation using PID control, all nanoparticle distributions achieve a CEM43 $\geq$ 60 min in at least ~90% of tumor area. This shows that modulating power with temperature feedback from a probe on tumor-tissue boundary can deliver clinically relevant thermal doses to the tumor. The percent of healthy tissue area with CEM43 $\geq$ 60 min is less than 5% for all the nanoparticle distributions except for E1 (5.7%) and E3 (14.9%).

Comparison of the temperatures achieved inside the tumor subjected to constant power and modulated power heating, allows us to effectively assess the efficacy of one method over the other. Figure 3.11 and Figure 3.12, show the temperature distributions for each of the nanoparticle distribution models after heating using both the methods. It can be seen that for all the nanoparticle distribution models, the temperatures achieved by modulated power heating are lower than those achieved by constant power heating. The maximum and minimum temperatures T_{max}, and T_{min}, are lower for power modulated heating compared to constant power heating. For instance, for E1 model, T_{max}, and T_{min}, for modulated power heating were 53.1 °C, and 43.2 °C, compared to 55.3 °C, and 44.0 °C, for constant power heating. Similarly, even for an off centered distribution model E3, the maximum temperatures inside the tumor were 16.1% lower for modulated power heating when compared to constant power heating for the same model. Additionally, the homogeneity of the temperatures, achieved by both heating methods, can be assessed by comparing T_{10}, and T_{90}, (temperature achieved by at least 10% and 90% of tumor respectively) and the dimensionless heterogeneity coefficient HC defined as $HC = (T_{10} - T_{90})/(T_{90} - T_{core})$ [70]. It can be seen that for all the models, T_{10}, and T_{90}, are lower for power modulated heating compared to constant power heating. The results for modulated power and constant power heating show that HC reduces for power modulated heating for all models except E2. The temperature distributions along the major and minor axis of the tumor and healthy tissue, obtained after 20 minutes of heating with modulated power and constant power, are shown in Figure 3.13. The results show that lower temperatures are

Table 3-3 Percentage area of tumor and healthy tissue with thermal dose CEM43 ≥ 60 min after 20 min of heating with power modulation based on temperature feedback from 8 probe location (P1 – P8, Figure 3.3) (Note: For models M1 & M2, symmetry was taken into account for the probe locations).

Probe location	Tumor area with CEM43 ≥ 60 min (%)					
	E1	E2	E3	M1	M2	M3
P1	89.29	93.96	95.56	90.82	93.54	92.96
P2	67.35	90.06	57.89	90.82	93.54	93.08
P3	85.89	31.01	58.89	53.47	55.54	53.79
P4	45.63	73.49	50.78	53.47	55.54	53.75
P5	92.73	68.10	88.07	72.49	79.21	78.51
P6	47.08	78.72	86.74	72.49	79.21	78.67
P7	77.44	54.84	37.75	72.49	79.21	78.77
P8	35.10	84.92	41.60	72.49	79.21	78.67
Probe location	Healthy tissue area with CEM43 ≥ 60 min (%)					
	E1	E2	E3	M1	M2	M3
P1	5.10	4.07	20.26	0.54	3.14	3.49
P2	0.82	3.23	0.84	0.54	3.14	3.57
P3	4.24	0.00	1.00	0.00	0.00	0.00
P4	0.00	1.40	0.20	0.00	0.00	0.00
P5	6.11	0.95	13.34	0.00	0.21	0.35
P6	0.00	1.87	12.77	0.00	0.21	0.35
P7	2.54	0.15	0.00	0.00	0.21	0.39
P8	0.00	2.55	0.00	0.00	0.21	0.35

Table 3-4 Open loop response and PID control parameters for the nanoparticle distributions

Model	u_{ctrl}	$\Delta T(K)$	g(K)	$\tau_1(s)$	$\tau_2(s)$	f(rad/s)	ζ	K_p (1/K)	K_i (s-K)	K_d (s/K)
E1	0.3	6.41	21.37	3.6	213.7	2	1.0	10.16	0.047	33.47
E2	0.3	6.81	22.7	3.0	220.5	2	1.0	9.83	0.044	26.68
E3	0.3	5.29	17.63	10.4	253.1	2	1.0	14.93	0.057	145.54
M1	0.3	7.14	23.8	0.16	177.34	2	1.0	7.45	0.042	-0.67
M2	0.3	6.76	22.53	4.3	234.2	2	1.0	10.57	0.044	42.05
M3	0.3	6.71	22.37	6.6	227.9	2	1.0	10.47	0.045	64.63
T1	0.3	5.02	21.03	0.03	152.97	2	1.0	7.26	0.048	-1.63
T2	0.3	5.10	17.0	8.0	222.0	2	1.0	13.52	0.059	101.09
T3	0.3	4.74	15.8	7.3	232.7	2	1.0	15.17	0.063	103.72

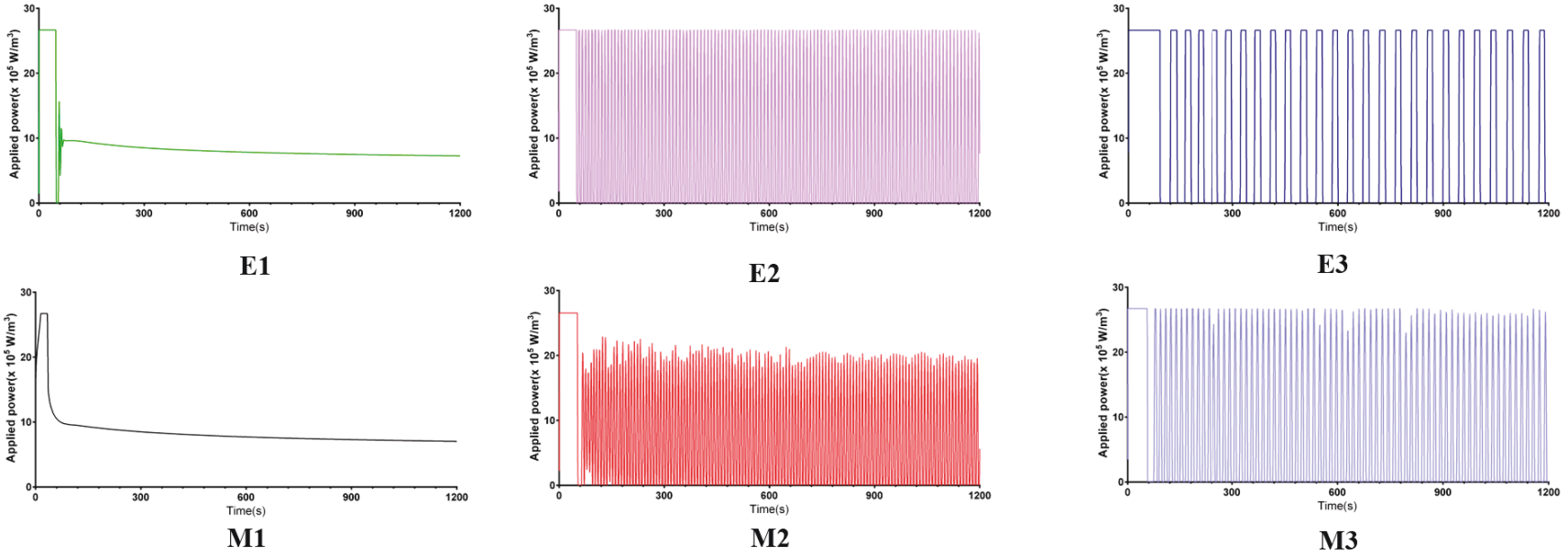

Figure 3.9 Variation of power with time depends on nanoparticle distribution Modulation of heating power with time using a PID control algorithm to achieve and maintain a target temperature of 43.5 °C at the probe location for (a) E1- nanoparticles relatively uniformly distributed; (b) E2- concentrated distribution along the major axis; (c) E3- concentrated and offset along the minor axis; (d) M1 – uniform; (e) M2 – uniformly concentrated in 40% of tumor area; (f) M3 – Gaussian.

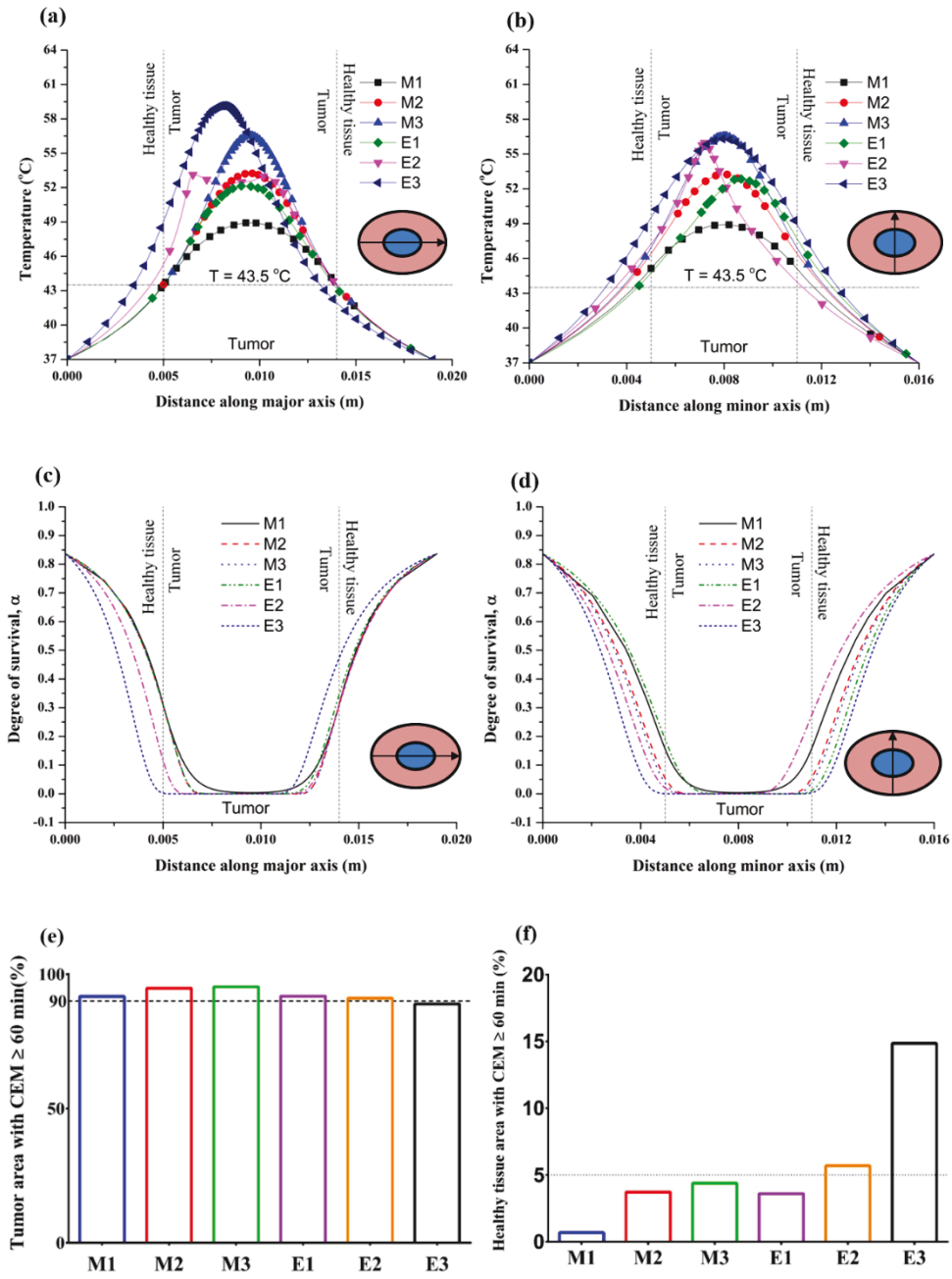

Figure 3.10 PID controlled modulated power heating achieves therapeutic temperatures inside the tumor. (a) and (b) Temperature distribution, (c) and (d) Degree of survival α, along the major and minor axes of computational model. Percent of (e) tumor area, and (f) surrounding healthy tissue area, with CEM43 ≥ 60 min, for the six nanoparticle distributions after 20 min of heating by power modulation with PID control based on temperature feedback from the tumor-tissue boundary with the modified Arrhenius perfusion model.

obtained by modulated power heating in comparison to constant power heating along the major and minor axis of the tumor and healthy tissue for all the nanoparticle distribution models. Additionally, it can also be seen that more points in the tumor have similar temperatures in the case of modulated power heating when compared to constant power heating. Thermal dose, measured as CEM43, deposited in the tumor and healthy tissue, after 20 minutes of heating with constant power and modulated power is shown in Figure 3.14(a). Significant thermal dose is deposited at tumor areas with or adjacent nanoparticles for both heating methods. Healthy tissue regions near the nanoparticles achieve high thermal doses (CEM43 > 60 min) whereas regions distal to the nanoparticles are unaffected. Comparison of time evolution of thermal dose deposition in the tumor (Figure 3.14(b) and (c)), using both heating methods, revealed notable differences. With modulated power heating, more than 60% of tumor area achieved a therapeutic thermal dose of CEM43 $\geq$ 60 min in fewer than two minutes, for all the nanoparticle distribution models except M1 (uniform) model. Conversely, after two minutes of constant power heating, a maximum of ~ 30% (for E3 model) of tumor area achieved thermal dose of CEM43 $\geq$ 60 min. Even for the case of M1 (uniform) distribution, with modulated power heating, therapeutic thermal dose was achieved in 60% of the tumor in six minutes compared to fourteen minutes with constant power heating. Until now, we implemented the modulated power heating with temperature feedback from tumor-tissue boundary, for different nanoparticle distributions in a 2D model. In order to test whether this heating method would compensate for variable nanoparticle distributions in a 3D model, we implemented this method for three nanoparticle distributions. Figure 3.15 shows the variation of applied power with time for the three 3D nanoparticle distribution models considered. For the T1

(uniform) model, the applied heating power peaks and then reduces to a lower power. In the case of T2 (Gaussian-centered) model, the applied power reaches a maximum and oscillates with damped amplitude before stabilizing at a lower power. The applied heating power oscillates continuously between a maximum and minimum heating power for the T3 (3-point Gaussian) model.

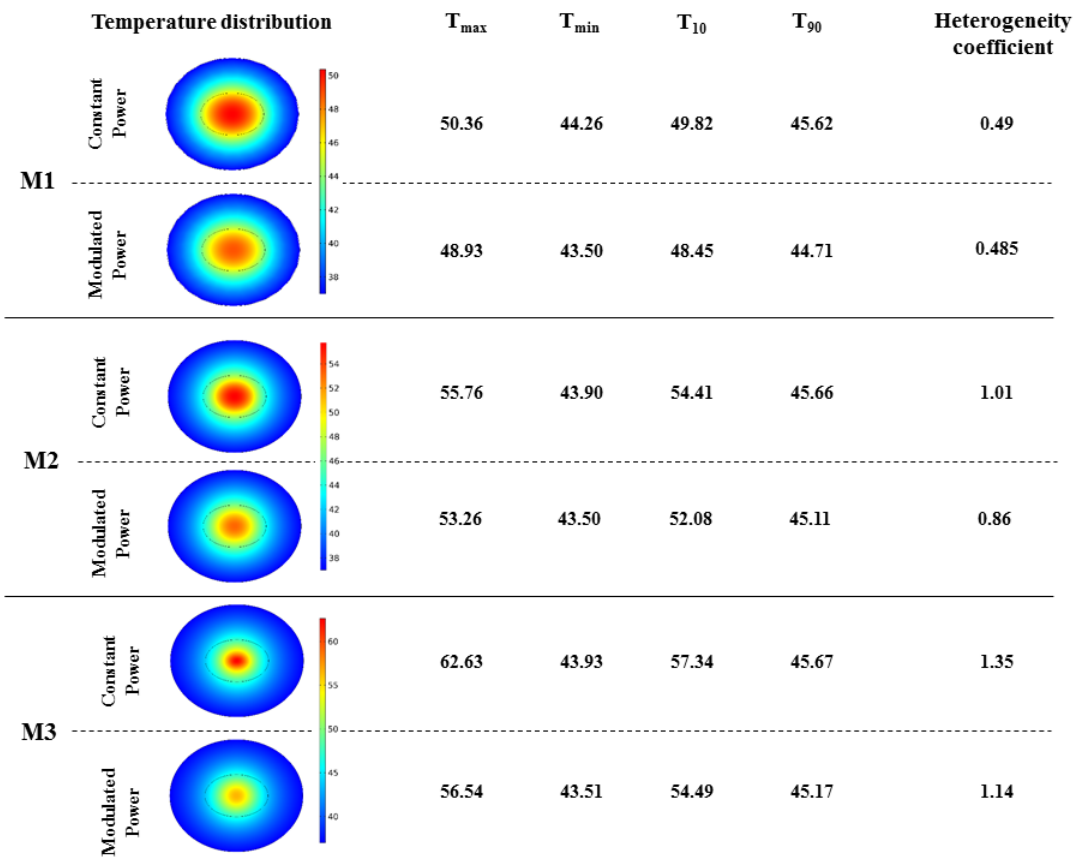

Figure 3.11 Controlled power heating results in increased temperature homogeneity and lower temperatures when compared to constant power heating Temperature distributions achieved in the tumor and healthy tissue after 20 min of heating by constant power and by power modulation with PID control based on temperature feedback from probe tumor-healthy tissue boundary for ideal mathematical distribution models

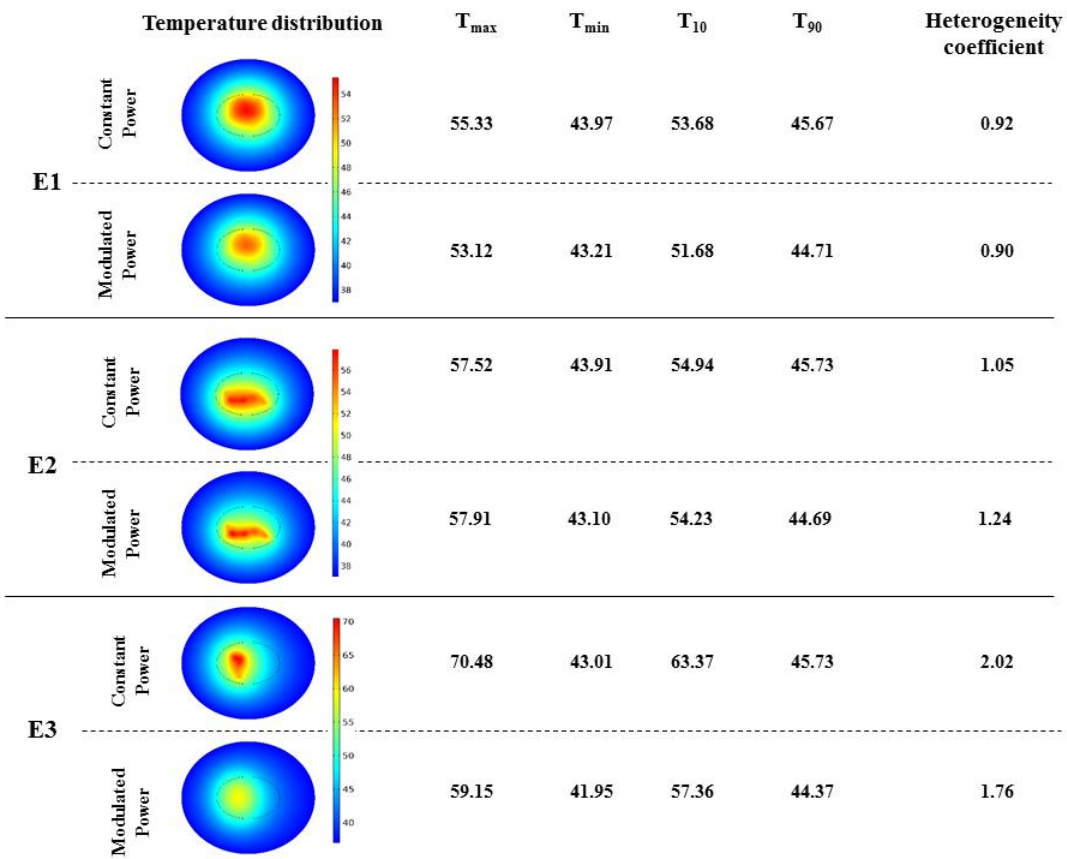

Figure 3.12 Controlled power heating results in increased temperature homogeneity and lower temperatures when compared to constant power heating Temperature distributions achieved in the tumor and healthy tissue after 20 min of heating by constant power and by power modulation with PID control based on temperature feedback from probe tumor-healthy tissue boundary for image derived nanoparticle distributions.

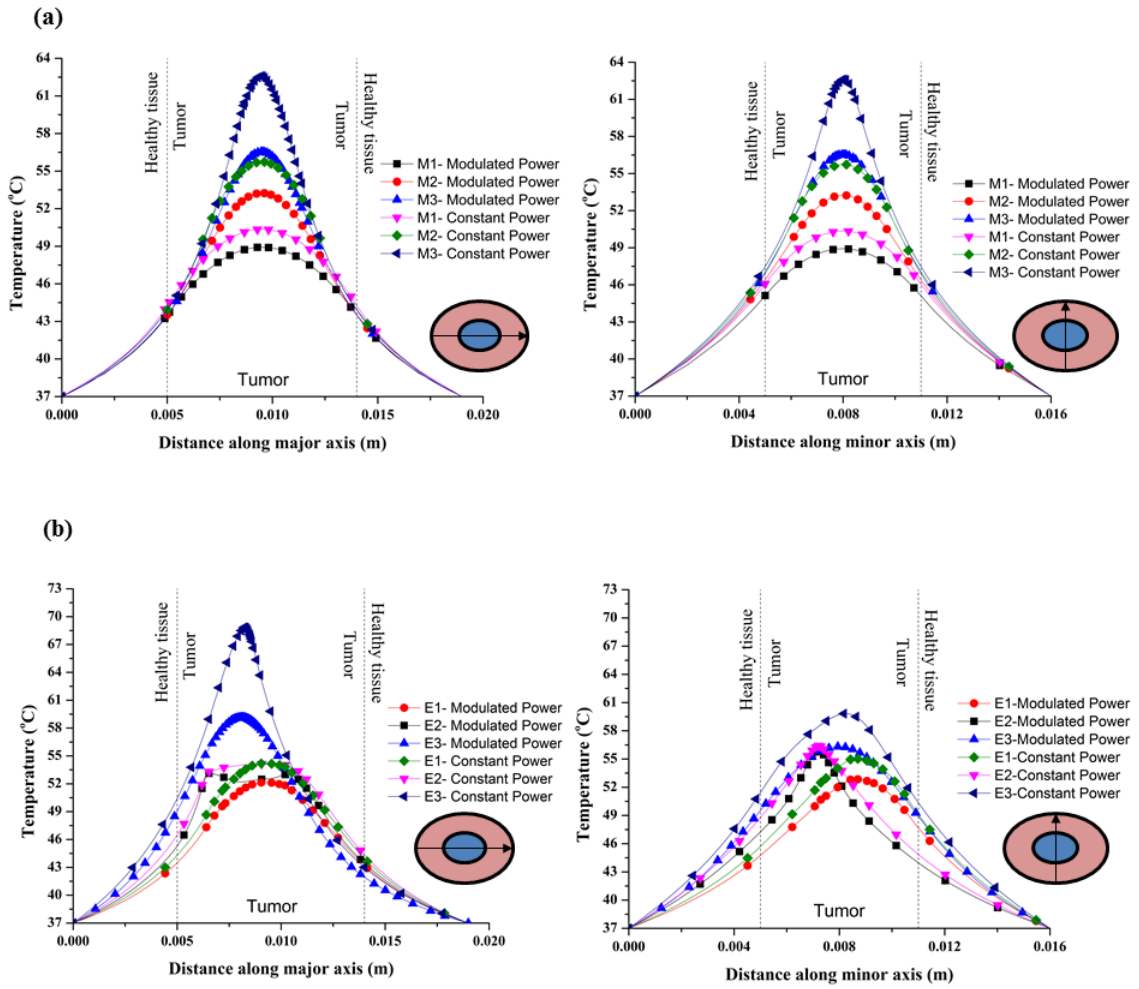

Figure 3.13 Power modulated heating using PID controller results in overall lower temperatures when compared to constant power heating Temperature distribution along the major and minor axis of computational model for (a) ideal mathematical distribution models, (b) image derived nanoparticle distributions, after 20 min of heating (i) by constant isoeffective power and (ii) by power modulation with PID control based on temperature feedback from probe at tumor-tissue boundary, with the modified Arrhenius perfusion model.

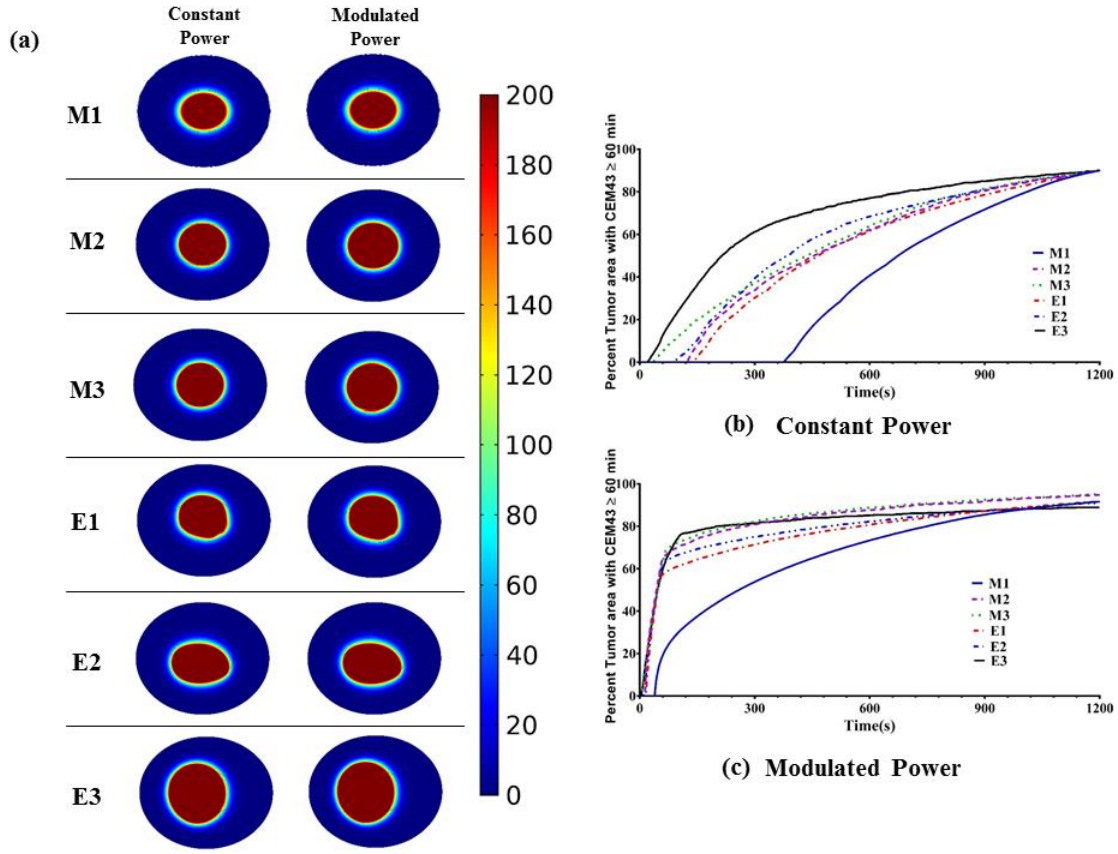

Figure 3.14 Power modulated heating using PID controller leads to faster thermal dose deposition when compared to constant power heating (a) Thermal dose, measured as CEM, distribution for the six distributions, after 20 min of heating (i) by constant isoeffective power and (ii) by power modulation with PID control based on temperature feedback from probe at tumor-tissue boundary, with the modified Arrhenius perfusion model. Variation of percent of tumor area with thermal dose of CEM43 ≥ 60 min with time, by (b) constant isoeffective power heating, and (c) power modulated heating with PID control based on temperature feedback from probe at tumor-tissue boundary, with the modified Arrhenius perfusion model

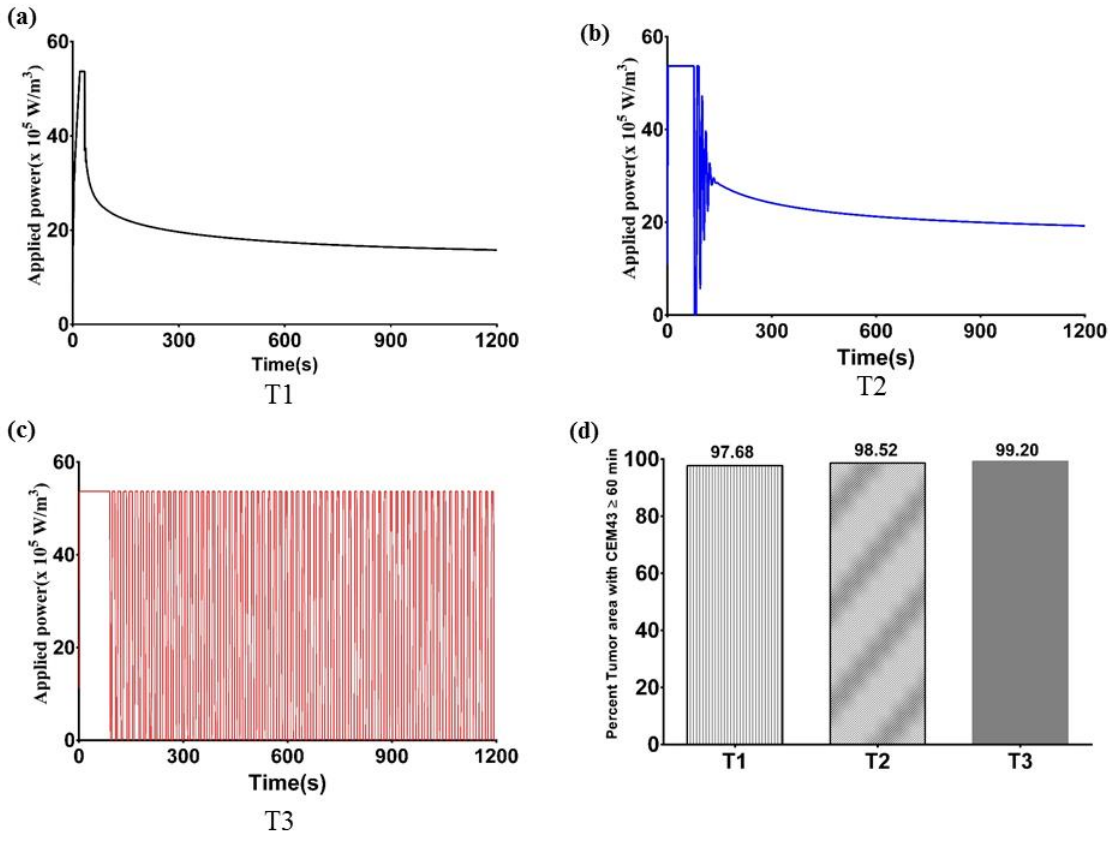

Figure 3.15 Variation of power with time for 3D models. Modulation of heating power with time using a PID control algorithm to achieve and maintain a target temperature of 43.5 °C at the probe location for (a) T1 – Uniform distribution, (b) T2 - Gaussian centered; (c) T3 – 3pt Gaussian distribution mimicking 3 point nanoparticle injection; (d) percent of tumor area with CEM43 ≥ 60 min after 20 min of heating with PID controlled modulated power heating for the three 3D nanoparticle distribution models.

Temperature distributions achieved in the tumor and healthy tissue along the XY, YZ, and ZX planes at the center of the tumor for the three 3D nanoparticle distribution models is shown in Figure 3.16. As expected regions with or adjacent to the nanoparticles achieve higher temperatures than distal regions. T2 (Gaussian-centered) distribution achieved the highest maximum temperature inside the tumor (91.29 °C) while the T1 (uniform) model achieved the lowest maximum temperature of 51.6 °C. T2 model characterized by concentrated nanoparticle distribution resulted in higher thermal

gradients across the tumor when compared to both the T1 (uniform) and T3 (3-point Gaussian) model.

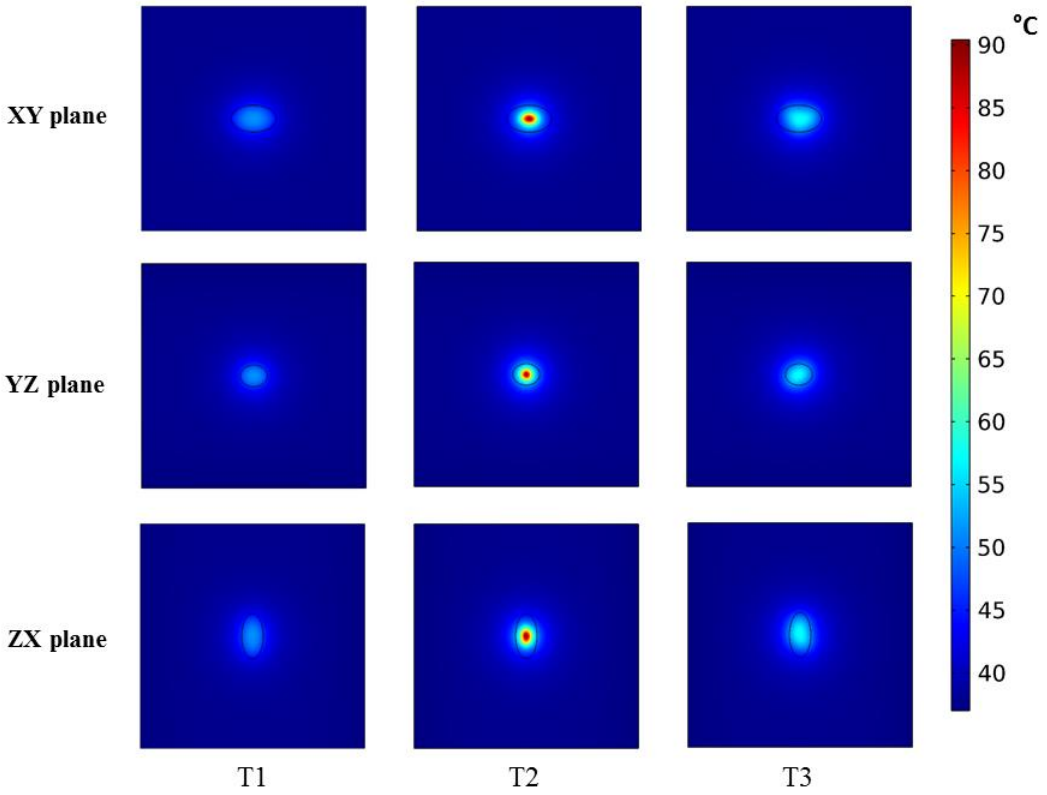

Figure 3.16 PID controlled power modulation achieves therapeutic temperatures inside the tumor. Temperature distributions achieved inside the tumor and healthy tissue, (a) XY plane, (b) YZ plane, (c) ZX plane, for the three 3D nanoparticle distribution models T1, T2 and T3, after 20 min of heating by power modulation with PID control based on temperature feedback from probe at tumor-tissue boundary with the modified Arrhenius perfusion model

Figure 3.17 shows the damage to healthy tissue, given by degree of stasis DS, for the three 3D nanoparticle distribution models, after 20 minutes of power modulated heating. It can be seen that the variation of damage in the healthy tissue clearly depends on the proximity of the nanoparticles to the tumor-healthy tissue boundary. In the XY plane, the region of highest damage (DS = 1) is symmetrically distributed close to the tumor-healthy tissue boundary for both the T1 and T2 distributions, while it is asymmetrically distributed with more damage occurring at the tumor-healthy tissue boundary close to the

nanoparticle concentrated areas. Similar distributions of damage were seen in the YZ and ZX planes. It can also be seen that the T1 (uniform) model displays the least damage compared to other nanoparticle distribution models T2 (Gaussian) and T3 (3-pt Gaussian) distribution models.

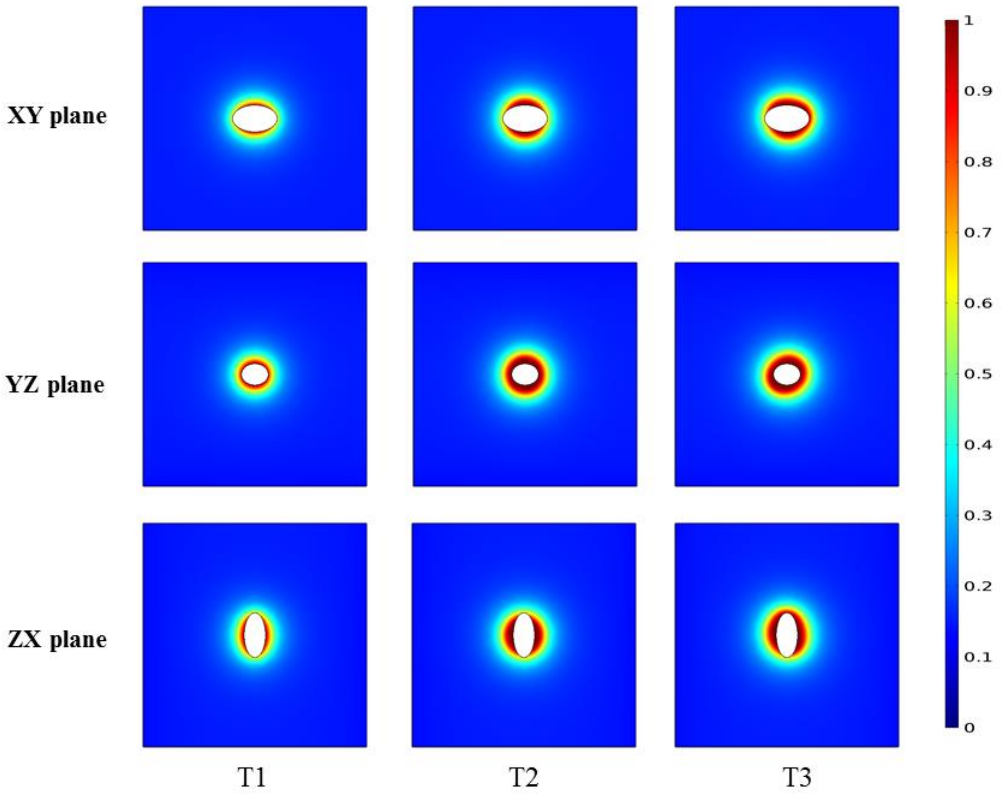

Figure 3.17 Healthy tissue damage is higher for regions closer to nanoparticle distributions. Degree of thermal damage (DS) achieved inside the healthy tissue, (a) XY plane, (b) YZ plane, (c) ZX plane, for the three 3D nanoparticle distribution models T1, T2 and T3, after 20 min of heating by power modulation with PID control based on temperature feedback from probe at tumor-tissue boundary with the modified Arrhenius perfusion model

3.4 Discussion

Temperature distributions achieved in the tumor and surrounding healthy tissue during magnetic nanoparticle hyperthermia are mainly influenced by the nanoparticle

distributions achieved and the diffusion of heat (combining the effect of heat conduction and capillary blood perfusion). These determine the thermal dose deposited in the tumor and in turn the treatment efficacy. Previous experimental studies [52,53] have shown that variable nanoparticle distributions often result even with convection-enhanced delivery of nanoparticle suspensions that are directly injected into tumors. Diffusion of heat in the tissue is primarily influenced by perfusion. Blood perfusion acts as a heat sink that carries away and distributes the heat generated by the nanoparticles throughout the tissue. As the amount of heat deposited in the tissue increases, temperature induced damage reduces the blood perfusion in the affected region, ultimately decreasing it to zero. Thus, any potential strategy for mNPH, should consider the variability of nanoparticle distribution and the temperature effects on blood perfusion. At constant power, the nanoparticle distribution strongly affects temperature distributions inside the tumor (Figure 3.7). Tumor regions having high concentration of nanoparticles exhibit higher temperatures in contrast to regions with few or no nanoparticles. Temperatures and temperature gradients decrease rapidly in regions farther away from the nanoparticle clusters. The high concentration of nanoparticles in the tumor center causes the M2 (Gaussian) model to achieve the highest maximum temperature inside the tumor. The M1 (uniform) model attains the lowest local maximum tumor temperature because the nanoparticles are distributed throughout the tumor and heat generated by isolated nanoparticles rapidly diffuses through the tissue yielding much smaller gradients. When temperature-dependent perfusion was considered (Figure 3.8), temperatures attained in the tumor and healthy tissue were much higher than with the constant perfusion model. Locally high temperatures produced decreased perfusion due to thermal damage, leading to decreasing heat transfer rates and further

increased local temperature, because blood perfusion is the dominant heat diffusing mechanism from regions containing nanoparticles. Thus, it is important to consider temperature-dependent perfusion when developing treatment strategies to improve efficacy.

Response to hyperthermia was computed by calculating the thermal dose deposited in the tumor. A uniform temperature distribution in the tumor is often considered desirable, but achieving a minimum effective temperature in 90% of tumor area is more clinically realistic, relevant, and is demonstrably effective [9,113]. Previous nanoparticle hyperthermia studies focused on temperature distribution alone, however achieving a minimum clinically relevant thermal dose (CEM43 $\geq$ 60 min) in a larger volume of the tumor [9,32,43] is considered a better measure of treatment outcome. The isoeffective heating power, Q_{iso}, was chosen as the minimum heating power required to achieve a thermal dose equivalent of CEM43 $\geq$ 60 min in at least 90% of tumor area (T90) during a simulated 20-min treatment duration. With constant perfusion, significant differences of isoeffective heating power were determined for the six nanoparticle distributions (Table 3-2). The E3 model required the highest isoeffective power of 19.6×10^5 W/m^3 and the uniform model required the lowest, 10.6×10^5 W/m^3. When temperature-dependent perfusion was considered, all models required at least 20% less heating power than for constant perfusion. This can be attributed to the fact that as perfusion (and the associated heat removal) decreases with increasing thermal damage, more of the heat produced by the nanoparticles is retained in the tumor, leading to higher thermal dose. Moreover, the difference in isoeffective power required was significantly reduced for all distributions (maximum difference of 22.1% for constant perfusion and 9.1% for the Arrhenius model,

between M1 & E2) except for the E3 model. Thermal damage, induced by increased heat deposition and reduced heat loss due to perfusion, minimized the effect of differences in nanoparticle distributions, leading to similar isoeffective heating powers for a variety of distributions. Therefore, our results demonstrate that the commonly used constant perfusion model underestimates tumor temperatures and overestimates the required heating needed to achieve a clinically effective thermal dose.

While estimating the isoeffective heating power Q_{iso} is computationally feasible, determining it experimentally is challenging. Isoeffective heating power Q_{iso}, allows us to determine the power required to deposit an ideal thermal dose in the tumor. But it does not take into consideration the resulting damage/ thermal dose deposited in the surrounding healthy tissue. A better heating method should aim to deposit therapeutic heat in the tumor while simultaneously minimizing the damage to the surrounding healthy tissue.

Invasive thermometry during hyperthermia treatment is often practiced clinically to measure the thermal dose and compare among treatments [34,113,152]. While multiple thermal measurements would ensure better estimation of thermal dose, its invasiveness often makes possible only single-point temperature measurements during treatment.. A treatment strategy which takes advantage of single point thermometry measurements, using real time temperature feedback from this sensor, is realistic for clinical applications.

In the previous chapter, we showed that modulating power using temperature feedback from a sensor at the tumor-tissue boundary can ensure a minimal effective thermal dose deposition (CEM43 T90), for uniform and concentrated nanoparticle distributions, in a spherical model. However, asymmetry in tumor shape and nanoparticle distribution would require a more precise placement of temperature sensor on the tumor-

tissue boundary. Choosing a probe location too close to the nanoparticles will result in under treatment of tumor while choosing it far away can result in increased healthy tissue damage. Thus, eight locations equidistant on the tumor-tissue boundary were chosen to determine the best probe location for temperature feedback. The criteria for choosing a probe location was to ensure that thermal dose of CEM43 $\geq$ 60 min was achieved in 90% of tumor area and in less than 5% of healthy tissue. Except for E3, all other nanoparticle distribution models had probe locations that satisfied the above criteria (Table 3-3). This highlights the fact that concentration of nanoparticles closer to the tumor-tissue boundary is unwanted and can lead to ineffective treatment and undesirable healthy tissue damage.

A proportional-integral-derivative (PID) controller is often used in industry and medicine to control temperature at a given location. Its robustness and ease of implementation has made it the most widely used controller in many industries for sensitive control. In the current study, we implemented a PID temperature controller (Figure 3.4) to regulate temperature at the probe location on the tumor-tissue boundary determined previously for each nanoparticle distribution. To implement the PID controller, we computed the open loop gains for each of the nanoparticle distribution models (Table 3-4). Of the six nanoparticle distributions, uniform model (M1) had the highest open loop gain *g* (23.8 K) while the E3 model had the least gain (17.63 K). Location of nanoparticles closer to the probe would result in higher open loop gains, while the distributions with probes away from the nanoparticles would have lower open loop gains. Distributions with higher open loop gains required lower proportional gains, with M1(uniform) model having the lowest proportional gain (7.45 1/K) and E3 model having the highest proportional gain

(14.93 1/K). Since the derivative controller allows for higher proportional gains, models with higher proportional gain have higher derivative gains (for E3, K_d = 145.54 s/K).

Significant differences were seen in the variation of power with time for the six nanoparticle distributions (Figure 3.9). For distributions M1 and E1, the applied power reached a maximum and plateaus out at a lower power for the remainder of the treatment duration. This implies that the probe reached the target temperature faster and the controller was able to control the probe temperature effectively. For distributions M2, M3 and E2, E3 the applied power reached a plateau, after which it oscillated between a set of maximum and minimum powers. For the three distributions M3, E2, and E3, the peak of this oscillations was the maximum power possible Q_{max}, while for M2 it was around 75% of Q_{max}. For M1 and E1 models, which were characterized by a uniform and diffused nanoparticle distribution in the tumor, the probe attained the target temperature relatively faster and at lower powers. The tumor models that were characterized by concentrated and clustered nanoparticle distributions (M2, M3 and E2, E3) required the controller to operate at maximum and minimum power. The distance of the probe location from the nanoparticle heat sources for these distributions results in a delay between the control action and the temperature output. This required the controller to actively control the temperature output which resulted in the observed oscillatory input. Arora et al. [153] reported similar oscillating control inputs in their thermal dose control system developed for ultrasound treatments. Further tuning of the PID controller can improve its performance and lead to a smoother power input.

By controlling and achieving the target temperature of 43.5 °C at the tumor-healthy tissue boundary, we were able to achieve a temperature of at least 43.5 °C, along the major

and minor axes inside the tumor, for all the six nanoparticle distributions except E3 (Figure 3.10(a)). Similarly, the degree of survival α is the lowest in the tumor region for all the nanoparticle distributions (Figure 3.10(b)). However, for E3 model, the location of nanoparticles are off set from the tumor center and closer to the tumor-tissue boundary, results in low degree of survival α both along the major and minor axes in the surrounding healthy tissue. PID controlled power modulation delivers clinically relevant thermal dose of CEM43 $\geq$ 60 min in ~ 90% of tumor area in all the nanoparticle distribution models (Figure 3.10(c)), while minimizing the healthy tissue damage (Figure 3.10 (d)). This is true for all the nanoparticle distributions except E3. For E3 distribution, increased healthy tissue damage occurs (~ 14.9%), clearly showing that off center concentrated nanoparticle distribution close to the tumor-tissue boundary is highly undesirable.

Comparison of the temperatures achieved for each of the distribution models with constant power heating and PID controlled modulated power heating highlights the advantages of the modulated power heating. Overall, lower temperatures were achieved for all the models, with power-modulated heating compared to constant power heating (Figure 3.11Figure 3.12). The maximum and minimum temperatures attained in the tumor were lower with modulated power heating compared to constant power heating, for all the models except E2 (Figure 3.12). E2 model, characterized by concentrated nanoparticle distribution along the tumor major axis, has a slight increase in T_{max} with modulated power heating (T_{max} = 57.91 °C) compared to constant power heating (T_{max} = 57.52 °C). Comparison of heterogeneity coefficient *HC* [155], obtained from both heating methods for all the models, allow us to comment on the homogeneity of the temperature distributions achieved. The results show that the *HC* decreases for all the nanoparticle

distribution models except E2, with modulated power heating compared to constant power heating. The improvement in homogeneity is more striking with the E3 model where *HC* decreases from 2.02 (constant power) to 1.76 (modulated power). The time evolution of thermal dose deposition in the tumor with modulated power heating significantly differ to that with constant power heating (Figure 3.14 (b), (c)). Higher thermal doses were deposited faster with modulated power heating compared to constant power heating. For the models M2, M3, E1, E2, and E3, at least 60% of the tumor achieved a thermal dose of CEM43 $\geq$ 60 min in ~65 s with modulated power heating. With constant power, the same models require ~560 s, to achieve a similar thermal dose. Even for M1 (uniform) model, constant power heating took more time (468 s) compared to modulated power (63 s) to achieve a CEM43 $\geq$ 60 min in at least 20% of tumor area. Thus, modulated power heating would allow for faster deposition of higher thermal doses, allowing for optimizing and reduction of total treatment time. Additionally, pulsing of magnetic field amplitude implemented in animal experiments show that pulsed high amplitude AMF are well tolerated by mice [49,154].

We further implemented the PID controlled modulated power heating in 3D models with three distributions – T1 (uniform), T2 (Gaussian-centered), and T3 (3-pt Gaussian) distributions. For all the three models, clinically relevant thermal dose of CEM43 $\geq$ 60 min was deposited in more than 90% of tumor area, after 20 minutes of heating with modulated power heating (Figure 3.15(d)). The variation of applied power with time for T1 (uniform) distribution (Figure 3.15 (a)) followed a similar trend to that observed for the corresponding 2D model (Figure 3.9). For T2 (Gaussian-centered) model, the applied power increases, reaches a maximum, and then oscillates with reduced amplitude before

plateauing to a constant value (Figure 3.15 (b)). This is in contrast to the trend that we observed for the corresponding 2D model (M3, Figure 3.9). In the 2D model, it is assumed that there is no heat transfer occurring in the third dimension and all the heat generated is diffused in the remaining two dimensions. But in the case of 3D model, heat transfer occurs in all the three dimensions resulting in the different applied power profile. This difference is not apparent in the 3D model of uniform distribution since the heat sources are distributed everywhere in the tumor replicating the assumption in 2D model. For T3 (3-pt Gaussian) model, the applied power reaches a maximum power and oscillates between a maximum and minimum power condition. Temperatures achieved in the tumor and healthy tissue were dependent on the nanoparticle distributions, with regions adjacent or with nanoparticles exhibiting higher temperatures compared to regions away from the nanoparticles (Figure 3.16). The degree of healthy tissue damage (DS) for the three 3D nanoparticle distribution models after 20 min of modulated power heating (Figure 3.17), shows that healthy tissue regions proximal to the nanoparticle concentrations incur more damage compared to regions away from them. Of the three models, T1 (uniform) model has the least healthy tissue damage and T3 (3pt-Gaussian) has the highest healthy tissue damage (~ 2x that of uniform model). The above results show that PID controlled modulated power heating enables us to deliver a therapeutic thermal dose into the tumor with overall lower temperatures and better temperature homogeneity, compared to constant power heating, for various nanoparticle distributions.

One of the limitations of our current computational study is that the effect of onset of eddy current heating in the healthy tissue when exposed to high amplitude alternating magnetic fields was not considered. By laws of induction this heating power is proportional

to the square of the product of applied magnetic field amplitude (H), frequency (f) and diameter (D) of the induced current loop. For large volumes of tissue (a patient torso of ~ 30 cm diameter), the product of frequency and amplitude limits for applied magnetic field should be $H.f \leq 4.85 \times 10^8$ A/(m-s) [156,157]. This onset of eddy current heating at high amplitudes could lead to unwanted heating of healthy tissue leading to possible thermal damage. This could also potentially lead to increased blood flow in the healthy tissue due to marginal increase in temperature as the body activates its thermoregulation. This could result in increased thermal gradients at the tumor-healthy tissue boundary, cooling of the tumor and increased heat flux at the tumor tissue boundary. Including the eddy current heating could further improve the above proposed PID controlled power modulation with temperature feedback at tumor-tissue boundary making it translatable to the clinic. Another limitation of the current study is that effect of temperature on the thermal properties of the tissue such as thermal conductivity, specific heat capacity has not been considered. Change in thermal properties due to thermal damage can affect the heat transfer in the tumor and tissue which can then influence the temperature distributions achieved. As next steps, experimental investigation should be performed to validate the model.

3.5 Conclusions

In this study, we proposed a new heating method of modulating the heating power of nanoparticles based on temperature feedback from the tumor-healthy tissue boundary. We hypothesized that attaining a target temperature of 43.5 °C at a specific location on the tumor-tissue boundary allows us to achieve effective treatment of tumor with minimal healthy tissue damage and can compensate for variable nanoparticle distributions. First, we tested this hypothesis on 2D FEM models with six nanoparticle distributions – three

obtained from animal models and three idealized mathematical models. We considered three perfusion models available in literature to demonstrate the importance of considering the temperature effects on perfusion and the resulting temperature distributions. We then implemented a PID controller to control the power output of nanoparticles based on temperature feedback. The thermal dose deposited into the tumor and healthy tissue was computed to assess the effectiveness of this method. Modulated power heating allowed for effective tumor treatment with overall lower temperatures compared to constant power heating. We then showed that our proposed modulated power heating method successfully deposits clinically significant thermal dose in three 3D nanoparticle distribution models. The presented method is clinically significant as it addresses one of the principal challenges of mNPH of variable intra-tumor nanoparticle distributions. Experimental and clinical investigations are further needed to validate the above method. Also, the effect of non-specific heating due to eddy currents should be considered as this can lead to unwanted healthy tissue heating at higher applied fields. Overall, our method shows that with single-point thermometry and power modulation, effective tumor treatment is consistently achievable despite variability in nanoparticle distributions.

Chapter 4
Temperature-control power modulated hyperthermia in mouse models of liver cancer

In this chapter, we report the results of a pilot study where we implemented the temperature control power modulated magnetic nanoparticle hyperthermia in mice with subcutaneous xenograft liver cancer tumors. Two nanoparticle distributions were generated by employing two injection methods – 2-pt and 3-pt injection using a syringe pump. Temperatures were measured at four locations in the tumor and applied power was

modulated to attain and maintain a target maximum temperature at the tumor-healthy tissue interface of 43.5 °C. The outcome of the treatment for 2-pt and 3-pt injected mice was determined. Additionally, 2-pt and 3-pt injected tumors were harvested, fixed, sectioned, and stained with Perl's reagent to characterize the nanoparticle distribution inside the tumors. 3D computational models were built and analyzed to correlate and understand the findings from the animal experiments.

4.1 Introduction

Pre-clinical animal studies are used to test new treatment strategies and can provide useful information for further refinement and improvement before testing them in humans. Mice share many physiological and pathological features with humans [158] and have been used for pre-clinical testing for more than 100 years. Extensive analysis of mice and human genomes have led to genomic manipulations in the mouse to generate models of human pathologies [159] such as heart disease, different cancers, hypertension, diabetes, obesity, glaucoma, blindness, anxiety, depression etc. Mice are relatively inexpensive, easy to maintain and can be bred in captivity. This makes mice an ideal model for preclinical studies with more than 25 million mice used in research laboratories every year [158]. Multiple optimization studies [112,115,136–141] have been proposed for improving the efficacy of magnetic nanoparticle hyperthermia, by delivering a therapeutic dose in the tumor and minimizing healthy tissue damage. While some of the models were based on realistic organ geometries developed from CT images [139], none of the above were tested or implemented in either pre-clinical animal models or clinical studies. As discussed previously, computational models are usually based on simplified geometry and physics often due to lack of information regarding tissue anatomy or thermal properties and also

tissue response. While computational models are an excellent tool for gaining a better understanding of the physiological processes and developing new strategies, the developed strategies should be tested in animal models, in order to understand the complexities of implementing the assumptions in the model, to gather feedback for further improving the method and to validate it.

In the recent years, LeBrun et al. [160] and Pearce et al. [105] compare their numerical simulation models with *in vivo* mouse studies. LeBrun et al. [160] validated the treatment efficacy of their MicroCT-based theoretical simulation approach in prostate cancer PC3 xenografts. Their theoretical approach [161] was based on using MicroCT images to generate volumetric heat generation rate distributions and control the treatment time either for partial or complete ablation. The experimental end points in their animal study were tumor growth delay and histology. Results showed complete ablation confirming their simulations. However, they did not measure/report any temperature data and they assume repeatable nanoparticle distributions for every tumor based on their previous experiments [69]. Pearce et al. [105] coupled their numerical models to experimental measurements to study the effectiveness of current thermal damage prediction models [29]. However, they did not present or test any optimization methods for effective tumor treatment or minimal healthy tissue damage.

The goal of this study was to implement and evaluate a temperature control modulated power heating protocol similar to the one described in chapter 3 in mouse tumor models. We sought to test this protocol for two nanoparticle distributions generated using two injection methods – 2-pt and 3-pt injections. Applied power was manually modulated based on temperature feedback from the tumor-healthy tissue interface, instead of a PID

controller presented in chapter 3. Temperatures were measured at multiple locations and temperature at the tumor-healthy tissue interface was controlled. Thermal dose and total applied power were calculated and compared. 3D nanoparticle distributions were generated from slides stained with Prussian blue to compare the distributions obtained from 2-pt and 3-pt distributions. Ablation of tumors after treatment prevented us from evaluating the therapeutic efficacy of the heating protocol using tumor growth delay studies. We successfully showed that the temperature at the tumor-healthy tissue boundary can be controlled for both the distributions. Simulations were then carried out to compare and understand the results from experiments. Overall, the challenges for *in vivo* implementation of our modulated power heating protocol have been identified and future steps for further testing of this protocol have been presented.

4.2 Material and Methods

4.2.1 Experimental design

The goal of this pilot study was to evaluate whether temperature-controlled power modulated magnetic nanoparticle hyperthermia can compensate for variable nanoparticle distribution in animal tumor models. To do so, we generated two nanoparticle distributions in subcutaneous tumors using two injection methods – 2-pt and 3-pt injections. The experiment consisted of culturing HepG2 liver cells under recommended conditions and injecting them into male nude mice for growing subcutaneous xenograft tumors. Once the tumors reached the target volume, mice were divided into two groups based on injection method, 2-pt, and 3-pt. Mice in each group were assigned to two cohorts, viz. modulated

AMF treatment cohort, and nanoparticle distribution cohort. The number of mice in each group and cohorts are shown in Table 4-1. For animals in the modulated AMF treatment cohort, temperature probes were inserted at four locations in the tumor- intra-tumor, tumor surface, and on either side of tumor-healthy tissue interface after injection. Mice were then treated with temperature control power modulated magnetic nanoparticle hyperthermia for 20 min. The power was modulated so as to rapidly achieve and maintain a target temperature of 43.5 °C at the tumor-healthy tissue interface. After treatment, the outcome of the experiment was coded – no ablation (0), partial ablation (1) and ablation (2). The temperature and applied power data were analyzed to calculate the thermal dose deposited and total energy applied. The schematic for the experimental design of modulated power nanoparticle hyperthermia is shown in Figure 4.1.

For animals in the nanoparticle distribution cohort, tumors were harvested and fixed in formalin immediately after injection. They were paraffin embedded and ten slices were obtained at 0.2 mm distance apart and stained with Perl's reagent to obtain the nanoparticle distribution. The stained slides were then scanned and digitally stored. The images were processed in ImageJ and MATLAB to obtain the 3D nanoparticle distribution.

4.2.2 Magnetic iron oxide nanoparticles

Two batches of commercially available Bionised nanoferrite (BNF) magnetic iron oxide nanoparticles obtained from micromod Partikeltechnologie (Rostock, Germany) were used in this study. BNF nanoparticles are a mixture of magnetite (Fe_3O_4) with maghemite (γ-Fe_2O_3) and their magnetic, heating and imaging properties have been extensively characterized [55–57]. The iron concentration of the received BNF nanoparticles was determined using a ferene-s-assay. Ferene-s-assay is a colorimetric assay

that uses a chromogenic compound ferene-s for quantification of iron in samples containing iron oxide nanoparticles [162]. It consists of digesting a known volume of iron oxide nanoparticle in acid and compared with iron standards. The color of the sample depends on the amount of iron present in the samples. The absorbance for both the nanoparticle sample and iron standards are measured using a spectrometer and then compared to determine the iron quantity in the nanoparticle sample. The iron concentration for the two batches of BNF nanoparticles used in this study is shown in Table 4-4.

Table 4-1 Treatment groups and cohorts considered in this study with the number of mice in each cohort

	2-pt	3-pt
Treatment	6	6
NP distribution	3	3

Nanoparticle distribution within a tumor after direct intratumor injection is determined by tumor physiological and mechanical properties such as interstitial pressure, tissue density, stromal content, and vascularity, and injection parameters such as injection rate, volume, and solution viscosity. Using a low injection volume and injection rate allows for a controlled and concentrated nanoparticle distribution in the tumors [132]. High concentration of nanoparticles would allow lower injection volumes thereby reducing the injection times. Hence, the stock BNF nanoparticle samples were further concentrated by magnetic-assisted settling using a strong rare earth permanent magnet for 24 hrs. The nanoparticle rich fraction was collected by removing the supernatant. The iron content of these concentrated nanoparticles was determined again by ferene-s assay [162] and are summarized in Table 4-4.

The specific loss power (SLP) of these nanoparticles was determined by methods described in chapter 6. Briefly, 1 mL volume samples of the nanoparticles with 5 mg Fe/mL concentration were prepared in Type I 51 glass tubes (LaMotte, Chestertown, MD) and weighed before they were inserted into a cylindrical Styrofoam holder. The holder was then inserted into four-turn modified vertical solenoid coil which generates a magnetic field (± 10% peak amplitude) at fixed frequency of 155 ± 10 kHz. Magnetic field amplitude of 8 – 44 kA/m (peak) were applied for a duration of 100 s and the temperature rise in the nanoparticle samples was measured using a fiber optic temperature probe. The SLP was then estimated from the heating rate data that satisfy the (quasi)-adiabatic criteria [60].

4.2.3 Animal tumor models

Human hepatocellular carcinoma cells (HepG2) were used in this study. HepG2 cells were purchased from ATCC® (VA, USA) and cultured under sterile conditions. Cells were cultured in Minimum Essential Medium (MEM, Sigma Aldrich) with L-glutamine, Earle's salts and sodium bicarbonate, containing 10% fetal bovine serum (FBS), at 37 °C and 5% CO_2. Cells were grown in T-175 cm^2 flasks and were harvested when 80 - 90% confluence was reached. Harvesting of cells included trypsinizing followed by 5 minutes of incubation. The cells were then resuspended in the media and were spun down for 5 min at 1000 rpm. The supernatant was removed and cells resuspended in PBS for counting. After counting, cells were again spun down for 5 min at 1000 rpm and were resuspended in PBS to yield a concentration of 30 million cells per mL. They were then transported to the animal facility in ice for injection into mice.

Eighteen male nude mice (Athymic Nude – Foxn1^{nu}, Charles River Labs, Germantown, MD) aged 4-6 weeks (weight 20 – 30 g) were used in this study. All animals were housed in an Association for Assessment and Accreditation of Laboratory Animal Care (AAALAC) accredited facility in compliance with the guide for care and use of laboratory animals. All animals received food and water *ad libitum*. They were housed in temperature and humidity controlled rooms with 12/12 light/dark cycles. All the animals were monitored on a daily basis to ensure their health and any distress associated with treatment. The animals were euthanized immediately when they showed any signs of distress that prohibited them from eating, drinking, or moving. The Johns Hopkins Institutional Animal Care and Use Committee approved all procedures. 3×10^6 HepG2 cells suspended in 0.1mL of PBS were injected into the right flank of the mouse. Animals were monitored on a regular basis for overall health and tumor growth. Once the tumors became palpable (usually in 2-3 weeks), tumor volumes were measured regularly (once every 2-3 days) using a calipers. Tumor volumes were calculated by measuring tumor dimensions in three orthogonal directions and were calculated using the formula [163],

$$Volume = \frac{\pi}{6}\, a\, b\, c \tag{4.1}$$

Here a, b, and c, are the caliper measurements of tumor in orthogonal directions. Once the tumor reached 0.3 $cm^3 \pm 0.05$ cm^3, the mice were injected with nanoparticles and were treated with AMF.

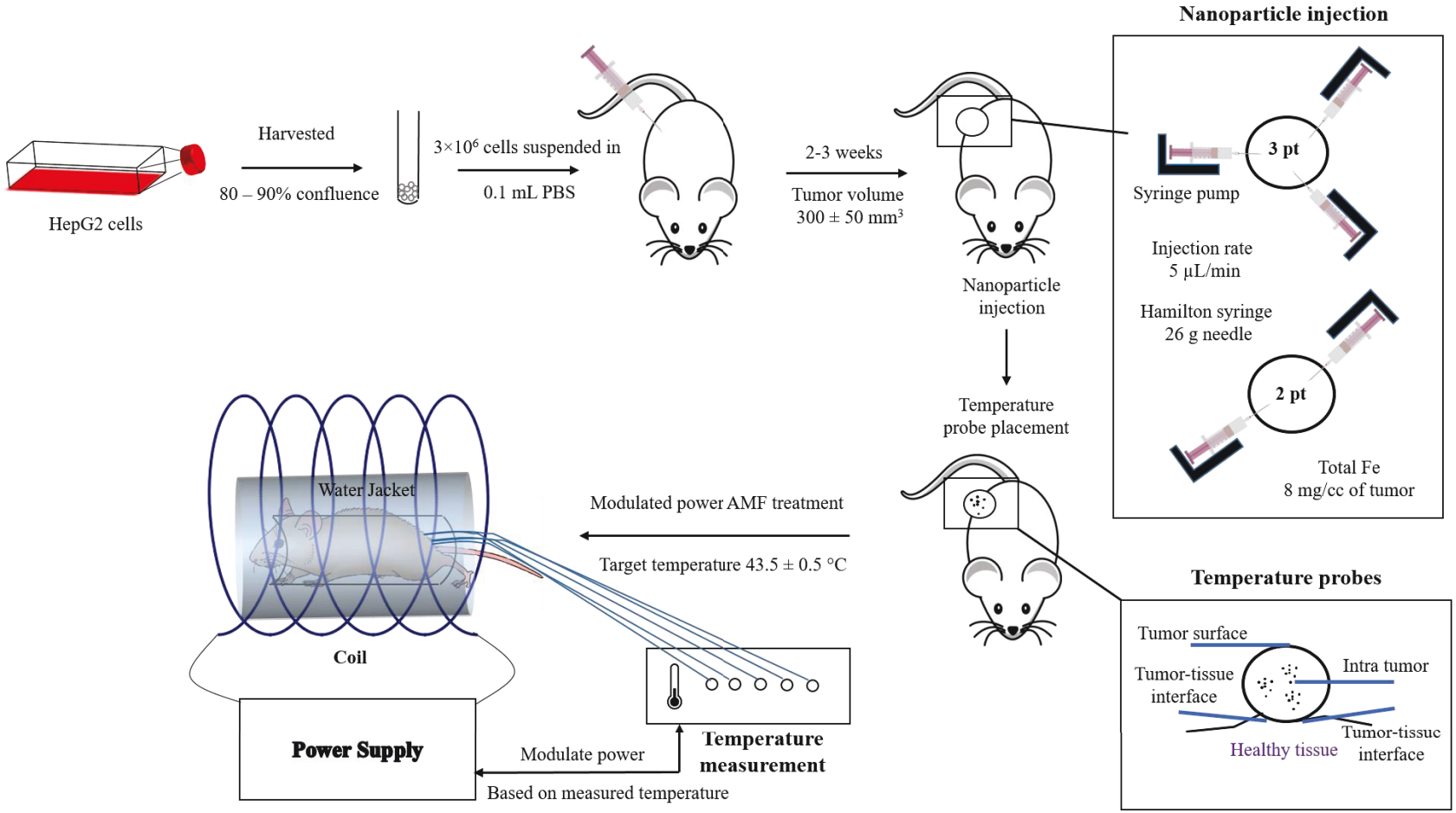

Figure 4.1 Schematic of the experimental design of *in vivo* modulated power magnetic nanoparticle hyperthermia study

4.2.4 Nanoparticle injections

Mice were anaesthetized with ketamine-xylazine, with a dose 0.01 mL per gram of mouse weight, for nanoparticle injections. BNF nanoparticles were injected using a syringe pump (Harvard Apparatus, South Natick, MA) with a Hamilton syringe and 26 gauge needles. The total iron dose was fixed at 8mg of Fe per gram of tumor for each of the injection methods. A slow injection rate of 5 μL/min was chosen [132]. Slow injection rates and lower injection volumes (achieved by using concentrated BNF nanoparticles) and use of syringe pump for injections allow for controlled and repeatable injection of nanoparticles with minimal leakage of nanoparticles [132]. Two injection methods were used to generate different nanoparticle distributions. Three point injection method (3-pt) consisted of injecting the nanoparticles into three sites in the tumor, which are in a triangular formation, with equal volume ($1/3^{rd}$ of total injection volume) in each injection site (Figure 4.1). Two point injections (2-pt) consisted of injecting the nanoparticles into two injection sites, located in diagonally opposite directions in the tumor, with equal volume (1/2 of total injection volume). After the nanoparticle injection, mice were immediately treated with alternating magnetic field (AMF) using the horizontal mouse coil configuration and water jacket described below.

4.2.5 Alternating magnetic field system and water jacket

The AMF system and the water jacket used for nanoparticle heating system has been previously described [52,164,165]. The AMF equipment mainly consists of three components: power supply, an external matching capacitance network, and a horizontal modified solenoid coil. The power supply consists of a 120-kW induction heating system

which provides an alternating current to a resonant circuit with variable frequencies (135-445 kHz). The external capacitance network was adjusted for stable oscillations at 155 ± 10 kHz. The horizontal modified solenoid coil has a diameter of 10 cm and generates a uniform (±10 % of peak amplitude) magnetic field. The power supply, capacitance network and the coil are all cooled using a closed-loop circulating water system connected to a 200-L reservoir of distilled water.

A concentric polyacrylic water jacket filled with distilled water was placed inside the horizontal coil [164]. The water jacket was connected to a closed-loop bench-top circulating bath (Hoefer Scientific Instruments, San Francisco, CA) capable of circulating water at 4L/min. The water jacket provides thermal regulation of anaesthetized mice which lose thermoregulatory control and become hypothermic. It also allows for minimizing the thermal interaction between the mouse and the coil, which can either be a heat source or heat sink depending on the power setting used [52,164,165].

4.2.6 Thermometry

Mouse and water jacket temperatures were measured with RF-resistant fiber-optic temperature probes (FISO, Quebec, Canada). All probes were calibrated using a NIST certified standard thermometer before use. Temperatures were recorded at 0.45 s intervals, and for at least 30s after the rectal temperature reached at least 35 °C, before AMF field was switched on. For each mouse, five temperature probes were used, inserted in the rectum, inside the tumor, on the tumor surface, and two (one on each side) at the tumor-healthy tissue interface (Figure 4.1). Another probe was used to measure the water jacket temperature before and during the experiment. Temperatures measured at the tumor-healthy tissue interface were used to control the AMF power applied. The aim was to reach

a target temperature of 43.5 ± 0.5 °C, at the tumor-healthy tissue interface rapidly and control it for the remainder of the treatment duration. The maximum temperature achieved between the two tumor-healthy tissue interface probes was used to control the AMF power applied in the experiment. This results in minimizing the temperatures achieved in the healthy tissue and thereby the thermal damage.

4.2.7 Modulated power thermal therapy

The aim of the current study was to evaluate the temperature controlled power modulated AMF heating for two nanoparticle distributions in mice. The applied power was modulated based on temperatures measured at the tumor-healthy tissue interface. For each cohort, 3-pt, and 2-pt, six mice were considered (Table 4-1). Mice were randomly assigned into the two experimental cohorts. Total AMF exposure was 20 min. Heating for all the mice was started by applying a magnetic field amplitude of 44 kA/m (peak) and monitoring the temperatures at the two locations on the tumor-healthy tissue interface. AMF amplitude was then manually modulated to achieve a target temperature of 43.5 ± 0.5 °C at the tumor-healthy tissue interface. The water jacket temperature was dynamically adjusted to ensure the rectal temperature was always below 41 °C. Applied AMF field amplitudes were noted with time to calculate the total energy applied for each mouse, based on the total iron injected and the measured SLP of the nanoparticles. After treatment, mice were euthanized after 48-72 hours based on the treatment outcome. Treatment outcome was arbitrarily coded based on degree of ablation observed, 0 (no ablation), 1 (partial ablation, <50% of tumor volume ablated) and 2 (ablation, > 50% of tumor volume ablated).

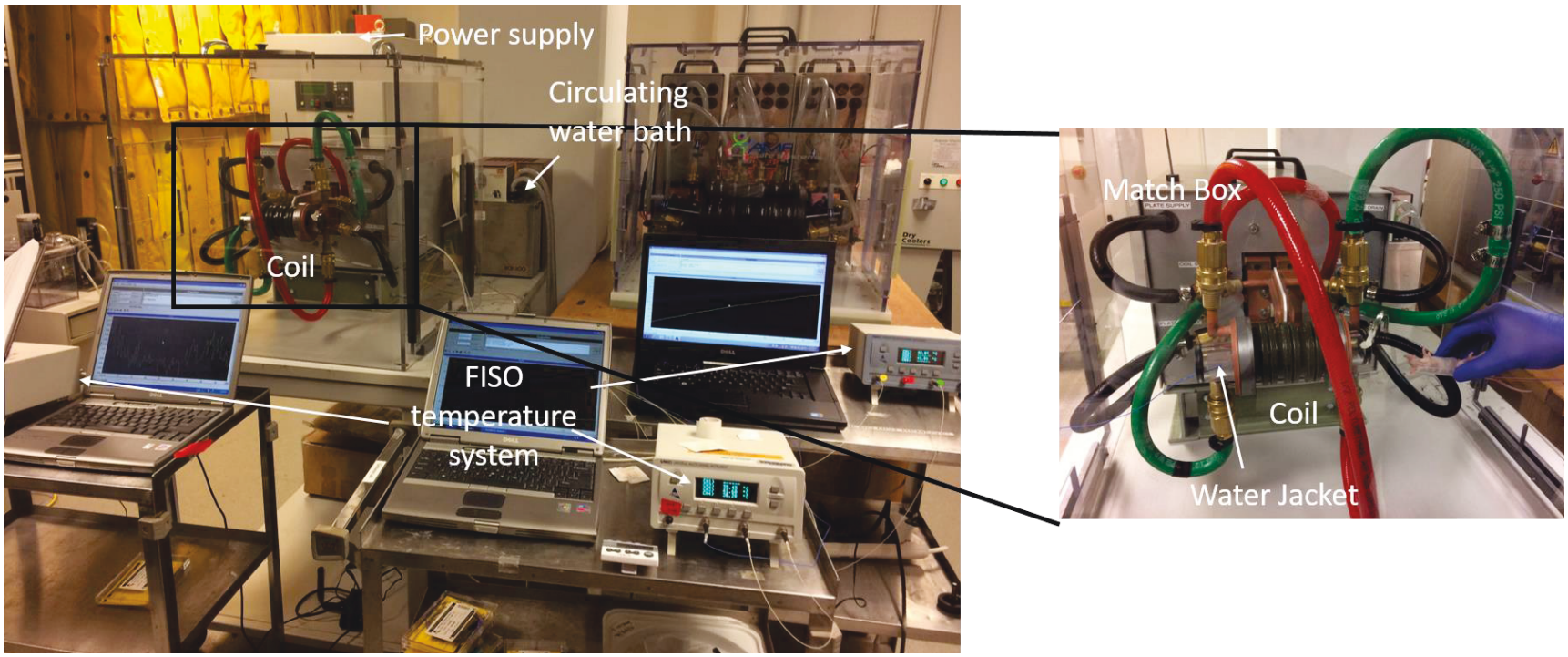

Figure 4.2 Setup for *in vivo* modulated power nanoparticle hyperthermia experiments. Setup consists of AMF heating system, water jacket and FISO temperature measurement system. AMF heating system consists of three main components – 1. Horizontal modified solenoid coil (Coil in figure), 2. Power supply, and 3. Matching capacitance network (Match box in figure). Water jacket connected to closed loop circulating benchtop water bath. FISO temperature system consists of optical fiber temperature probes connected to a module which allows for recording of temperatures using a computer.

4.2.8 Total energy applied and thermal dosimetry

The total energy deposited in the tumor can be calculated by using the mass of iron injected into the tumor (m_{Fe}), the applied field (H), duration applied (Δt) and SLP of the nanoparticles. The total applied energy is given by,

$$Total\ energy = \sum_{\forall\, \Delta t} m_{Fe} SLP(H)\, \Delta t \tag{4.2}$$

The temperature measured at the tumor-healthy tissue interface was normalized to convert time-temperature curve to an equivalent time at 43 °C (CEM43) to calculate the thermal dose [25]. The thermal dose is given by the expression, $CEM43 = \int_0^t R^{43-T(\tau)} d\tau$, where $R = 0.5$ for $T > 43$ °C and $R = 0.25$ for $T < 43$ °C.

4.2.9 Intratumor nanoparticle characterization – Prussian blue staining

Mice selected for intratumor nanoparticle distribution were euthanized immediately after nanoparticle injection and the tumors were harvested. Tumors were fixed in 10 % formalin for 48-hrs for histopathology. To accurately assess the nanoparticle distribution in the tumors with 2-pt and 3-pt injections, ten sections of each tumor were taken and stained by the following method. Formalin fixed tumors were paraffin embedded and ten slices of 0.5 micron thickness each were taken at 0.2 mm distance separation beginning with the top. All these sections were stained with Perl's reagent (Prussian blue) [52,166] to qualitatively assess distribution of BNF nanoparticles (positive stain for ferric, Fe^{3+}). The stained slides were scanned at 40x magnification using Aperio Scanscope™ slide scanner (Leica Biosystems, IL). The scanned images were then processed in ImageJ and

MATLAB to obtain the distribution of nanoparticles in the tumors. Briefly, the scanned images were first imported into ImageJ as low resolution images using the Bioformats plugin. They were then converted into RGB format and the stained blue pixels were then segmented by color thresholding. The segmented image was then converted into a binary image with dark pixels showing the nanoparticle distribution. This binary image was exported as a text image and read into MATLAB as a matrix. The matrices obtained from the ten slices of each tumor were then reconstructed into a 3D distribution in MATLAB (Figure 4.3).

4.2.10 Computational model

Simulations were conducted to compare with the *in vivo* experiments. Three dimensional FEM computational models were constructed and implemented in COMSOL 5.2a (COMSOL Inc., Burlington, MA). Tumors were modeled as ellipsoids with the dimensions similar to the measured animal tumor dimensions (volume ~ 0.3 cm^3 ± 0.05 cm^3). The healthy tissue computational domain was modeled as a cuboid of dimensions 2.5 cm (x-direction), 3.5 cm (y-direction), and 1.5 cm (z-direction). The healthy tissue domain was further divided into two layers: skin layer (0.75 mm thickness) and muscle layer (Figure 4.4). The tumor was centered in the top layer of the healthy domain with a skin layer to mimic the in vivo mouse experiments.

Heat transfer in the tumor and healthy tissue was modeled using the Pennes' bioheat equation [81] given by,

$$\rho_n c_n \frac{\partial T_n}{\partial t} = k_n \nabla^2 T_n + \rho_b c_b \omega_{b,n} (T_b - T_n) + Q_{m,n} + Q_p \qquad (4.3)$$

here n and b represent tissue (tumor, n = 1; muscle tissue, n = 2; skin tissue, n = 3) and blood; respectively. The density, specific heat capacity, thermal conductivity, local temperature, and metabolic heat generation rate are denoted by ρ_n, c_n, k_n, T_n, $Q_{m,n}$ and t is the treatment time. The thermophysical properties considered in the study were shown in Table 4-2.

Constant core body temperature of 37 °C was assumed at the bottom surface. All the four sides were assumed to be thermally insulating and the adiabatic boundary condition was considered. Continuity of temperature and conservation of heat flux conditions were considered at the different tissue interfaces. For the skin surface, both on the tumor and muscle, convective boundary condition with free convection heat transfer coefficient of h = 10 W/m^2 K was considered. The boundary condition is given by,

$$k_{skin} \frac{\partial T}{\partial z}|_{skinsurface} = h\,(T - T_{wj}(t)) \tag{4.4}$$

T_{wj} is the water jacket temperature and z is the normal to the skin surface. The initial temperature was considered to be 35 °C to match with the experiments. The variation of water jacket temperature T_{wj} with respect to time is taken from the measured experimental data.

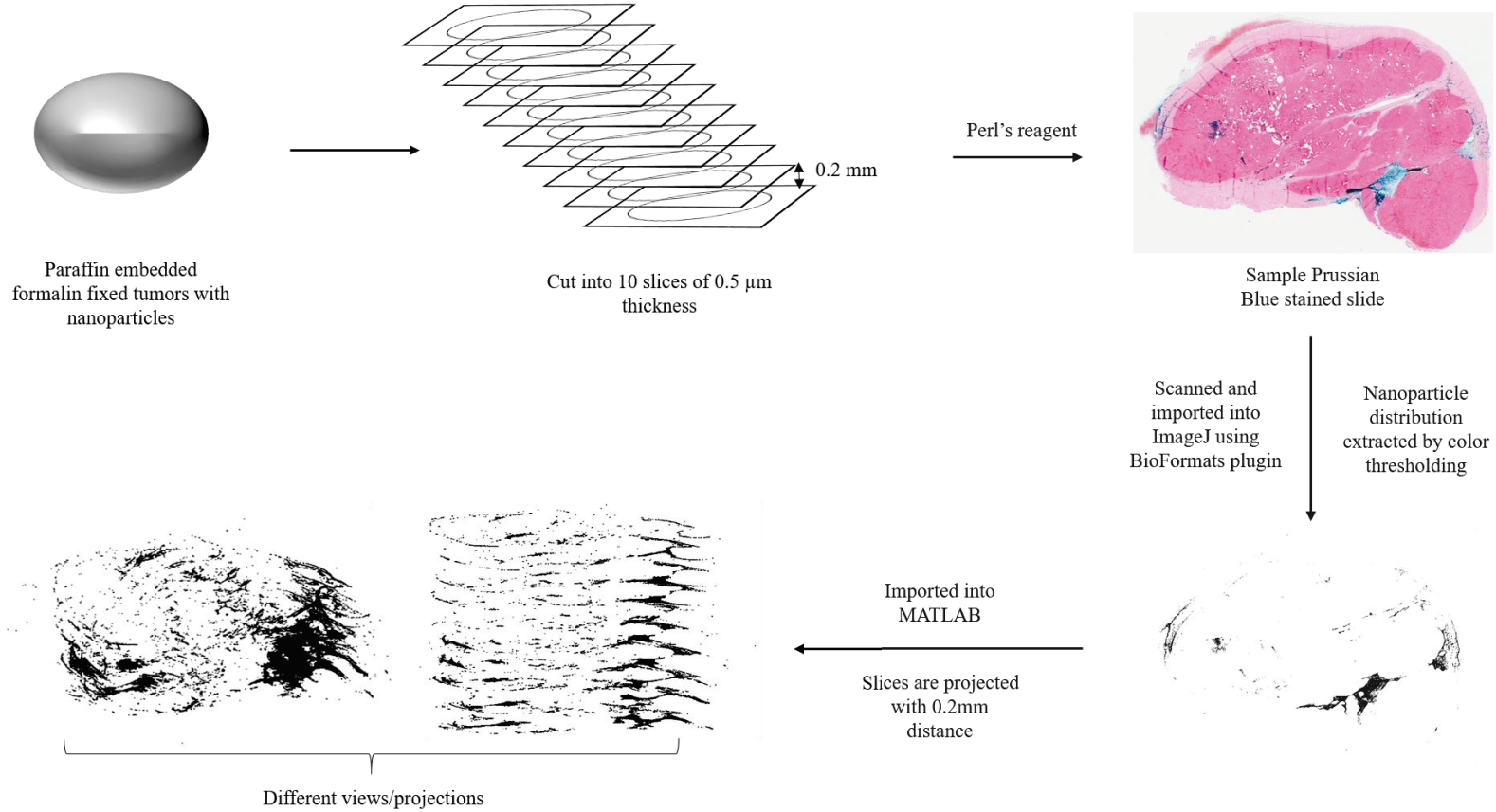

Figure 4.3 Workflow for intratumor nanoparticle distribution characterization by Prussian blue staining. Paraffin embedded formalin fixed tumors were cut into 10 slices of 0.5 µm each at 0.2 mm apart. They are stained with Perl's reagent to qualitatively assess iron nanoparticle distribution. Prussian blue stained slides were then scanned and imported to ImageJ. Nanoparticle distribution was extracted by color thresholding and the resulting binary images were imported into MATLAB. Images were then projected using *scatter3* plot in MATLAB to obtain the 3D distribution of nanoparticles.

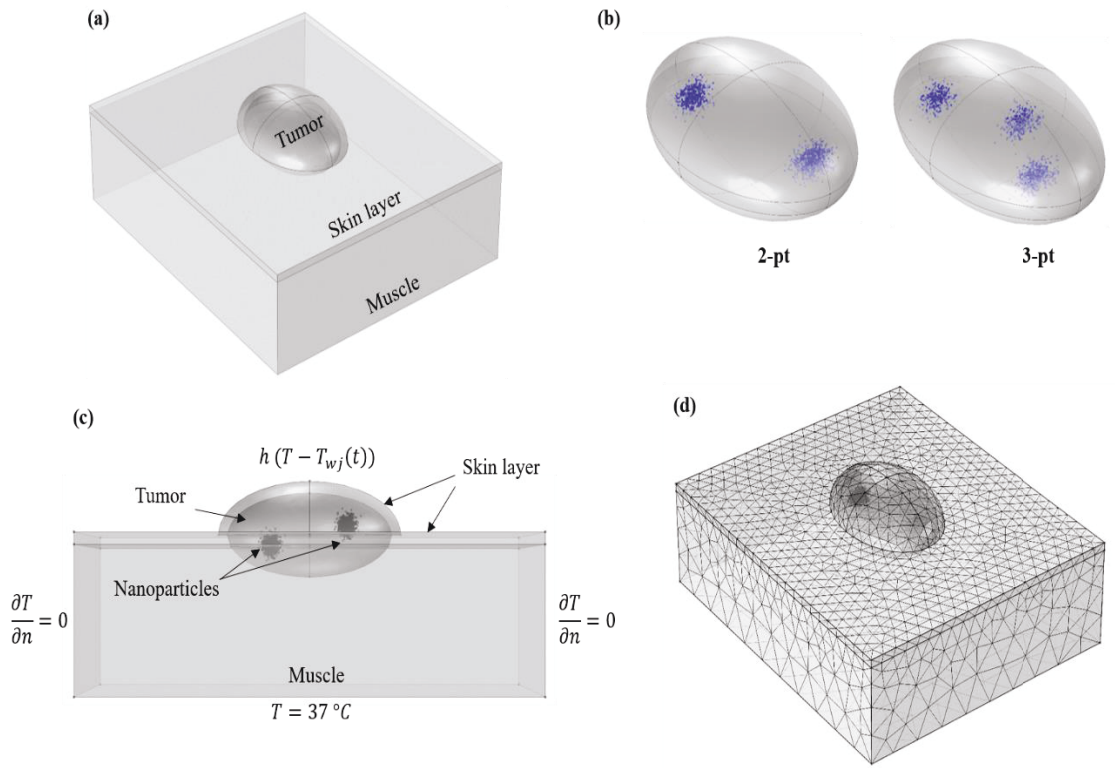

Figure 4.4 Schematic of the computational model used in the study. (a) Schematic of the computational model with the tumor, muscle, and skin layer. Skin layer is chosen above the tumor to mimic the subcutaneous mouse tumor model used in experiments. (b) Tumors with the two nanoparticle distributions considered in this study – 2-pt and 3-pt distribution. (c) Cross-sectional view of the computational model showing the tumor, skin layer, and muscle. The boundary conditions considered in the study are shown on the respective boundaries. Core body temperature of 37 °C is assumed on the bottom boundary. Adiabatic boundary conditions are assumed on the side boundaries. On the skin surface, free convection boundary condition is considered with the temperature of water jacket as the ambient temperature. (d) Sample mesh for the computational model shown in (a).

Two nanoparticle distributions mimicking the 2-pt and 3-pt injections were considered in this study. Nanoparticles were modeled as point heat sources and the total number of nanoparticles considered in the study was equal for both the distributions and was fixed at ~1400. This means the heating power of the individual nanoparticle is the same and is determined by the heating protocol followed in experiments. Nanoparticle

distributions at the injection point were considered to be a Gaussian distribution [112]. The Gaussian distributions were generated similar to those described in section 3.2.1. The heating protocol used in simulations mimicked experimental conditions used in AMF treatment of mice. The corresponding water jacket temperatures for each of the heating protocol were also taken. For blood perfusion, modified Arrhenius model (as described previously in section 3.2.2) was considered. The initial perfusion values for each of the three tissues was shown in Table 4-2. The activation energy E_a, and the frequency factor A, required for computing the thermal damage to vasculature for each of the tissues was shown in Table 4-3.

Table 4-2 Thermophysical properties of tissues considered in this study

	Density, ρ (kg/m^3)	Specific heat, c (J/kg K)	Thermal conductivity, k (W/m K)	Blood Perfusion rate, ω (1/s)	Metabolic heat generation rate, Q_m (W/m^3)
Tumor	900 [105]	3700 [105]	0.4 [105]	0.018 [167]	1500 [168]
Muscle	1050 [105]	3700 [105]	0.5 [105]	0.00175 [105]	1000 [105]
Skin	700 [105]	3700 [105]	0.3 [105]	0.00088 [105]	250 [105]
Blood*	1060 [125]	3770 [125]	N/A	N/A	N/A

*Temperature of blood (T_b) was fixed at 37ºC [125]. (N/A – not applicable)

Table 4-3 Values of activation energy E_a and frequency factor A considered in this study

	Activation Energy, E_a (J/mol)	Frequency factor A (1/s)
Tumor	5.064×10^5 [141,148]	2.984×10^{80} [141,148]
Muscle	1.38×10^5 [169]	6.36×10^{19} [169]
Skin	3.06×10^5 [169]	1.606×10^{45} [169]

COMSOL Multiphysics 5.2a was used to solve for the temperature distributions. Grid sensitivity and time step sensitivity studies were carried out to ensure that the chosen grid size and time step size had negligible effect on the computed temperatures.

4.3 Results

4.3.1 Characterization of BNF nanoparticles

For the two batches of BNF nanoparticles used in the animal experiments, iron concentrations of the stock and concentrated versions were determined by the ferene-s assay and summarized in Table 4-4. The high concentration of nanoparticles allow us to minimize the injection volume which in turn minimizes the injection time. The SLP of both batches of nanoparticles was measured for magnetic fields of 8 – 44 kA/m (peak) at fixed frequency of 155±10 kHz and shown in Figure 4.5. Both batches exhibited a similar S-shaped heating curve with change in amplitude which is characteristic of BNF nanoparticles [56,57]. Also, this non-linear variation of SLP with amplitude allows us to generate more heat by minimal change in the applied field amplitude.

Table 4-4 Measured concentration of nanoparticles used in the study

Batch	Iron concentration, Stock solution (mg Fe/mL)	Iron concentration, Concentrated solution (mg Fe/mL)
BNF – 0651710	45.77	179.56
BNF - 1231710	39.14	177.62

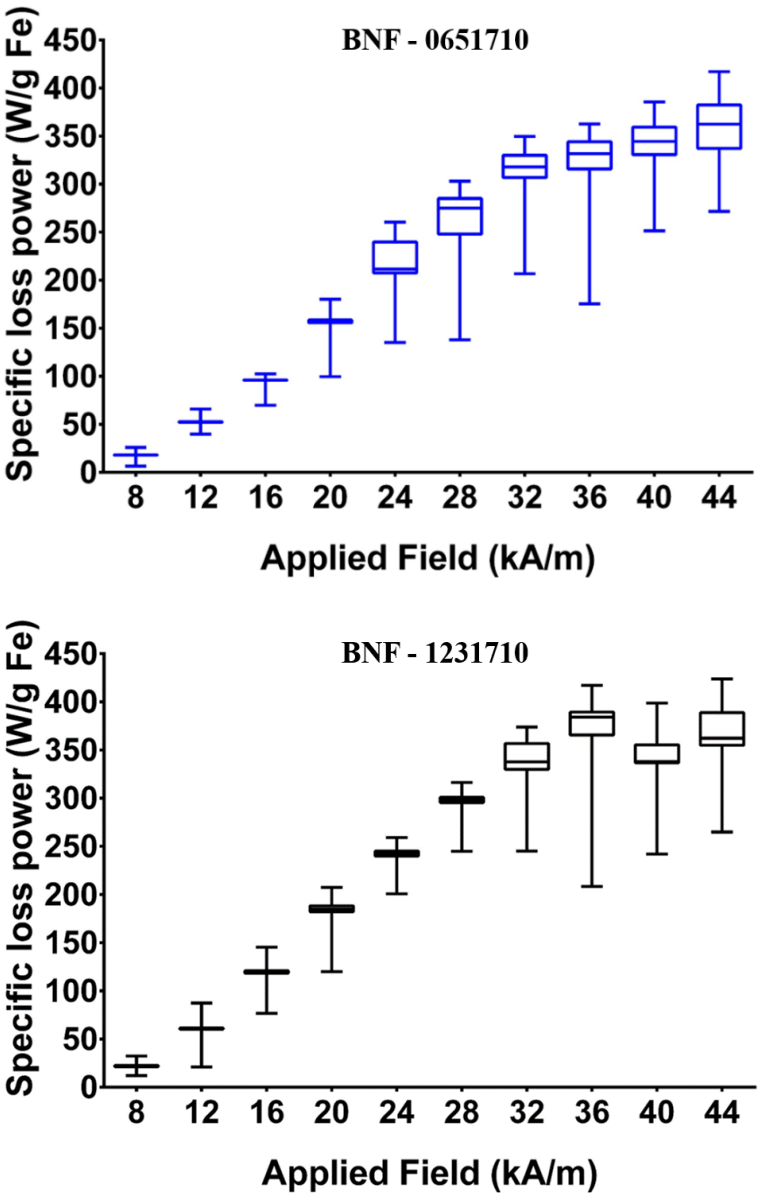

Figure 4.5 Specific loss power of two batches of nanoparticle BNF-0651710 and BNF-1231710 used in this study. The box represents the inter-quartile range of the measured SLPs at that field and the whiskers show the range of the estimated SLPs which are outside the interquartile range.

4.3.2 Modulated power AMF thermal therapy

For mice subjected to modulated power AMF therapy, a summary of tumor volumes, quantity of iron injected, total energy deposited for unit tumor volume, thermal dose measured at the tumor-tissue interface and the outcome of the therapy (0 – no ablation, 1 – partial ablation, 2 – ablation) are provided in Table 4-4. Power modulated AMF treatments were well tolerated by all mice. Tumor volumes of 2-pt injected mice were 0.281 ± 0.029 cm^3, while for 3-pt injected mice were 0.292 ± 0.026 cm^3 (mean ± SD). Statistical analysis using Mann-Whitney non-parametric tests showed there is no difference (p-value = 0.5887 > 0.05) between the tumor volumes considered for 2-pt and 3-pt injection. After injection, five temperature probes were inserted, four inside the tumor and one in the rectum. AMF treatment was well tolerated by mice with rectal temperatures for all the mice were controlled and maintained well below 41 °C. Temperatures were measured at the tumor – healthy tissue interface using two probes on either side of the tumor (right and left). The aim of the experiment was to attain and maintain the maximum temperature measured at the interface (either left or right) to 43.5 ± 0.5 °C. Representative temperatures measured during the experiment for mice injected with 2-pt and 3-pt nanoparticle injections is shown in Figure 4.6. All the mice were initially exposed to a field of 44 kA/m (peak) and this applied field was later modulated based on the maximum temperature measured at the tumor-healthy tissue interface. It can be seen that temperature at the interface can be controlled robustly for both the nanoparticle distribution models by modulating the AMF amplitude appropriately. The temperatures initially increased steeply and reached a maximum, due to high initial AMF amplitude applied. This was done to

attain the target temperature as fast as possible so as to generate a higher thermal dose in the tumor in less treatment time.

Figure 4.7 shows the applied power-time curve for each of the mice in the modulated power hyperthermia groups. While the initial applied field (44 kA/m, peak) is same for all the mice, the applied power differs slightly because of the slight difference in tumor volumes which in turn resulted in different iron content in the tumors. As mentioned previously, nanoparticles were injected based on tumor volume to yield a fixed concentration of 8 mg/mL. Thus, the injected iron content was different for different mice resulting in different initial heat input. The median duration of high field (44 kA/m) was higher for 2-pt nanoparticle injected mice (91 s) compared to 3-pt nanoparticle injected mice (70 s). The measured thermal dose at the tumor-tissue interface for each of the mice with 2-pt and 3-pt injection is plotted in Figure 4.8(a). The median thermal doses measured for mice with 2-pt injection was 28.45 min (CEM43) compared to 32.14 min (CEM43) for mice with 3-pt injection. However, statistical analysis using the Mann-Whitney test showed no statistically significant difference between the thermal doses deposited at the tumor-healthy tissue boundary for the two groups of mice (*p-value* 0.1320 > 0.05). The total input heat energy normalized to tumor volume (J/cc of tumor) deposited in the tumors with 2-pt and 3-pt injection was computed and compared in Figure 4.8(b). It can be seen that 2-pt injected tumors required higher median heat energy (1267 J/cc) compared to 3-pt injected tumors (1102 J/cc). But it can be observed that there is a significant overlap in the interquartile ranges of the total energy plots for 2-pt and 3-pt injected tumors. This shows that while there is a difference in the median values for the total energy for the 2-pt and

Table 4-5 Summary of the tumor data, measured thermal dose and outcome for mice exposed to modulated power AMF. Codes for Outcome – NA – no ablation, PA – Partial ablation, and A – Ablation

Nanoparticle Injection	Mouse	Tumor Volume (cm^3)	Total iron injected (mg)	Total Energy deposited (J/cm^3)	CEM43 at tumor-tissue boundary (min)	Outcome
2-PT	M1	0.259	2.07	1295	30.04	2 (A)
	M2	0.279	2.23	1436	23.64	2 (A)
	M3	0.332	2.66	946	30.77	2 (A)
	M4	0.252	2.02	948	26.22	1 (PA)
	M5	0.290	2.32	1238	29.30	1 (PA)
	M6	0.271	2.17	2227	27.60	1 (PA)
3-PT	M7	0.322	2.58	1599	35.32	0 (NA)
	M8	0.256	2.05	1042	30.28	1 (PA)
	M9	0.268	2.14	1130	35.07	2 (A)
	M10	0.317	2.53	1074	29.11	1 (PA)
	M11	0.289	2.31	657	33.99	0 (NA)
	M12	0.302	2.42	1209	27.53	1 (PA)

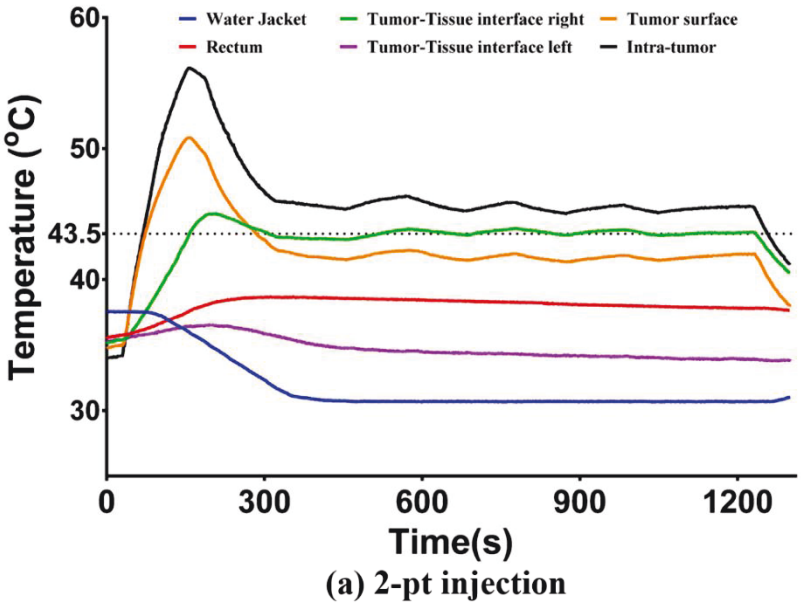

(a) 2-pt injection

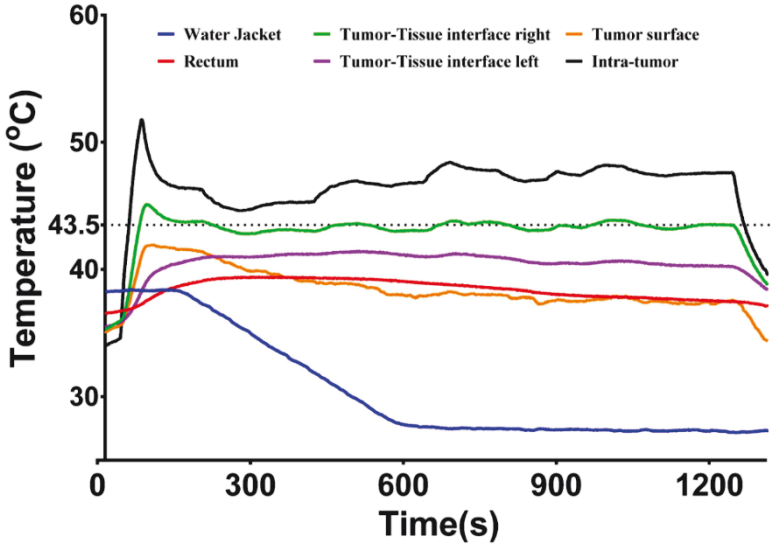

(b) 3-pt injection

Figure 4.6 Measured temperatures during modulated power nanoparticle hyperthermia of mice injected with nanoparticles intratumorally using 2-pt and 3-pt injection methods. Temperatures were measured at five locations in the mouse and inside the water jacket. The aim was to achieve the target temperature of 43.5 ± 0.5 °C at the tumor-tissue interface and control it for the remainder treatment duration. Treatment duration was 20 min. (a) Time-temperature data for mouse with 2-pt injection of nanoparticles measured intra-tumor, tumor surface, tumor-tissue interface (left & right), rectum, and the water-jacket. (b) Same as in (a) for mouse with 3-pt injection

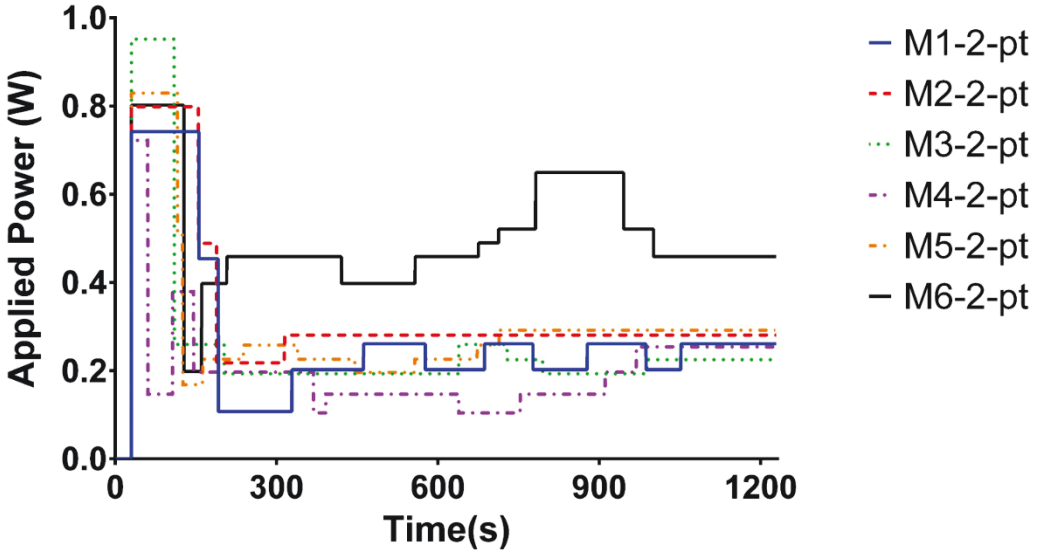

(a) 2-pt injection

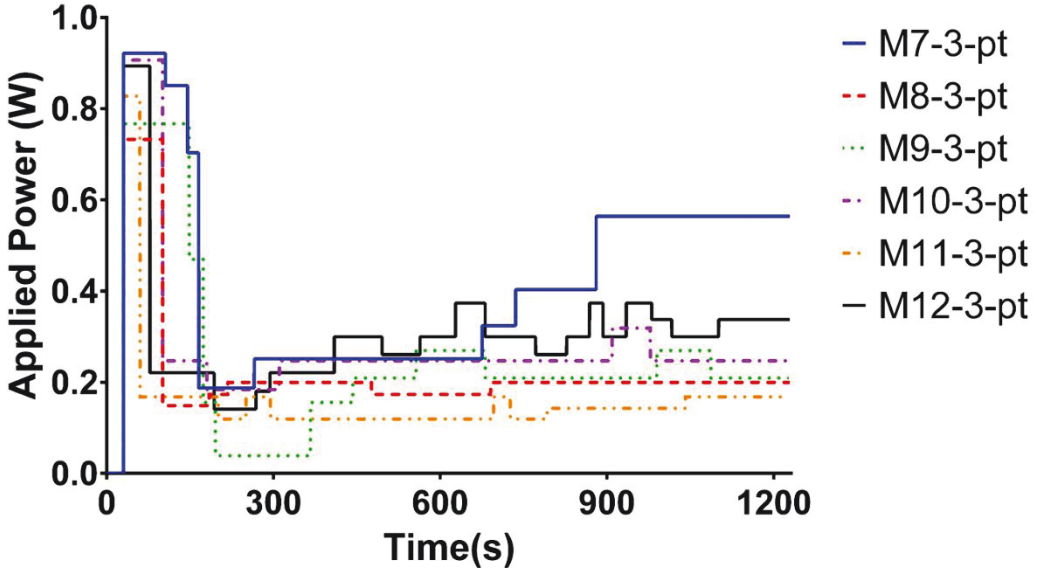

(b) 3-pt injection

Figure 4.7 Applied power variation with time for mice in (a) 2-pt injection group, (b) 3-pt injection group treated with modulated power magnetic hyperthermia treatment for 20 min. Applied power was computed using the total injected iron and SLP at the applied field. Overall, median duration of higher field amplitude (44 kA/m) was higher for mice in 2-pt injection group compared to 3-pt injection group.

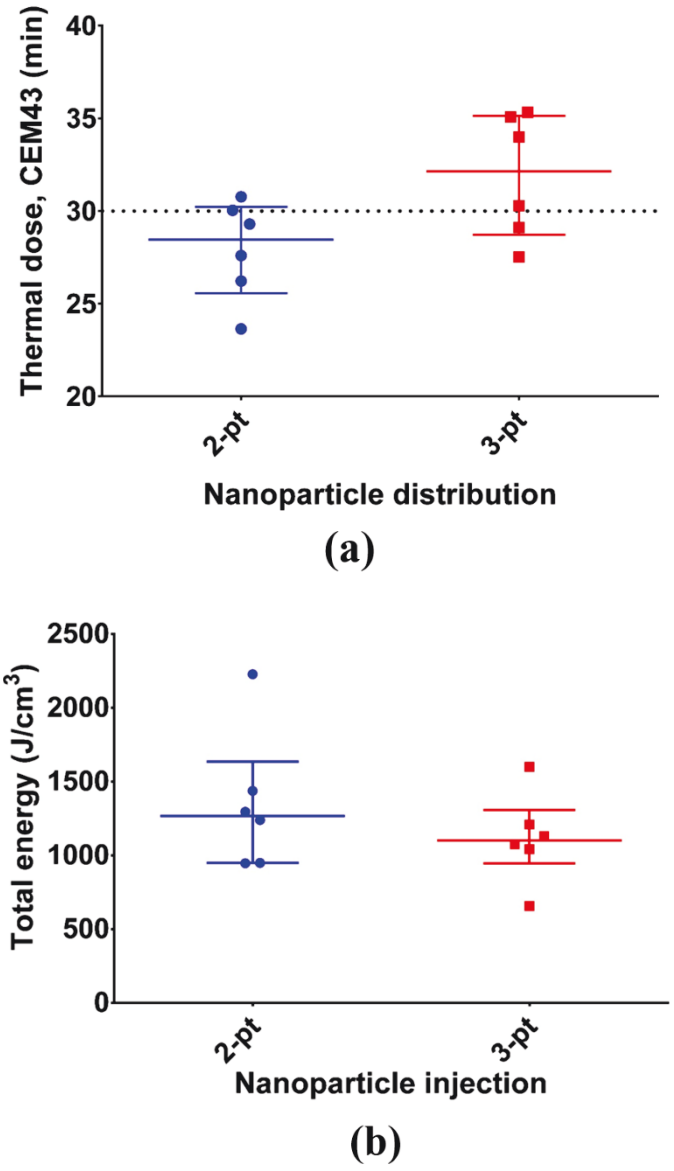

Figure 4.8 Measured thermal dose (CEM43) at the tumor-healthy tissue boundary and total energy deposited normalized to tumor volume for mice in 2-pt injection group and 3-pt injection group after 20 min of treatment with modulated power nanoparticle hyperthermia. Measured thermal dose for 2-pt and 3-pt injected mice was similar with their medians in the range of 30.45 ± 2 min and the difference was statistically not significant ($p = 0.13 > 0.05$). Similarly, the difference in total energy deposited for the two groups normalized to tumor volume was statistically not significant ($p = 0.49 > 0.05$)

and 3-pt injected tumors, overall the difference is not significant. This was further confirmed by conducting non-parametric Mann-Whitney test which yielded a *p-value* of 0.4848 (> 0.05).

Nanoparticle distributions in tumors for mice injected with 2-pt (n = 3) and 3-pt (n = 3) injections were assessed by Prussian blue staining. Representative sample slides for each of the six tumors along with reconstructed distributions is shown in Figure 4.9. Analysis of the Prussian blue slides for the six tumors show particles in the external plasma membrane and extracellular space. This is consistent with previous observations by Giustini et al. [48] where they observed more than 95% of the nanoparticles in the extracellular space within the first hour post-injection. It can also be observed that more nanoparticles are present in the injection path. 3D distributions generated from the stained individual slices show a clear difference in nanoparticle distributions. For mice injected with nanoparticles using the 2-pt injection method, two concentrated regions of nanoparticles can be seen in the generated distributions showing possibly the injection locations. A similar observation can be made for two of the mice injected with nanoparticles using the 3-pt injection method. For the third case, Prussian blue images show all particles clustered in a single extracellular space thereby clearly not showing the three sites of injection. It can be inferred from the 3D projections that the distributions achieved with 2-pt and 3-pt injections are different and no two tumors have the same nanoparticle distribution. This also highlights the fact that controlling the nanoparticle distribution by controlling the injection methods alone is insufficient and depends heavily on the tumor physiology [44,52,130,132].

The outcome of temperature-control modulated power hyperthermia on all the mice with two different distributions was summarized in Table 4-5. The outcomes were categorized using the following codes – 0 (no ablation), 1 (partial ablation, <50% of tumor volume ablated) and 2 (ablation, more than 50% of tumor volume ablated). Maximum ablation was observed for 2-pt injected tumors (code-2, n = 3) compared to 3-pt injected tumors (code-2, n =1). All 2-pt injected tumors were either ablated or partially ablated. For the 3-pt injected tumors, only one of the tumors was ablated and two were partially ablated.

Simulations were carried out to further understand the results obtained through experiments. For this, two nanoparticle distributions mimicking the 2-pt and 3-pt injections were considered. The heating power of the nanoparticles was varied based on the applied power measurements from mouse experiments. Temperature distributions achieved for 2-pt and 3-pt distributions at the center of the tumor across the XY, YZ, and ZX planes was plotted in figure 4.10. The green contour line plotted is the 43.5 °C isotherm in each of the plots. As expected, higher temperatures were observed at the nanoparticle concentrated regions compared to regions away from nanoparticles. Ablative temperatures of greater of 45 °C can be observed for the skin layer above the tumor with temperatures going higher than 50 °C in some areas. On the other hand, temperatures at the tumor-healthy tissue layer were lower than those compared to the skin layer above the tumor. Thermal damage given by Ω,

$$\Omega = \int_0^{\tau} Ae^{\frac{-E_a}{RT}} dt \tag{4.5}$$

is plotted for the tumor, muscle and skin layer at the center along the YZ plane. $\Omega > 1$ is generally associated with irreversible thermal damage and burn injury for skin [169]. In the current plots (Figure 4.11), only regions with $\Omega > 1$ are shown. It can be seen for the 2-

pt distribution model, extensive damage occurs in the skin layer above the tumor while for the 3-pt model no damage is seen. This is consistent with our experimental observations.

Variation of temperature with time at one location below the tumor-healthy tissue boundary is plotted for the two nanoparticle distribution models to compare with experiments and is shown in Figure 4.12. It can be seen that initially the temperature rises steeply reaching a maximum and then reduces and settles down and oscillates close to 43.5 °C. This trend is similar to the trend observed in experiments (Figure 4.6). For the 2-pt distribution, the temperature reached a maximum of 48.31 °C and then settled down to 43.5 ± 0.5 °C, while for the 3-pt distribution model the temperature rise is not so steep and has a temperature < 43.5 °C for a majority of the treatment time.

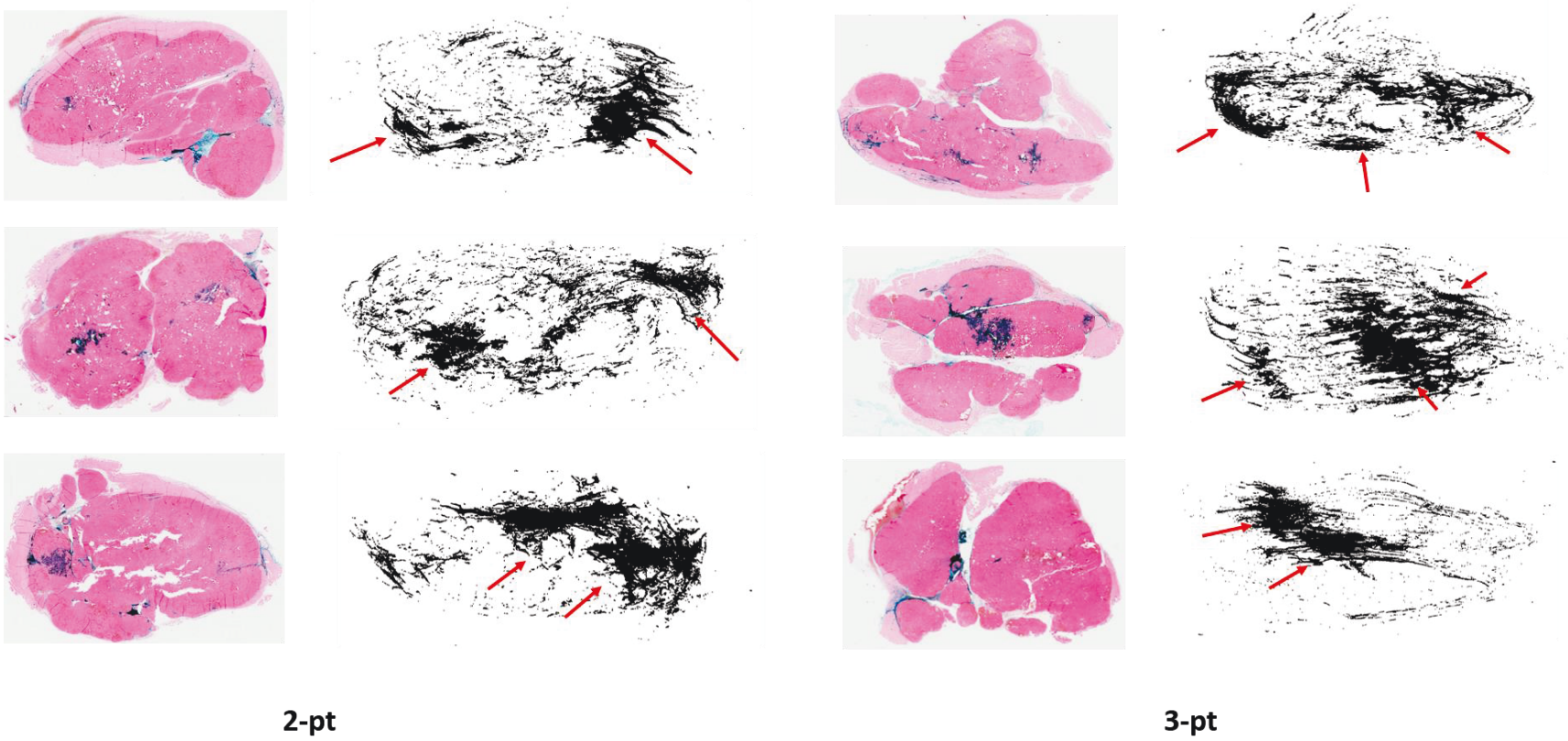

Figure 4.9 Intratumor nanoparticle distribution characterization by Prussian blue staining. 3D nanoparticle distributions obtained from Prussian blue slides of 2-pt and 3-pt injected tumors. Highly concentrated regions (showed by red arrows) show the injection sites. Observed distributions are vastly different for each of the tumors highlighting the role of tumor physiology in addition to injection parameters.

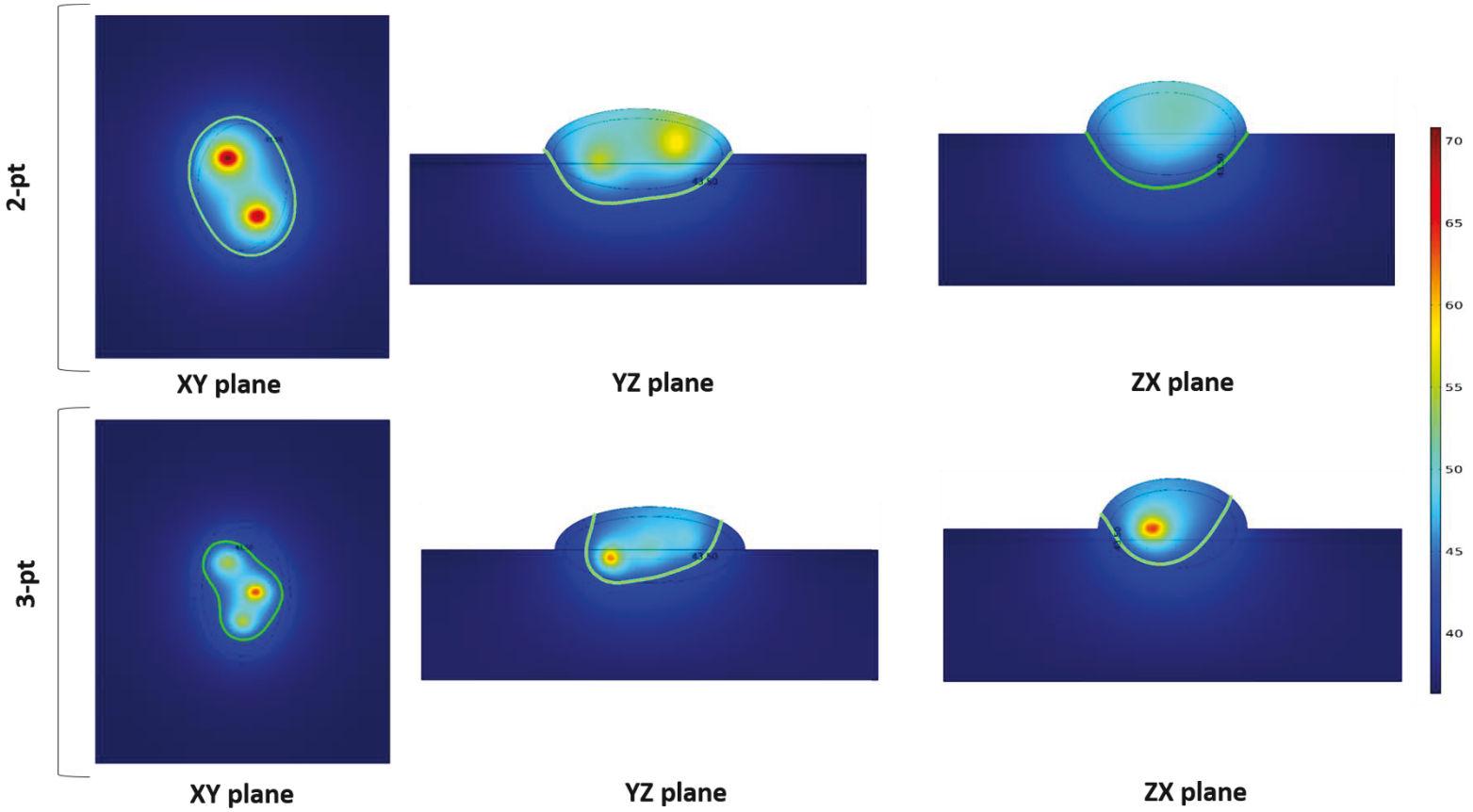

Figure 4.10 Ablative temperatures are achieved in the skin layer above the tumor for 2-pt distributions compared to 3-pt distributions Temperature distributions along the XY, YZ, ZX planes at the center of the tumor for the 2-pt and 3-pt distribution models after 20 min of heating with applied power-time curve from experiments

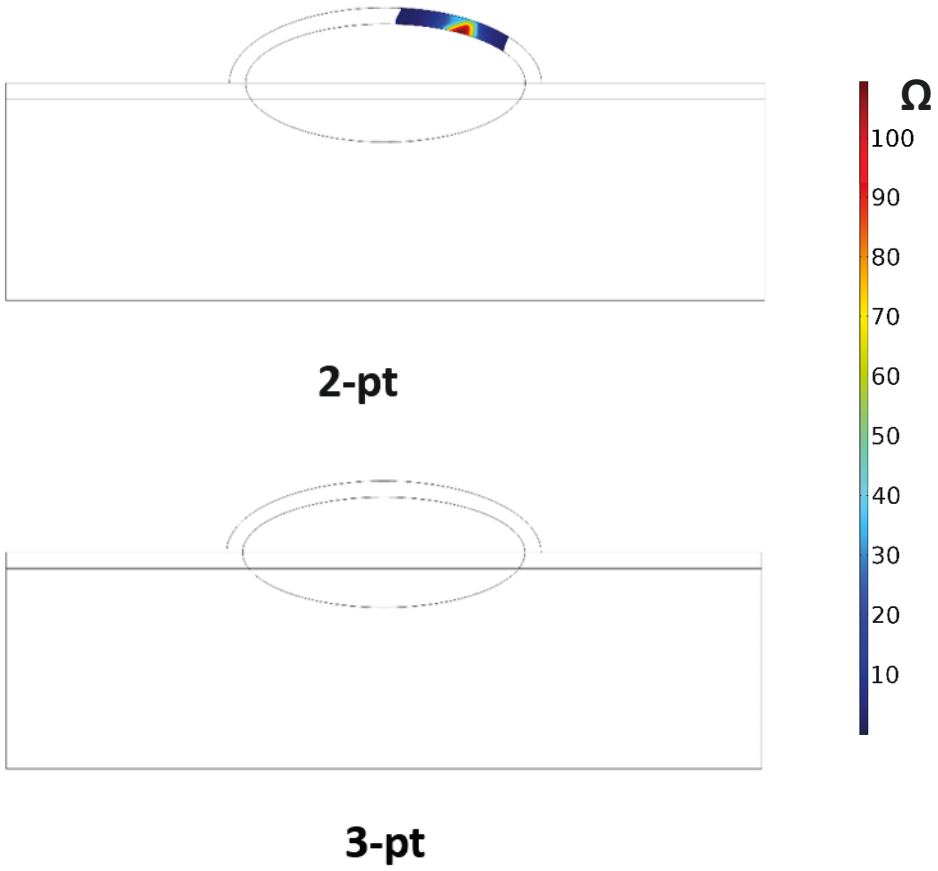

Figure 4.11 High degree of thermal damage Ω (Equation 4.5) is observed in the skin layer above the tumor for the 2-pt distribution model with no significant damage observed for the 3-pt distribution. Regions with degree of thermal damage ($\Omega > 1$, associated with burn injury) shown for the YZ plane at the center of the tumor for the 2-pt distribution and 3-pt distribution model after 20-min of heating with applied power – time curve from experiments. Note: Color map only shows the regions with thermal damage $\Omega > 1$

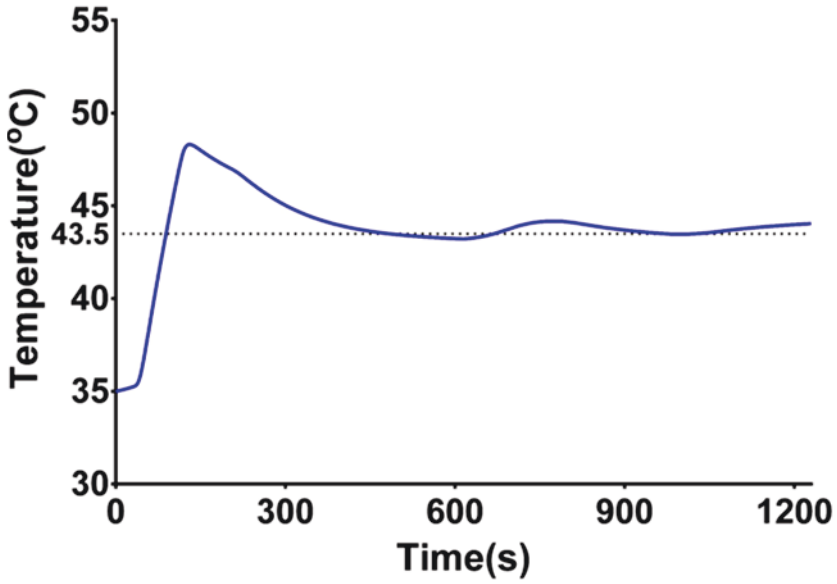

(a) 2-pt

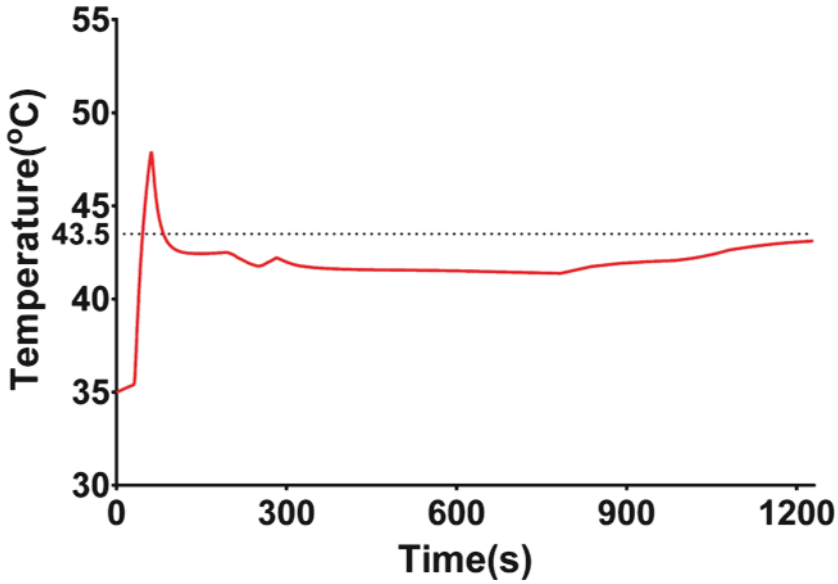

(b) 3-pt

Figure 4.12 Variation of temperature with time at one location below the tumor-healthy tissue boundary for the (a) 2-pt distribution model, (b) 3-pt distribution model. The temperatures initially increased rapidly reaching a maximum and decreased close to 43.5 °C. This trend is similar to the temperatures measured at tumor-healthy tissue boundary in our *in vivo* experiments.

4.4 Discussion

The potential of magnetic nanoparticle hyperthermia to achieve targeted, tumor-specific heating while minimizing damage to surrounding healthy tissues has been shown in multiple preclinical and clinical studies [39,41,42,45,46,49,50,52,133,170]. However, challenges remain for magnetic nanoparticle hyperthermia to become a clinical modality. The main challenges have been, 1) the ability to generate sufficient therapeutic heating at lower magnetic field amplitudes and frequencies to minimize non-specific eddy current heating; 2) to deliver sufficient quantity of nanoparticles into the tumor to achieve sufficient thermal damage, and 3) to achieve a nanoparticle distribution which can lead to desirable temperature elevations across the entire tumor volume. Considerable efforts have been made to develop optimization methods to address these challenges [112,115,136–141]. However, none of these models/methods have been tested in preclinical or clinical models.

The aim of this pilot study was to implement the temperature control power modulated magnetic nanoparticle hyperthermia (similar to methods developed in chapters 2 and 3) in an animal model of liver cancer. In doing so, we wanted to understand the challenges associated in implementing a computationally developed strategy and to improve the proposed method based on our findings. One of the main advantages of our proposed modulated power heating method was that necessary tumor damage can be achieved for a range of nanoparticle distributions with minimal surrounding healthy tissue damage. Hence, to test this we chose to generate two nanoparticle distributions by considering two injection methods – 2-pt and 3-pt. The nanoparticle injections were carried out using concentrated BNF nanoparticles (Table 4-4), whose SLP has been determined at

the range of operating fields (8 - 44 kA/m, peak) at fixed frequency of 155 ± 10 kHz (Figure 4.5). This enabled us to inject lower volumes of nanoparticles (< 15 μL) at a low injection rate of 5 μL/min, thereby attaining controlled nanoparticle release. Despite this, a slight backflow of nanoparticles along the needle track was observed. With the two injection methods, we were able to generate two different nanoparticle distributions consistently as evidenced by the analysis of Prussian blue images (Figure 4.9). A high concentration of particles can be observed at the injected locations (two for 2-pt and three for 3-pt). Most of the nanoparticles were observed within the extracellular space, which is consistent with observations done by Giustini et al. [48]. However, it is important to note that despite using the same controlled injection method, the distributions were vastly different even in the same injection method cohort. This highlights the fact that controlling the nanoparticle distribution inside the tumors needs further optimization and tumor physiology has an important role to play.

Temperature feedback controlled power modulated hyperthermia was implemented successfully for both the nanoparticle distributions. We were able to achieve a good control of the temperature at the tumor-healthy tissue boundary by modulating the power based on temperature feedback at the same location. The target temperature of 43.5 °C was achieved for all the mice independent of the nanoparticle distribution (Figure 4.6). There was no difference (statistically insignificant) among the two groups for the thermal dose deposited or the total energy applied (Figure 4.8). However, the treatment outcome was different for the two groups. 3 mice in the 2-pt injection group experienced complete ablation (code -2) compared to only 1 mouse with 3-pt injection. Tumor regions with high concentration of nanoparticles for the 2-pt case compared to 3-pt injection, could have resulted in significant

ablation. As mentioned previously, the backflow of nanoparticles along the needle path could result in the concentration of nanoparticles close to the skin surface which could have led to skin injury. We then performed simulations on subcutaneous ellipsoidal tumor model to compare and understand our experimental observations. We implemented the same heating protocol that was used in our experiments and also included the variation in water jacket temperature as the surface boundary condition. This is important for subcutaneous tumors because the heat transfer between the mouse and water jacket takes place through the skin. Performed simulations show a similar trend, predicting skin burn and ablative temperatures for 2-pt nanoparticle distribution tumor compared to 3-pt model (Figure 4.10). For the 2-pt tumor model, high degree of thermal damage, $\Omega >> 4$, can be observed, comparable to our experiments [169]. Additionally, it can be seen that the temperature at the tumor-healthy tissue boundary for both the simulated 2-pt and 3-pt tumor models exhibits a temperature-time curve similar to that of our experiments (Figure 4.12). Thus, it can be inferred that our simulations qualitatively predict the experimental outcomes.

The therapeutic efficacy of temperature-controlled modulated power hyperthermia could not be tested in this study. Tumor ablation combined with skin burns precluded tumor growth delay studies, as this violates our IACUC protocol. However, some significant conclusions and lessons can be made from our *in vivo* testing of temperature-controlled modulated power nanoparticle hyperthermia. We were able to show that the temperature at the tumor-healthy tissue boundary can be controlled consistently for both the distribution models. This shows that temperature-controlled modulated power hyperthermia can be implemented in *in vivo* mouse tumor models for different nanoparticle distributions. Another important conclusion from the study is that controlling the nanoparticle injection

parameters cannot lead to repeatable nanoparticle distributions inside the tumor, as evidenced from the analysis of Prussian blue images. Our method of generating of 3D nanoparticle distributions using Prussian blue images provides an alternative method to visualize and understand the nanoparticle distributions for labs which do not have access to imaging technologies.

One limitation of the study is the use of subcutaneous tumors. While subcutaneous tumors allow for easier delivery of nanoparticles by direct intratumor injection and tumor size measurements, the proximity of the tumor to the skin surface causes significant limitations. Simulations from our deep tissue tumor models in Chapter 2 and Chapter 3, and our subcutaneous tumor models in this chapter do show limited thermal damage in the healthy tissue, however the change in thermal boundary conditions for the subcutaneous models especially on the skin surface results in enhanced heat transfer at the skin surface causing higher temperatures and thermal damage at the skin surface. Future studies should be focused on orthotopic tumors so as to overcome this limitation. Additionally deep seated tumors have more clinical relevance compared to subcutaneous tumors. It should also be noted that for critical organs, the margins for healthy tissue damage are minimal highlighting the need for more careful planning before implementing this method.

Another limitation of the study is the uncertainty associated with temperature probe placement at the tumor-healthy tissue interface. We have shown in our simulations that the location of the temperature probe placement (Table 3.3) is indeed critical for the success of the method and this location depends on the nanoparticle distribution inside the tumor. Hence, future studies should use imaging methods such as CT imaging, to determine the tumor nanoparticle distribution and use ultrasound guided temperature probe placement for

better results. This approach can be used to determine the individualized heating protocol and probe placement before the treatment. In addition, the use of PID controlled power modulation method presented in simulations could give a more controlled heating compared to step heating method implemented in this study.

While the method to generate 3D nanoparticle distributions using Prussian blue images presents a cost-effective method, it has some limitations. It should be noted that the method produces an approximate 3D nanoparticle distribution as it is generated from a discrete number of tumor slices separated by a distance. Also, the processing of tumors from harvesting to embedding in paraffin can have an effect on the distribution of particles and tumor volume. In addition, the difficulty of image registration among the different slices can have an effect on the generated 3D distributions. This method can be improved by ensuring registration of images which would give a more aligned and realistic nanoparticle distribution.

As mentioned above, future experiments should be aimed to work with orthotopic tumor models compared to subcutaneous models for a better understanding of the efficacy of power modulated hyperthermia. Also, to test the therapeutic efficacy of the modulated power hyperthermia, tumor growth delay results should be compared to both untreated controls and constant power hyperthermia treated mice.

4.5 Conclusions

In summary, *in vivo* experiments were conducted in subcutaneous HepG2 tumors implanted in male nude mice. Temperature-control modulated power heating method similar to the methods proposed in the previous chapters (chapters 2 and 3) was implemented in two nanoparticle distribution models, generated using two injection

methods, 2-pt, and 3-pt. Using Prussian blue staining, it has been shown that the generated nanoparticle distributions for the 2-pt and 3-pt models are qualitatively different. Additionally, it was also shown that the generated distributions are qualitatively different for each tumors in the same group. Temperature data from the experiments show that the tumor-healthy tissue boundary temperature can be consistently controlled with modulated power heating method for both the distribution models. However, tumor ablation and skin burns on the tumor surface prevented us to pursue tumor growth delay studies to test the efficacy of this method. Results from our numerical simulations using a subcutaneous models do predict the response observed in our experiments. In conclusion, while temperature at the tumor-healthy tissue boundary can be controlled using our heating method, studies in large animals using orthotropic tumors models should be conducted to test the therapeutic efficacy of the proposed heating method.

Chapter 5
Thermal and electromagnetic modeling of magnetic nanoparticle hyperthermia

This chapter focuses on developing a coupled thermal and electromagnetic model for simulation of magnetic nanoparticle hyperthermia. The model will help us estimate the non-specific eddy current heating in large volumes during magnetic nanoparticle hyperthermia and can equip us to develop effective treatment strategies for clinical translation of magnetic nanoparticle hyperthermia. The coupled electromagnetic and thermal model was developed using COMSOL's AC/DC and Heat Transfer modules. A

cylindrical model was first developed and the temperatures achieved due to electromagnetic heating were computed. This model was verified with analytical expression for power absorbed by a cylinder exposed to an alternating magnetic field at a fixed frequency. Uncertainty analysis was conducted to determine the effect of uncertainty in input parameters on the computed temperature distribution. We then identified the important parameters that have a significant effect on the computed temperature distribution. The computational model was then validated with experimental data obtained from agar gel phantoms exposed to an alternating magnetic field. After this, a three dimensional model of rabbit liver was built from computed tomography images. The resulting temperature distributions achieved due to non-specific heating of exposed tissues after 20 min of treatment at given AMF field and frequency conditions was computed. Our results show significant temperature elevations due to non-specific eddy current heating in the exposed tissues.

5.1 Introduction

The quantity of heat generated by magnetic nanoparticles increases with increasing applied magnetic field amplitude and frequency. However, at higher fields and frequencies, exposed tissues can generate significant non-specific heating due to generation of eddy currents. Larger treatment volumes or large volumes of tissue exposed to an alternating magnetic field generate more heat resulting in more off-target tissue heating [61,156,171]. Also, time-varying magnetic field can induce other effects on the exposed tissue [172]. The heat generated due to these eddy currents can propagate throughout the body and can stimulate a complex thermoregulatory response in the body. This thermoregulatory response can result in perfusion changes affecting the temperatures achieved in the tumor

and the exposed healthy tissue. Thus, the limits due to off-target eddy current heating should be considered when optimizing the applied field and frequency for magnetic nanoparticle hyperthermia.

In *in vivo* experiments, monitoring eddy currents and eddy current heating is difficult. Hence, to develop methods for mitigating the effects of eddy currents, modeling of eddy current generation and heating is important. Efforts have been made to model eddy current heating by developing coupled electromagnetic and thermal models [173,174]. Both of these models were based on specific coil designs and were not extensively validated with experimental data. Stigliano et al. [174] conducted a partial validation of their model by comparing their simulated temperature with measured temperatures in a agar gel phantom only at one time point. Additionally, the effect of input parameter uncertainties on the simulated eddy current heating and temperatures was not considered.

During the past fifty years, there has been a significant increase in the use of computational simulations to model physical and biological processes in research, analysis, and design of engineering processes. The impact of modeling and simulation can be seen across different areas encompassing both the physical and biological world. For example, modeling has been used to understand cardiovascular flows, designing new equipment, modeling environmental phenomena, designing engines, etc. Considering the impact of computational modeling and simulations, the credibility of these models is of paramount importance. Often, one of the main concerns cited by field engineers, doctors, fund managers, and lay people is whether the predictions made by these simulations are credible. Thus, it is very important to assess the accuracy of a given model so that decisions can be taken based on the predictions. The primary means to assess accuracy and reliability of any

computational model is by verification and validation [175]. Assessment of the accuracy of a solution to a computational model with known solutions (often analytical) is known as verification. Validation, on the other hand, is the assessment of the accuracy of a computational solution by comparison with experimental data [175]. It is therefore important to verify and validate a computational model before using it for devising treatment strategies or understanding of complex phenomena.

In this study, a coupled thermal and electromagnetic model was developed using COMSOL. The model was then verified with the analytical model and validated with temperature measurements obtained from gel phantoms. Uncertainty analysis was carried out to estimate the uncertainties in the computed temperature distributions and to determine the parameters that have the most influence on the computed temperature distributions. A realistic rabbit liver model was then built by importing the liver geometry from X-ray computed tomography (CT) imaging data. The temperature distributions achieved due to eddy current heating were computed. Significant rise in temperatures was observed at the edges of the liver. Our model is the first step towards building a robust and validated clinical treatment planning model for magnetic nanoparticle hyperthermia.

5.2 Materials and Methods

5.2.1 Coupled electromagnetic and heat transfer model

Electromagnetic and heat transfer analysis was carried out in COMSOL 5.2a, a multi-physics finite element solver, on a cylindrical geometry of diameter D_{gel} and height H_{gel} representing a gel phantom, as shown in Figure 5.1. Three concentric cylinders were considered to represent the gel phantom, water jacket, and magnetic coil respectively. The

dimensions of the gel phantom were chosen to be close to the size of a human liver [176]. Electromagnetic and heat transfer simulations were simultaneously carried out by coupling Maxwell's equations and transient heat conduction equation. The effect of alternating magnetic field on the cylindrical gel phantom with conductivity σ can be described by Maxwell's equations:

$$\nabla \times H = J \tag{5.1}$$

$$B = \nabla \times A \tag{5.2}$$

$$E = -jfA \tag{5.3}$$

$$B = \sigma E + jfD, \tag{5.4}$$

where J is the current density, A is the magnetic vector potential, E is the electric field intensity, B is the magnetic flux density, and D is electric flux density. Heat transfer in the gel phantom due the heat generated by induced eddy currents can be described by,

$$\rho C_p \frac{\partial T}{\partial t} = k\nabla^2 T + Q_{eddy} \tag{5.5}$$

where ρ is the density, C_p is the specific heat, T is the temperature, k is the thermal conductivity and Q_{eddy} is the heat produced due to eddy currents. The boundary conditions for the electromagnetic modeling, given by a uniform alternating magnetic field of amplitude H and frequency f, was imposed on the outer surface of the coil. For heat transfer modeling, the outer surfaces of the water jacket were subjected to an external forced convection boundary condition with plate averaged heat transfer coefficient, given by

$$q_o = h_{conv}\,(T - T_{ext}) \tag{5.6}$$

$$h_{conv} = h_{water}(L, U, T_{ext}) \tag{5.7}$$

where L is the length of the water jacket, U is the water flow velocity, and T_{ext} is the water temperature. The open faces of the water jacket were modeled by free convection boundary condition given by,

$$q = h_{free}(T - T_{\infty}) \tag{5.8}$$

where T_{∞} is the ambient temperature and h_{free} is the free convection heat transfer coefficient. The thermal and electrical properties used in the simulations are summarized in Table 5.1.

Equations (5.1) – (5.8) were coupled and simultaneously solved using finite element analysis. Sensitivity of the solution to grid size and time step size were carried out to ensure choice of mesh size and time step has negligible effect on the computed temperature. For example, when the number of domain element were changed from 9523 to 17244 elements, the resulting temperature at three locations (gel center, at $r_{gel}/3$ from center, and $2r_{gel}/3$ from center) changed by less than 0.01%.

5.2.2 Verification with analytical model

The analytical expression for the power absorbed by a cylindrical tissue of radius r exposed to an alternating magnetic field of constant amplitude H and frequency f is given by,

$$P_{tissue} = \pi^2 \frac{\mu_0^2 \sigma}{2} f^2 H^2 r^2 \tag{5.9}$$

Where μ_o is the permeability of free space, σ is the electrical conductivity [156,157,177]. This equation is valid only for constant field amplitude H and when $\sqrt{f\sigma\mu_o} r_{max} \ll 1$. The

computational model was verified with the analytical model by comparing the computed temperatures at three locations along the radius and plotted.

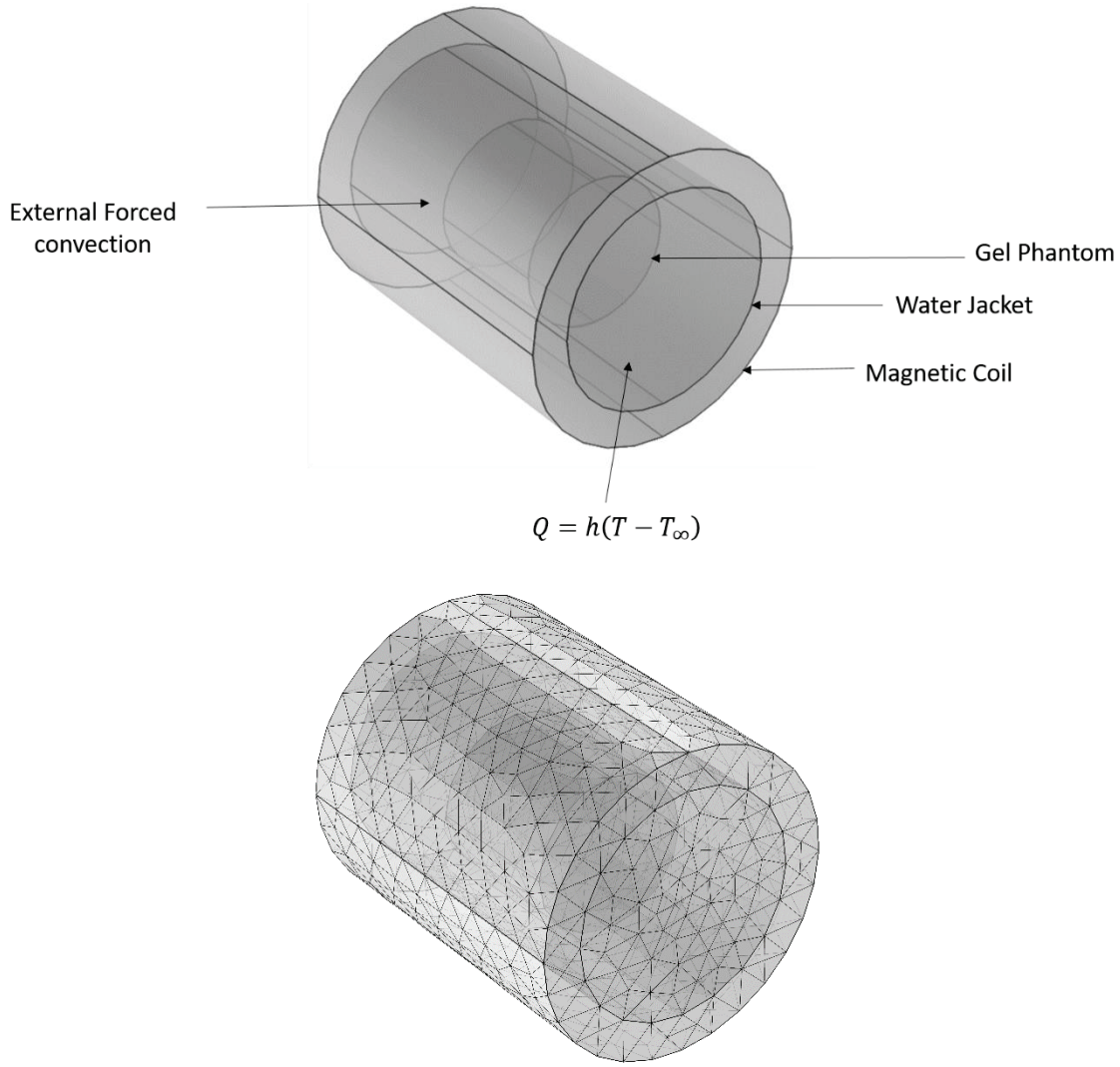

Figure 5.1 Schematic of the computational model considered in the study Computational model consists of three concentric cylindrical domains with the innermost domain being the gel phantom, the second layer being the water jacket and the outermost being the magnetic coil. (b) Sample mesh for the computational domains.

5.2.3 Validation with experimental model – Gel phantom model

Cylindrical gel phantoms were prepared by heating a solution of 1% agarose (Type I-A, low EEO, Sigma Aldrich, Lot #SLBC0292V), with Sodium Chloride, crystal (J. T. Baker, Lot K17586) in 750 ml of distilled deionized water. The solution was heated using a heating plate and a magnetic stirrer until all agar was dissolved in the solution. The solution was then allowed to solidify and cool to room temperature for more than 12 hours to ensure uniform temperature inside the gel. The dimensions of the gel were then measured using a measuring scale. The electrical conductivity of the gel was calculated using the formula [178],

$$\sigma[\frac{S}{m}] = 215 \times \frac{(grams\ of\ NaCl)}{(solution\ volume,\ mL)} + 0.0529 \qquad (5.10)$$

5.2.4 Alternating magnetic field system

The AMF system consists of three main components: a power supply, an external capacitance-impedance matching network, and a modified Maxwell coil. The AMF system has been well described by Attaluri et al [179]. Briefly, it consists of three-piece induction coil set connected to a power supply. The power supply is a 120-kW induction heating system (PPECO, Watsonville, CA) that provides alternating current to a resonant circuit with variable frequencies (135 – 440 kHz). The external impedance matching network (AMF Life Systems, Auburn Hills, MI) was adjusted for stable oscillations at 155 ± 10 kHz. The uniformity of the field generated was measured and it was shown that the variation in the generated field was < 10 % at ± 5 cm along the length of the coil and in the radial direction. A polyacrylic water jacket was inserted into the coil to minimize the heat

transfer between the gel and the coil. It was connected to a chiller (ThermoFlex, Thermo Fisher Scientific, Newington, NH) which was maintained at 20 °C.

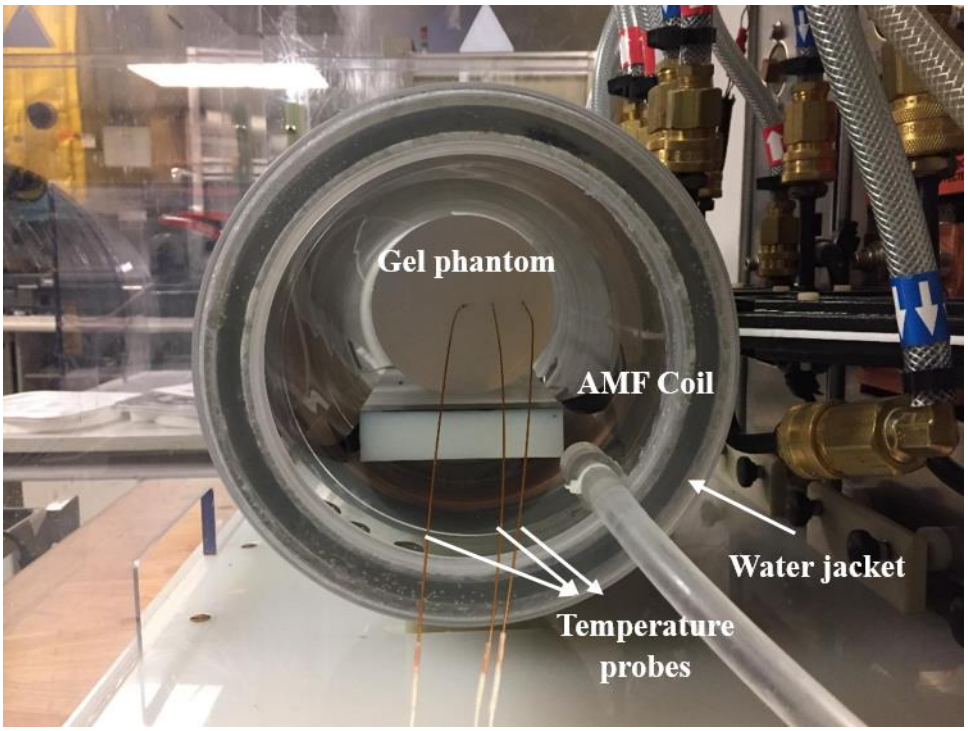

Figure 5.2 Experimental setup for the gel phantom experiments. Agar gel phantoms were inserted in the center of a 20 cm horizontal modified Maxwell coil inside a water jacket with temperature controlled at 25 °C. Temperatures were measured at the center of the gel, r/3, and 2r/3 distance along the radius of the gel, where r is the gel radius.

The gel phantom was allowed to equilibrate to room temperature for more than 12 hours before inserting it into the coil. The gel was then inserted into the coil and exposed to a constant alternating magnetic field of amplitude 6.96 kA/m (peak) and at fixed frequency 160 kHz (observed) for 15 minutes. Temperatures were measured radially at three locations (r = 0, $r_{gel}/3$, $2r_{gel}/3$) at the center of the gel (H/2) using optical fiber temperature probes (FISO, Quebec, Canada). These measurements were then used to compare with the computed temperatures for validation of the computational model.

5.2.5 Uncertainty analysis

Uncertainty exists with any measurements conducted and are often reported for experimental data. It is therefore important to consider uncertainties associated with the parameters when they are applied to mathematical models. Often, average values are considered for mathematical models which might lead to difficulty validating mathematical models using experimental data. Sensitivity analysis is required to evaluate the propagation of measurement uncertainties into mathematical models. It becomes more critical when experimental data are used to validate the results of a computational model, because the uncertainties can become highly significant. Rabin [180] proposed a general model for the propagation of uncertainty in measurements into heat transfer simulations and applied it to a cryosurgery model. We apply the same model to compute the uncertainty associated with the computed temperatures due to the uncertainties associated with the input parameters.

In our current model, the temperature T generated in the gel due to eddy current heating depends on the gel dimensions, like diameter (D_{gel}) and height (H_{gel}), thermal properties like density (ρ), thermal conductivity (k), and specific heat capacity (C_p), electrical conductivity (σ), applied magnetic field conditions like magnetic field strength (H), frequency (f), the gel position inside the coil determined with respect to the coil center given by radial distance of the center of the gel from coil center (x_pos), and along the axis of the coil (y_pos), and the location of the probe. To compute the uncertainty in the temperature attained in the gel we must consider the uncertainty associated with each of the above input parameters. The mean values of the parameters were based on recorded data and/or applied conditions. The mean values of the parameters and their uncertainty values are shown in Table 5-1. For the applied magnetic field and frequency, the

uncertainty range was determined from the coil specifications. For the electrical conductivity of the agar gel phantom with salt, the uncertainty was assumed to be 5% based on data from Bennett [178]. The density of the gel was determined by weight and volume measurements and the uncertainty was based on the measured variations. The specific heat capacity of the gel was taken from [181]. The thermal conductivity of the gel and the uncertainty values were based on data from Zhang et al. [182]. The diameter and height of the gel were measured using a ruler and the uncertainty was taken to be half of the lowest distance marker (1 mm). The position of the gel with respect to the coil was measured using a ruler and the uncertainty of 5 mm was chosen based on experience. The location of probes was measured using a ruler placed on the top of the gel and the corresponding uncertainty was chosen based on the diameter of the fiber-optic probe [183], the least count of the ruler and the gel structure. The ambient temperature was measured using a standard room thermometer and the water jacket temperature was measured using a fiber-optic temperature probe.

The temperature at any time can be represented as a function of all input model parameters:

$$T = f(p_1, p_2, p_3, \dots\dots, p_n) \tag{5.11}$$

here $p_1, p_2, p_3, \dots\dots, p_n$ are the individual parameters.

Assuming the value of each parameter is independently associated with an uncertainty δ, the uncertainty in the temperature distribution can be calculated as,

$$T \pm \delta T = f(p_1 \pm \delta p_1, p_2 \pm \delta p_2, p_3 \pm \delta p_3, \dots\dots, p_n \pm \delta p_n) \tag{5.12}$$

The uncertainty in the temperature distribution is then given by [180,184],

$$\pm\delta T = \sum_{i=1}^{n} \frac{\partial f}{\partial p_i} \delta p_i \tag{5.13}$$

The partial derivatives can be computed by:

$$\frac{\partial f}{\partial p_i} \delta p_i \cong \frac{T_i - T_0}{\Delta p_i} \delta p_i = [T_i - T_0]_{\Delta p_i = \delta p_i} \equiv \Delta T_i \tag{5.14}$$

The overall uncertainty can then be calculated as [180,184]:

$$\delta T = \sqrt{\sum_{i=1}^{n} (\frac{\partial f}{\partial p_i} \delta p_i)^2} \tag{5.15}$$

The effect of uncertainty in each individual parameter on the temperature distribution was calculated individually by varying each parameter individually using values shown in Table 5-1. The uncertainty at each of the probe locations was computed. After this, the top two parameter uncertainties that produce the highest uncertainty in the computed temperatures were identified. Based on this, the maximum uncertainty in those parameters was considered while the remaining parameters were fixed at nominal values. The temperature distributions were then computed at each of the probe locations and the uncertainty in probe location (±3 mm) was also considered. The initial temperatures were adjusted to match with the measured values. If the difference between any of the three computed temperatures at each probe location (T (probe), T (probe+3mm), and T (probe-3 mm)) and the measured temperature was < 5%, then the computational model is said to be validated.

Table 5-1 Mean parameter values and their uncertainties considered in the simulation

Parameter	Mean value	Uncertainty
Magnetic field amplitude, H (kA/m)	6.96 kA/m	±10% [179]
Frequency (kHz)	160	±10% [179]
Electrical Conductivity (S/m)	0.3325 [178]	±10% [178]
Density (kg/m^3)	960	±5%
Specific heat capacity (J/kg-K)	3900 [181]	±10% [181]
Thermal conductivity (W/m-K)	0.566 [182]	±5% [182]
Diameter of gel (m)	0.103	±0.5 mm
Height of gel (m)	0.093	±0.5 mm
Position along radius of gel (cm)	0	±5 mm
Position along axis of gel (cm)	7.0	±5 mm
Probe location (cm)	0.05, 1.85, 3.45	±3 mm
Water Jacket Temperature (°C)	20	±0.5 °C
Ambient Temperature (°C)	20	±1 °C

5.2.6 3D models of rabbit liver from CT images

X-ray computed tomography (CT) images of a rabbit liver, which is part of our ongoing liver cancer study, was used to build a 3D model in this study. The CT scan experiments were conducted by Dr. Eleni Liapi and Dr. Sahar Mirpour. Briefly, adult white New Zealand rabbits were housed in an Association for Assessment and Accreditation of Laboratory Animal Care (AAALAC) - accredited facility in compliance with the Guide for the Care and Use of Laboratory Animals and procedures were approved by the Johns Hopkins Institutional Animal Care and Use Committee (IACUC). White New Zealand rabbits were selected for their relevance to intra-arterial procedures and liver tumor

imaging. At specific time points, each animal was selected for VX2 tumor implantation in the liver and subsequently underwent CT imaging.

The CT images of rabbit were first imported into 3DSlicer [185], an open source software for visualization and medical image computing. 3DSlicer allows simultaneous tri-axial display of the sagittal, coronal, and transverse medical images, as well as a 3D view of the segmented structure. Manual segmentation was done to extract the liver from the other organs. The gray level value for each of the tissues was determined by pointing the crosshairs on the input image in the region of interest. Then, manual segmentation was done by inputting the lower and higher threshold gray level value in the processing window and the smoothness parameter was set to maximum. Since the gray level values of the soft tissue organs are very close to each other, automatic segmentation does not yield a desirable result.

After segmentation, the files were converted into *.stl* format and then imported into MeshLab® [186], for meshing. Surface treatment was necessary to smooth sharp edges and artifacts obtained in reconstructed geometries to ensure convergence in finite element simulations. The imported liver geometry was first meshed and then it was smoothed by using a Laplacian mesh smoothing method. Several iterations of mesh smoothing were carried out to ensure a well smoothened geometry and convergence in finite element simulations. The meshed geometry was exported and saved as a *.stl* file. It was then imported into COMSOL Multiphysics 5.2a, a commercially available finite element solver, using the mesh import functionality. The imported mesh was then converted into a geometry using the convert mesh to geometry method available and the resulting geometry

was again meshed to conduct finite element heat transfer and electromagnetic simulations. The workflow of building 3D models from CT scan images is shown in Figure 5.3.

Coupled electromagnetic and heat transfer simulations were then carried out on the liver model and the geometry considered is shown in Figure 5.4. The computational geometry mainly consists of three domains: 1. the extracted liver domain, 2. spherical tumor inside the liver, and 3. muscle tissue surrounding the liver. The complete geometry was exposed to a constant field of amplitude of 19.89 kA/m at fixed frequency of 160 kHz.

Heat transfer in the tissues were modeled using the Pennes bioheat equation [81], given by

$$\rho_n c_n \frac{\partial T_n}{\partial t} = k_n \nabla^2 T_n + \rho_b c_b \omega_{b,n} \left(T_b - T_n \right) + Q_{m,n} + Q_p \tag{5.16}$$

Where n and b represent tissue (liver, n =1; tumor, n =2; muscle, n=3) and blood; respectively. ρ_n, c_n, k_n, T_n, $Q_{m,n}$ denote the density, specific heat, thermal conductivity, local temperature, and metabolic heat generation rate, for either tumor or healthy tissue and t is the heating time. ρ_b, c_b, $\omega_{b,n}$, T_b denote density, specific heat, perfusion rate, and temperature, of blood respectively. Constant perfusion was considered in the current study for ease of computation and to gain preliminary insights into the temperature distributions. The thermal and electrical properties of the tissues considered in the model were given in Table 5-2 and Table 5-3.

.

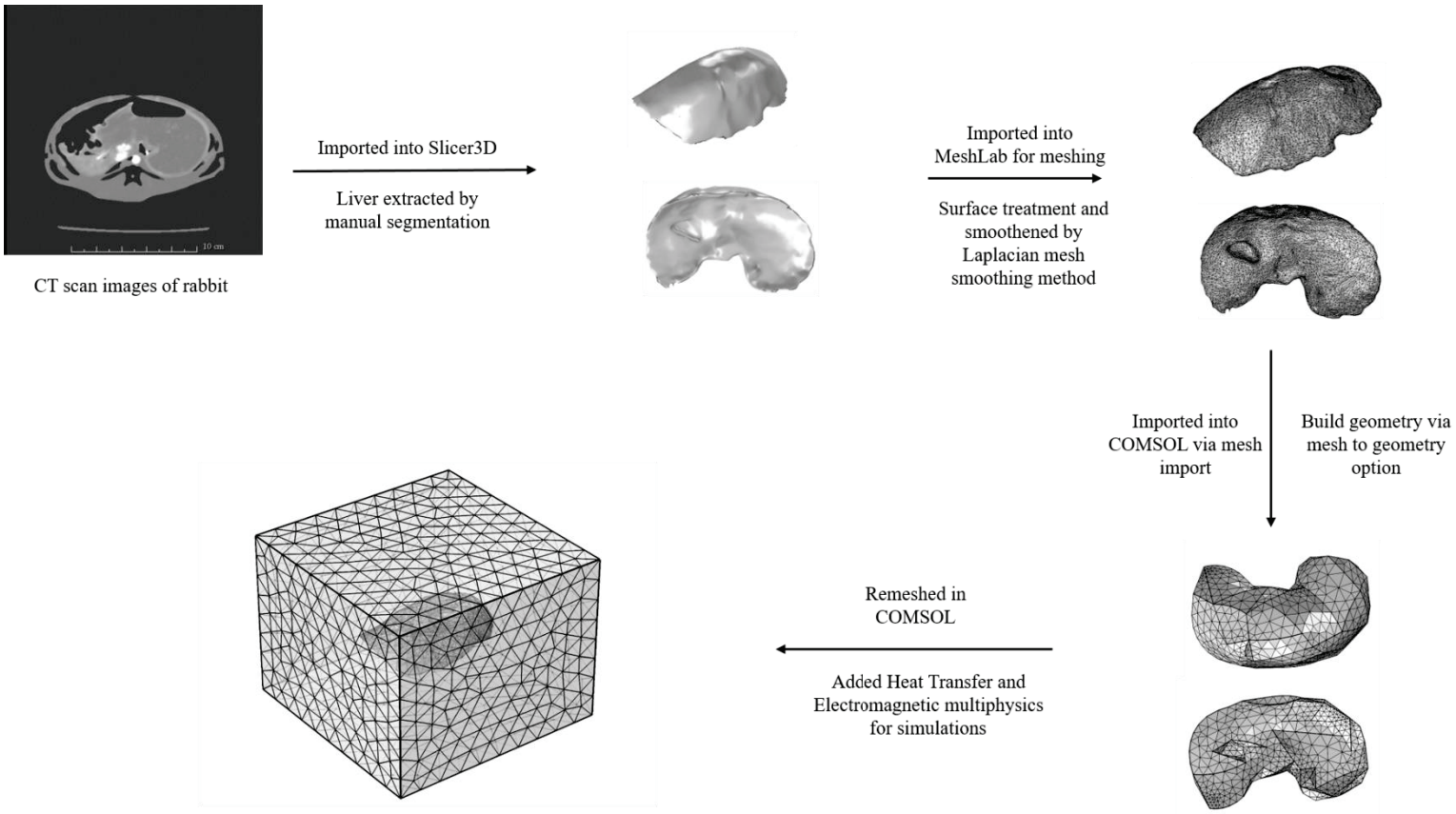

Figure 5.3 Workflow for building 3D models of rabbit liver from CT scan images CT scan images of rabbit liver were first imported into Slicer3D and the liver was extracted by manual segmentation. The file was then imported into MeshLab for meshing and smoothing of sharp edges to allow for import into finite element software for simulations. File was then imported into COMSOL via mesh import option and converted into geometry. The geometry is then remeshed in COMSOL and multiphysics is added for simulations.

Table 5-2 Thermal properties of tissues considered in the present study

	Density, ρ (kg/m^3)	Specific heat, c (J/kg K)	Thermal conductivity, k (W/m K)	Blood Perfusion rate, ω (1/s)	Metabolic heat generation rate, Q_m (W/m^3)
Liver	1079 [122]	3540 [122]	0.52 [122]	0.018 [167]	14414 [168]
Tumor	1079 [122]	3540 [122]	0.52 [122]	0.018 [167]	72070 [74]
Muscle	1090 [122]	3421[122]	0.49 [122]	0.0027 [74]	684.2 [74]
Blood*	1060 [125]	3770 [125]	N/A	N/A	N/A

*Temperature of blood (T_b) was fixed at 37ºC [125]. (N/A – not applicable)

Thermal boundary conditions considered for this model are: constant core body temperature of 37 °C at all the outside boundaries of the muscle domain and the continuity of temperature and heat flux at the domain interfaces. For the electromagnetic boundary conditions, a constant magnetic field of 19.89 kA/m (peak) at a fixed frequency of 160 kHz is applied on the outer boundaries of the muscle layer. Simulations were carried out for a treatment duration of 20 min at constant amplitude and the resulting temperature distributions were computed.

Table 5-3 Tissue electrical properties used in the simulations

	Electrical conductivity, σ (S/m)	Permittivity (1)
Liver	0.0954 [122]	6090 [122]
Tumor	0.0954 [122]	6090 [122]
Muscle	0.373 [122]	7110 [122]

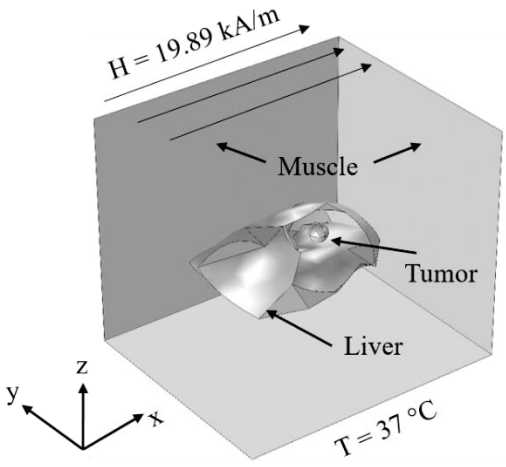

(a)

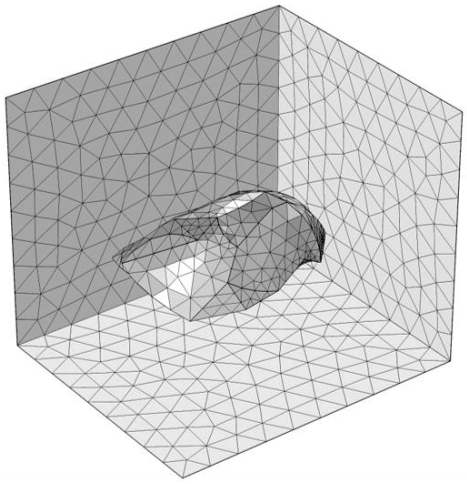

(b)

Figure 5.4 Schematic of the computational model used for simulations (a) Isometric projection of the geometry showing the liver, tumor and muscle tissue. Thermal and magnetic field boundary conditions are shown. (b) Sample mesh for the computational model shown in (a).

5.3 Results and Discussion

For clinical implementation of magnetic nanoparticle hyperthermia, it is important that the nanoparticles generate substantial heat for tumor thermal damage. The heat generated by nanoparticles increases with increasing applied magnetic field amplitude and frequency as stated previously. Thus, it can be thought of that increasing the applied field and frequency can help in attaining therapeutic temperatures. However, the interaction of surrounding healthy tissue with the applied magnetic field results in unwanted non-specific eddy current heating which can effect body thermoregulation leading to perfusion changes which in turn can effect tumor heating. This places limits on the range of applied magnetic field amplitudes and frequencies that can be used [61,62]. Additionally, monitoring and measurement of eddy currents and eddy current heating in *in vivo* studies is challenging [187]. Coupled thermal and electromagnetic model can help us estimate the temperatures due to eddy current and can help develop treatment strategies to reduce it.

Accuracy of computer simulation models and confidence in their results needs to be critically assessed before they can be used for prediction or research. Validation and verification are the primary methods in gaining confidence in the results and quantifying it [175]. In this study, we verify our computational model with the available analytical solution for temperature distribution in a cylinder exposed to an alternating magnetic field. We then validate our computational model with experimental data obtained from gel phantoms exposed to an alternating magnetic field.

5.3.1 Verification with analytical model

The temperature distribution in the computational cylindrical phantom after 15 min exposure to a constant alternating magnetic field of 13.94 kA/m at a fixed frequency of 160 kHz is shown in Figure 5.5. It can be observed that temperature increases away from the center of the phantom, with the lowest temperatures at the center and highest temperatures at the periphery. This shows that more heat is being generated in regions away from the phantom center compared to center of the phantom. This trend is indeed consistent with that predicted by the analytical solution given by equation 5.9, where the heat generated is proportional to the square of the distance from the center of the field.

Equation 5.9 gives the analytical expression for the heat generated by a body exposed to an alternating magnetic field. Equation 5.9 is valid for cylindrical domains exposed to a constant magnetic field and if $\sqrt{f\sigma\mu_o}r_{max} \ll 1$ [156,157,177]. In our case, the value of $\sqrt{f\sigma\mu_o}r_{max}$ is 0.04 << 1. Hence, the analytical solution can be used to verify our computational model. The computed temperatures at three locations in the phantom, center, *r/3* and *2r/3* were compared to temperatures calculated using the analytical expression and plotted in Figure 5.6. Excellent agreement can be seen between the computed temperatures and the temperatures calculated using the analytical expression, thus verifying the computational model.

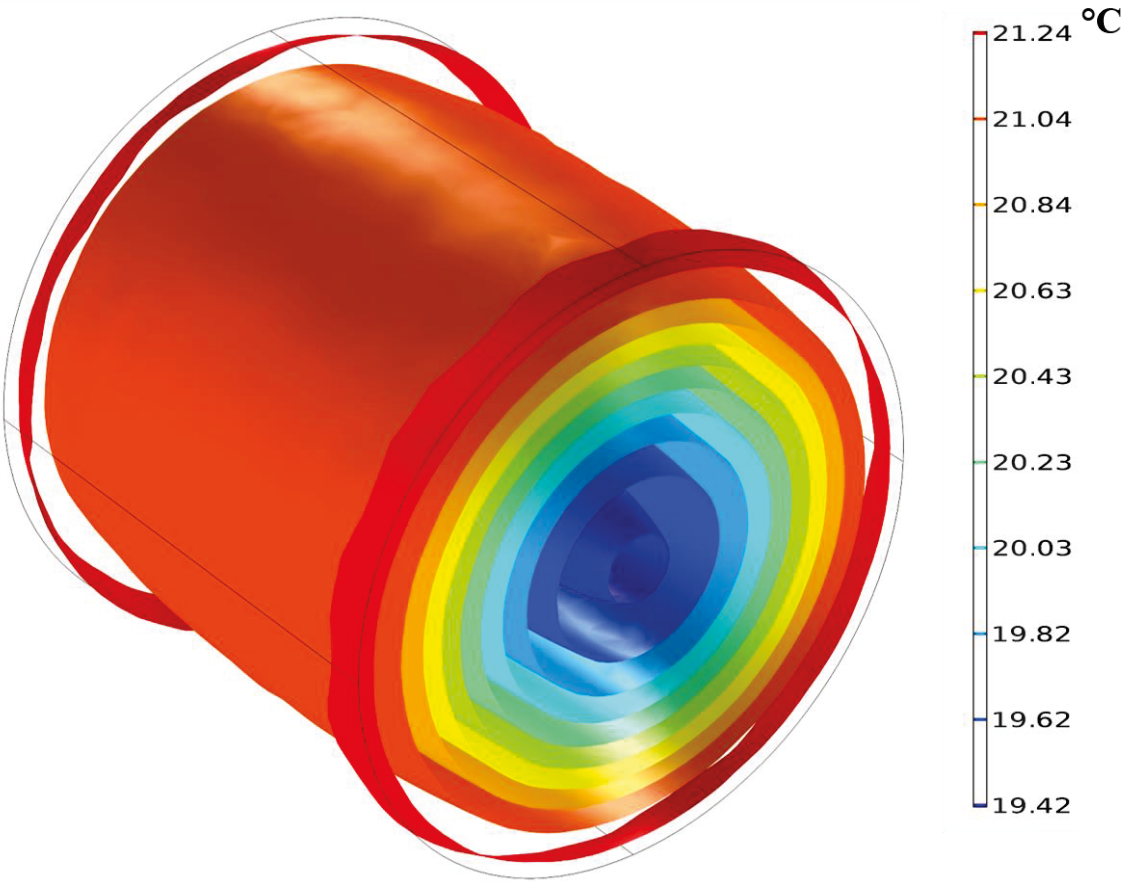

Figure 5.5 Isothermal contours showing the temperature distributions achieved inside the phantom after 15 min of exposure to an alternating magnetic of 13.97 kA/m at a fixed frequency of 160 kHz.

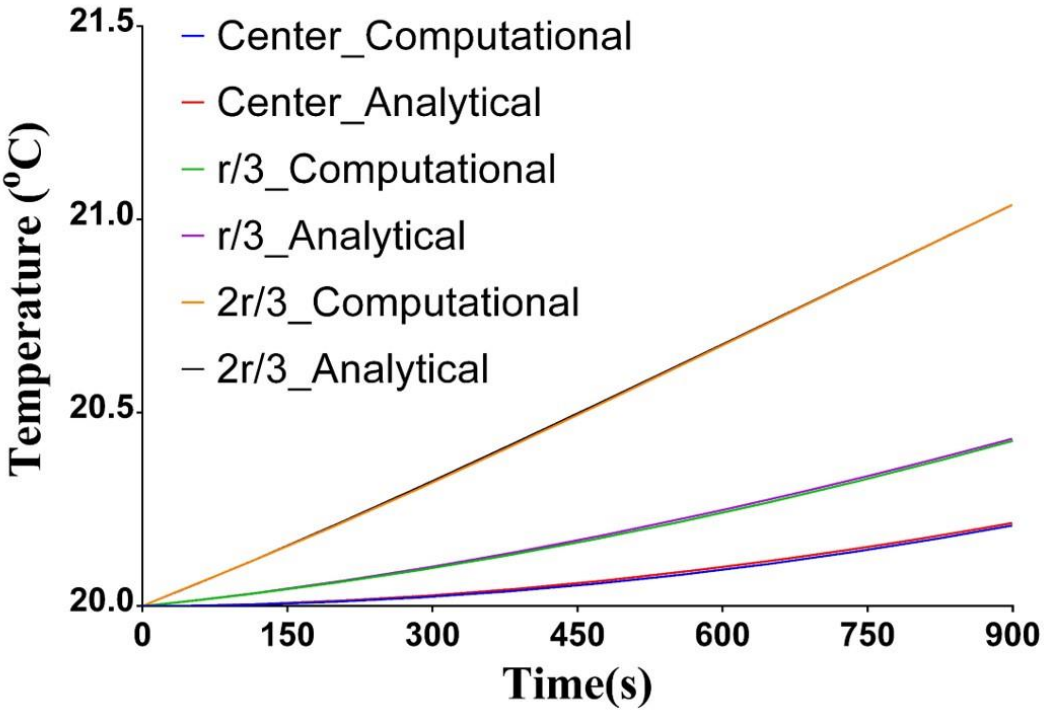

Figure 5.6 Verification of computational model with analytical expression Comparison of computed temperatures with the coupled electromagnetic and heat transfer model with temperatures calculated using the analytical expression for power absorption at center of gel shows excellent agreement therefore verifying the model.

5.3.2 Uncertainty analysis and validation with experimental model

Validation of computational model is done by comparing the data from simulations with experimental data. However, one of the main challenges is the uncertainty present in the input parameters used in simulation. Neglecting the uncertainties associated with the measured data, can yield incorrect results of either invalidating a correct model or validating an incorrect model [188]. Also, uncertainty propagation from parameters is often neglected in bioheat transfer simulations as only the average values are used [180]. However, estimation of uncertainties for all the parameters would be impractical and would even be expensive. It is thus important to identify the parameters that are most important

or that can influence the outcome significantly. Using uncertainty analysis the parameters to which the predicted temperature distribution is most sensitive to can be determined.

Uncertainty analysis was carried out for all the relevant parameters in the simulation as shown in Table 5-1. The corresponding uncertainties were calculated based on the procedure as explained in section 5.2.5. The uncertainty in computed temperatures due to individual parameter uncertainties and the overall uncertainty was plotted in figure 5.7. Temperature uncertainty was plotted at three locations, center of the phantom, *r/3* distance from the phantom center and *2r/3* distance from phantom center. It can be seen that the uncertainty in the temperature is most sensitive to the parameters that influence the heat generation term followed by parameters that influence heat transfer. The parameters that result in heat generation are applied magnetic field H, frequency f, probe location, and electrical conductivity σ. The parameters that influence heat transfer are density ρ, specific heat capacity C_p, thermal conductivity k, and temperatures of water jacket and ambient. As predicted the uncertainties in the parameters that influence generation have the most effect on the computed temperatures. The rate of heat generation, given by equation 5.9, is proportional to the square of the product Hf. Hence, variability in either of them has a strong effect on the computed temperatures. Of the other parameters, the next sensitive parameter is the uncertainty in probe placement. This can also be predicted as the heat generation term is also directly proportional to the square of the distance (r) from the center. The variability in electrical conductivity has the next important effect on the computed temperatures. Of the parameters that influence the heat transfer in the gel, the variability in specific heat and density had the most effect on the computed temperatures. When the

overall uncertainty is compared for each of the three locations, the uncertainty increases significantly as we move away from the phantom center.

After this we compared the computed temperatures with the experimental values for validation of the computational model. If the measured temperatures fall within the range of computed temperatures (± 5%) with corresponding uncertainties at a given location, then the model is said to be validated. This was satisfied for all the three probe locations. However, we wanted to test the model more rigorously to compare with experimental data. To do this, we chose to find the parameter values which fit the computed temperatures at the center to the measured values (difference of < 5%) and for the same parameter values we compared the computed and measured at the other two locations. The parameter values were the mean values reported in Table 5-1 for all the parameters, except for H, Cp, and, ρ. The uncertainty in probe placement was still shown as this was independent of the gel properties and coil properties. The computed and measured temperatures were then plotted for each of the locations along with probe placement uncertainties and shown in Figure 5.8. Excellent agreement can be observed between the computed and measured values with the maximum absolute error <2 % at each of the probe location. This validates our computational model.

5.3.3 3D models of rabbit liver

The verified and validated coupled thermal and electromagnetic model was then implemented on a 3D liver model generated from CT scan images as shown in Figure 5.4. Simulations were performed for a constant magnetic field of 19.89 kA/m (peak) at a fixed frequency of 160 kHz leads for 20 min. The resulting temperature distributions after 100s and 1200s are shown in Figure 5.9. Temperature gradients can be observed in the liver,

with the temperatures lower closer to the liver center and increasing radially away with the maximum temperatures achieved on the liver edges. Even after 100s of exposure, considerable heating occurs at the liver edges with a temperature increase of ~ 1.5 °C. After 20 min of exposure, the temperatures further increase with a maximum of 40.81 °C observed at the liver edges. Thus, mild hyperthermic temperatures (39 – 41 °C) are obtained in the liver due to eddy current heating. Our model successfully simulates the eddy current heating in large organs such as liver and highlights the importance of considering heating due to eddy currents when optimizing magnetic nanoparticle hyperthermia for clinical studies.

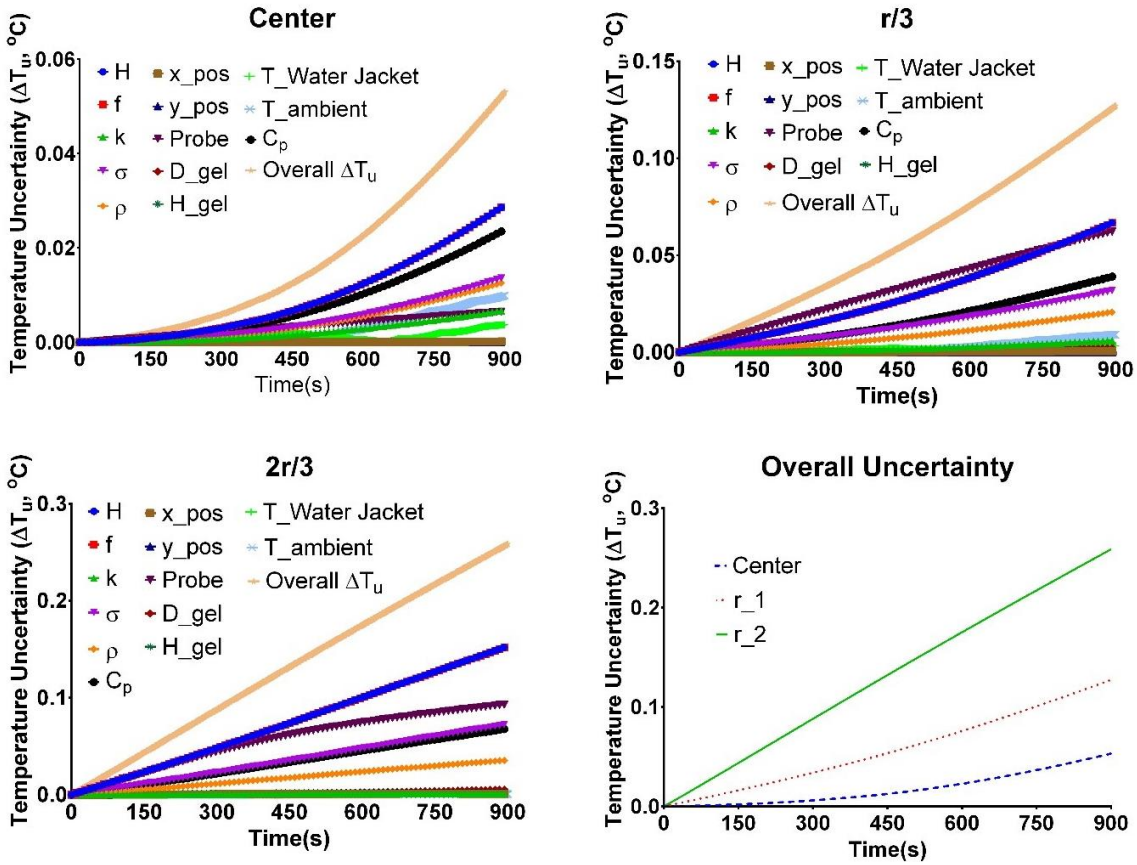

Figure 5.7 Variation of uncertainty in temperatures measured at the center, *r/3*, and *2r/3*, with time, due to uncertainty in individual parameters identified in Table 5-1. The variation in overall uncertainty of temperature with time was plotted for each probe location. It can be seen that the computed temperatures are most sensitive to the uncertainties in applied field (*H*), frequency (*f*), probe placement (*Probe)*, specific heat capacity (C_p), electrical conductivity (σ) and gel density (ρ).

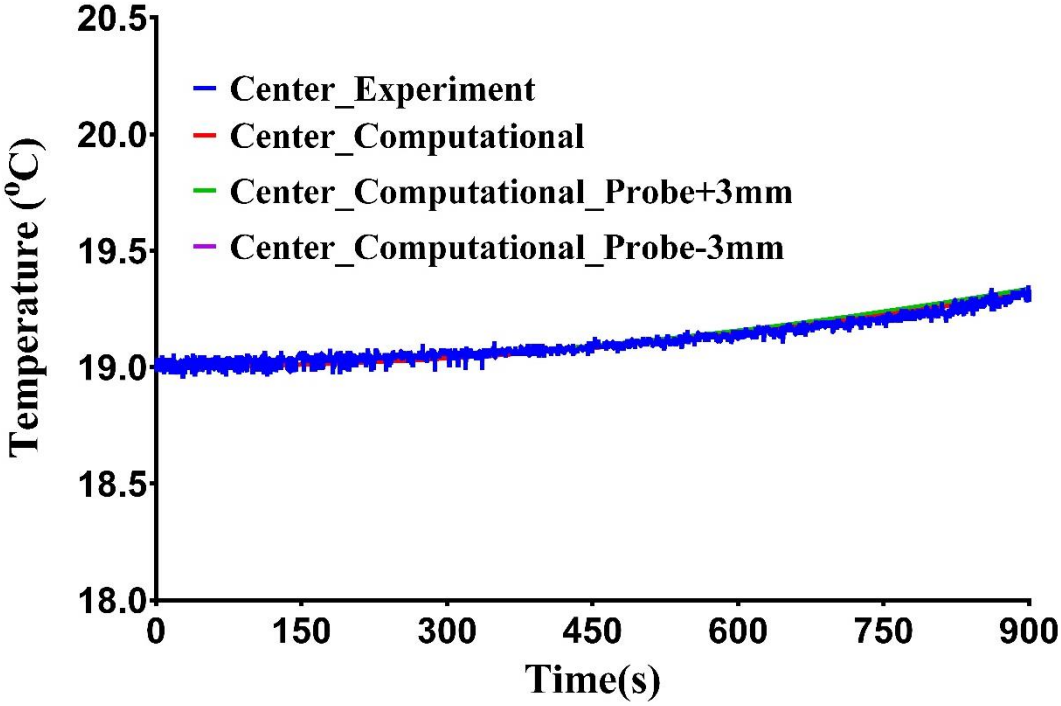
Center_Experiment
Center_Computational
Center_Computational_Probe+3mm
Center_Computational_Probe-3mm
Temperature (°C)
20.5
20.0
19.5
19.0
18.5
18.0
0
150
300
450
600
750
900
Time(s)

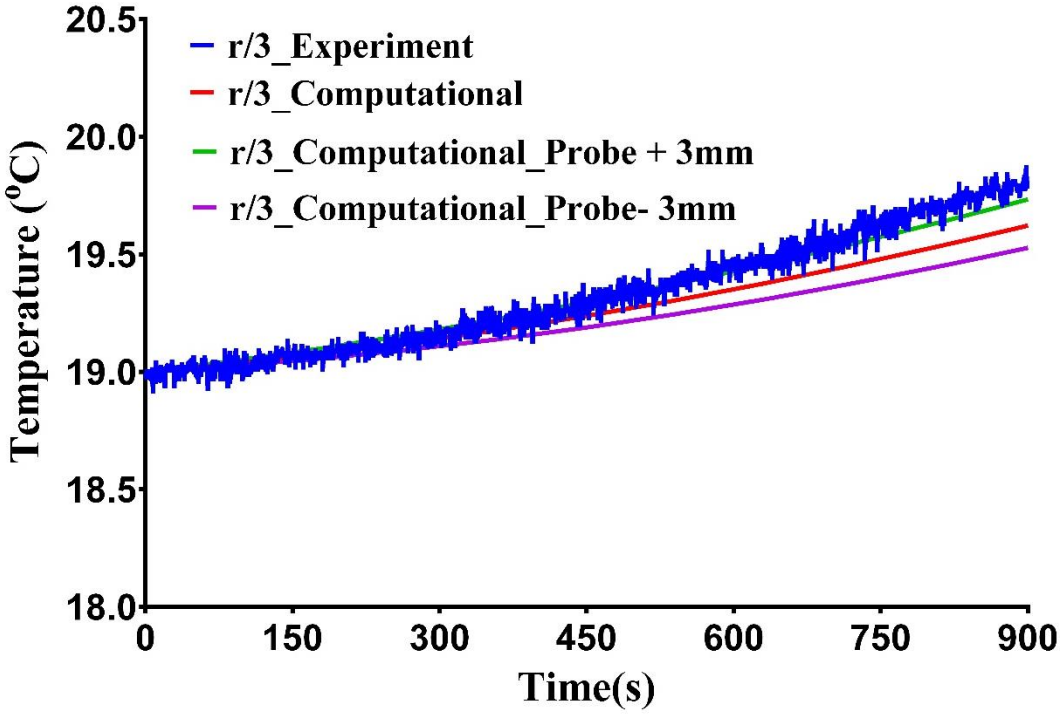
r/3_Experiment
r/3_Computational
r/3_Computational_Probe + 3mm
r/3_Computational_Probe- 3mm
Temperature (°C)
20.5
20.0
19.5
19.0
18.5
18.0
0
150
300
450
600
750
900
Time(s)

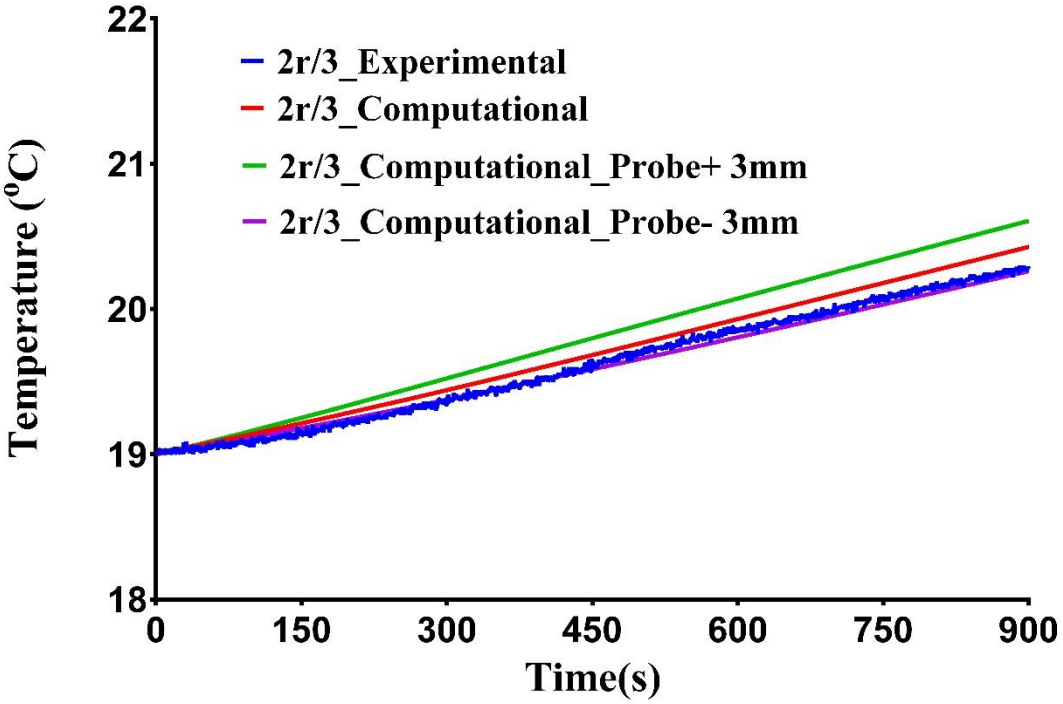

Figure 5.8 Validation of computational model with experimental data Comparison of measured temperatures and computed temperatures at (a) center of the gel, (b) r/3 along the radius of the gel, (c) 2r/3 along the radius of the gel, where r is the gel radius. Excellent agreement between the computational and measured temperature is observed confirming the validity of the computational model. The effect of uncertainty in probe placement (given by ±3 mm) on the computed temperatures is also shown. The maximum absolute percent error is < 2% for all the three locations compared to the measured data.

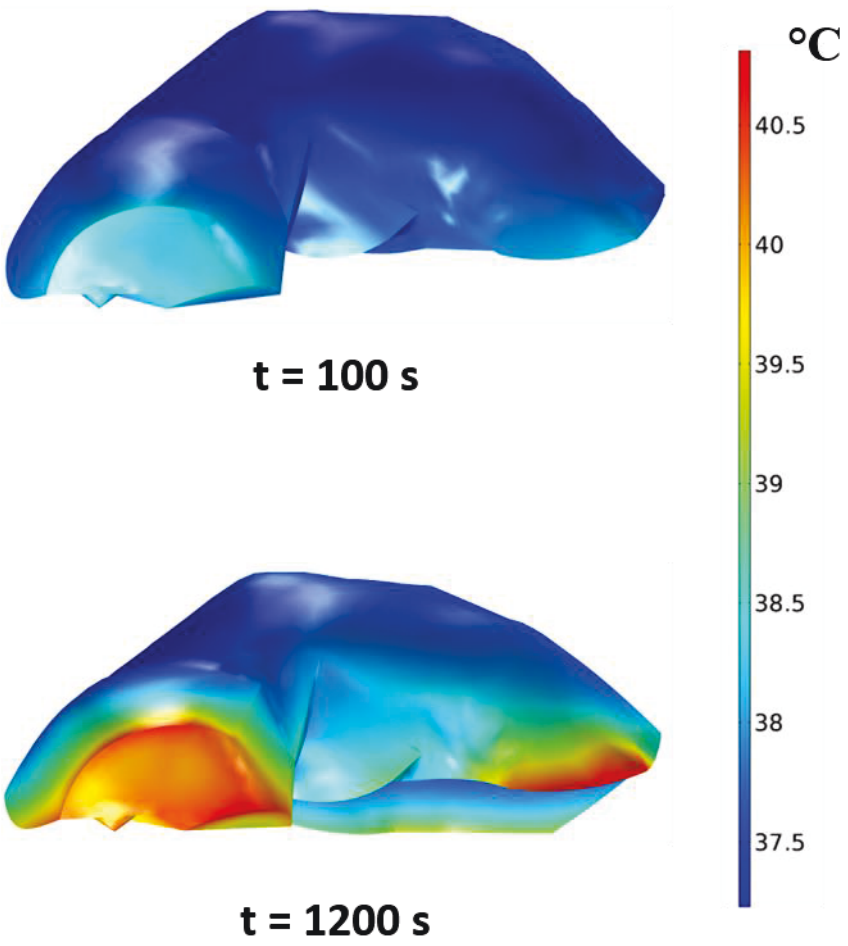

Figure 5.9 Temperature distribution in the liver after 20 min of exposure to an alternating magnetic field of 19.89 kA/m (peak) at a fixed frequency of 160 kHz. Elevated temperatures can be observed at the edges of the liver with temperature of 40.81 °C at the end of 20 min of exposure

5.4 Summary & Conclusions

In summary, we developed a coupled thermal and electromagnetic model in COMSOL for simulating the temperature distribution achieved due to eddy current heating during magnetic nanoparticle hyperthermia. Maxwell's equations were used to model the electromagnetic interaction while the thermal component was modeled using the transient heat conduction equation. Finite element analysis was used to solve for the resulting

temperature distribution. This model was then verified using the analytical solution (equation 5.8) by implementing it on simple cylindrical model. Temperatures were computed at three locations (center, *r/3,* and *2r/3*) and compared to the calculated temperatures using the analytical solution. Excellent agreement was obtained between the computational model and analytical model verifying our computational model.

Uncertainty analysis was conducted to determine the variation in computed temperatures with uncertainty in input parameters. We identified that the variability in parameters in the heat generation term has the most influence on the computed temperatures followed by the parameters in heat transfer terms. Overall uncertainty increases with increase in distance from the gel center. The computed temperatures were then compared with the measured temperatures in gel phantom. The difference in the computed and measured temperatures was < 2% validating our computational model.

The model was then implemented on a realistic rabbit liver model developed from CT images. Pennes bioheat transfer equation was used to model the macroscopic heat transfer in liver tissue. Simulations were performed for a constant field with amplitude of 19.89 kA/m (peak) and fixed frequency of 160 kHz. Simulation show a significant heating at the edges of liver with temperatures reaching up to mild hyperthermia range of ~ 40.81 °C.

Our verified and validated model lays the foundation for developing effective treatment strategies optimizing tumor therapeutic thermal dose and minimizing the off-target eddy current heating. This model can also help in designing new magnetic coils so as to minimize off-target tissue heating. The model can further be improved by implementing temperature-dependent perfusion instead of constant perfusion model.

Temperature dependent perfusion can take into account the thermoregulation function of the human body which can further help in designing better treatment strategies. This model can be further used to the test limitations of the modulated power heating method proposed in the previous chapters and help in improving it to scale for larger organs.

Chapter 6
Thermal and magnetic characterization of nanoparticle formulations for image guided hyperthermia

In this chapter, thermal and magnetic properties of dual contrast magnetic iron oxide nanoparticle formulations were characterized. The dual contrast magnetic iron oxide nanoparticle formulations considered in this chapter were magnetic iron oxide nanoparticles combined with lipiodol®, an ethiodized oil. These formulations have both CT and MRI imaging capabilities combined with potential to generate heat when exposed to

an alternating magnetic field. These can be used in intra-arterial therapies such as transarterial chemoembolization (TACE) to administer chemotherapy and hyperthermia simultaneously for primary liver cancer. The heating potential of these new lipiodol nanoparticle formulations was extensively characterized by measuring their thermal properties at fixed frequency with different magnetic field amplitudes. These were then compared to the original aqueous formulations (as-synthesized) for assessing the differences between both the formulations. Bulk magnetic properties of both aqueous and lipiodol formulations were measured and compared. Lipiodol formulations of magnetic iron oxide nanoparticles showed higher temperatures compared to aqueous formulations at different applied magnetic field amplitudes at fixed frequency. Comparison of thermal properties show that lipiodol formulations have lower volumetric heat capacities compared to aqueous formulations resulting in higher rise in temperatures despite reduction in SLP. Magnetization of lipiodol formulations was significantly lower compared to aqueous formulations at all temperatures showing that lipiodol has a shielding effect on the magnetic nanoparticles. These results highlight the importance of evaluating the heating performance of any new nanoparticle formulations by measuring the change in both the thermal and magnetic properties.

6.1 Introduction

Magnetic nanoparticles have gained significant importance in the recent past for their use in biomedical applications [38]. The ability to control their size, responsiveness to magnetic fields and biocompatibility have led to their use in many medical applications such as imaging [189,190], therapy [43,49,50], and drug delivery [191]. Magnetic nanoparticle hyperthermia (mNPH) is the heating of tissues with magnetic nanoparticles

which generate heat when exposed to an alternating magnetic field [51]. The ability to selectively heat tumor tissue compared to other hyperthermia modalities such as microwave, whole body hyperthermia etc., makes mNPH a very attractive treatment modality [37]. The biological rationale, that thermal damage to cells is complementary to DNA damage, plus the effects of elevated temperature on tumor blood perfusion and oxygenation, support the use of hyperthermia as a combined therapy modality along with radio- or chemo-therapies [9,10,13,192–196].

Primary liver cancer is the second leading cause of cancer-related death in the world and fifth most frequently diagnosed in men in the US [1,197]. Patients are often diagnosed at advanced stages of cancer resulting in limited non-surgical palliative treatment options. Image guided therapies for primary liver cancer, such as TACE, are minimally invasive treatment options that offer selective tumor targeting by delivering drugs through the hepatic artery [198–201]. Combining magnetic nanoparticles with chemotherapeutic drugs and delivering them through TACE allows for combination treatment using hyperthermia and chemotherapy. Several efforts were carried out to implement magnetic nanoparticle hyperthermia with TACE [66,128,129,202–205]. The principal challenges identified were the lack of sufficient heating from the nanoparticles and the MRI artefacts created by nanoparticles [129]. Recent studies show significant increase in heat generation by nanoparticles [53,55,66]. Attaluri et al. [66] developed new nanoparticle formulations and conducted a feasibility study to show that these nanoparticle formulations generate significantly higher temperatures. These nanoparticle formulations were made combining the BNF nanoparticles with ethiodized oil (Lipiodol®) [206]. It was shown that these nanoparticle formulations exhibit both CT and MRI contrast and generate higher

temperatures when compared to BNF nanoparticles without lipiodol. However an extensive characterization of thermal and magnetic properties was not done. The success of any nanoparticle formulation would depend on efficient synthesis, complete characterization, and performance under operating conditions [59]. Thus it is important to characterize the thermal properties and magnetic properties of these formulations and compare them with their original samples to understand the effect of lipiodol on the nanoparticles.

The aim of the current work was to determine the thermal and magnetic properties of lipiodol formulations of nanoparticles which can offer both CT and MRI imaging capabilities. Two magnetic iron oxide nanoparticles and their lipiodol formulations were considered. The heating rates of these four nanoparticle formulations were determined by measuring the change in temperature at different amplitudes. The higher rise in temperatures observed for BNF-lip in comparison to BNF-water is mainly attributed to the change in thermal properties of solvent. SLP of lipiodol formulations of both BNF and JHU nanoparticles was lower than the corresponding aqueous formulations. Bulk magnetization measurements show a significant reduction in magnetization and changes in approach to saturation magnetization for both BNF-lip and JHU-lip compared to their respective aqueous formulations. These results show that the changes in magnetic and thermal properties of the formulations need to be considered for estimating the heating performance of nanoparticle formulations, to ensure optimal heating with imaging features.

6.2 Materials and Methods

6.2.1 Magnetic iron oxide nanoparticles

The magnetic iron oxide nanoparticles used in this study are: Bionised nanoferrite (BNF) nanoparticles and Johns Hopkins University (JHU) nanoparticles. BNF nanoparticles (micromod Partikeltechnologie, Rostock, Germany) are starch-coated iron oxide solid core nanoparticles synthesized by a high temperature and high pressure homogenization process [55,57]. They have a mean hydrodynamic diameter of 80 nm and iron concentration of 19.2 mg/mL (lot 0601610-02). JHU nanoparticles (NanoMaterials Technology, Singapore) are citric acid coated iron oxide core-shell particles which are synthesized by a high gravity controlled precipitation process [53,57]. They have a mean hydrodynamic diameter of 56.8 nm and iron concentration of 85 mg/mL (lot Fe000H1503225). Both the nanoparticles are a mixture of magnetite (Fe_3O_4) with maghemite (γ Fe_2O_3) have been extensively characterized previously and their heating potential measured [57].

6.2.2 Preparation of lipiodol formulations of BNF and JHU nanoparticles

Lipiodol®, an ethiodized oil, is a commonly used carrier fluid for image guided procedures such as TACE, mainly due to its radio-opacity, drug delivery and transient and plastic embolization of tumors [206]. It is a pale yellow to amber color clear liquid with an iodine concentration of 480 mg/mL (37% w/w). Lipiodol formulations of BNF and JHU nanoparticles, BNF-lip and JHU-lip, were prepared as follows. 1% of polysorbate-20 (Tween®-20, Sigma Aldrich, St Louis, MO) was added to aqueous suspensions of BNF nanoparticles and vortexed for 1 min. Lipiodol (Lipiodol Ultra-Fluide, Guerbet,

Bloomington, IN) was then added to this mixture by 1:1 v/v ratio, followed by vortexing for 5 minutes, giving the BNF-lip emulsion, as previously described [66]. JHU-lip, emulsion of JHU nanoparticles and lipiodol, was prepared by mixing the aqueous suspension of JHU nanoparticles and lipiodol with a 1:1 v/v ratio and sonicating for 15 minutes. Fresh batches of lipiodol formulations of both the particles were prepared using the same starting materials for each of the experiments described in this chapter.

6.2.3 Physical characterization by transmission electron microscopy (TEM)

The sizes and arrangement of nanoparticles in the aqueous and lipiodol formulations of both BNF and JHU nanoparticles were characterized using TEM (Philips/FEI BioTwin CM120) working at 80 keV. The samples were diluted to 200 μL/mL, and 5 μL of sample was placed onto a 400 mesh carbon coated copper grid and dried overnight before imaging. The lipiodol formulations were intractable for imaging since the non-volatile lipiodol prevented drying on sample grids for TEM [66]. Hence surrogate suspensions for both BNF-lip and JHU-lip, were prepared as follows [66]. The nanoparticle rich fractions for BNF-lip and JHU-lip formulations were collected by magnetic-assisted settling using strong rare earth permanent magnets for 60 min and the supernatant was removed. The nanoparticle rich fractions were then re-suspended in lipiodol and sonicated for 15 min. The suspensions were then filtered through a MILLEX®-HV (0.45 μm) filter unit to yield a concentrated paste of BNF-lip and JHU-lip emulsions which were used for TEM imaging.

6.2.4 Temperature measurements

The change in temperatures of aqueous and lipiodol formulations of BNF and JHU nanoparticles were measured by using alternating magnetic field (AMF) equipment and methods previously described [56,165,207]. The AMF equipment mainly consists of three components: power supply, a matching external impedance network (matchbox in Figure 6.1), and a vertical solenoid configuration (coil in Figure 6.1). The power supply is a 120-kW induction heating system (PPECO, Watsonville, CA) that supplies an alternating current to an external impedance match network (AMF Life Systems, Auburn, MI) which was adjusted to oscillate at a stable frequency of 155 ± 10 kHz. The vertical four turn modified solenoid coil generates a magnetic field (± 10% peak amplitude) and is cooled using a closed-loop circulating water cooling system. The generated magnetic field was measured using magnetic field probes (AMF Life Systems, Auburn Hills, MI) and mapped to the applied voltage of the power supply. The solenoid coil was calibrated for SLP measurements with a copper wire [207].

The experimental setup for measuring the rate of temperature changes of BNF, BNF-lip, JHU and JHU-lip, is shown in Figure 6.1. An insulating cylindrical Styrofoam holder was used to minimize the thermal interactions between the sample and the surroundings, especially to limit the heat transfer from the vertical solenoid coil during the experiment. 1 mL volume samples of all the four nanoparticle formulations were prepared in Type I 51 glass tubes (LaMotte, Chestertown, MD) and weighed before inserting them into the cylindrical Styrofoam holder. The iron concentration in all the nanoparticle formulations was fixed at 5 mg/mL. Temperatures of the samples were measured using a calibrated fiber optic temperature probe (FOT-L probe, FISO Technologies, Quebec City,

Canada). Care was taken to ensure that the probe was immersed inside the solution and the probe was sealed using parafilm. The samples were allowed to equilibrate with the surroundings before heating. This was ensured by monitoring the temperature and letting it to stabilize to a constant temperature (maximum deviation of ± 0.05 °C) for 30 s. After this, alternating magnetic field was applied for a duration of 100 s and the temperatures were recorded at 0.45 s intervals. The samples were then removed from the chamber and allowed to cool down before subjecting them to heating at another amplitude. The process was repeated for all the samples at different magnetic field amplitudes.

The change in temperatures of the four nanoparticle formulations, BNF-water, BNF-lip, JHU-water, and JHU-lip, were measured at a range of magnetic field amplitudes, beginning at 8 kA/m to 32 kA/m at 4 kA/m intervals, at a constant frequency of 155 ± 10 kHz. Samples of water, lipiodol-polysorbate20-water (BNF-lip background) and lipiodol-water (JHU-lip background), were prepared and temperatures measured at each power setting to account for heating contributions from solvent(s) and the calorimeter. The rise in temperatures for the nanoparticle formulations was determined by subtracting the initial temperature of the sample from the measured temperatures at each time point. The rise in temperatures due to nanoparticle heating, given by the net increase in temperatures with time, of the nanoparticle formulations were then determined by subtracting the temperatures of their respective background samples from these temperatures.

6.2.5 Specific heat capacity measurements

Lipiodol, BNF, BNF-lipiodol, JHU, and JHU-lipiodol, samples were sent to Intertek laboratories (Allentown, PA) for specific heat measurements. The heat capacity of the samples was determined using a differential scanning calorimeter (TA Instruments

Q2000) DSC, calibrated at 10°C/min with an Indium standard. Approximately 10 mg samples were encapsulated in T-zero hermetic DSC pans. All pans were matched within 0.050 mg. The samples were then analyzed from 22 to 115°C using a sapphire heat flow standard. ASTM E-1269-05 was followed with the exception that a heating rate of 10°C/min. was used. The purge gas was nitrogen with a flow rate of 50 cc/min.

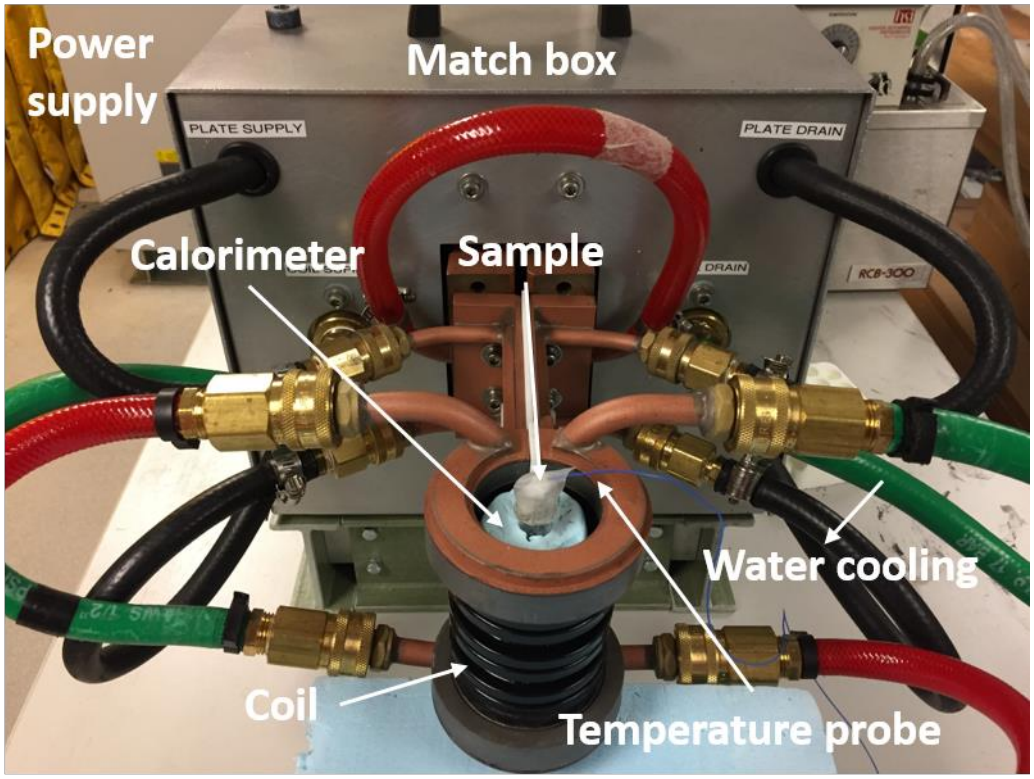

Figure 6.1 Experimental setup for measuring the heating rates of nanoparticle formulations

6.2.6 Specific loss power determination

The heat generated by the nanoparticles (SLP) exposed to AMFs is defined as the thermal power generated per unit mass of magnetic material. Heat generated by the nanoparticles can be estimated by measuring the temperature evolution with time of a nanoparticle sample exposed in an alternating magnetic field [59]. The rate of rise in

temperature can be used to estimate the SLP of the nanoparticles based on the principle of conservation of energy, which is described in section 1.4. Based on first law of thermodynamics, if there is no mass or energy exchange between the nanoparticle sample and surroundings (adiabatic conditions), and if the heat generated is solely due to the nanoparticles, then the heating rate (SLP) of the nanoparticles can be estimated by ,

$$SLP = \frac{C}{m_{Fe}} \frac{\Delta T}{\Delta t} \tag{6.1}$$

Here C is the heat capacity of the sample, m_{Fe} is the mass of iron in the sample, ΔT is the temperature increase, Δt is the change in time and $\frac{\Delta T}{\Delta t}$ is the rate of change of temperature with time [56,60]. The SLP for the aqueous and lipiodol formulations of BNF and JHU nanoparticles were determined from the temperature measurements and measured specific heat capacities using Equation 6.1., which is valid only under (quasi-) adiabatic conditions [60]. It was estimated by using methods and MATLAB code developed by Soetaert et al. [60]. Briefly, the method consists of identifying the (quasi)-adiabatic regions, where the ratio of net temperature rise and the time difference is within 5% of the net temperature increase slope. This net temperature rise slope was then used to estimate SLP using equation 6.1, where heat capacity C was determined by the product of specific heat capacity of the sample and the mass of the sample. This procedure was repeated for multiple time intervals (minimum of 6 s and maximum 100 s) and every time range that resulted in (quasi)-adiabatic conditions was considered to yield a new SLP-value. The average of all obtained SLP values was defined the measured SLP value and the standard deviation of these values was used to determine the error bars.

6.2.7 Computational model – *in vitro* heating

Heat transfer simulations were carried out to understand the role of heat transfer in the higher temperature changes observed for lipiodol formulations of nanoparticles. The heat generated by the nanoparticles is mainly stored in the formulation and is transferred to the surroundings by conduction, convection, and radiation. Computational simulations were carried out to compute the temperature rise in the sample for a heating rate (given by SLP) at a given magnetic field amplitude and frequency. For the lipiodol formulations of both BNF and JHU nanoparticles, two different SLP values were considered. In the first case, it was assumed that there was no difference in SLPs between the aqueous and lipiodol formulations. This was done to clearly understand the role of change in thermal properties of lipiodol formulations compared to aqueous formulations. In the second case, measured SLPs of lipiodol formulations were chosen. This allows us to understand the combined effect of change in thermal properties and SLPs on the rate of change in temperatures for lipiodol formulations.

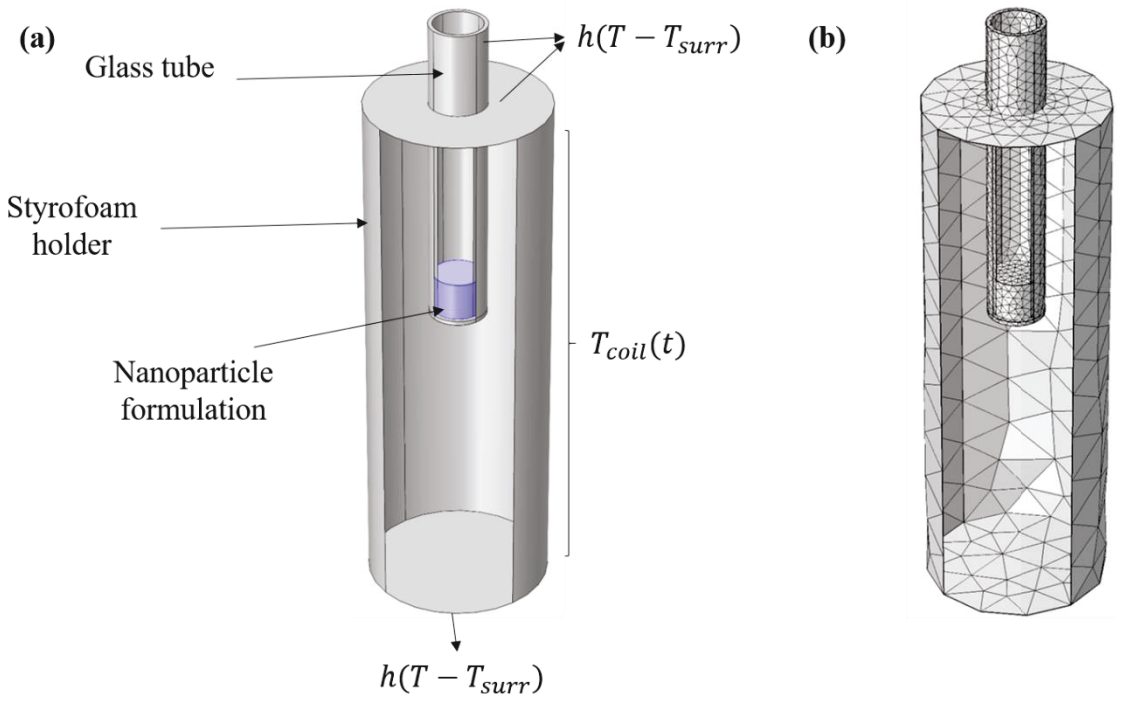

Figure 6.2 Schematic of the computational model used for heat transfer simulations for aqueous and lipiodol nanoparticle formulations (a) Schematic showing the glass tube with nanoparticle formulation placed in a Styrofoam holder. The outside of the Styrofoam holder was exposed to the coil inside, hence a temperature T_{coil} *(t)* boundary condition was considered. For all other surfaces exposed to the surroundings, free convection boundary condition was considered. (b) Mesh for the computational model considered in (a).

The model consists of 3D glass tube placed in a Styrofoam holder similar to the one used in the experiments. The glass tube has thickness of 1 mm, an outer diameter of 13.75 mm and length of 75 mm. The schematic of the model is shown in Figure 6.2. The thermal properties of the glass were taken as follows, density of glass as 2600 kg m^{-3}, thermal conductivity of 1.10 W/m K and specific heat capacity of 840 J/kg-K [208,209]. For the nanoparticle formulations, the thermal conductivity for aqueous formulations were taken to be that of water (0.609 W/m-K) [210], while for that of lipiodol formulations it was calculated to be 0.29688 W/m K, by taking the thermal conductivity of water and lipiodol at a 1:1 v/v ratio. The thermal conductivity of lipiodol was approximated to be 0.15 W/m-K as that of oil [211,212]. The specific heat capacities of the samples were taken from the

values measured. The density of the samples were taken that of water (1000 kg/m^3) for aqueous formulations and for lipiodol formulations it was taken to be 1140 kg/m^3 which was determined by using the lipiodol density (1280 kg/m^3) [206]. The thermal properties of styrofoam were chosen as follows, density (50 kg/m^3) [210], thermal conductivity (0.033 W/m-K) [213], and specific heat capacity (1215 J/kg-K) [214]. The temperature for the surroundings was assumed to be 23 °C (296.15 K) based on the experimental measurements. The outside of the styrofoam holder was exposed to the coil inside, hence a temperature boundary condition of $T_{coil}\ (t)$ was considered. For all other surfaces exposed to the surroundings, free convection heat transfer coefficient of 10 W/m^2 K was considered. Heat loss due to radiation was neglected. Simulations were carried out for a time step of 0.45s similar to that of our experimental conditions. SLPs were considered at two magnetic field amplitudes in the simulation, 12 kA/m, and 20 kA/m. The temperature changes for the aqueous and lipiodol formulations of both BNF and JHU nanoparticles were computed to compare with the observed experimental results.

6.2.8 Magnetic characterization by magnetometry

Any magnetic material is well defined by its saturation magnetization (M_s) which is defined as the maximum magnetization observed when all the magnetic moments of the material are aligned parallel to the applied external magnetic field [51]. Saturation magnetization for the four nanoparticle formulations can be determined from the hysteresis loops measured at different temperatures. In this work, hysteresis loops were measured at temperatures from 5 K to 300 K at an applied field of ± 5570 kA/m using a superconducting quantum interference device vibrating sample magnetometer (SQUID VSM, Quantum Design, Inc., San Diego, CA). The samples were loaded into Kel-F liquid capsules

(LakeShore Cryogenics) and sealed with epoxy to prevent evaporation of the water solvent during measurement under vacuum. Contributions from sample holder, water, polysorbate-20, and lipiodol, were subtracted from the respective sample data. These experiments were conducted by Dr. Cindi Dennis at the Material Measurement Laboratory, National Institute of Standards and Technology, Gaithersburg, MD, USA.

6.2.9 Computational model – *in vivo* heating

Computational simulations were carried out to estimate the temperatures achieved in tissues with aqueous and lipiodol nanoparticle formulations of nanoparticles. Two concentric spheres (Figure 6.3) were considered to represent the tumor and healthy tissue model in this study. The inner sphere of volume 1 cm^3 (d = 1.24 cm) represents the tumor while the outer sphere of diameter 12 cm represents the healthy tissue. The healthy tissue was chosen to be sufficiently large so as to impose a constant core body temperature boundary condition of 37 °C [141]. Heat transfer in the tumor and healthy tissue was modeled using the Pennes' bio-heat transfer equation [81] given by,

$$\rho_n c_n \frac{\partial T_n}{\partial t} = k_n \nabla^2 T_n + \rho_b c_b \omega_{b,n} (T_b - T_n) + Q_{m,n} + Q_p \qquad (6.2)$$

here n and b represent tissue (tumor, n = 1; healthy tissue, n = 2) and blood; respectively. ρ_n, c_n, k_n, T_n, $Q_{m,n}$ denote the density, specific heat, thermal conductivity, local temperature, and metabolic heat generation rate, for either tumor or healthy tissue and t is the heating time. ρ_b, c_b, $\omega_{b,n}$, T_b denote density, specific heat, perfusion rate, and temperature, of blood respectively. For the current simulations, thermophysical properties of liver [122] were taken for healthy tissue which are summarized in Table 6-1. The metabolic heat generation rate for the tumor was taken to be five times that of the healthy liver. Q_p denotes the total

power generated by nanoparticles in the tumor. In the current simulations, homogeneous uniform distribution of nanoparticle formulations were assumed inside the tumor. The volume of nanoparticle solution injected in the tumor was taken to be half the tumor volume [66]. The mean values of specific heat c_1, density ρ_1, and thermal conductivity k_1, for the tumor with the two nanoparticle formulations, BNF-water and BNF-lip, was approximated by,

$$c_1 = (1 - \eta)c_2 + \eta c_{np} \tag{6.3}$$

$$\rho_1 = (1 - \eta)\rho_2 + \eta \rho_{np} \tag{6.4}$$

$$\frac{1}{k_1} = \frac{(1 - \eta)}{k_2} + \frac{\eta}{k_{np}} \tag{6.5}$$

Here ρ_{np}, c_{np}, k_{np}, are the density, specific heat capacity, and thermal conductivity, of the nanoparticle formulations [215] and η is the volume fraction. The specific heat capacities of the nanoparticle formulations were taken from the values determined from measurements described in section 6.2.5. For the BNF-water formulation, the density and thermal conductivity were taken that of water, (1000 kg/m^3, and 0.609 W/m-K) [210]. Since BNF-lip formulations consist of 1:1 v/v of water and lipiodol, the density was determined by using equation 6.4 with density of lipiodol taken as 1280 kg/m^3 [206] and density of water to be 1000 kg/m^3. Similarly thermal conductivity was determined using equation 6.5, with thermal conductivity of lipiodol taken as that of oil, given by 0.15 W/m-K [211,212]. The SLP of BNF nanoparticles estimated at 20 kA/m in section 6.2.6 was used for Q_p, the heat generated by the nanoparticles in this simulation.

Thermal damage in tissue depends on the temperature achieved and time at temperature. Previous *in vitro* studies [26,29,30,32] have shown that thermal damage to cells follows an Arrhenius relationship given by:

$$\frac{\partial \Omega(\mathbf{r}, \mathrm{T}, \mathrm{t})}{\partial t} = A\, e^{\frac{-\Delta E_a}{RT(\boldsymbol{r},t)}} \tag{6.6}$$

where Ω is the Arrhenius damage index, A is the frequency factor, ΔE_a is the activation energy barrier, and R is the universal gas constant. The survival fraction α is then given by:

$$\alpha(\boldsymbol{r}, T, t) = e^{-\Omega(\mathbf{r},\mathrm{T},\mathrm{t})} \tag{6.7}$$

The values for A and ΔE_a were taken to be 2.984×10^{80} 1/s, and 5.064×10^{5} J/mol respectively [141,148].

Perfusion in tumor and healthy tissue was modeled as a function of thermal damage, which is based on modified Arrhenius model of thermal damage which was described in section 3.2.2. The initial perfusion ω_{bi} for both tumor and healthy tissue was taken to be 0.018 1/s [141,167].

Continuity of temperature and conservation of heat flux boundary conditions were applied at the tumor-healthy tissue interface and the constant core body temperature boundary condition was assumed at the healthy tissue boundary. Summarized, the boundary conditions are:

$$k_{tissue} \left.\frac{\partial T_{tissue}}{\partial r}\right|_{r=r_{tumor}} = k_{tumor} \left.\frac{\partial T_{tumor}}{\partial r}\right|_{r=r_{tumor}} \tag{6.8}$$

$$T_{tissue}(r = r_{tumor}, t) = T_{tumor}(r = r_{tumor}, t) \tag{6.9}$$

$$T(r = r_{tissue}) = 37\ ^{\circ}\mathrm{C} \tag{6.10}$$

The equations (6.2, 6.8 – 6.10) were solved numerically using finite element methods. Grid dependency tests were carried out to ensure that the chosen grid size had negligible effect on the computed temperatures. Changing the grid size from normal (10181 tetrahedral elements) to fine (18889 tetrahedral elements) resulted in less than 0.04% change in temperature along the line from tumor center to healthy tissue boundary.

Similarly changing the time step from 1 s to 0.5 s, resulted in negligible change in computed temperatures.

Table 6-1 Thermophysical properties of healthy tissue and blood

	Density, ρ (kg/m^3)	Specific heat, c (J/kg K)	Thermal conductivity, k (W/m K)	Blood Perfusion rate, ω (1/s)	Metabolic heat generation rate, Q_m (W/m^3)
Healthy tissue	1079 [122]	3540 [122]	0.52 [122]	0.018 [167]	14414 [168]
Blood*	1060 [124]	3770[124]	N/A	N/A	N/A

*Temperature of blood (T_b) was fixed at 37ºC [124]. (N/A – not applicable)

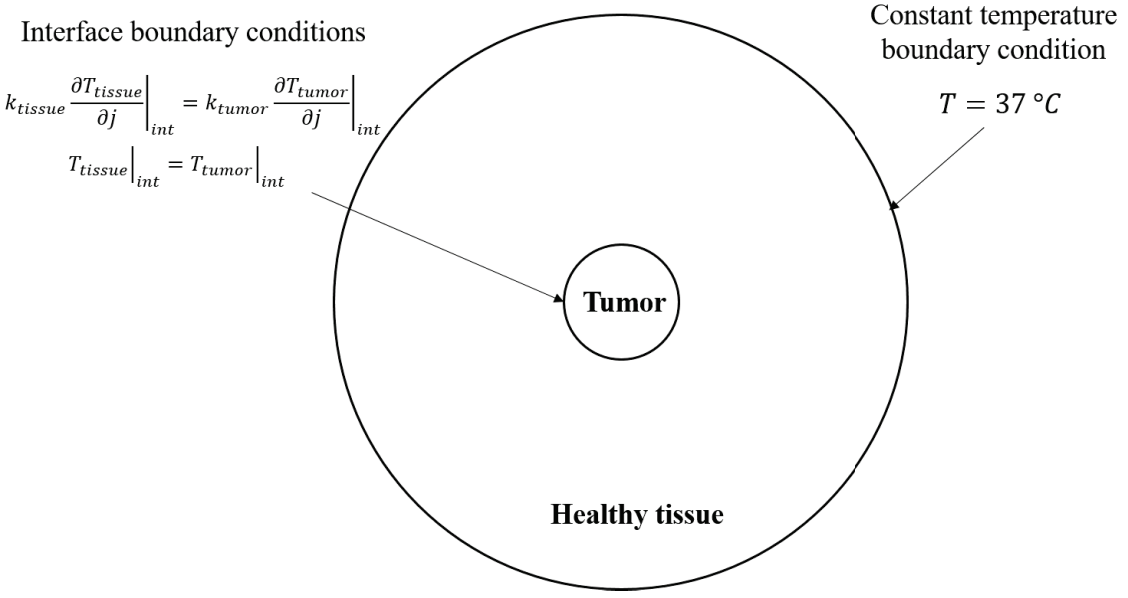

Figure 6.3 Schematic of the computational model with tumor (d = 1.24 cm) in the center and healthy tissue (d = 12 cm).

6.3 Results

6.3.1 Physical characterization by TEM

TEM images of aqueous and lipiodol formulations of BNF and JHU nanoparticles is shown in Figure 6.4. Aqueous formulation of BNF nanoparticles show individual particle cores comprising iron oxide crystals forming small aggregates. The particles form elongated arms and the crystallites are in parallelepiped shapes consistent with previous observations [57,66]. When suspended in lipiodol (BNF-lip), the particles form large dark spherical clusters surrounded by lighter oil coating. In the case of JHU nanoparticles, a dense core of multiple spherical crystallites can be seen for the aqueous formulations. For the lipiodol formulations of JHU nanoparticles, dense particle aggregates are formed similar to the ones observed with BNF-lipiodol. The alteration of lipiodol formulations of BNF and JHU nanoparticles to make them tractable for TEM imaging limits the interpretation of the results obtained from these images.

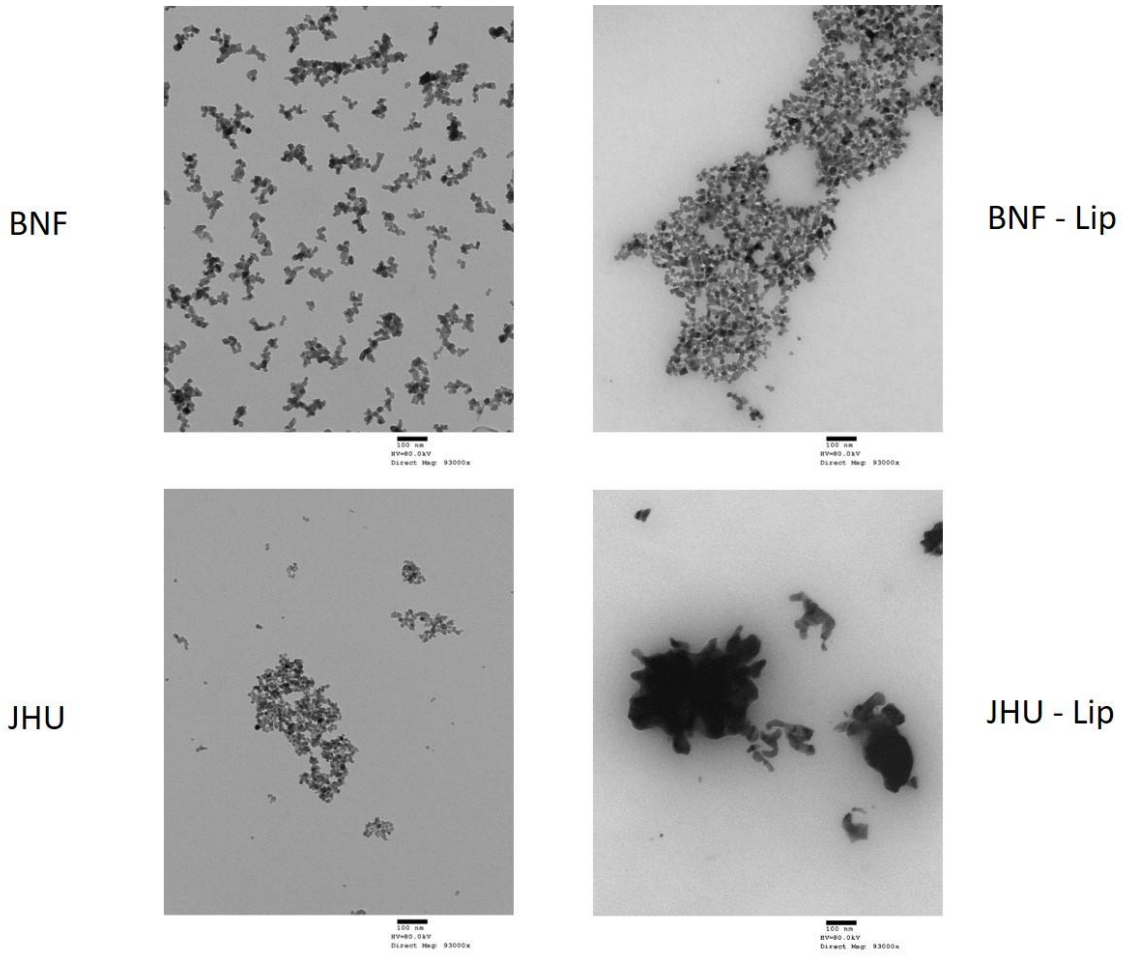

Figure 6.4 Aggregation of nanoparticles is observed in lipiodol formulations of both BNF and JHU nanoparticles. TEM images of aqueous and lipiodol formulations of BNF and JHU nanoparticles (clockwise) BNF nanoparticles in water; BNF-Lip – BNF nanoparticles suspended in lipiodol; JHU-Lip – JHU nanoparticles suspended in lipiodol; and JHU nanoparticles in water (Scale – 100 nm)

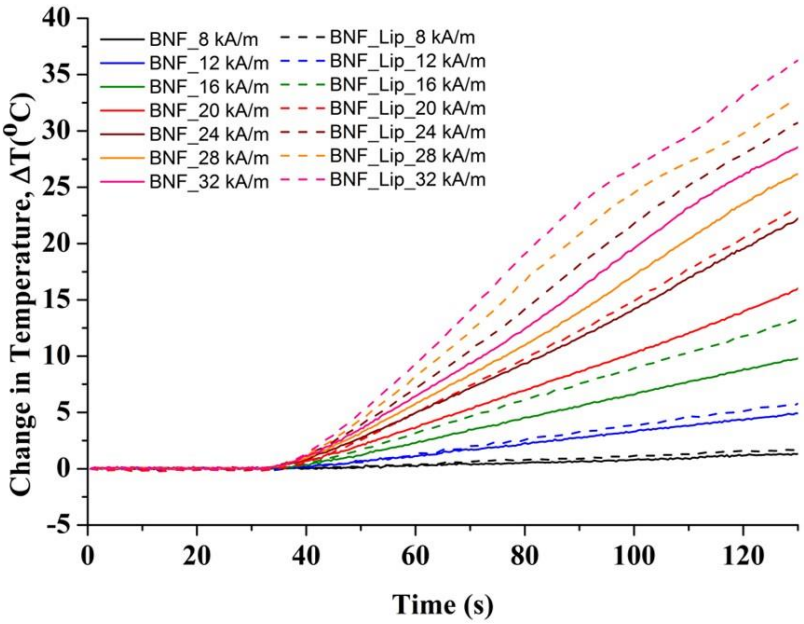

(a) BNF

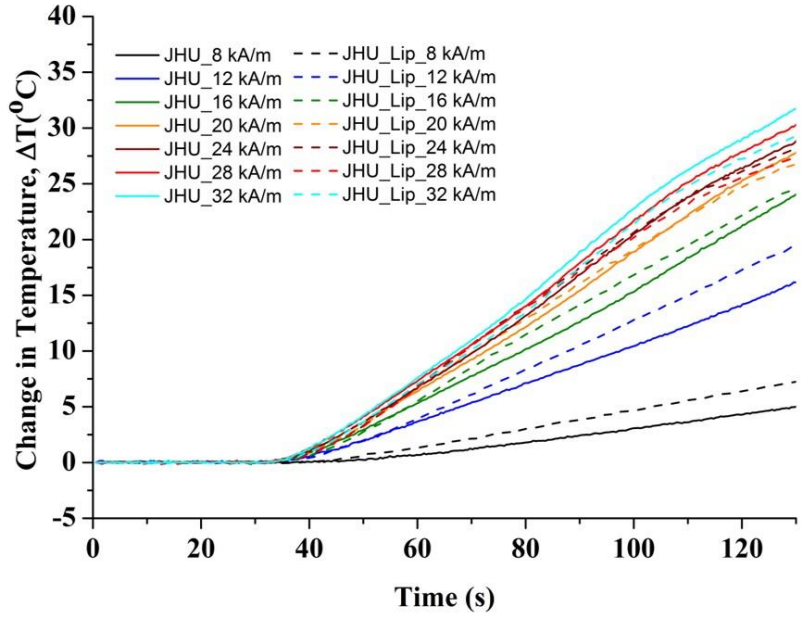

(b) JHU

Figure 6.5 Measured change in temperatures with time for aqueous and lipiodol formulations of (a) BNF and (b) JHU nanoparticles with varying magnetic field amplitude (8 – 32 kA/m) at constant frequency of 155 ± 5 kHz. Contributions from water, lipiodol-water, and lipiodol-polysorbate20-water backgrounds were removed.

6.3.2 Heating rates of aqueous and lipiodol formulations

The net change in temperature with time for the aqueous and lipiodol formulations of BNF and JHU nanoparticles measured at a range of magnetic field amplitudes beginning with 8 kA/m to 32 kA/m at 4 kA/m intervals at 155 ± 10 kHz frequency is shown in Figure 6.5. As explained earlier, in the time-temperature data shown here the contributions from the respective backgrounds has been subtracted. Higher temperature changes were consistently observed for lipiodol formulation of BNF nanoparticles, compared to corresponding aqueous formulations across all measured amplitudes. This was not the case for JHU nanoparticles. While JHU-lip had higher temperature changes at lower amplitudes (8-16 kA/m), at higher amplitudes (20 – 32 kA/m) the difference in the change in temperature gradually decreased and were lower than that of aqueous formulations. These trends can be seen clearly when the difference in temperature changes between lipiodol and aqueous formulations is plotted in Figure 6.6. For BNF nanoparticles, lipiodol formulations consistently exhibited higher temperature changes across all amplitudes when compared to aqueous formulations. The difference in temperature change with time for the BNF nanoparticles increased consistently with increasing amplitude from 8 – 24 kA/m, while at higher amplitudes (28 – 32 kA/m) a slight decrease was seen.

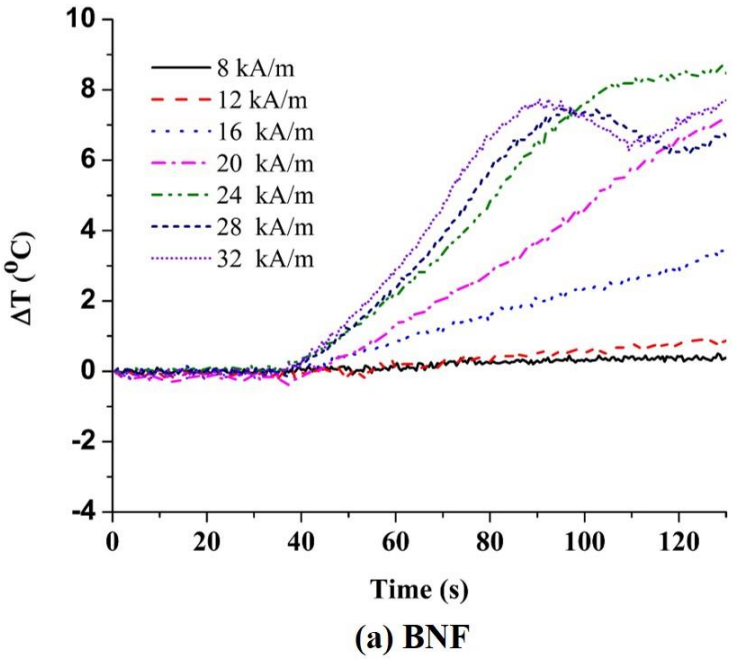

(a) BNF

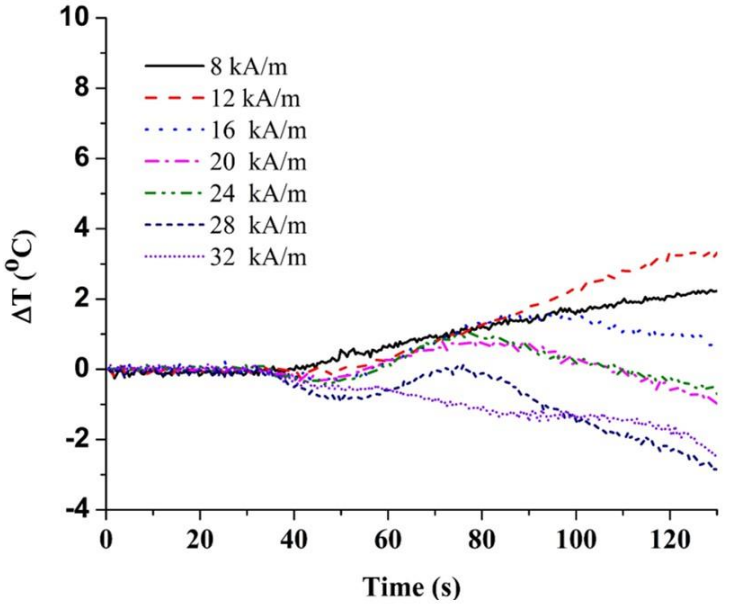

(b) JHU

Figure 6.6 Higher temperature rise was observed in lipiodol formulations of BNF nanoparticles at higher applied fields, while for JHU nanoparticles this is not true. Difference of temperature changes between lipiodol and aqueous formulations of (a) BNF and (b) JHU nanoparticles with varying applied magnetic field amplitude (8 – 32 kA/m) at constant frequency of 155 ± 5 kHz

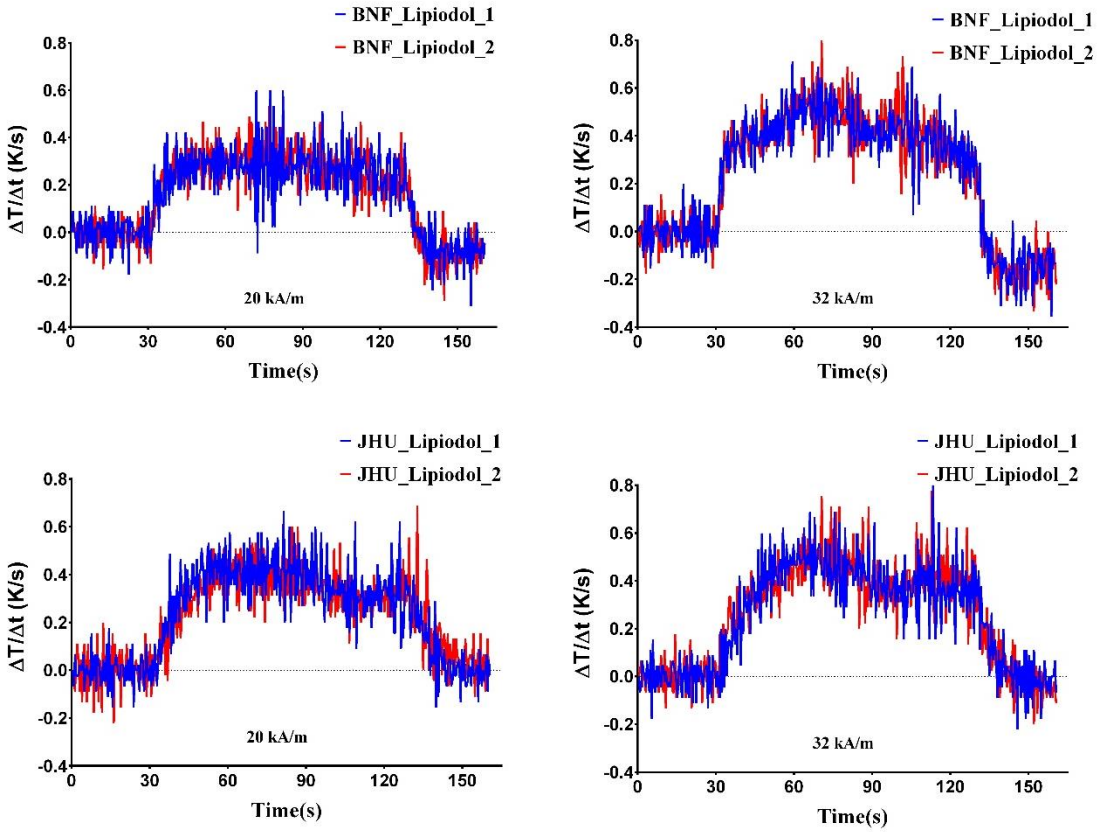

Figure 6.7 No deterioration was observed in nanoparticle formulations due to repeated exposure to alternating magnetic field. Rate of change in temperature with time for lipiodol formulations of BNF and JHU nanoparticles when exposed to magnetic field amplitude of 20 and 32 kA/m at constant frequency of 155 ± 5 kHz

Replicate measurements of a given sample for the lipiodol formulations of BNF and JHU nanoparticles were carried out at 20 kA/m and 32 kA/m to estimate the reproducibility of the observed heating and the effect of repeated heating. The first derivative, approximated as the net temperature rise for each time step, was plotted with time (Figure 6.7), to determine if there were any changes. The plots show a similar change in the rate of change in temperature for both the lipiodol formulations suggesting that repeated exposure to alternating magnetic fields and heating have negligible effect on the heating rates of the samples.

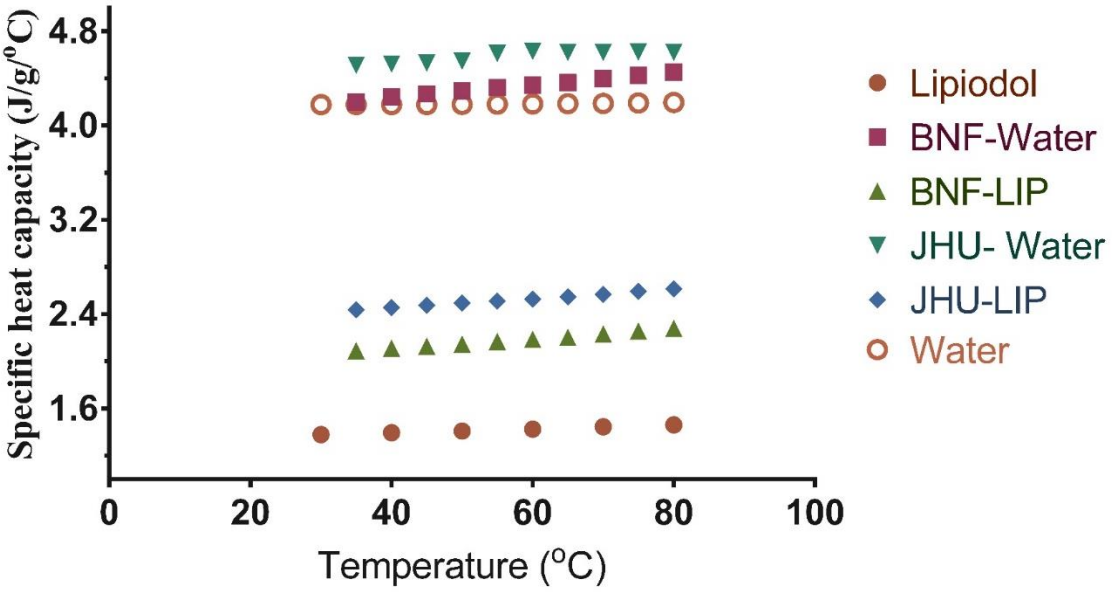

Figure 6.8 Lipiodol formulations of nanoparticles have lower specific heat capacities than the corresponding aqueous formulations. Specific heat capacities of lipiodol, aqueous and lipiodol formulations of BNF and JHU nanoparticles measured using a differential scanning calorimeter between the temperatures 30 – 80 °C. (Specific heat capacity values for water were taken from [210])

Table 6-2 Specific heat capacity of lipiodol and nanoparticle formulations at 35 °C

	Specific heat capacity (J/g/°C) at 35 °C
Lipiodol	1.394
BNF-Water	4.199
BNF-Lipiodol	2.089
JHU-Water	4.513
JHU-Lipiodol	2.440

The rate of change in temperature is primarily influenced by the quantity of heat generated by the nanoparticles and the degree of heat transfer occurring which depends on the thermal properties of the formulation. Heat transfer in the formulation is mainly described by thermal diffusivity which is proportional to the thermal conductivity of the

solvent and inversely proportional to the sample density and specific heat capacity. Measured values of specific heat capacities of lipiodol, BNF-water, BNF-lipiodol, JHU-water and JHU-lipiodol were plotted in Figure 6.8. It can be seen that lipiodol has ~ 3 times lower specific heat capacity than that of water (1.394 J/g/°C at 35 °C). This resulted in lower (< ~2 x) specific heat capacities for BNF-lip and JHU-lip when compared to their aqueous formulations. It can also be observed that specific heat capacities remain relatively constant with change in temperature in the temperature range of 30-80 °C (Figure 6.8).

Heat generated by nanoparticles, denoted by specific loss power (SLP), of the four nanoparticle formulations were reported in Figure 6.9. The temperature change rates and specific heat capacities of the nanoparticle formulations determined previously were used to determine the SLP for all the formulations. SLP estimated for the aqueous formulations of BNF and JHU nanoparticles were consistent with previously measured values [56,57,60]. They exhibit a non-linear amplitude dependent response (S-shaped curve) with both the aqueous and lipiodol formulations of BNF and JHU nanoparticles following a similar trend [56,57,216]. Both JHU-water and JHU-lip nanoparticles generate higher heating when compared to BNF-water and BNF-lip nanoparticles at lower amplitudes and this difference reduces at higher fields. This is consistent with previously reported values of SLP for BNF and JHU nanoparticles. However it is interesting to note that, while JHU-lip exhibits higher SLP than BNF-lip, the difference reduces further from 82% at 8 kA/m to ~0 % at 32 kA/m.

Interestingly, SLP values for lipiodol formulations of both BNF and JHU nanoparticles were consistently lower than that of their corresponding aqueous formulations for all applied fields (8-32 kA/m). For BNF nanoparticles, this difference in

SLPs between the aqueous and lipiodol formulations is lower (average 26%) when compared with JHU nanoparticles (average 32%). Additionally, JHU-lip appears to be reaching saturation at lower fields (~ 20 kA/m) when compared to other nanoparticle formulations which were not close to saturation at the highest measured field amplitude of ~ 32 kA/m. Further statistical analysis was carried out to compare the SLPs of the aqueous and lipiodol formulations of nanoparticles. To do this, all obtained values of SLPs for all formulations at each field were plotted using the box-whisker plots (Figure 6.10 and Figure 6.11). In this plot, the boxes show the interquartile range (first (25%) and third (75%) quartiles, with the inside solid line showing the median SLP value. The whiskers show the maximum and minimum SLP values obtained for the formulations at each field. Mann-Whitney analysis was conducted to compare the medians of both the formulations for BNF and JHU nanoparticles. Statistically significant difference (*p-value <0.0001*) was observed between the median SLPs of the aqueous and lipiodol formulations of both BNF and JHU nanoparticles. Both the reduced SLP and saturation of SLPs at lower amplitudes for lipiodol formulations, compared to aqueous formulations, suggests changes in the magnetic properties of lipiodol formulations.

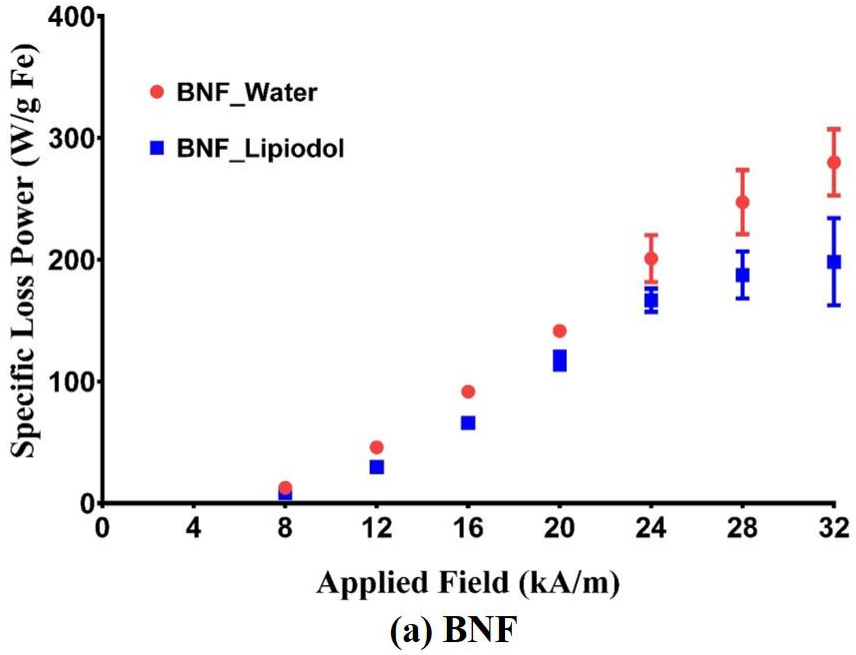

(a) BNF

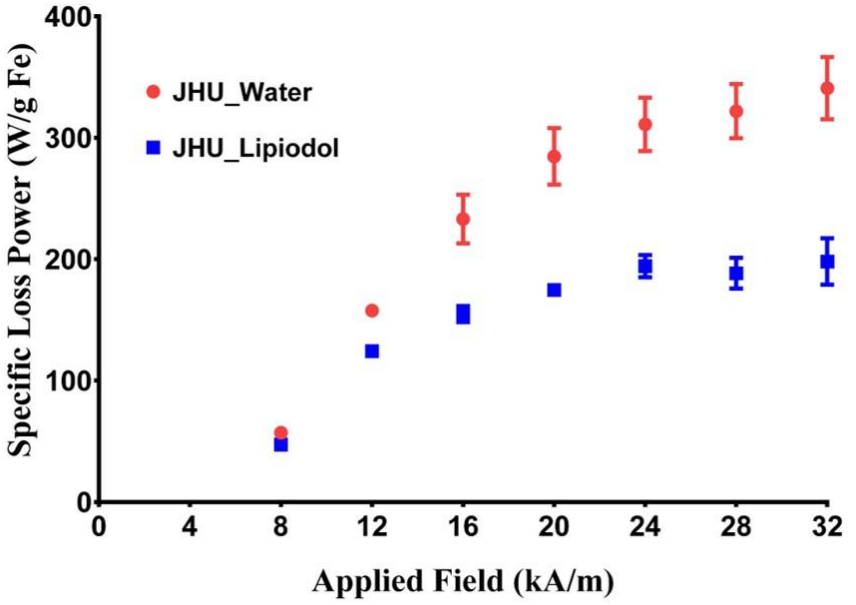

(b) JHU

Figure 6.9 Specific loss power (SLP) of lipiodol formulations of BNF and JHU nanoparticles is lower than that of their aqueous formulations SLP of aqueous and lipiodol s formulations of (a) BNF and (b) JHU nanoparticles with varying magnetic field amplitude at constant frequency of 155 ± 5 kHz

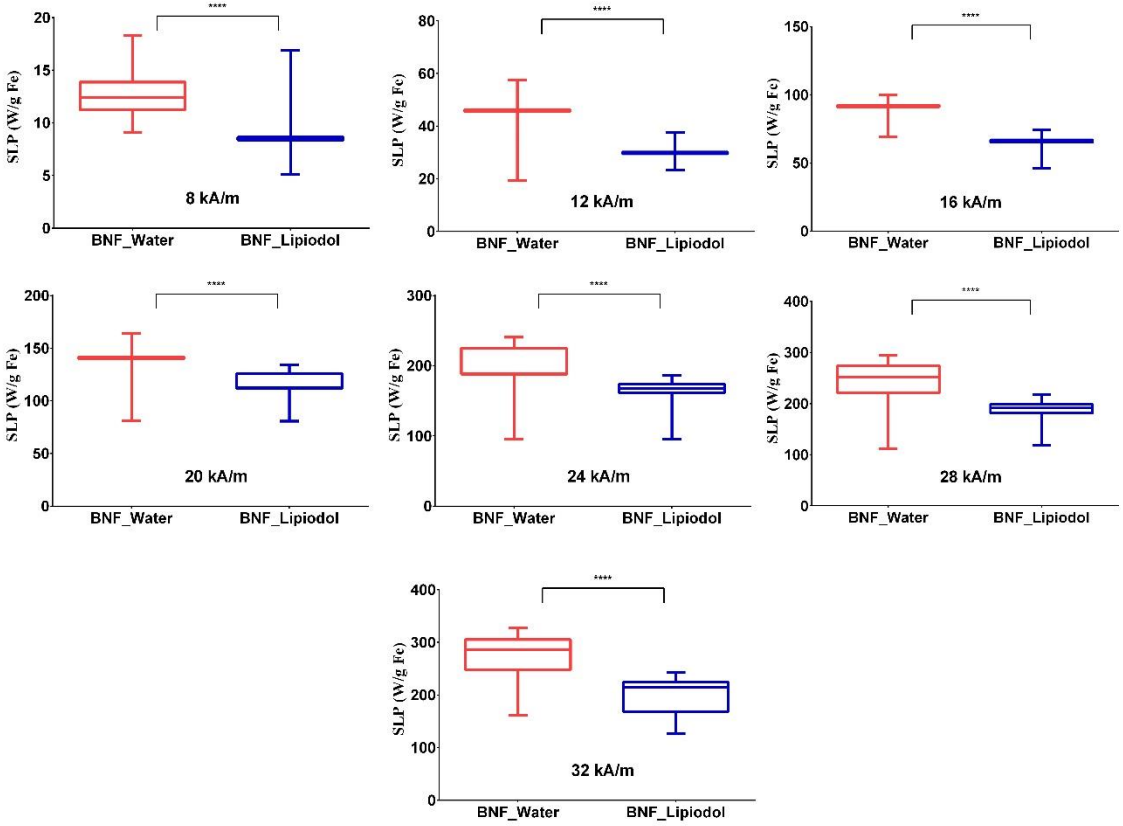

Figure 6.10 Statistical analysis of SLP for aqueous and lipiodol BNF nanoparticle formulations show significant difference. Box and whisker plots for the measured SLPs for BNF_Water and BNF_Lipiodol at fields of 8 – 32 kA/m at fixed frequency of 155 ± 10 kHz. Boxes denote the interquartile range while the center line shows the median SLP measured for each formulation at a given field. The whiskers denote the maximum and minimum values measured. Statistically significant reduction in SLP is observed ($p<0.0001$, ****) for lipiodol formulations compared to aqueous formulations.

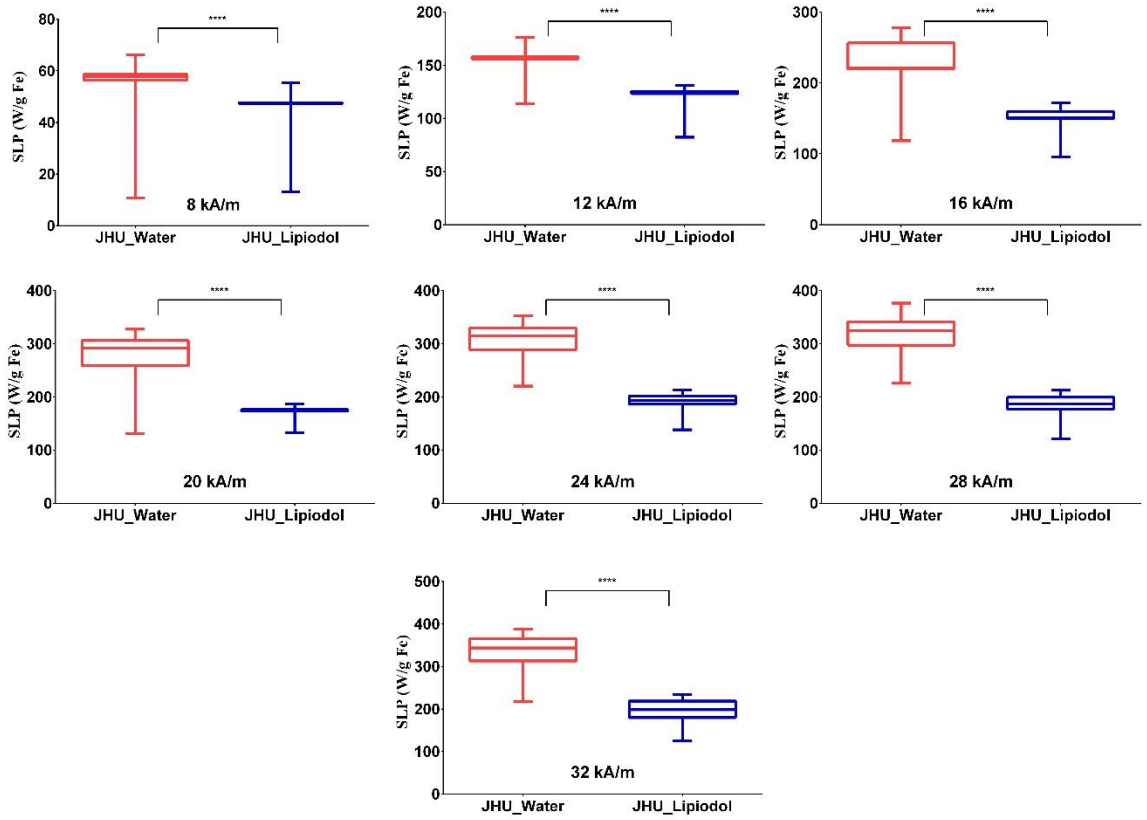

Figure 6.11 Statistical analysis of SLP for aqueous and lipiodol JHU nanoparticle formulations show significant difference Box and whisker plots for the measured SLPs for JHU_Water and JHU_Lipiodol at fields of 8 – 32 kA/m at fixed frequency of 155 ± 10 kHz. Boxes denote the interquartile range while the center line shows the median SLP measured for each formulation at a given field. The whiskers denote the maximum and minimum values measured. Statistically significant reduction in SLP is observed ($p<0.0001$, ****) for lipiodol formulations compared to aqueous formulations.

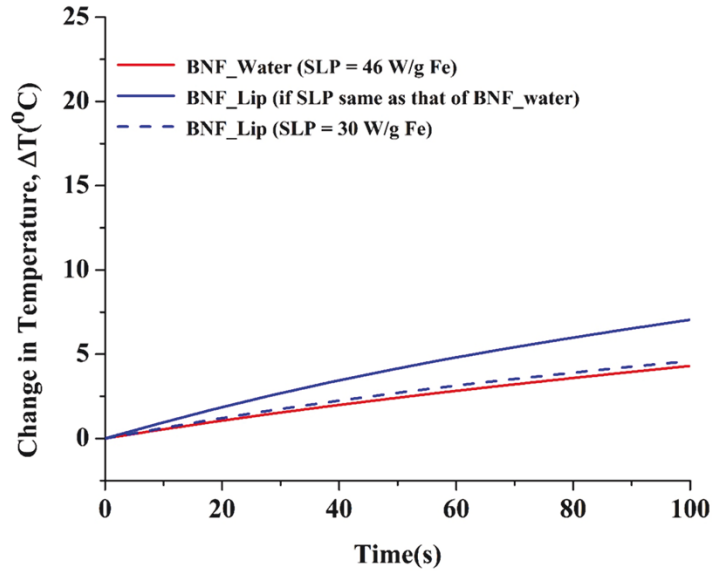

(a) 12 kA/m

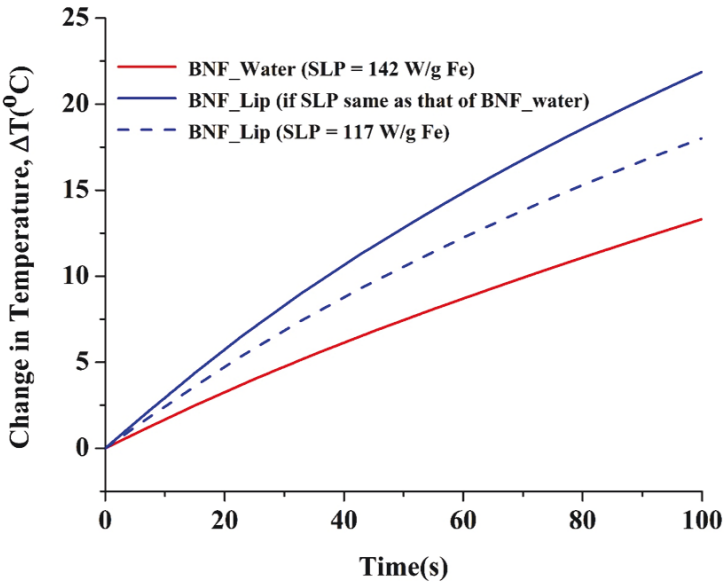

(b) 20 kA/m

Figure 6.12 Simulations predict that observed heating for lipiodol formulations are due to both change in thermal properties and decrease in SLP. Simulated change in temperature with time for BNF-water and BNF-lip samples using measured SLPs from figure 6.8 for (a) 12 kA/m and (b) 20 kA/m.

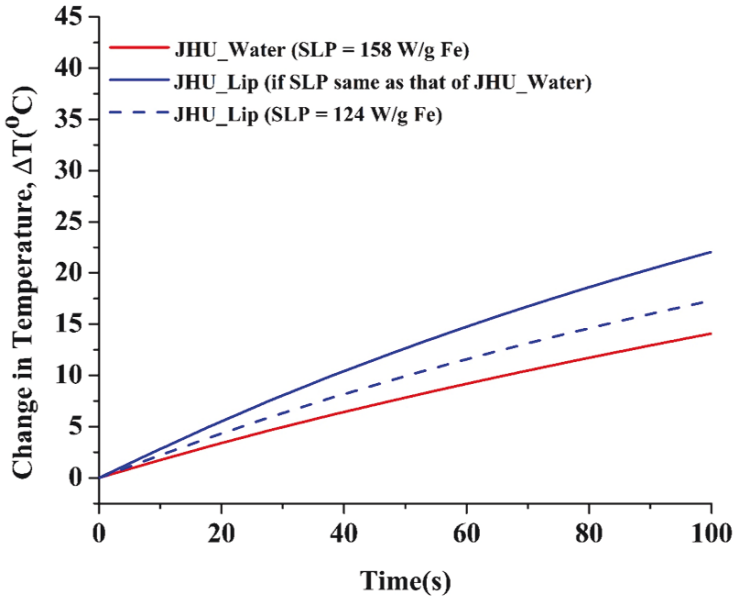

(a) 12 kA/m

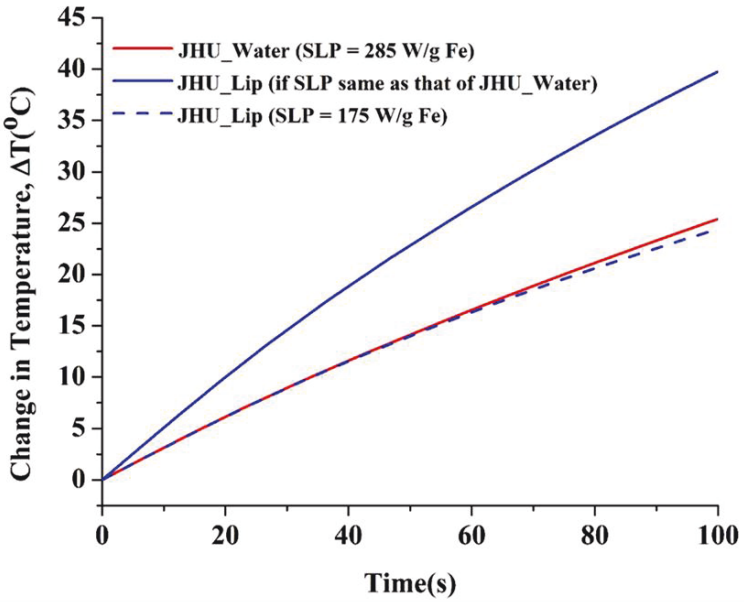

(b) 20 kA/m

Figure 6.13 Simulations predict that observed heating for lipiodol formulations are due to both change in thermal properties and decrease in SLP. Simulated change in temperature for JHU_Water and JHU_Lipiodol samples using measured SLPs from figure 6.8 for (a) 12 kA/m and (b) 20 kA/m.

6.3.3 *In vitro* heating simulation results

Computed temperature changes with time for aqueous and lipiodol formulations of both BNF and JHU nanoparticles using measured SLPs are shown in Figure 6.12 and Figure 6.13. Temperature change was computed for SLP values at two field amplitudes of 12 kA/m and 20 kA/m. For BNF nanoparticles, temperatures were consistently higher for lipiodol formulations at both amplitudes as observed in experiments (Figure 6.12). For same SLP, BNF-lip formulation exhibited higher temperatures than BNF-water and this was even higher at 20 kA/m when compared to 12 kA/m. When SLPs measured for BNF-lip was used, the temperature of lipiodol formulation was lower than that with same SLP as that of aqueous formulation. However, the temperature was still higher than that of BNF-water. For JHU nanoparticles, at both fields, for same SLPs, JHU-lip exhibited a higher temperature rise compared to JHU-water. However, when the measured SLP values for JHU-lip were used, the temperature change for JHU-lip was higher than JHU-water at 12 kA/m and it was lower at 20 kA/m. This was similar to the trend observed in experiments (Figure 6.5 and Figure 6.6). These results show that lipiodol significantly influences both the thermal properties and the heat generation rates for the lipiodol formulations.

6.3.4 Magnetic characterization

Hysteresis loops for the aqueous and lipiodol formulations of BNF and JHU nanoparticles at temperatures between 2 K and 300 K were shown in Figure 6.14 and Figure 6.15. It can be seen that both the aqueous and lipiodol formulations of BNF and JHU nanoparticles have similar S-shaped curves at all temperatures. But the lipiodol formulations of BNF and JHU nanoparticles have lower maximum magnetization

compared to their aqueous formulations. Magnified view of hysteresis loops with virgin curves in the range of applied field of ± 36 kA/m for all the four nanoparticle formulations is shown in Figure 6.16 and Figure 6.17. It can be observed that the area enclosed by the hysteresis loops for all the nanoparticle formulations decreases with increase in temperature from 2 K – 300 K. Also, area enclosed by the hysteresis loops for lipiodol formulations of both BNF and JHU nanoparticles was lower than the corresponding aqueous formulations across all temperatures.

The variation in maximum magnetization for the four nanoparticle formulations is shown in Figure 6.18. For BNF nanoparticles, the lipiodol formulations have an average ~36% lower maximum magnetization than BNF-water. In the case of JHU nanoparticles, this difference was slightly lower with lipiodol formulations having a mean ~ 24% lower maximum magnetization than JHU-water (Figure 6.18). Of all the four nanoparticle formulations, BNF-water has the highest maximum magnetization across all temperatures, with a maximum of 23.26 ± 0.67 kA m^2 g^{-1} at 2 K. Interestingly, while BNF-water had higher maximum magnetization when compared to JHU-Water, for lipiodol formulations JHU-lipiodol had higher maximum magnetization compared to BNF-lipiodol. There was little difference in coercivity between lipiodol and aqueous formulations for both BNF and JHU nanoparticles (Figure 6.19). Overall, as expected coercivity of both the formulations of JHU nanoparticles was lower than that of BNF nanoparticles [51,53]. The approach to saturation for each of the nanoparticle formulations is shown in Figure 6.20. If it is assumed that the easy axis of nanoparticles for all the four formulations is aligned along the direction of the applied field, for large anisotropy, it can be assumed that [58],

$$M(H) = Nm\tanh(\frac{m\mu_0 H}{k_B T}) \quad (6.23)$$

where *M(H)* is the total magnetic moment, *N* is the number of particles, *m* is the magnetic moment per particle, k_B is the Boltzmann constant and *T* is the temperature. The measured *M-H* data were fitted to the above equation and the difference in the measured and fitted data were plotted for all the nanoparticle formulations as shown in Figure 6.21and Figure 6.22. The second peak position in the field shows the effective anisotropy field which is proportional to the area enclosed by the loops. At 250K, the estimated effective anisotropy field for BNF-water and BNF-lipiodol was found to be 342.6 kA/m and 412.1 kA/m respectively. Similarly, the estimated effective anisotropy field for JHU-water and JHU-lipiodol at 250K was 129 kA/m and 173 kA/m respectively. The area enclosed by the hysteresis loop can then be estimated to be proportional to the product of the effective anisotropy and maximum magnetization. This product was higher for BNF-Water (8.3 J/kg) when compared to BNF-lipiodol (6.7 J/kg). Conversely, for JHU-Water this was slightly lower (2.8 J/kg) compared to JHU-lipiodol (2.9 J/kg).

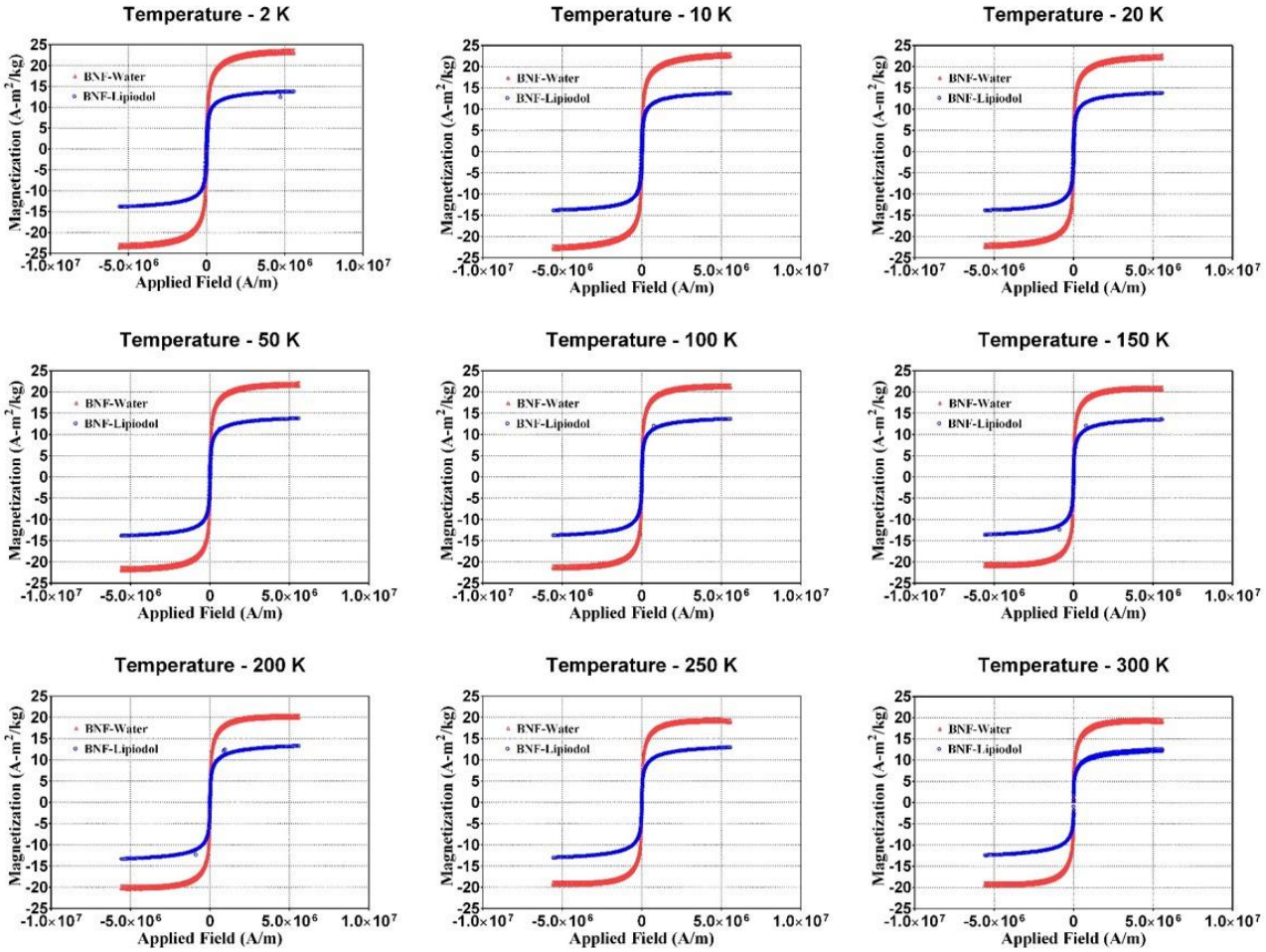

Figure 6.14 Lipiodol formulations of BNF have lower saturation magnetization compared to aqueous formulations. Normalized hysteresis loops for BNF-water and BNF-lipiodol nanoparticles at temperatures 2 K – 300 K. The magnetic moments were normalized to mass of sample. Contributions from sample holder, water, and lipiodol-polysorbate20-water were removed

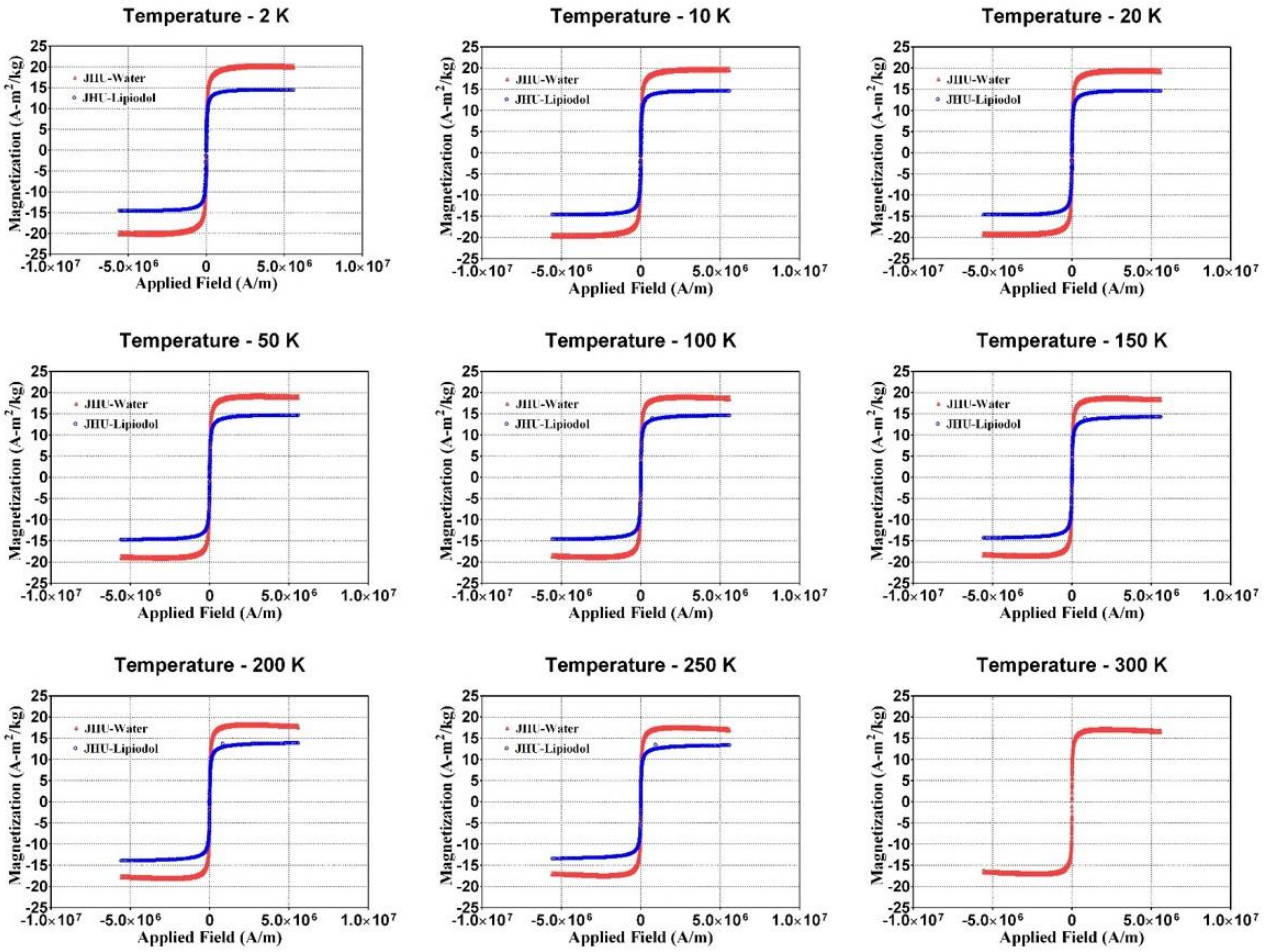

Figure 6.15 Lipiodol formulations of JHU have lower saturation magnetization compared to aqueous formulations. Normalized hysteresis loops for JHU-water and JHU-lipiodol nanoparticles at temperatures 2 K – 300 K. The magnetic moments were normalized to mass of sample. Contributions from sample holder, water, and lipiodol- water were removed.

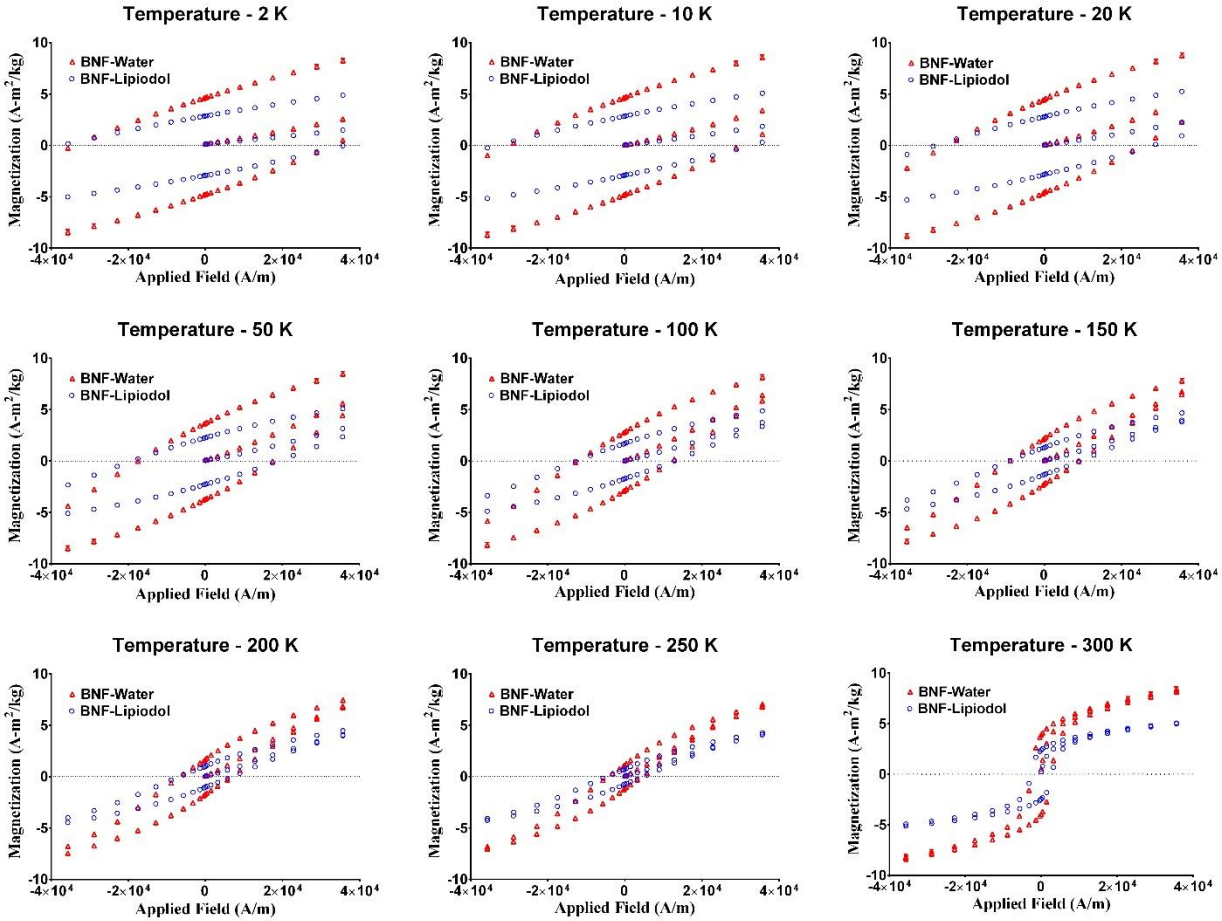

Figure 6.16 Area enclosed decreases with increase in temperature for both aqueous and lipiodol formulations of BNF nanoparticles. Magnified view of measured of normalized hysteresis loops for BNF-water and BNF-lipiodol nanoparticles at temperatures 2 K – 300 K, for applied fields of ±36 kA/m

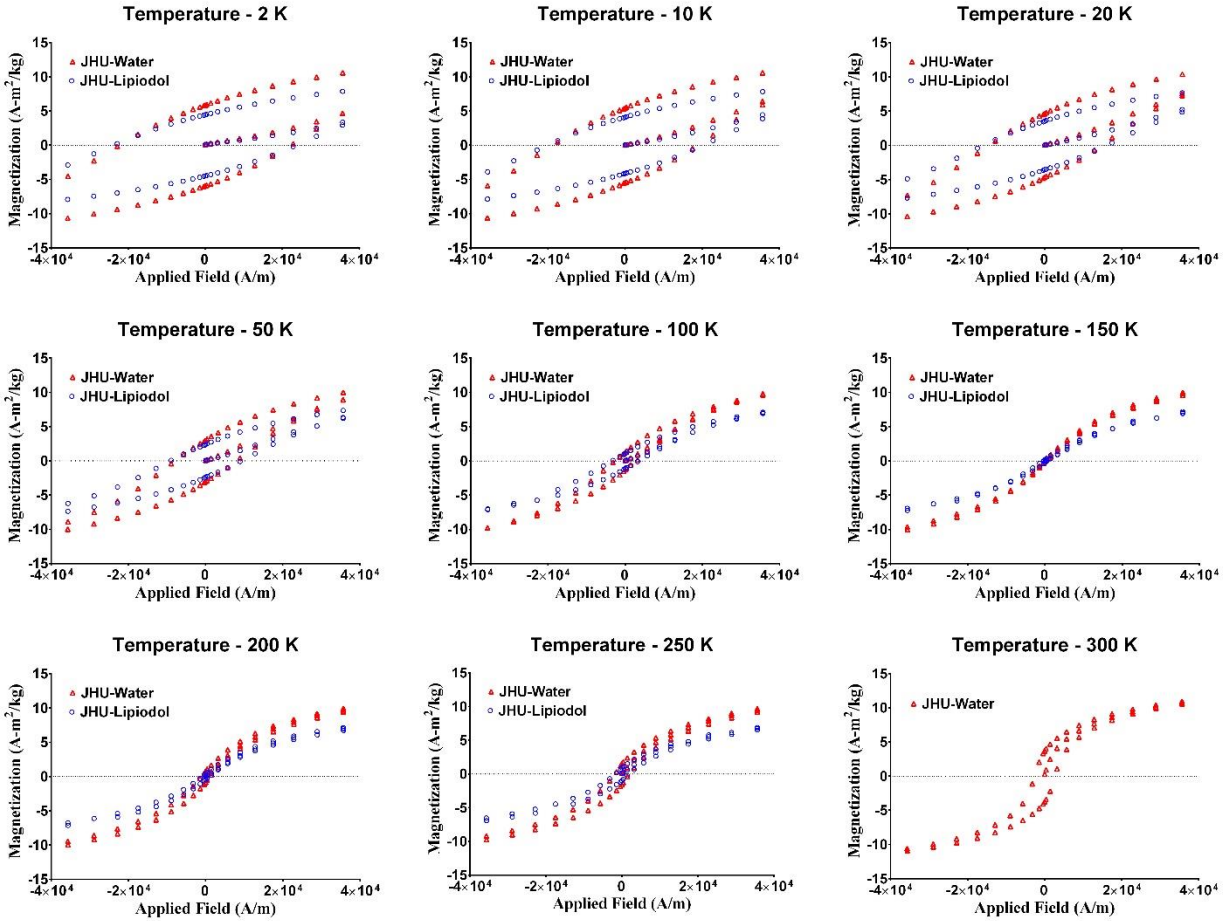

Figure 6.17 Area enclosed decreases with increase in temperature for both aqueous and lipiodol formulations of JHU nanoparticles. Magnified view of measured of normalized hysteresis loops for JHU-water and JHU-lipiodol nanoparticles at temperatures 2 K – 300 K, for applied fields of ±36 kA/m

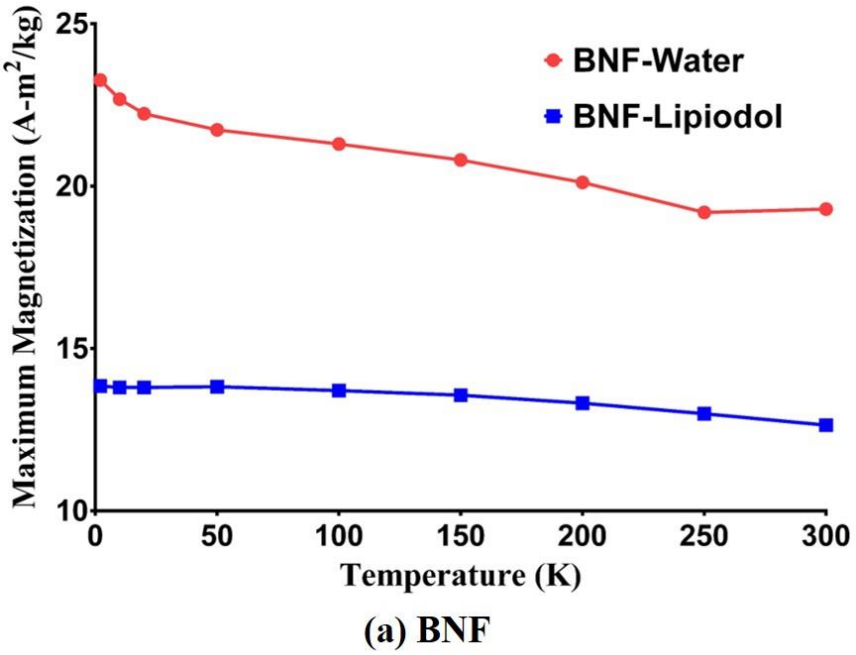

(a) BNF

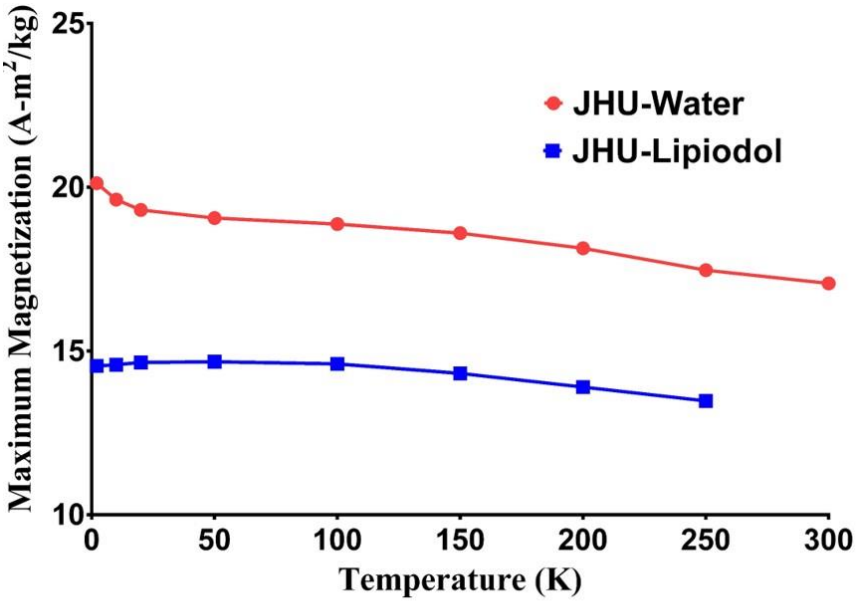

(b) JHU

Figure 6.18 Lipiodol formulations have lower maximum magnetization compared to aqueous formulations Maximum magnetization of lipiodol and aqueous formulations of (a) BNF and (b) JHU nanoparticles measured at temperatures 2 K – 300 K normalized to the sample mass.

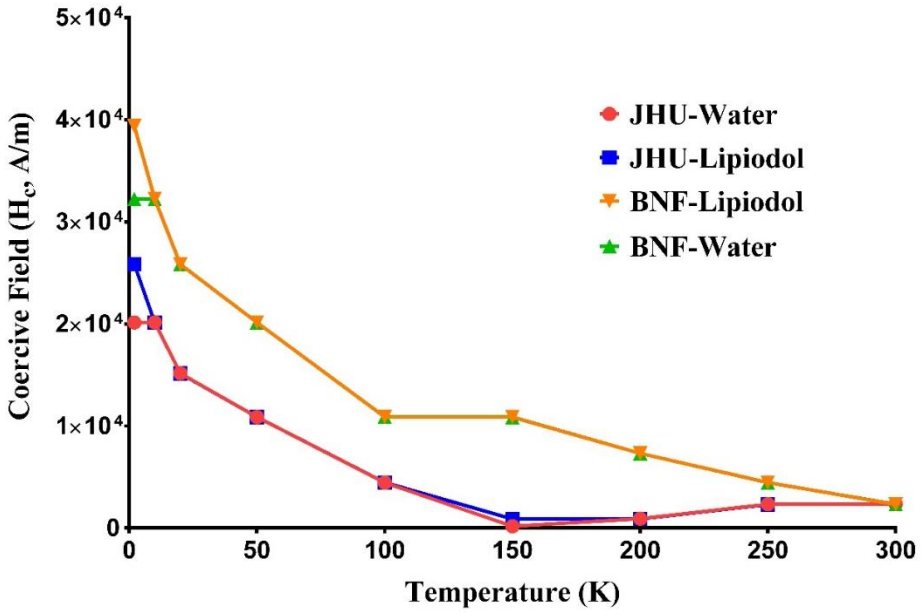

Figure 6.19 Lipiodol and aqueous formulations of BNF and JHU nanoparticles have similar coercivity Coercivity of lipiodol and aqueous formulations of BNF and JHU nanoparticles measured at temperatures 2 K – 300 K.

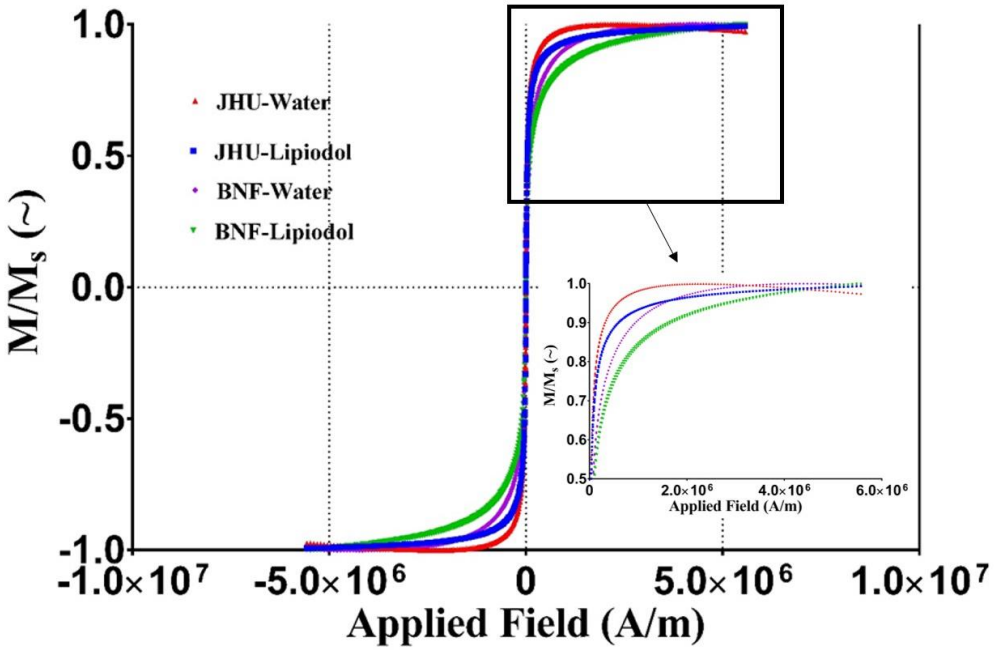

Figure 6.20 Approach to saturation for lipiodol and aqueous formulations of BNF and JHU nanoparticles show distinct differences.

6.3.5 *In vivo* heating simulation results

To estimate the heating of aqueous and lipiodol formulations of nanoparticles in tissues, simulations were carried out using the spherical tumor-healthy tissue model described in section 6.2.9. The mean values of thermal properties of tumor after injection of BNF-water and BNF-lipiodol, were calculated using equations 6.3 - 6.5, and shown in Table 6-3. The thermal diffusivity α_t defined as the ratio of thermal conductivity and volumetric heat capacity, for tumor injected with BNF-lipiodol was lower (0.121 mm^2/s) when compared to BNF-water (0.140 mm^2/s). A higher thermal diffusivity will result in enhanced heat diffusion leading to more transfer of heat away from the heat sources (nanoparticles) in the tumor into the surrounding healthy tissue.

Temperatures achieved at various distances from the center of the tumor after 20 minutes of heating at constant power of 20 kA/m was shown in Figure 6.23 (a). Higher temperatures were achieved in tumor injected with BNF-lipiodol nanoparticles in comparison to BNF-water nanoparticles. The maximum temperature achieved in the tumor with BNF-lipiodol nanoparticles was 54.03 °C compared to 48.34 °C (10.5% lower) for tumor with BNF-water nanoparticles. The decrease in thermal diffusivity of the tumor results in higher temperatures leading to increased thermal damage and decreased survival as can be seen in Figure 6.23 (b). Volume of tumor with $\alpha_t = 0$ is higher for BNF-lipiodol nanoparticles (237.18 mm^3) compared to BNF-water (6.71 mm^3).

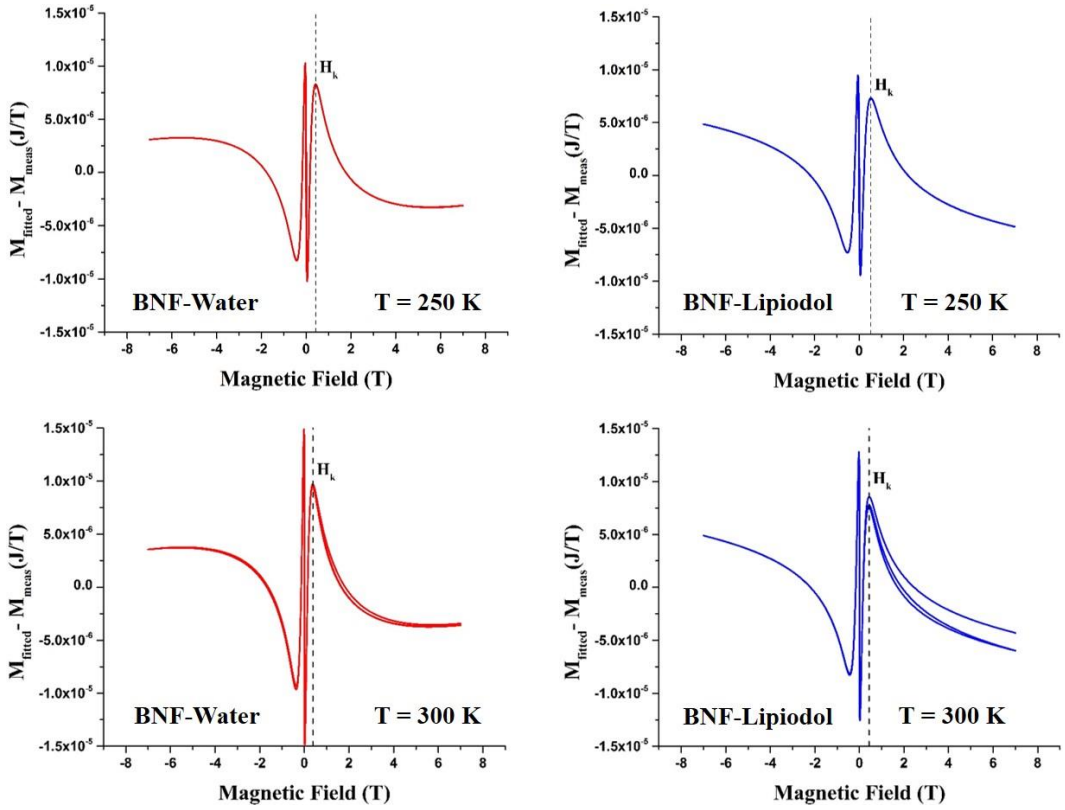

Figure 6.21 Anisotropy field estimation using the Langevin function Difference in the measured magnetization and magnetization determined from fitting a Langevin function to the measured data for BNF-water and BNF-lipiodol

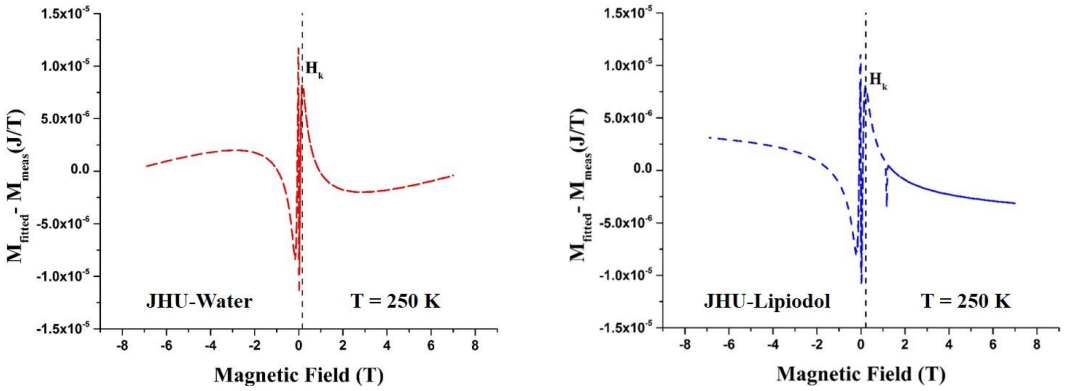

Figure 6.22 Anisotropy field estimation using the Langevin function Difference in the measured magnetization and magnetization determined from fitting a Langevin function to the measured data for JHU-water and JHU-lipiodol

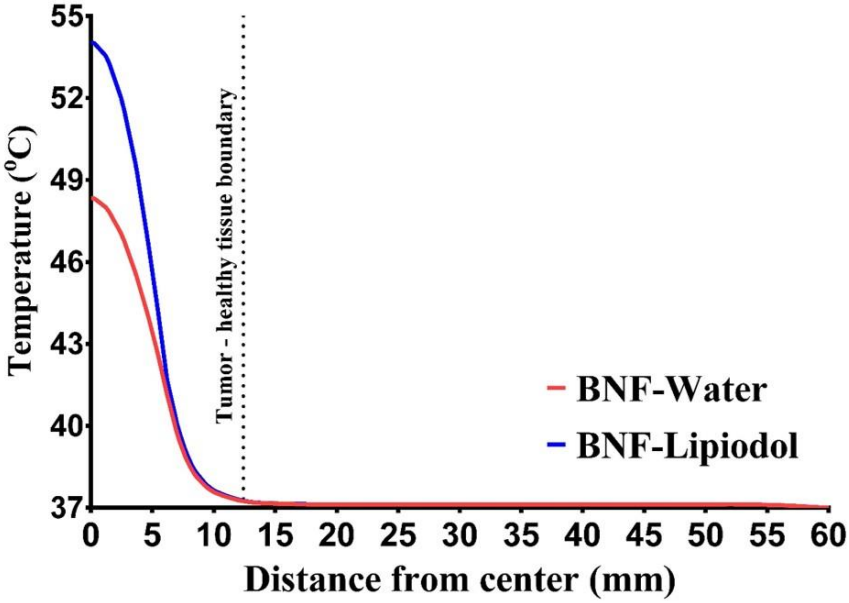

(a)

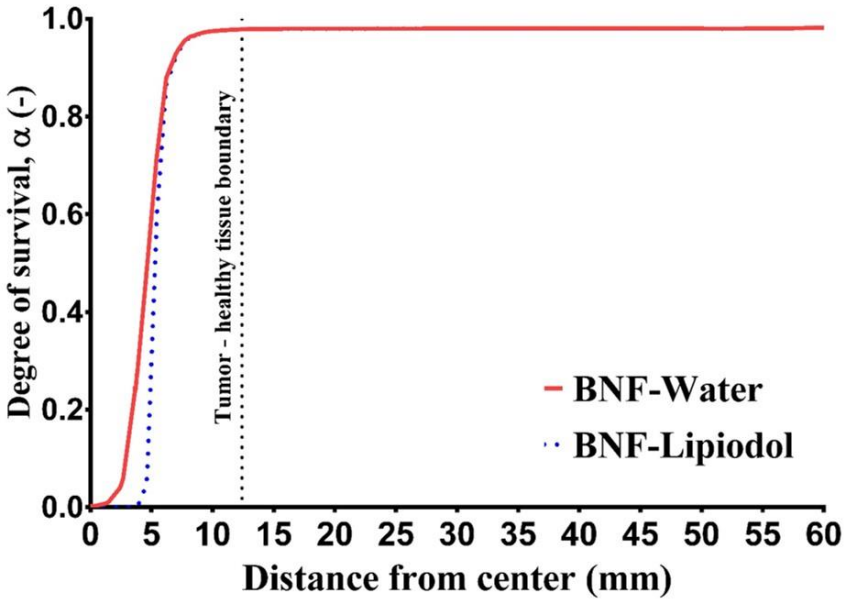

(b)

Figure 6.23 Higher intra-tumor temperatures and thermal damage are achieved in tumors with BNF-lipiodol compared to tumors with BNF-water nanoparticles Computed (a) temperatures, (b) degree of survival at various distances from the tumor center after 20 min of heating at constant field of 20 kA/m.

Table 6-3 Thermal properties of tumor with BNF-water and BNF-lipiodol nanoparticles

	Tumor with BNF – Water	Tumor with BNF-Lipiodol
Thermal conductivity, k_l (W/m-K)	0.561	0.378
Density, ρ_l (kg/m^3)	1039.5	1109.5
Specific heat, C_l (J/kg-K)	3860	2814.5

6.4 Discussion

Magnetic nanoparticles have demonstrated increasing importance for medical applications such as *in vivo* imaging and therapy [38]. Magnetic nanoparticle hyperthermia has advanced for treatment of solid tumor cancers with magnetic iron oxide nanoparticles (MIONs) following favorable demonstrations of their biocompatibility and ability to generate hysteresis heating with an applied alternating magnetic field (AMF) [37]. Lipiodol is an iodinated oil, approved and preferentially used in many clinical image-guided procedures, both as an imaging agent and carrier fluid for active targeting of anti-cancer chemotherapy agents [206]. Formulations containing nanoparticles and lipiodol were previously used for intra-arterial therapies [66,128,129,202–205] but little efforts were made to understand the effect of lipiodol on the thermal and magnetic properties of these nanoparticles. The aim of the current study was to characterize the thermal and magnetic properties of these formulations containing nanoparticles and lipiodol to understand the

increased change in temperatures previously observed and using simulations to accurately estimate the temperatures that can be achieved inside tissue.

TEM images of nanoparticles allow us to estimate the size and organization of the nanoparticles in its aqueous and lipiodol formulations. Size of nanoparticles is an important physicochemical property which can influence their use in imaging and therapeutic applications [217]. The size of the nanoparticle core and formation of complex structures such as chains, or clusters, has an influence on the overall heating power of these nanoparticles [51,60,216]. Complex structures can result from dipole-dipole interactions and can modulate the time-dependent relaxations of the magnetic domains as well as changes in anisotropy (colloidal anisotropy vs magnetocrystalline anisotropy) [51]. These can affect the overall heating efficiency of these nanoparticles. TEM images of aqueous formulations of BNF and JHU nanoparticles were consistent with previous results [57,66]. Surrogate samples of BNF-lip and JHU-lip nanoparticles show large particle clusters with central dark core of nanoparticles and a coating of lipiodol. However, the alteration of lipiodol formulations of BNF and JHU nanoparticles to make them tractable for TEM imaging limits the interpretation of the results obtained from these images. Cryo-TEM imaging also turned out to be futile as the lipiodol formulation sample was too thick for the beam to pass through. Additional measurements will be needed to verify and quantify these clusters but it is to be understood that lipiodol presents a significant challenge to use various measurement techniques.

Heating rates of nanoparticle formulations are generally estimated by taking a sample of nanoparticle formulation in a tube, placing it in an AMF coil using an insulated holder and measuring the temperature rise using a fiber optic sensor (Figure 6.1)

[56,60,218]. The measured temperature rise of the sample is a measure of the change in internal energy of the sample. The rate of change in internal energy normalized to the mass of the nanoparticles depends on both the amount of heat generated by the nanoparticles and the volumetric heat capacity (product of density and specific heat capacity) of the formulations. Most of the formulations used for biological applications are generally water-based and hence the effect of these thermal properties (density, specific heat capacity) on the heating rate and determination of SLP were generally neglected [218].

Rise in temperatures of BNF-lipiodol were consistently higher (Figure 6.5) compared to BNF-water across all the fields tested (8 – 32 kA/m) and were consistent with those reported by Attaluri et al. [66]. But a similar comparison of temperature rise for JHU-water and JHU-lipiodol do not show a similar trend (Figure 6.5 and Figure 6.6). At lower amplitudes (8 – 16 kA/m), JHU-lipiodol has higher rise in temperatures compared to JHU-water but at higher amplitudes (20 – 32 kA/m) this gradually decreases and eventually becomes lower than that of JHU-water. Increased particle sizes (below a specific size) result in higher heat generation by magnetic iron oxide nanoparticles [51]. While TEM images for both BNF-lipiodol and JHU-lipiodol show formation of large clusters, the measured heating rates for JHU-lipiodol were lower (at higher amplitudes) and do not show a clear trend as expected. As explained previously, the TEM imaging was conducted on concentrated surrogate formulations of BNF-lip and JHU-lip, which although can give a general idea of the particle sizes however limits the interpretation of these results.

The volumetric heat capacity of the formulation is the product of density and specific heat capacity of the formulation. Under otherwise similar conditions, for a given heat generation rate of sample, lower volumetric heat capacities result in higher

temperature rises [218]. The density of lipiodol is 1280 kg/m^3 [206], which is 1.28 times that of water. The specific heat capacity of lipiodol was measured to be 1394 J/kg K, which is ~3 times lower than that of water (4180 J/kg K). Thus, the volumetric heat capacity of lipiodol is ~2.3 times lower than that of water. Hence, the increased rise in temperatures observed for BNF-lip compared to BNF-water can be partly explained by the lower volumetric heat capacity of BNF-lip (2381460 J/m^3-K) compared to that of BNF-water (418000 J/m^3-K). However, the lack of replication of a similar trend by JHU-lip in comparison to JHU-water despite having a similar lower volumetric heat capacities suggests possible changes in the heat generated (SLP) by the nanoparticles.

Interestingly, SLPs of lipiodol formulations of both BNF and JHU nanoparticles were lower when compared to their corresponding aqueous formulations (Figure 6.8). The difference in SLP between the lipiodol and aqueous formulations of both BNF and JHU nanoparticles increased with increasing amplitude of applied magnetic field. Statistical analysis of the SLPs for both aqueous and lipiodol formulations signify a statistical difference for the both the BNF and JHU nanoparticles (Figure 6.10 and Figure 6.11). This shows that there is a significant change in the magnetic properties of the nanoparticles when they are suspended in lipiodol. For BNF nanoparticles, the difference in SLP between BNF-water and BNF-lip reduces from ~33% at 8 kA/m to ~17% at 24 kA/m and increases to ~29% at 32 kA/m. This reduction in difference in SLP between BNF-water and BNF-lip combined with lower volumetric heat capacity results in higher rise in temperatures for BNF-lip compared BNF-water (Figure 6.6). The slight decrease in temperature rise for BNF-lip compared to BNF-water at higher amplitudes (28 – 32 kA/m) can be due to

unwanted solvent heating due to heat transfer from the coil through the styrofoam [56], as evidenced by the measured background temperatures at those fields.

The reduction in SLP for lipiodol formulation of JHU (average 31.6%) compared to JHU-water was significantly higher than that of BNF nanoparticles (average 25.8%). Also, in contrast to BNF nanoparticles, the difference in SLP between JHU-lip and JHU-water increases consistently from ~17% at 8 kA/m to ~42% at 32 kA/m. This reduction in SLP with increasing amplitude results in higher temperatures for JHU-lip at lower amplitudes (8 – 16 kA/m) and lower temperatures at higher amplitudes (20 – 32 kA/m) despite having lower volumetric heat capacity, compared to JHU-water. These results show that while lower volumetric heat capacity of lipiodol formulations can enhance the rate of rise in temperatures, significant reduction in SLP could result in overall lower rate of rise in temperatures. This is further confirmed with the computed change in temperatures (Figure 6.12 and Figure 6.13) for the nanoparticle formulations using the computational model described in 6.2.7.

The magnetic properties of the aqueous and lipiodol formulations of BNF and JHU nanoparticles were characterized by measuring the hysteresis loops at temperatures ranging between 2 K and 300 K. Maximum magnetization of BNF-lip and JHU-lip were significantly lower than the corresponding aqueous formulations of BNF and JHU nanoparticles at all measured temperatures. For BNF nanoparticles, the average maximum magnetization for BNF-lip was ~36.1 % lower than that of BNF-water. This significant difference in magnetization suggests that the nanoparticle cores of the two formulations are different. The difference of SLP that was obtained from temperature measurements can be attributed to this observed decrease in magnetization [51,57]. Similarly, for JHU

nanoparticles, the average maximum magnetization for JHU-lip was ~24% lower than that of JHU-water. This is lower than the average difference in SLP (~31.6 %) for JHU-lip which suggests that this observed difference cannot be attributed to reduction in magnetization alone. Change in magnetic anisotropy and size of nanoparticles can also significantly impact the heating efficiency of these nanoparticles [51,57]. Suspending the nanoparticles in lipiodol had little effect on the coercivity of the nanoparticles (Figure 6.19). The approach to saturation for the lipiodol and aqueous formulations of BNF and JHU nanoparticles shows distinct variations (Figure 6.20). These differences can be attributed to different magnetic anisotropies or changes in interactions or change in crystal structure/compositions [57,58]. The estimated effective anisotropies showed that the lipiodol formulations have higher anisotropy compared to aqueous formulations for both BNF and JHU nanoparticles. The area enclosed by *M-H* loop which is proportional to the product of saturation magnetization and effective anisotropy can be used to qualitatively compare the observed differences in SLP. For BNF nanoparticles, this product was significantly lower (~18.6 %) for lipiodol formulation compared to aqueous formulation. This is similar to the observed differences in SLP (average ~ 25.8% lower) for BNF-lip compared to BNF-water. However, for JHU nanoparticle formulations, this product was slightly higher (~3%) for JHU-lip compared to JHU-water. Thus, while DC bulk magnetic measurements can be helpful in determining the saturation/maximum magnetization for the nanoparticle formulations, the energy dissipated by these nanoparticle formulations depends critically on the internal magnetic structure and further measurements would need to be done to clearly understand the observed differences in SLP [51].

The higher temperature rates observed with BNF-lipiodol compared to BNF-water translated to higher intra-tumor temperatures in simulations carried out on a spherical tumor-healthy tissue model. SLP of nanoparticles *in vivo* can vary significantly depending on multiple factors such as aggregation of particles, interparticle interactions, protein/cell-nanoparticle interactions [48,216,219]. Hence, the same SLP (142 W/g Fe @ 20 kA/m) for BNF and BNF-lipiodol was taken to understand the effect of solvent on the temperature distribution inside the tumor. As expected, BNF-lip results in higher intratumor temperatures and thermal damage compared to BNF-water. This was consistent with the enhanced heating observed by Attaluri et al. [66] in their *in vivo* experiments. The lower volumetric heat capacity of lipiodol results in lower thermal diffusivity, helping concentrate the heat inside the tumor, resulting in higher intratumor temperatures. Also, lipiodol can also introduce biological effects such embolization [206] which can result in decrease of blood perfusion. As blood perfusion acts as a heat sink, the reduction in blood perfusion can lead to further increase in intratumor temperatures and thermal damage.

The methods for estimating the SLPs of the formulations have some limitations. Despite the water cooling of the coil, the temperature inside the coil surface rises significantly during the experiment. The styrofoam used as the sample holder is not completely insulating and this results in heat transfer from the coil to the sample. With the relative change in specific heats of formulations, subtraction of background blanks itself will not compensate for the heat transfer from the coil. This can lead to error in estimation of SLPs for the formulation. The shape of the sample tube and volume of sample can also have an effect on the estimated SLPs [218]. Using a spherical shaped bottom sample and higher sample volumes can reduce the error in estimation of SLPs. The computational

model used for estimating the effects of lipiodol on intratumor temperatures has some limitations. First, the assumption of homogeneous distribution of nanoparticles is impractical. In reality, the nanoparticle distribution inside the tumor is highly heterogeneous. Further, a porous tumor model would be more realistic representation of the tumor compared to the current model considered. Additionally, the effect of lipiodol on the vascular structure and thereby on blood perfusion should be considered.

6.5 Conclusion

In this chapter, the thermal and magnetic properties of lipiodol and aqueous formulations of BNF and JHU nanoparticles were determined. The rise in temperatures of the nanoparticle formulations was measured at different fields and compared. The enhanced rise in temperatures observed for BNF-lip in comparison to BNF-water is mainly attributed to the change in thermal properties of solvent. SLP of lipiodol formulations of both BNF and JHU nanoparticles was lower than the corresponding aqueous formulations. Bulk magnetization measurements showed a significant reduction in magnetization for both BNF-lip and JHU-lip compared to their respective aqueous formulations. These results show that both heat generation, which is governed by magnetic properties, and heat transfer, which is governed by the thermal properties, of the formulation need to be considered to estimate the heating performance of nanoparticle formulations to ensure optimal heating with imaging features. Additional physical and magnetic characterization would further allow us to understand the effect of lipiodol on the core of these nanoparticle which can enable us to develop better formulations.

Chapter 7

Thesis summary and future work

7.1 Thesis summary

With cancer becoming one of the leading causes of death worldwide, extensive research efforts are being focused to understand the disease and develop treatments for it. Current standard of care treatments such as surgery, chemotherapy, and radiation therapy have not been effective for all cancers and have been known to have a significant effect on patient's quality of life. Many efforts are currently being undertaken across the world to come up with alternative treatment strategies to improve the efficacy of these treatments and to improve the overall quality of life. One such treatment strategy is hyperthermia –

selectively raising tissue temperatures to inflict thermal damage to cancer cells and sensitize them to traditional treatments such as chemotherapy and radiation therapy. Of the different hyperthermia treatment modalities, magnetic nanoparticle hyperthermia has emerged as one of the most promising because of its ability to selectively heat causing precise and localized thermal damage. The potential to deliver tumor specific heating while minimizing surrounding healthy tissue heating makes it the most attractive hyperthermia modality. Principal challenges for magnetic nanoparticle hyperthermia to become a treatment modality are intratumor nanoparticle distribution, nanoparticle targeting, and minimizing off-target eddy current heating. This thesis has been an attempt to address these challenges by developing strategies and new computational tools. Using heat transfer analysis, computational and experimental efforts were carried out to develop an understanding of the above challenges and present strategies for optimization.

Nanoparticle distribution inside tumor following direct intratumor injection is influenced by injection parameters and by tumor physiological and mechanical properties. This leads to limited control of the nanoparticle distribution inside the tumor. In chapter 2, we first studied the effect of nanoparticle distribution on the temperatures generated inside the tumor using a spherical tumor model with two distributions – uniform and concentrated. Constant power simulations were conducted to understand and highlight the temperature distributions achieved. We then conducted modulated power heating based on temperature feedback at three different locations and showed that modulating power using temperature feedback from the tumor-healthy tissue boundary can deliver therapeutic dose to the tumor for both the distributions.

In chapter 3, this modulated power heating was then improved and implemented in both 2D and 3D computational models for a range of distributions including those derived from animal models. Temperature effects on perfusion were included by modeling it as a function of thermal damage. The modulated power heating method presented in chapter 2 was further improved by implementing a PID controller with temperature feedback from tumor-healthy tissue boundary. It was shown that PID controlled modulated power heating can deliver therapeutic thermal doses to the tumor with minimal surrounding healthy tissue damage. We then compared modulated power heating with constant power heating to show that, with modulated power heating effective thermal damage can be achieved with overall lower temperatures and more temperature homogeneity. Overall, controlling the temperatures achieved at the tumor-healthy tissue boundary with modulated power heating can deliver effective thermal dose to the tumor while simultaneously minimizing healthy tissue damage, compensating for nanoparticle distributions.

We then conducted an *in vivo* pilot study to implement the modulated power heating in subcutaneous xenograft models of liver cancer in mice. Subcutaneous tumors were generated by injecting HepG2 cells on the right thigh of tumor. When the tumor reached the target treatment volume, nanoparticles were injected using two injection methods, 2-pt, and 3-pt with a syringe pump. This was done to generate two intratumor nanoparticle distributions. Using Prussian blue staining combined with image analysis, we generated 3D nanoparticle distributions for the tumors. The generated 3D nanoparticle distributions show that in spite of using controlled nanoparticle injection methods, achieving similar distributions is not possible. For animals in the AMF treatment group, we then manually modulated the applied magnetic field based on temperature feedback from tumor-healthy

tissue interface, to achieve a target temperature of 43.5 ± 0.5 °C. Our results showed that effective control of temperature at the tumor-healthy tissue interface can be achieved for both the distributions consistently. However, treatment resulted in ablation of tumors and skin damage, restricting our study to determine the therapeutic potential. We then carried out a computational study to compare and understand the results from the animal experiments. Results from our simulations predict ablation and skin damage as observed in experiments. This shows that the chosen subcutaneous models, despite their advantages for ease of nanoparticle delivery and tumor measurements, are unsuitable to test our modulated power heating strategy. Additionally, qualitative agreement can be observed between our animal experiments and computational simulations.

Chapter 5 included a rigorous verification and validation of a computational model incorporating both electromagnetic and heat transfer physics. We first developed a computational model which can be used to simultaneously solve for both electromagnetic and heat transfer physics allowing us to understand and model both nanoparticle heating and off-target eddy current heating. The model was first verified with the analytical model and then validated by temperature measurements in agar gel phantom with no nanoparticles exposed to an alternating magnetic field. After this, we developed a 3D model of rabbit liver from CT scan images and computed the temperature distribution due to off-target eddy current heating. Our results showed that hyperthermic temperatures can be achieved at the edges of the liver which can result in significant thermal damage. These models may possibly be used for treatment planning to determine the optimum field parameters for effective tumor damage and minimal healthy tissue damage.

Magnetic nanoparticles suspended in lipiodol can offer dual imaging capabilities in addition to combined chemotherapy and hyperthermia. In chapter 6, we determined the heating efficiency of these dual contrast magnetic nanoparticle formulations used for image-guided magnetic nanoparticle hyperthermia. We measured the specific heat for the lipiodol nanoparticle formulations to be half that of aqueous nanoparticle formulations. With this we showed that the observed higher rise in temperatures for lipiodol nanoparticle formulations was due to reduced specific heat compared to aqueous formulations. Additionally, we also showed that the suspending nanoparticles in lipiodol reduces their heating efficiency compared to aqueous suspensions. Using simulations, we showed that the observed difference in rise in temperatures for BNF and JHU nanoparticle formulations was due to a combined effect of change in specific heat capacity and decreased heating efficiency. Additionally, bulk magnetic measurements also showed a reduction in maximum magnetization for lipiodol formulations compared to aqueous formulations confirming the observed reduced heating efficiency.

7.2 Future work

The temperature control modulated power heating strategy presented in this thesis relies on temperature feedback from single location on the tumor-healthy tissue boundary. With the advent of real-time 3D temperature mapping, temperature feedback from multiple locations on the tumor can be utilized to design a more robust control heating method which can further improve the efficacy of modulated power heating. This becomes important for tumors near sensitive organs such as brain, where the allowance for healthy tissue damage is minimal. Also, employing imaging techniques to determine the vascular structure inside

the tumor can enable us to employ more realistic and accurate bioheat transfer models, some of which were introduced in chapter 1. This would lead to a better understanding of the role of blood perfusion in the temperature distributions generated both inside the tumor and in its vicinity. It is also important to include the role of large blood vessels and artery-vessel pairs when modeling tissues located closer to them. When quantifying thermal damage computationally, it is important to include the thermal sensitivity of that individual cell line instead of using a generic model [29].

Experimental investigation of modulated power MNPH should be carried out in deep seated orthotopic tumor models in large animals. Our *in vivo* experiments clearly show that subcutaneous mouse tumor models are unsuitable for testing modulated power MNPH due to ablation. Also use of imaging resources such as CT imaging for nanoparticle distribution and ultrasound for temperature probe placement would be required and critical for accurately testing this treatment strategy. Additionally, large animal models also allow us to test the limits of power modulation hyperthermia as eddy current heating effects become significant for large animals. This would then require a careful improvement of the temperature control modulated heating strategy to ensure maximizing tumor thermal damage and minimizing healthy tissue heating both due to nanoparticle heating and eddy currents. The combined electromagnetic and heat transfer model developed in chapter 5 can be used to for further improving the modulated power heating strategy to include non-specific eddy current heating effects. The interplay between maximizing tumor thermal dose while ensuring minimal heating of healthy tissue with increases in healthy tissue perfusion due to mild heating can be a very interesting problem to solve. This combined

with realistic tissue-tumor models generated from CT images (as presented in chapter 5) can be used to develop treatment strategies that can be readily translated to the clinic.

The methods developed for generating 3D nanoparticle distribution using Prussian blue images can be used as relatively cheaper method for determining the nanoparticle distribution for labs with limited access to imaging facilities. However, care should be taken for registration of individual tissue slides to ensure that the generated nanoparticle distributions represent the real intratumor nanoparticle distribution. For lipiodol nanoparticle formulations, further magnetic characterization need to be conducted to understand the internal structure of the particles. Small angle neutron scattering experiments can be conducted to determine the internal magnetic structure of these formulations. However, it should be noted that the presence of lipiodol can make conducting these experiments very challenging.

Bibliography

1. Siegel RL, Miller KD, Jemal A. Cancer Statistics, 2017. CA Cancer J Clin. 2017;67(1):7–30.
2. Ferlay J, Soerjomataram I, Dikshit R, Eser S, Mathers C, Rebelo M, et al. Cancer incidence and mortality worldwide: Sources, methods and major patterns in GLOBOCAN 2012. Int J Cancer. 2015;136(5):E359–86.
3. Bray F, Jemal A, Grey N, Ferlay J, Forman D. Global cancer transitions according to the Human Development Index (2008-2030): A population-based study. Lancet Oncol. 2012;13(8):790–801.
4. Cancer Statistics [Internet]. [cited 2017 Feb 8]. Available from: https://www.cancer.gov/about-cancer/understanding/statistics
5. Cancer Moonshot Initiative [Internet]. [cited 2017 Aug 16]. Available from: https://www.cancer.gov/research/key-initiatives/moonshot-cancer-initiative

6. Lawrence T, Haken R Ten, Giaccia A. Principles of radiation oncology. Cancer: principles and practice of oncology. 2008.

7. Momparler RL, Karon M, Siegel SE, Avila F. Effect of Adriamycin on DNA, RNA, and Protein Synthesis in Cell-free Systems and Intact Cells. Cancer Res. 1976;36(8):2891–5.

8. Rudd GN, Hartley JA, Souhami RL. Persistence of cisplatin-induced DNA interstrand crosslinking in peripheral blood mononuclear cells from elderly and young individuals. Cancer Chemother Pharmacol. 1995;35(4):323–6.

9. Dewhirst M, Das S, Stauffer P, Craciunescu O, Vujaskovic Z, Thrall D. Chapter 21 – Hyperthermia. In: Clinical Radiation Oncology. 2012. p. 385–403.

10. Baronzio GF, Hager ED. Hyperthermia in Cancer Treatment: A Primer. Boston, MA: Springer US; 2006.

11. Stauffer PR. Evolving technology for thermal therapy of cancer. Int J Hyperthermia. 2005;21(8):731–44.

12. van den Tempel N, Horsman MR, Kanaar R. Improving efficacy of hyperthermia in oncology by exploting biological mechanisms. Int J Hyperth. 2016;32(4):446–54.

13. Horsman MR, Overgaard J. Hyperthermia: a Potent Enhancer of Radiotherapy. Clin Oncol. 2007;19(6):418–26.

14. Datta NR, Ordóñez SG, Gaipl US, Paulides MM, Crezee H, Gellermann J, et al. Local hyperthermia combined with radiotherapy and-/or chemotherapy: Recent advances and promises for the future. Cancer Treat Rev. 2015;41(9):742–53.

15. Singh BB. Hyperthermia: an ancient science in India. Int J Hyperth. 1991;7(February):1–6.

16. Sardari D, Verga N. Cancer Treatment with Hyperthermia. In: Ozdemir O, editor. Current Cancer Treatment - Novel Beyond Conventional Approaches. 2011. p. 455–74.

17. Toraya-Brown S, Fiering S. Local tumour hyperthermia as immunotherapy for metastatic cancer. Int J Hyperth. 2014;30(8):1464–5157.

18. Hildebrandt B, Wust P, Ahlers O, Dieing A, Sreenivasa G, Kerner T, et al. The cellular and molecular basis of hyperthermia. Crit Rev Oncol Hematol. 2002;43(1):33–56.

19. Bettaieb A, Wrzal PK, Averill-Bates DA. Hyperthermia: Cancer Treatment and Beyond. In: Cancer Treatment - Conventional and Innovative Approaches. InTech; 2013. p. 135–52.

20. Vaupel PW, Kelleher DK. Pathophysiological and vascular characteristics of tumours and their importance for hyperthermia: heterogeneity is the key issue. Int J Hyperthermia. 2010;26(3):211–23.

21. Bergs JWJ, Franken N a P, Haveman J, Geijsen ED, Crezee J, van Bree C. Hyperthermia, cisplatin and radiation trimodality treatment: a promising cancer treatment? A review from preclinical studies to clinical application. Int J Hyperthermia. 2007;23(4):329–41.

22. Hurwitz M, Stauffer P. Hyperthermia, radiation and chemotherapy: The role of heat in multidisciplinary cancer care. Semin Oncol. 2014;41(6):714–29.

23. Vaupel P, Kallinnowski F. Physiological effects of hyperthermia. In: Hyperthermia and the therapy of malignant tumors. Springer Berlin Heidelberg; 1987. p. 71–109.

24. van Rhoon GC. Is CEM43 still a relevant thermal dose parameter for hyperthermia

treatment monitoring? Int J Hyperth Off J Eur Soc Hyperthermic Oncol North Am Hyperth Gr. 2016;6736(January):1–13.

25. Sapareto SA, Dewey WC. Thermal dose determination in cancer therapy. Int J Radiat Oncol Biol Phys. 1984;10(6):787–800.

26. Pearce JA. Relationship between Arrhenius models of thermal damage and the CEM 43 thermal dose. Energy-based Treat if Tissue Assess V. 2009;7181(2):1–15.

27. He X, Bhowmick S, Bischof JC. Thermal Therapy in Urologic Systems: A Comparison of Arrhenius and Thermal Isoeffective Dose Models in Predicting Hyperthermic Injury. J Biomech Eng. 2009;131(7):74507.

28. Franken NAP, Rodermond HM, Stap J, Haveman J, van Bree C. Clonogenic assay of cells in vitro. Nat Protoc. 2006;1(5):2315–9.

29. Pearce J a. Comparative analysis of mathematical models of cell death and thermal damage processes. Int J Hyperthermia. 2013;29(4):262–80.

30. Dewey WC. Arrhenius relationships from the molecule and cell to the clinic. Int J Hyperth. 1994;10(4):457–83.

31. Leopold KA, Dewhirst M, Samulski T, Harrelson J, Tucker JA, George SL, et al. Relationships among tumor temperature, treatment time, and histopathological outcome using preoperative hyperthermia with radiation in soft tissue sarcomas. Int J Radiat Oncol Biol Phys. 1992;22(5):989–98.

32. Dewhirst MW, Viglianti BL, Lora-Michiels M, Hanson M, Hoopes PJ. Basic principles of thermal dosimetry and thermal thresholds for tissue damage from hyperthermia. Int J Hyperth. 2003;19(3):267–94.

33. He X, John B. Quantification of Temperature and Injury Response in Thermal

Therapy and Cryosurgery. Crit Rev Biomed Eng. 2003;31(5–6):355–422.

34. Wust P, Cho CH, Hildebrandt B, Gellermann J, Wust P, Cho CH, et al. Thermal monitoring : Invasive , minimal-invasive and non-invasive approaches. 2017;6736(February).

35. Ni Y, Mulier S, Miao Y, Michel L, Marchal G. A review of the general aspects of radiofrequency ablation. Abdom Imaging. 2005;30(4):381–400.

36. Manuchehrabadi N, Zhu L. Gold Nanoparticle-Based Laser Photothermal therapy. In: Kulacki FA, editor. Handbook of Thermal Science and Engineering. Springer International Publishing; 2017. p. 1–33.

37. Ivkov R. Magnetic nanoparticle hyperthermia: A new frontier in biology and medicine? Int J Hyperth. 2013;29(8):703–5.

38. Pankhurst QA, Thanh NTK, Jones SK, Dobson J. Progress in applications of magnetic nanoparticles in biomedicine. J Phys D Appl Phys. 2009;42(22):224001.

39. Maier-Hauff K, Ulrich F, Nestler D, Niehoff H, Wust P, Thiesen B, et al. Efficacy and safety of intratumoral thermotherapy using magnetic iron-oxide nanoparticles combined with external beam radiotherapy on patients with recurrent glioblastoma multiforme. J Neurooncol. 2011;103(2):317–24.

40. Gilchrist RK, Medal R, Shorey WD, Hanselman RC, Parrott JC, Taylor CB. Selective Inductive Heating of Lymph Nodes *. Ann Surg. 1957;146(4):596–606.

41. Maier-Hauff K, Rothe R, Scholz R, Gneveckow U, Wust P, Thiesen B, et al. Intracranial thermotherapy using magnetic nanoparticles combined with external beam radiotherapy: Results of a feasibility study on patients with glioblastoma multiforme. J Neurooncol. 2007;81(1):53–60.

42. Zadnik PL, Molina CA, Sarabia-Estrada R, Groves ML, Wabler M, Mihalic J, et al. Characterization of intratumor magnetic nanoparticle distribution and heating in a rat model of metastatic spine disease. J Neurosurg Spine. 2014;20(6):740–50.

43. Johannsen M, Gneveckow U, Thiesen B, Taymoorian K, Hee C, Waldo N, et al. Thermotherapy of Prostate Cancer Using Magnetic Nanoparticles : Feasibility , Imaging , and Three-Dimensional Temperature Distribution. 2007;52:1653–62.

44. Johannsen M, Gneveckow U, Taymoorian K, Thiesen B, Waldöfner N, Scholz R, et al. Morbidity and quality of life during thermotherapy using magnetic nanoparticles in locally recurrent prostate cancer: results of a prospective phase I trial. Int J Hyperth. 2007;23(May):315–23.

45. Johannsen M, Thiesen B, Wust P, Jordan A. Magnetic nanoparticle hyperthermia for prostate cancer. Int J Hyperth. 2010;26(8):790–5.

46. Johannsen M, Gneveckow U, Eckelt L, Feussner A, Waldöfner N, Scholz R, et al. Clinical hyperthermia of prostate cancer using magnetic nanoparticles: presentation of a new interstitial technique. Int J Hyperthermia. 2005;21(March 2016):637–47.

47. Dennis CL, Jackson AJ, Borchers JA, Hoopes PJ, Strawbridge R, Foreman AR, et al. Nearly complete regression of tumors via collective behavior of magnetic nanoparticles in hyperthermia. Nanotechnology. 2009;20(39):395103.

48. Giustini AJ, Ivkov R, Hoopes PJ. Magnetic nanoparticle biodistribution following intratumoral administration. Nanotechnology. 2011;22(34):345101.

49. DeNardo SJ, DeNardo GL, Natarajan A, Miers LA, Foreman AR, Gruettner C, et al. Thermal dosimetry predictive of efficacy of 111In-ChL6 nanoparticle AMF--induced thermoablative therapy for human breast cancer in mice. J Nucl Med.

2007;48(3):437–44.

50. DeNardo SJ, DeNardo GL, Miers LA, Natarajan A, Foreman AR, Gruettner C, et al. Development of tumor targeting bioprobes (111In-chimeric L6 monoclonal antibody nanoparticles) for alternating magnetic field cancer therapy. Clin Cancer Res. 2005;11(19 II):7087–93.

51. Dennis CL, Ivkov R. Physics of heat generation using magnetic nanoparticles for hyperthermia. Int J Hyperthermia. 2013;29(8):715–29.

52. Attaluri A, Kandala SK, Wabler M, Zhou H, Cornejo C, Armour M, et al. Magnetic nanoparticle hyperthermia enhances radiation therapy: A study in mouse models of human prostate cancer. Int J Hyperthermia. 2015;31(4):359–74.

53. Hedayati M, Attaluri A, Bordelon D, Goh R, Armour M, Zhou H, et al. New iron-oxide particles for magnetic nanoparticle hyperthermia: an *in-vitro* and *in-vivo* pilot study. 2013;8584:858404.

54. Moroz P, Jones SK, Gray BN. Magnetic Mediated Hyperthermia: Current Status and Future Directions. Int J. 2002;18(4):267–84.

55. Grüttner C, Müller K, Teller J, Westphal F, Foreman A, Ivkov R. Synthesis and antibody conjugation of magnetic nanoparticles with improved specific power absorption rates for alternating magnetic field cancer therapy. J Magn Magn Mater. 2007;311(1 SPEC. ISS.):181–6.

56. Bordelon DE, Cornejo C, Grttner C, Westphal F, Deweese TL, Ivkov R. Magnetic nanoparticle heating efficiency reveals magneto-structural differences when characterized with wide ranging and high amplitude alternating magnetic fields. J Appl Phys. 2011;109(12).

57. Dennis CL, Krycka KL, Borchers JA, Desautels RD, Van Lierop J, Huls NF, et al. Internal Magnetic Structure of Nanoparticles Dominates Time-Dependent Relaxation Processes in a Magnetic Field. Adv Funct Mater. 2015;25(27):4300–11.

58. Carrey J, Mehdaoui B, Respaud M. Simple models for dynamic hysteresis loop calculations of magnetic single-domain nanoparticles: Application to magnetic hyperthermia optimization. J Appl Phys. 2011;109(8).

59. Andreu I, Natividad E. Accuracy of available methods for quantifying the heat power generation of nanoparticles for magnetic hyperthermia. Int J Hyperth. 2013;29(8):739–51.

60. Soetaert F, Kandala SK, Bakuzis A, Ivkov R. Experimental estimation and analysis of variance of the measured loss power of magnetic nanoparticles. Sci Rep. 2017;7(1):6661.

61. Atkinson WJ, Brezovich IA, Chakraborty DP. Usable Frequencies in Hyperthermia with Thermal Seeds. IEEE Trans Biomed Eng. 1984;BME-31(1):70–5.

62. Dutz S, Hergt R. Magnetic nanoparticle heating and heat transfer on a microscale: Basic principles, realities and physical limitations of hyperthermia for tumour therapy. Int J Hyperthermia. 2013;29(8):790–800.

63. Cole AJ, Yang VC, David AE. Cancer theranostics: The rise of targeted magnetic nanoparticles. Trends Biotechnol. 2011;29(7):323–32.

64. Wilhelm S, Tavares AJ, Dai Q, Ohta S, Audet J, Dvorak HF, et al. Analysis of nanoparticle delivery to tumours. Nat Rev Mater. 2016;1(5):16014.

65. Kozissnik B, Bohorquez AC, Dobson J, Rinaldi C. Magnetic fluid hyperthermia: advances, challenges, and opportunity. Int J Hyperthermia. 2013;29(8):706–14.

66. Attaluri A, Seshadri M, Mirpour S, Wabler M, Marinho T, Furqan M, et al. Image-guided thermal therapy with a dual-contrast magnetic nanoparticle formulation: A feasibility study. Int J Hyperth. 2016;6736(June):1–15.

67. van Landeghem FKH, Maier-Hauff K, Jordan A, Hoffmann KT, Gneveckow U, Scholz R, et al. Post-mortem studies in glioblastoma patients treated with thermotherapy using magnetic nanoparticles. Biomaterials. 2009;30(1):52–7.

68. Salloum M, Ma RH, Weeks D, Zhu L. Controlling nanoparticle delivery in magnetic nanoparticle hyperthermia for cancer treatment: experimental study in agarose gel. Int J Hyperthermia. 2008;24(4):337–45.

69. LeBrun A, Joglekar T, Bieberich C, Ma R, Zhu L. Identification of infusion strategy for achieving repeatable nanoparticle distribution and quantification of thermal dosage using micro-CT Hounsfield unit in magnetic nanoparticle hyperthermia. Int J Hyperth. 2016;6736(February):1–12.

70. Borgnakke C, Sonntag R. Fundamentals of thermodynamics. Wiley Global Education; 2016.

71. Moros E. Physics of thermal therapy: fundamentals and clinical applications. CRC Press; 2012.

72. Bergman T, Incropera F, Dewitt D, Lavine A. Fundamentals of heat and mass transfer. John Wiley & Sons; 2011.

73. Bhowmik A, Singh R, Repaka R, Mishra SC. Conventional and newly developed bioheat transport models in vascularized tissues: A review. J Therm Biol. 2013;38(3):107–25.

74. Cetingül MP, Herman C. A heat transfer model of skin tissue for the detection of

lesions: sensitivity analysis. Phys Med Biol. 2010;55(19):5933–51.

75. Yue K, Zheng S, Luo Y, Zhang X, Tang J. Determination of the 3D temperature distribution during ferromagnetic hyperthermia under the influence of blood flow. J Therm Biol. 2011;36(8):498–506.

76. Despa F, Orgill DP, Neuwalder J, Lee RC. The relative thermal stability of tissue macromolecules and cellular structure in burn injury. Burns. 2005;31(5):568–77.

77. Arkin H, Xu LX, Holmes KR. Recent Developments in Modeling Heat Transfer in Blood Perfused Tissues. IEEE Trans Biomed Eng. 1994;41(2):97–107.

78. Khaled ARA, Vafai K. The role of porous media in modeling flow and heat transfer in biological tissues. Int J Heat Mass Transf. 2003;46(26):4989–5003.

79. Charny CK. Mathematical Models of Bioheat Transfer. Adv Heat Transf. 1992;22(C):19–155.

80. Baish JW, Ayyaswamy PS, Foster KR. Heat transport mechanisms in vascular tissues: a model comparison. J Biomech Eng. 1986;108(4):324–31.

81. Pennes HH. Applied Physiology. J Appl Physiol. 1948;1:93–122.

82. Wulff W. The Energy Conservation Equation for Living Tissue. IEEE Trans Biomed Eng. 1974;BME-21(6):494–5.

83. Mitchell JW, Myers GE. An Analytical Model of the Counter-Current Heat Exchange Phenomena. Biophys J. 1968;8(8):897–911.

84. Keller KH, Seiler L. An analysis of peripheral heat transfer in man. J Appl Physiol. 1971;30(5).

85. Chen MM, Holmes KR. Microvascular Contributions in Tissue Heat Transfer. Ann N Y Acad Sci. 1980;335(1):137–50.

86. Jiji LM, S. Weinbaum DEL. Theory and Experiment for the Effect of Vascular iicrostructure on Surface Tissue Heat Transfer — Part I : Anatomical Foundation and Model Conceptualization. J Biomech Eng. 1984;106(4):331–41.

87. Jiji LM, S. Weinbaum DEL. Theory and Experiment for the Effect of Vascular iicrostructure on Surface Tissue Heat Transfer — Part II : Model Formulation and Solution. J Biomech Eng. 1984;106(4):331–41.

88. Weinbaum S, Jiji LM. A new simplified bioheat equation for the effect of blood flow on local average tissue temperature. J Biomech Eng. 1985;107(2):131–9.

89. Song WJ, Weinbaum S, Jiji LM. A theoretical model for peripheral tissue heat transfer using the bioheat equation of Weinbaum and Jiji. J Biomech Eng. 1987;109(1):72–8.

90. Baish JW, Ayyaswamy PS, Foster KR. Small-scale temperature fluctuations in perfused tissue during local hyperthermia. J Biomech Eng. 1986;108(3):246–50.

91. Wissler EH. Comments on Weinbaum and Jiji's Discussion of Their Proposed Bioheat Equation. 1987;109(November 1987):355–6.

92. Charny CK, Weinbaum S, Levin RL. An evaluation of the Weinbaum-Jiji bioheat equation for normal and hyperthermic conditions. J Biomech Eng. 1990;112(1):80–7.

93. Baish JW. Formulation of a statistical model of heat transfer in perfused tissue. J Biomech Eng. 1994;116(4):521–7.

94. Xu F, Lu T, Seffen KA. Dual-Phase-Lag model of skin bioheat transfer. Biomed Eng Informatics New Dev Futur - Proc 1st Int Conf Biomed Eng Informatics, BMEI 2008. 2008;1:505–11.

95. Roetzel W, Xuan Y. Transient response of the human limb to an external stimulust. Int J Heat Mass Transf. 1998;41(1):229–39.

96. Shih T-C, Kou H-S, Liauh C-T, Lin W-L. Thermal Models of Bioheat Transfer Equations in Living Tissue and Thermal Dose Equivalence Due To Hyperthermia. Biomed Eng Appl Basis Commun. 2002;14(2):86–96.

97. Nakayama A, Kuwahara F. A general bioheat transfer model based on the theory of porous media. Int J Heat Mass Transf. 2008;51(11–12):3190–9.

98. Lagendijk JJ. The influence of bloodflow in large vessels on the temperature distribution in hyperthermia. Phys Med Biol. 1982;27(1):17–23.

99. Lagendijk JJ, Schellekens M, Schipper J, van der Linden PM. A three-dimensional description of heating patterns in vascularised tissues during hyperthermic treatment. Phys Med Biol. 1984;29(5):495–507.

100. Mooibroek J, Lagendijk JJW. A fast and simple algorithm for the calculation of convective heat transfer by large vessels in three-dimensional inhomogeneous tissues. IEEE Trans Biomed Eng. 1991;38(5):490–501.

101. Van Leeuwen GMJ, Kotte TJ, Crezee J, Lagendijk JJW. Tests of the geometrical description of blood vessels in a thermal model using counter-current geometries. Phys Med Biol Phys Med Biol. 1997;42(42):1515–32.

102. Kotte TJ, Van Leeuwen MJ, Lagendijk JJW. Modelling the thermal impact of a discrete vessel tree. Phys Med Biol Phys Med Biol. 1999;44(4499):57–74.

103. Shrivastava D, Roemer RB. Readdressing the issue of thermally significant blood vessels using a countercurrent vessel network. J Biomech Eng. 2006;128(2):210–6.

104. Shrivastava D, Vaughan JT. A generic bioheat transfer thermal model for a perfused

tissue. J Biomech Eng. 2009;131(7):74506.

105. Pearce J, Petryk AA, Hoopes J. Numerical Model Study of In Vivo Magnetic Nanoparticle Tumor Heating. IEEE Trans Biomed Eng. 2017;9294(c):1–1.

106. Wissler EH. 50 years of JAP Pennes ' 1948 paper revisited. J Appl Physiol. 2012;35–41.

107. Nelson D a. Invited editorial on "Pennes' 1948 paper revisited". J Appl Physiol. 1998;85(1):2–3.

108. Nunneley DANSA. Brain temperature and limits on transcranial cooling in humans, quantitative modeling results. Eur J Appl Physiol Occup Physiol. 1998;78(4):353–9.

109. Datta A, Rakesh V. An Introduction to Modeling of Transport Processes : Application to Biomedical Systems. Cambridge University Press; 2010.

110. COMSOL Multiphysics 5.2a.

111. Takahashi I, Emi Y, Hasuda S, Kakeji Y, Maehara Y, Sugimachi K. Clinical application of hyperthermia combined with anticancer drugs for the treatment of solid tumors. Surgery. 2002;131(1 SUPPL.):78–84.

112. Salloum M, Ma R, Zhu L. Enhancement in treatment planning for magnetic nanoparticle hyperthermia: Optimization of the heat absorption pattern. Int J Hyperth. 2009;25(4):309–21.

113. Leopold KA, Dewhirst MW, Samulski T V., Dodge RK, George SL, Blivin JL, et al. Cumulative minutes with T90 greater than tempindex is predictive of response of superficial malignancies to hyperthermia and radiation. Int J Radiat Oncol Biol Phys. 1993;25(5):841–7.

114. Andrä W, D'Ambly CG, Hergt R, Hilger I, Kaiser WA. Temperature distribution as function of time around a small spherical heat source of local magnetic hyperthermia. J Magn Magn Mater. 1999;194(1):197–203.

115. Bagaria HG, Johnson DT. Transient solution to the bioheat equation and optimization for magnetic fluid hyperthermia treatment. Int J Hyperth. 2005;21(1):57–75.

116. Durkee JW, Antich PP. Exact solutions to the multi-region time-dependent bioheat equation with transient heat sources and boundary conditions. Phys Med Biol. 1991;36(3):345–68.

117. Giordano MA, Gutierrez G, Rinaldi C. Fundamental solutions to the bioheat equation and their application to magnetic fluid hyperthermia. Int J Hyperth. 2010;26(5):475–84.

118. Fasla B, Benmouna Ŕ, Benmouna M. Modeling of tumor's tissue heating by nanoparticles. J Appl Phys. 2010;108(12).

119. Xu R, Yu H, Zhang Y, Ma M, Chen Z, Wang C, et al. Three-dimensional model for determining inhomogeneous thermal dosage in a liver tumor during arterial embolization hyperthermia incorporating magnetic nanoparticles. IEEE Trans Magn. 2009;45(8):3085–91.

120. Attar MM, Haghpanahi M, Amanpour S, Mohaqeq M. Analysis of bioheat transfer equation for hyperthermia cancer treatment. J Mech Sci Technol. 2014;28(2):763–71.

121. Tompkins DT, Vanderby R, Klein S a, Beckman W a, Steeves R a, Frye DM, et al. Temperature-dependent versus constant-rate blood perfusion modelling in

ferromagnetic thermoseed hyperthermia: results with a model of the human prostate. Int J Hyperth. 1994;10(4):517–36.

122. Hasgall P, Neufeld E, Gosselin M, Klingenböck A. IT'IS Database for thermal and electromagnetic parameters of biological tissues. Version 2.6. 2015.

123. Buckley DL, Roberts C, Parker GJM, Logue JP, Hutchinson CE. Prostate cancer: evaluation of vascular characteristics with dynamic contrast-enhanced T1-weighted MR imaging--initial experience. Radiology. 2004;233(3):709–15.

124. Duck F. Physical properties of tissues: a comprehensive reference book. Academic Press; 2013.

125. Torvi D a, Dale JD. A finite element model of skin subjected to a flash fire. J Biomech Eng. 1994;116(3):250–5.

126. Folkman J. The Vascularization of Tumors. 1976;234(5):58–73.

127. Jones EL, Oleson JR, Prosnitz LR, Samulski T V., Vujaskovic Z, Yu D, et al. Randomized trial of hyperthermia and radiation for superficial tumors. J Clin Oncol. 2005;23(13):3079–85.

128. Moroz P, Jones SK, Winter J, Gray BN. Targeting liver tumors with hyperthermia: Ferromagnetic embolization in a rabbit liver tumor model. J Surg Oncol. 2001;78(1):22–9.

129. Moroz P, Pardoe H, Jones SK, Pierre TGS, Song S, Gray BN. Arterial embolization hyperthermia : hepatic iron particle distribution and its potential determination by magnetic resonance imaging. Phys Med Biol. 2002;47:1591–602.

130. Kossatz S, Ludwig R, Dähring H, Ettelt V, Rimkus G, Marciello M, et al. High therapeutic efficiency of magnetic hyperthermia in xenograft models achieved with

moderate temperature dosages in the tumor area. Pharm Res. 2014;31(12):3274–88.

131. Rodrigues HF, Mello FM, Branquinho LC, Zufelato N, Silveira-Lacerda EP, Bakuzis AF. Real-time infrared thermography detection of magnetic nanoparticle hyperthermia in a murine model under a non-uniform field configuration. Int J Hyperthermia. 2013;29(8):752–67.

132. Attaluri A, Ma R, Qiu Y, Li W, Zhu L. Nanoparticle distribution and temperature elevations in prostatic tumours in mice during magnetic nanoparticle hyperthermia. Int J Hyperth. 2011;27(5):491–502.

133. Johannsen M, Thiesen B, Gneveckow U, Taymoorian K, Waldöfner N, Scholz R, et al. Thermotherapy using magnetic nanoparticles combined with external radiation in an orthotopic rat model of prostate cancer. Prostate. 2006;66(1):97–104.

134. Johannsen M, Thiesen B, Jordan A, Taymoorian K, Gneveckow U, Waldöfner N, et al. Magnetic fluid hyperthermia (MFH) reduces prostate cancer growth in the orthotopic Dunning R3327 rat model. Prostate. 2005;64(3):283–92.

135. Pavel M, Stancu A. Ferromagnetic nanoparticles dose based on tumor size in magnetic fluid hyperthermia cancer therapy. IEEE Trans Magn. 2009;45(11):5251–4.

136. Candeo A, Dughiero F. Numerical fem models for the planning of magnetic induction hyperthermia treatments with nanoparticles. IEEE Trans Magn. 2009;45(3):1658–61.

137. Mital M, Tafreshi H V. A methodology for determining optimal thermal damage in magnetic nanoparticle hyperthermia cancer treatment. Int j numer method biomed eng. 2012;28(2):205–13.

138. Bellizzi G, Bucci OM, Ii F. On the optimal choice of the exposure conditions and the nanoparticle features in magnetic nanoparticle hyperthermia. Int J Hyperthermia. 2010;26(4):389–403.

139. Bellizzi G, Bucci OM, Chirico G. Numerical assessment of a criterion for the optimal choice of the operative conditions in magnetic nanoparticle hyperthermia on a realistic model of the human head. 2016;6736(August).

140. Koch CM, Winfrey AL. FEM Optimization of Energy Density in Tumor Hyperthermia Power Dissipation. Ieee Trans Magn. 2014;50(10).

141. Soetaert F, Dupré L, Ivkov R, Crevecoeur G. Computational evaluation of amplitude modulation for enhanced magnetic nanoparticle hyperthermia. Biomed Tech. 2015;60(5):491–504.

142. Salomir R, Vimeux FC, de Zwart JA, Grenier N, Moonen CTW. Hyperthermia by MR-guided focused ultrasound: Accurate temperature contSalomir, R., Vimeux, F. C., de Zwart, J. A., Grenier, N., & Moonen, C. T. W. (2000). Hyperthermia by MR-guided focused ultrasound: Accurate temperature control based on fast MRI and a . Magn Reson Med. 2000;43(3):342–7.

143. Mougenot C, Quesson B, De Senneville BD, De Oliveira PL, Sprinkhuizen S, Palussière J, et al. Three-dimensional spatial and temporal temperature control with MR thermometry-guided focused ultrasound (MRgHIFU). Magn Reson Med. 2009;61(3):603–14.

144. Haemmerich D, Webster JG. Automatic control of finite element models for temperature-controlled radiofrequency ablation. Biomed Eng Online. 2005;4:42.

145. Ebert JL, Van Der Linden GW, De Roover D, Porter LL, Kosut RL, Emami-Naeini

A. Model-based temperature control of heated plates. 18th Int Conf Adv Therm Process Semicond RTP 2010. 2010;(1):54–61.

146. Astrom K. PID controllers: theory, design and tuning. Instrument Society of America. 1995. p. 343.

147. He X, McGee S, Coad JE, Schmidlin F, Iaizzo P a, Swanlund DJ, et al. Investigation of the thermal and tissue injury behaviour in microwave thermal therapy using a porcine kidney model. Int J Hyperthermia. 2004;20(6):567–93.

148. Schutt DJ, Haemmerich D. Effects of variation in perfusion rates and of perfusion models in computational models of radio frequency tumor ablation. Med Phys. 2008;35(8):3462–70.

149. Youla DC, Bongiorno JJ, Lu CN. Single-loop feedback-stabilization of linear multivariable dynamical plants. Automatica. 1974;10(2):159–73.

150. COMSOL Webinar [Internet]. [cited 2017 Aug 1]. Available from: https://www.comsol.com/video/simulating-feedback-control-thermal-systems

151. Rylander MN, Feng Y, Zhang Y, Bass J, Jason Stafford R, Volgin A, et al. Optimizing heat shock protein expression induced by prostate cancer laser therapy through predictive computational models. J Biomed Opt. 2006;11(4):41113.

152. Oleson JR, Dewhirst MW, Harrelson JM, Leopold KA, Samulski T V., Tso CY. Tumor temperature distributions predict hyperthermia effect. Int J Radiat Oncol Biol Phys. 1989;16(3):559–70.

153. Arora D, Cooley D, Perry T, Skliar M, Roemer RB. Direct thermal dose control of constrained focused ultrasound treatments: phantom and in vivo evaluation. Phys Med Biol. 2005;50(8):1919–35.

154. Ivkov R, DeNardo SJ, Daum W, Foreman AR, Goldstein RC, Nemkov VS, et al. Application of high amplitude alternating magnetic fields for heat induction of nanoparticles localized in cancer. Clin Cancer Res. 2005;11(19 II):7093–103.

155. van der Koijk JF, Lagendijk JJ, Crezee J, de Bree J, Kotte a N, van Leeuwen GM, et al. The influence of vasculature on temperature distributions in MECS interstitial hyperthermia: importance of longitudinal control. Int J Hyperthermia. 1997;13(4):365–85.

156. Jordan a, Wust P, Fähling H, John W, Hinz a, Felix R. Inductive heating of ferrimagnetic particles and magnetic fluids: physical evaluation of their potential for hyperthermia. Int J Hyperthermia. 1993;9(1):51–68.

157. Stauffer PR, Cetas TC, Jones RC. Magnetic Induction Heating of Ferromagnetic Implants for Inducing Localized Hyperthermia in Deep-Seated Tumors. IEEE Trans Biomed Eng. 1984;BME-31(2):235–51.

158. Rosenthal N, Brown S. The mouse ascending: perspectives for human-disease models. Nat Cell Biol. 2007;9(9):993–9.

159. Peters LL, Robledo RF, Bult CJ, Churchill G a, Paigen BJ, Svenson KL. The mouse as a model for human biology: a resource guide for complex trait analysis. Nat Rev Genet. 2007;8(1):58–69.

160. LeBrun A, Joglekar T, Bieberich C, Ma R, Zhu L. Treatment efficacy for validating microCT based theoretical simulation approach in magnetic nanoparticle hyperthermia for cancer treatment. J Heat Transfer. 2016;139(c):1–7.

161. LeBrun A, Ma R, Zhu L. MicroCT image based simulation to design heating protocols in magnetic nanoparticle hyperthermia for cancer treatment. J Therm Biol.

2016;62:129–37.

162. Hedayati M, Abubaker-Sharif B, Khattab M, Razavi A, Mohammed I, Nejad A, et al. An optimised spectrophotometric assay for convenient and accurate quantitation of intracellular iron from iron oxide nanoparticles. Int J Hyperth. 2017;0(0):1–9.

163. Tomayko MM, Reynolds CP. ancer hemotherapy and harmacology Determination of subcutaneous tumor size in athymic (nude) mice *. Cancer Chemother Pharmacol. 1989;148–54.

164. Kumar A, Attaluri A, Mallipudi R, Cornejo C, Bordelon D, Armour M, et al. Method to reduce non-specific tissue heating of small animals in solenoid coils. Int J Hyperthermia. 2013;29(2):106–20.

165. Bordelon DE, Goldstein RC, Nemkov VS, Kumar A, Jackowski JK, DeWeese TL, et al. Modified solenoid coil that efficiently produces high amplitude AC magnetic fields with enhanced uniformity for biomedical applications. IEEE Trans Magn. 2012;48(1):47–52.

166. Kut C, Zhang Y, Hedayati M, Zhou H, Cornejo C, Bordelon D, et al. Preliminary study of injury from heating systemically delivered, nontargeted dextran-superparamagnetic iron oxide nanoparticles in mice. Nanomedicine. 2012;7(11):1697–711.

167. Van Beers BE, Leconte I, Materne R, Smith AM, Jamart J, Horsmans Y. Hepatic perfusion parameters in chronic liver disease: Dynamic CT measurements correlated with disease severity. Am J Roentgenol. 2001;176(3):667–73.

168. Werner J, Buse M. Temperature profiles with respect to inhomogeneity and geometry of the human body. J Appl Physiol. 1988;65(30):1110–8.

169. Wright NT. On a Relationship Between the Arrhenius Parameters from Thermal Damage Studies Neil. J Biomech Eng. 2007;125(April 2003):300–4.

170. Wust P, Gneveckow U, Johannsen M, Böhmer D, Henkel T, Kahmann F, et al. Magnetic nanoparticles for interstitial thermotherapy--feasibility, tolerance and achieved temperatures. Int J Hyperthermia. 2006;22(8):673–85.

171. Young JH, Wang MT, Brezovich I. Frequency / Depth-Penetration Considerations in Hyperthermia By Magnetically Induced Currents. Electron Lett. 1980;16(10):358–9.

172. Reilly JP. Magnetic field excitation of peripheral nerves and the heart: a comparison of thresholds. Med Biol Eng Comput. 1991;29(6):571–9.

173. Di Barba P, Dughiero F, Sieni E, Candeo A. Coupled field synthesis in magnetic fluid hyperthermia. IEEE Trans Magn. 2011;47(5):914–7.

174. Stigliano R V, Shubitidze F, Petryk AA, Tate JA, Hoopes PJ. Magnetic nanoparticle hyperthermia: Predictive model for temperature distribution. Proc Soc Photo Opt Instrum Eng. 2013;8584:858410.

175. Oberkampf WL, Trucano TG, Hirsch C. Verification, validation, and predictive capability in computational engineering and physics. Appl Mech Rev. 2004;57(5):345–84.

176. Wolf DC. Evaluation of the Size, Shape, and Consistency of the Liver. Clin Methods Hist Phys Lab Exam. 1990;62(6):478–81.

177. Brezovich I. Low frequency hyperthermia: capacitive and ferromagnetic thermoseed methods. Med Phys Monogr. 1988;16:82–111.

178. Bennett D. NaCl doping and the conductivity of agar phantoms. Mater Sci Eng C.

2011;31(2):494–8.

179. Attaluri A, Jackowski JK, Goldstein RC, Nemkov VS, Kumar A, Mirpour S, et al. Design and construction of an induction coil to treat deep tumors in large animals. Manuscr under Prep.

180. Rabin Y. A general model for the propagation of uncertainty in measurements into heat transfer simulations and its application to cryosurgery. Cryobiology. 2003;46(2):109–20.

181. Javidi M, Heydari M, Attar MM, Haghpanahi M, Karimi A, Navidbakhsh M, et al. Cylindrical agar gel with fluid flow subjected to an alternating magnetic field during hyperthermia. Int J Hyperth. 2015;31(1):33–9.

182. Zhang M, Che Z, Chen J, Zhao H, Yang L, Zhong Z, et al. Experimental Determination of Thermal Conductivity of Water - Agar Gel at Different Concentrations and Temperatures. J Chem Eng Data. 2011;(56):859–64.

183. FISO FOT-M Temperature sensor [Internet]. [cited 2017 Feb 8]. Available from: https://www.fiso.com/admin/useruploads/files/fot-m.pdf

184. Kline SJ. The Purposes of Uncertainty Analysis. J Fluids Eng. 1985;107(2):153.

185. 3D Slicer [Internet]. [cited 2017 Feb 8]. Available from: https://www.slicer.org/

186. MeshLab [Internet]. [cited 2017 Feb 8]. Available from: http://www.meshlab.net/

187. Stigliano R V., Shubitidze F, Petryk JD, Shoshiashvili L, Petryk AA, Hoopes PJ. Mitigation of eddy current heating during magnetic nanoparticle hyperthermia therapy. Int J Hyperth. 2016;6736(July):1–14.

188. Coleman HW, Stern F. Uncertainties and CFD code validation. J Fluids Eng Asme. 1997;119(4):795–803.

189. Swierczewska M, Lee S, Chen X. Inorganic nanoparticles for multimodal molecular imaging. Mol Imaging. 2011;10(1):3–16.

190. Gleich B, Weizenecker J. Tomographic imaging using the nonlinear response of magnetic particles. Nature. 2005;435(7046):1214–7.

191. Kim J, Lee JE, Lee SH, Yu JH, Lee JH, Park TG, et al. Designed fabrication of a multifunctional polymer nanomedical platform for simultaneous cancer-targeted imaging and magnetically guided drug delivery. Adv Mater. 2008;20(3):478–83.

192. Dewey WC, Hopwood LE, Sapareto SA, Gerweck LE. Cellular responses to combinations of hyperthermia and radiation. Radiology. 1977;123(2):463–74.

193. Roti Roti JL. Cellular responses to hyperthermia (40-46 degrees C): cell killing and molecular events. Int J Hyperthermia. 2008;24(1):3–15.

194. Wust P, Hildebrandt B, Sreenivasa G, Rau B, Gellermann J, Riess H, et al. Hyperthermia in combined treatment of cancer. Lancet Oncol. 2002;3(8):487–97.

195. Krawczyk PM, Eppink B, Essers J, Stap J, Rodermond H, Odijk H, et al. Mild hyperthermia inhibits homologous recombination, induces BRCA2 degradation, and sensitizes cancer cells to poly (ADP-ribose) polymerase-1 inhibition. Proc Natl Acad Sci U S A. 2011;108(24):9851–6.

196. Triantopoulou S, Efstathopoulos E, Platoni K, Uzunoglou N, Kelekis N, Kouloulias V. Radiotherapy in conjunction with superficial and intracavitary hyperthermia for the treatment of solid tumors: Survival and thermal parameters. Clin Transl Oncol. 2013;15(2):95–105.

197. McGlynn KA, Petrick JL, London WT. Global Epidemiology of Hepatocellular Carcinoma: An Emphasis on Demographic and Regional Variability. Clin Liver Dis.

2015;19(2):223–38.

198. Solomon SB, Silverman SG. Imaging in interventional oncology. Radiology. 2010;257(3):624–40.

199. Lencioni R, Crocetti L. Local-regional treatment of hepatocellular carcinoma. Radiology. 2012;262(1):43–58.

200. Liapi E, Geschwind J-FH. Intra-Arterial Therapies for Hepatocellular Carcinoma: Where Do We Stand? Ann Surg Oncol. 2010;17(5):1234–46.

201. Lewandowski RJ, Geschwind J, Liapi E, Salem R. Transcatheter intraarterial therapies: rationale and overview. Radiology. 2011;259(3):641–57.

202. Mitsumori M, Hiraoka M, Shibata T, Okuno Y, Masunaga S, Koishi M, et al. Development of intra-arterial hyperthermia using a dextran-magnetite complex. Int J Hyperth. 1994;10(6):785–93.

203. Mitsumori M, Hiraoka M, Shibata T, Okuno Y, Nagata Y, Nishimura Y, et al. Targeted hyperthermia using dextran magnetite complex: a new treatment modality for liver tumors. Hepatogastroenterology. 1996;43(12):1431–7.

204. Jones SK, Winter JG, Gray BN. Treatment of experimental rabbit liver tumours by selectively targeted hyperthermia. Int J Hyperthermia. 2002;18(2):117–28.

205. Moroz P, Jones SK, Gray BN. The effect of tumour size on ferromagnetic embolization hyperthermia in a rabbit liver tumour model. Int J Hyperth. 2002;18(2):129–40.

206. Idée J-M, Guiu B. Use of Lipiodol as a drug-delivery system for transcatheter arterial chemoembolization of hepatocellular carcinoma: A review. Crit Rev Oncol Hematol. 2013;88(3):530–49.

207. Attaluri A, Nusbaum C, Wabler M, Ivkov R. Calibration of a Quasi-Adiabatic Magneto-Thermal Calorimeter Used to Characterize Magnetic Nanoparticle Heating. J Nanotechnol Eng Med. 2013;4(1):11006.

208. Huang S, Wang S-Y, Gupta A, Borca-Tasciuc D-A, Salon SJ. On the measurement technique for specific absorption rate of nanoparticles in an alternating electromagnetic field. Meas Sci Technol. 2012;23(3):35701.

209. Lagally ET, Mathies R a. Integrated genetic analysis microsystems. J Phys D Appl Phys. 2004;37(23):R245–61.

210. Weast R. Handbook of chemistry and physics. CRC Press; 1984.

211. Choi SUS, Eastman JA. Enhancing thermal conductivity of fluids with nanoparticles. ASME Int Mech Eng Congr Expo. 1995;66(March):99–105.

212. Oommen T V. Vegetable oils for liquid-filled transformers. IEEE Electr Insul Mag. 2002;18(1):6–11.

213. Young H, Freedman R. University Physics. Pearson Education; 2008.

214. Gaur U, Wunderlich B. Heat Capacity and Other Thermodynamic Properties of Linear Macromolecules. V. Polystyrene. Vol. 11, Journal of Physical and Chemical Reference Data. 1982. p. 313–25.

215. Lv YG, Deng ZS, Liu J. 3-D Numerical Study on the Induced Heating Effects of Embedded Micro/Nanoparticles on Human Body Subject to External Medical Electromagnetic Field. IEEE Trans Nanobioscience. 2005;4(4):284–94.

216. Branquinho LC, Carrião MS, Costa AS, Zufelato N, Sousa MH, Miotto R, et al. Effect of magnetic dipolar interactions on nanoparticle heating efficiency: implications for cancer hyperthermia. Sci Rep. 2013;3:2887.

217. Wang YXJ, Hussain SM, Krestin GP. Superparamagnetic iron oxide contrast agents: Physicochemical characteristics and applications in MR imaging. Eur Radiol. 2001;11(11):2319–31.

218. Wang SY, Huang S, Borca-Tasciuc DA. Potential sources of errors in measuring and evaluating the specific loss power of magnetic nanoparticles in an alternating magnetic field. IEEE Trans Magn. 2013;49(1):255–62.

219. Jordan a, Scholz R, Wust P, Fähling H, Krause J, Wlodarczyk W, et al. Effects of magnetic fluid hyperthermia (MFH) on C3H mammary carcinoma in vivo. Int J Hyperthermia. 1997;13(6):587–605.

Vita

Sri Kamal Kandala was born in Visakhapatnam, India, in 1988. He obtained his Bachelors in Mechanical Engineering from the National Institute of Technology, Warangal, India in 2010. After that, he worked as an Engineer in Hindustan Petroleum Corporation Ltd. in Visakhapatnam, India for one year. Following this, he joined the Department of Mechanical Engineering at the Johns Hopkins University to pursue his graduate studies in 2011. He earned his Master's degree in December, 2012 and completed his doctoral study in 2017. His research focused on developing simulation based strategies for clinical translation of magnetic nanoparticle hyperthermia.